University of Southampton

Faculty of Engineering and Physical Sciences
Department of Physics & Astronomy

Theory and phenomenology of the Vector Dark Matter with Fermionic Portal

by

Nakorn Thongyoi

ORCiD: 0000-0002-2261-0569

A thesis for the degree of
Doctor of Philosophy

February 2024

University of Southampton

Abstract

Faculty of Engineering and Physical Sciences
Department of Physics & Astronomy

Doctor of Philosophy

Theory and phenomenology of the Vector Dark Matter with Fermionic Portal

by Nakorn Thongyoi

Even though the Standard Model (SM) of elementary particle physics is very successful in explaining countless microscopic phenomena, it is still not the ultimate theory of everything we have been seeking for. So far we witness several drawbacks of the SM, for example, the neutrino masses, Dark Matter (DM), dark energy, Baryon Asymmetry of the Universe (BAU) and the SM anomalies. Especially, the long standing issue of DM of the universe which has been well-established by multiple cosmological observations and constrained by several ground-based experiments. Additionally, the recent experiment on muon $g_\mu - 2$ by the Fermilab National Accelerator Laboratory (FNAL) has precisely measured the anomalous magnetic moment of the muon and implies a 5σ tension between SM prediction and experimental results. In this thesis, we have introduced a new mechanism to connect the SM and dark sector through a fermionic portal. This class of model extends the SM gauge group with a new $SU(2)_D \times U(1)^{\text{global}}_{Y_D}$ group while all SM particles are neutral with respect to the additional groups. Two of the new gauge bosons ($V_D^{(*)}$) form a complex gauge boson and carry $U(1)^{\text{global}}_{Y_D}$ charge. Thus, they can play a role as a DM candidate for this class. Moreover, two generic Vector Like (VL) fermions are introduced to mediate the interaction between the SM and dark sectors equipping us the opportunity to study the DM dark matter phenomenology at collider and non-collider environments. The origin of masses for new degrees of freedom is provided by the interaction with an additional complex scalar doublet (Φ_D) through the spontaneous breakdown of the $SU(2)_D \times U(1)^{\text{global}}_{Y_D}$ into $U(1)^{\text{global}}_{Q_D}$ when the scalar Φ_D acquires the Vacuum Expectation Value (VEV). The residual symmetry $U(1)^{\text{global}}_{Q_D}$ acts as a stabiliser of the DM candidate of the model. The key feature of this model is the Higgs portal to dark sector is not necessarily required but the connection to SM sector is induced by new Yukawa terms between SM and VL fermions, hence the title – the Vector Dark Mater with Fermionic Portal (FPVDM). The FPVDM model suggests numerous phenomenological implications for collider and non-collider studies. In this thesis, we will discuss only two scenarios from this class: the top quark and muonic portal scenarios, as presented in chapter 3 and 4, respectively.

In chapter 3, we discuss in detail a realisation with VL top quark partners (TPVDM), assuming no mixing between the two physical scalars of the theory, the SM Higgs boson and its counterpart in the dark sector. The material presented in this chapter is based on the publications [1, 2]. In collider phenomenology point of view, it predicts multiple interesting signatures that a complete set of signatures is presented in table 3.1. These are mono-jet from initial state radiation (ISR) or from loop, $t\bar{t} + E_{\mathrm{T}}^{\mathrm{miss}}$, 4-top quarks, and the production of hV' and $V'V'$. The VL $\mathbb{Z}_2$-odd partner t_D could be long-lived and leaves a charged track by decaying into the DM and the SM quarks and/or leptons. In addition, the new gauge boson V' could also be long-lived if its mass is below $t\bar{t}$ threshold and decays into a pair of $b\bar{b}$ via a loop diagram. The cosmological bounds (relic abundance, direct and indirect detection) play a vital role in constraining the parameter space of the model. Especially, the direct detection limit which is absent at tree level. However, at loop level, it leads to a crucial constraint based on the triangle loop of DM-DM-Z/γ. The generic formulas for these triangle loops are present here.

In addition, we also explore the possibility to apply the FPVDM framework to explain the muon anomalous magnetic moment or the so-called $g_\mu - 2$ and the DM at the same time where we assume the existence of VL muons μ_D and μ'. This scenario is referred to as the MPVDM and will be a topic of chapter 4 which is based on upcoming article entitled "The muon anomalous magnetic moment $g_\mu - 2$ from the Fermionic Portal to Vector Dark Matter" [3]. Like the TPVDM, we are not considering the Higgs portal in this study. The interplay between cosmological and $g_\mu - 2$ constraints plays a crucial role in limiting the parameter space of the MPVDM. We found that the allowed region appears on the resonance position of new scalar H_D. Moreover, the collider constraints from LHC data according to $pp \to \mu^+\mu^- + E_{\mathrm{T}}^{\mathrm{miss}}$ searches set up the lower limits on the VL muon masses around 700-800 GeV depending on the parameter space. Several interesting signatures are predicted with 6-10 leptons in the final state. We also provide benchmarks which are allowed by $g_\mu - 2$, cosmological and collider constraints for testing the model in future.

Contents

List of Figures

List of Tables

Declaration of Authorship

I declare that this thesis and the work presented in it is my own and has been generated by me as the result of my own original research.

I confirm that:

1. This work was done wholly or mainly while in candidature for a research degree at this University;
2. Where any part of this thesis has previously been submitted for a degree or any other qualification at this University or any other institution, this has been clearly stated;
3. Where I have consulted the published work of others, this is always clearly attributed;
4. Where I have quoted from the work of others, the source is always given. With the exception of such quotations, this thesis is entirely my own work;
5. I have acknowledged all main sources of help;
6. Where the thesis is based on work done by myself jointly with others, I have made clear exactly what was done by others and what I have contributed myself;
7. Parts of this work have been published as: *Fermionic portal to vector dark matter from a new gauge sector* [1, 2] and upcoming article entitled "*The muon anomalous magnetic moment $g_\mu - 2$ from the Fermionic Portal to Vector Dark Matter*" [3].

Signed:..... Date:.....

Acknowledgements

First of all, I would like to thank Development and Promotion of Science and Technology Talents Project (DPST) under Royal Government of Thailand scholarship that grants me a funding for studying at the University of Southampton where I have not only learnt physics but also met great fellow students who were pursuing the same thing.

Many thanks to my great supervisor, Professor Alexander Belyaev, who accepted me as his PhD student and helping me get through this journey successfully. I would not be able to finish my PhD without his support in several aspects. I have learnt many things from him not only physics but also how to be a successful person in the future and to work effectively under our limited lifetime.

I also thank my collaborators Aldo Deandrea, Stefano Moretti. Especially, Luca Panizzi whom I have learnt the dark matter model-building aspect from and Douglas A. Ross who taught me how to calculate the radiative correction to the triangle loops. Alexander Pukhov who implemented the special code for calculating dark matter direct detection with virtual photon.

Last but not least, I would like to thank my parents, Mr. Phattharathon and Mrs. Saengdao Thongyoi and my fiancee, Ms. Thidarat Srithip, who always give me a support whenever I was tired from my study and keep telling me to move forward.

Chapter 1

Introduction

In this chapter, we review a short summary of the Standard Model (SM) in section 1.1. Also, the elementary cosmology is briefly discussed in section 1.2 which includes the thermodynamics of the early universe and the Boltzmann equation. In section 1.3, we give a brief introduction to the Dark Matter (DM) of the universe including the relic density, (in)direct detection and collider constraints. In the last section 1.4, the anomalous magnetic moment of muon, so-called the muon $g_\mu - 2$, is considered in both experimental and theoretical aspects.

1.1 The standard model of particle physics

The Standard Model (SM) of particle physics is one of the most successful theory in physics which can successfully explain microscopic phenomena at fundamental level. The theory has been developed based on quantum field theory (QFT) [4, 5, 6] which is a theoretical framework of physics relying on three principles: 1) theory of classical fields, 2) quantisation and 3) special relativity. According to QFT, a particle is interpreted as an excited state of the corresponding quantum field. All fundamental particles have their underlying quantum fields and they interact with each other through force carriers.

Apart from those three principles, the SM is constructed based on the $SU(3)_c \times SU(2)_L \times U(1)_Y$ symmetry group which is a very crucial part of the theory because it governs how particles interact with each other. The elementary particles in the SM contains a *scalar* with spin-0 at the Electro-Weak (EW) scale, *fermions* with spin-1/2 and *gauge bosons* with spin-1. At the EW scale, the only one scalar in the SM is called the *Higgs boson* which gives masses to other particles through a process of *spontaneous symmetry breaking*. The fermions can be divided into *leptons* and *quarks* – according to whether they feel strong interaction or not. Leptons can have electromagnetic and weak interactions while quarks can additionally interact through strong nuclear force. The

gauge bosons are also elementary particles that mediate interactions amongst particles, sometimes we call them the mediators. All interactions have their own mediators or the corresponding gauge bosons, except for the Yukawa interactions.

The three fundamental forces or interactions such as electromagnetic, weak and strong forces can successfully explained by the SM theory – except for gravity which is successfully explained by Einstein's general relativity. These forces have their own force carriers or mediators. The mediator of electromagnetic, weak and strong interactions are called *photons*, Z and W bosons and *gluons*, respectively. Within the framework of the SM, a minimal set of fermions is comprised of *six leptons* (three charged leptons and three neutrinos) and *eighteen quarks* (there are six flavours of quarks and each of them has three colours) which implies six anti-leptons and eighteen anti-quarks. The neutral leptons only carry weak quantum numbers, while the charged leptons can carry both electromagnetic and weak quantum numbers. Unlike leptons, quarks and anti-quarks additionally carry colour charge, a quantum number for strong interaction.

In addition. the symmetry is also a central part of the SM which is intimately related to a group theory. The most simplest symmetry group is an Abelian group $U(1)$ endowed with only one generator of identity matrix. A more complicated symmetry group such as $SU(3)$ and $SU(2)$ is called a non-Abelian group. For any $SU(N)$ group, there are N^2-1 generators. According to gauge theory of particle physics, the number of generators of a theory corresponds to the number of gauge bosons. A generator of a group can be represented in various forms but the most familiar one in SM is either the *fundamental* or *adjoint* representations. For gauge field theory, every generator has the corresponding gauge boson field that plays a role as a mediator of the interaction. Therefore, $SU(3)_c$, $SU(2)_L$ and $U(1)_Y$ symmetry groups respectively contains eight gluons, three weak and one hypercharge gauge bosons. The labels c and Y are the corresponding quantum numbers for colour and hypercharge that identify the particle properties in the SM. However, the label L on the $SU(2)_L$ is not the quantum number but it indicates that the left-handed particles transform as a doublet under $SU(2)_L$.

As mentioned before that there exist six leptons in the SM, three of them are electrically charged leptons and other three are their corresponding neutrinos. A left-handed charged lepton and a neutrino form a doublet under $SU(2)_L$ giving us three left-handed doublets or three generations of leptons: $(\nu_e, e)_L^T$, $(\nu_\mu, \mu)_L^T$ and $(\nu_\tau, \tau)_L^T$. However, right-handed charged leptons (e_R, μ_R, τ_R) transform as a singlet under $SU(2)_L$. There are no right-handed neutrinos in the SM. Since they do not interact via the strong interaction they have no colour charge. Like leptons, left-handed quarks also transform as a doublet under $SU(2)_L$ group and they form three generations or doublets: $(u, d)_L^T$, $(c, s)_L^T$ and $(t, b)_L^T$ whereas all right-handed quarks transform as a singlet. The SM particles, masses and their corresponding quantum numbers under $SU(3)_c \times SU(2)_L \times U(1)_Y$ are succinctly summarised in table 1.1 for future reference.

Field	Symbol	Spin	$SU(3)_c$	$SU(2)_L$	$U(1)_Y$
Leptons	$L_L^I = \begin{pmatrix}\nu_e\\ e\end{pmatrix}_L, \begin{pmatrix}\nu_\mu\\ \mu\end{pmatrix}_L, \begin{pmatrix}\nu_\tau\\ \tau\end{pmatrix}_L$	$\frac{1}{2}$	**1**	**2**	$-\frac{1}{2}$
	$\ell_R^I = e_R, \mu_R, \tau_R$	$\frac{1}{2}$	**1**	**1**	-1
Quarks	$Q_L^I = \begin{pmatrix}u\\ d\end{pmatrix}_L, \begin{pmatrix}c\\ s\end{pmatrix}_L, \begin{pmatrix}t\\ b\end{pmatrix}_L$	$\frac{1}{2}$	**3**	**2**	$\frac{1}{6}$
	$u_R^I = u_R, c_R, t_R$	$\frac{1}{2}$	**3**	**1**	$\frac{2}{3}$
	$d_R^I = d_R, s_R, b_R$	$\frac{1}{2}$	**3**	**1**	$-\frac{1}{3}$
Hypercharge boson	B_μ	1	**1**	**1**	0
Weak bosons	$W_\mu^i = W_\mu^1, W_\mu^2, W_\mu^3$	1	**1**	**3**	0
Gluons	$G_\mu^a = G_\mu^1, G_\mu^2, ..., G_\mu^8$	1	**8**	**1**	0
Higgs boson	$\Phi = \begin{pmatrix}\phi^+\\ \phi_1 + i\phi_2\end{pmatrix}$	0	**1**	**2**	$\frac{1}{2}$

TABLE 1.1: The particles in the SM with their corresponding quantum numbers in gauge basis.

In addition, one of the most important components in the SM is the Higgs boson which interacts with all massive particles. When symmetry group of the SM breaks from $SU(3)_c \times SU(2)_L \times U(1)_Y$ to $SU(3)_c \times U(1)_Q$ due to the spontaneous symmetry breaking [7], Higgs boson will gives masses to other particle. This process is called the *Higgs mechanism* [8]. We will discuss this topic to some extent in section 1.1.3.

1.1.1 The SM Lagrangian and its particle content

As mentioned before, QFT relies on three fundamental elements. The first is the theory of fields which we assume that the universe is filled out with several quantum fields corresponding to fundamental particles. Thus, instead of finding the equation of motion of particles here, we consider the equation of motion of fields. The second is the quantisation principle which we promote a corresponding field to an operator satisfying the commutation relation between the field $\phi_i(x)$ where $i = 1, 2, ..., n$ and its associated momentum conjugate $\pi^i(x) = \partial\mathcal{L}/\partial\dot{\phi}_i(x)$. Here $\mathcal{L}$ is the Lagrangian of a system and $\dot{\phi}_i = \partial\phi_i/\partial t$. The last one is the principle of special relativity which implies that the Lagrangian of a system must be invariant under Lorentz transformation – the rotation and boost transformations. This means that the QFT Lagrangian describing a system of interest must obey all of these principles. However, some theories can also have gauge symmetries in addition to the Lorentz symmetry. For example, apart from the Lorentz invariance, the SM also satisfies the gauge symmetry of $SU(3)_c \times SU(2)_L \times U(1)_Y$ group.

Quantity	Symbol	Value
Fermi Constant	G_F	$1.166\,378\,7(6) \times 10^{-5}$ GeV^{-2}
weak-mixing angle	$\sin^2\theta_W$ ($\overline{\text{MS}}$)	0.231 22(4)
strong couple constant at m_Z	$\alpha_S(m_Z)$	0.1181(11)
fine-structure constant at m_W	$\alpha(m_W^2)$	1/128
Higgs boson mass	m_H	125.18(0.16) GeV
Higgs decay width	Γ_H	$3.2^{+2.4}_{-1.7}$ MeV
$W^\pm$ boson mass	m_W	80.377(0.012) GeV
$W^\pm$ decay width	Γ_W	2.085(0.042) GeV
Z boson mass	m_Z	91.1876(0.0021) GeV
Z decay width	Γ_Z	2.4955(0.023) GeV
top quark mass	m_t	172.69(0.30) GeV
top quark decay width	Γ_t	$1.42^{+0.19}_{-0.15}$ GeV
bottom quark mass	$m_b(m_b)$	$4.18^{+0.03}_{-0.02}$ GeV
charm quark mass	$m_c(m_c)$	1.27(0.02) GeV
strange quark mass	$m_s(2\ \text{GeV})$	$93.4^{+8.6}_{-3.4}$ MeV
up quark mass	$m_u(2\ \text{GeV})$	$2.16^{+0.49}_{-0.26}$ MeV
down quark mass	$m_d(2\ \text{GeV})$	$4.67^{+0.48}_{-0.17}$ MeV
tau mass	m_τ	1776.86(0.12) MeV
muon mass	m_μ	105.6583755(0.0000023) MeV
electron mass	m_e	0.51099895000(0.00000000015) MeV

TABLE 1.2: Some of the measured values of the SM parameters [9]. The number in the bracket indicates the uncertainty.

For the SM, the Lagrangian invariant under Lorentz symmetry and $SU(3)_c \times SU(2)_L \times U(1)_Y$ group is given by

$$\begin{aligned}\mathcal{L}_{\text{SM}} = &-\frac{1}{4}B_{\mu\nu}B^{\mu\nu} - \frac{1}{4}W^i_{\mu\nu}W^{i\mu\nu} - \frac{1}{4}G^a_{\mu\nu}G^{a\mu\nu} \\ &+ i\overline{L}^I_L \not{D} L^I_L + i\overline{\ell}^I_R \not{D} \ell^I_R + i\overline{Q}^I_L \not{D} Q^I_L + i\overline{u}^I_R \not{D} u^I_R + i\overline{d}^I_R \not{D} d^I_R \\ &- Y^I_\ell \overline{L}^I_L \Phi \ell^I_R - Y^{IJ}_d \overline{Q}^I_L \Phi d^J_R - Y^{IJ}_u \overline{Q}^I_L \tilde{\Phi} u^J_R + h.c. \\ &+ (D_\mu \Phi^\dagger)(D^\mu \Phi) - V(\Phi), \end{aligned} \tag{1.1}$$

where the indices i, j, k on the weak gauge bosons running over 1,2,3 corresponding to the number of $SU(2)$ generators. The indices a, b, c ranges from 1,2,...,8 indicating the number of $SU(3)$ generators. However, the indices I, J, K on quarks or leptons also runs over 1,2,3 but they identify the number of fermion generations which we have three generations for the SM fermions.

The first line of Eq.(1.1) describes the kinetic term of $U(1)_Y$, $SU(2)_L$ and $SU(3)_c$ gauge fields, respectively, and they are defined as follows

$$B_{\mu\nu} = \partial_\mu B_\nu - \partial_\nu B_\mu, \tag{1.2}$$
$$W^i_{\mu\nu} = \partial_\mu W^i_\nu - \partial_\nu W^i_\mu + g\,\epsilon^{ijk}\,W^j_\mu W^k_\nu, \tag{1.3}$$
$$G^a_{\mu\nu} = \partial_\mu G^a_\nu - \partial_\nu G^a_\mu + g_s\,f^{abc}\,G^b_\mu G^c_\nu. \tag{1.4}$$

where g and g_s are called the weak and strong coupling constants, respectively. The field strength tensors in Eqs.(1.2), (1.3) and (1.4) imply that the non-Abelian gauge fields are allowed to interact with themselves because they carry their own charges. This does not hold for B_μ or an Abelian field. Even though we call them the kinetic terms, they also describe the interaction amongst themselves. The ϵ^{ijk} and f^{abc} are the structure constants of $SU(2)$ and $SU(3)$ group which are defined through the commutation relation of their generators

$$[\tau^i, \tau^j] = i\epsilon^{ijk}\tau^k, \tag{1.5}$$
$$[t^a, t^b] = if^{abc}t^c, \tag{1.6}$$

and these generators are normalised with respect to

$$\mathrm{Tr}\{\tau^i\tau^j\} = \frac{1}{2}\delta^{ij}, \qquad \mathrm{Tr}\{t^a t^b\} = \frac{1}{2}\delta^{ab}, \tag{1.7}$$

where $\tau^i \equiv \sigma^i/2$ and $t^a \equiv \lambda^a/2$ are the generators of $SU(2)$ and $SU(3)$, respectively. Tr is a trace. The σ^i and λ^a are called the Pauli and Gell-man matrices given by

$$\sigma^1 = \begin{pmatrix} 0 & 1 \\ 1 & 0 \end{pmatrix}, \quad \sigma^2 = \begin{pmatrix} 0 & -i \\ i & 0 \end{pmatrix}, \quad \sigma^3 = \begin{pmatrix} 1 & 0 \\ 0 & -1 \end{pmatrix}, \tag{1.8}$$

and

$$\lambda^1 = \begin{pmatrix} 0 & 1 & 0 \\ 1 & 0 & 0 \\ 0 & 0 & 0 \end{pmatrix}, \quad \lambda^2 = \begin{pmatrix} 0 & -i & 0 \\ i & 0 & 0 \\ 0 & 0 & 0 \end{pmatrix}, \quad \lambda^3 = \begin{pmatrix} 1 & 0 & 0 \\ 0 & -1 & 0 \\ 0 & 0 & 0 \end{pmatrix},$$
$$\lambda^4 = \begin{pmatrix} 0 & 0 & 1 \\ 0 & 0 & 0 \\ 1 & 0 & 0 \end{pmatrix}, \quad \lambda^5 = \begin{pmatrix} 0 & 0 & -i \\ 0 & 0 & 0 \\ i & 0 & 0 \end{pmatrix}, \quad \lambda^6 = \begin{pmatrix} 0 & 0 & 0 \\ 0 & 0 & 1 \\ 0 & 1 & 0 \end{pmatrix},$$
$$\lambda^7 = \begin{pmatrix} 0 & 0 & 0 \\ 0 & 0 & -i \\ 0 & i & 0 \end{pmatrix}, \quad \lambda^8 = \frac{1}{\sqrt{3}}\begin{pmatrix} 1 & 0 & 0 \\ 0 & 1 & 0 \\ 0 & 0 & -2 \end{pmatrix}. \tag{1.9}$$

The second line of Eq.(1.1) contains only the kinetic terms of the SM fermions. Since the

SM is a chiral theory meaning that the left- and right-handed fields transform differently under the SM gauge group, we use a symbol L_L^I for a collection of three left-handed lepton doublets and Q_L^I for three left-handed quark doublets. On the other hand, we use u_R^I and d_R^I for a collection of three right-handed up-type and down-type quarks, respectively. Also, ℓ_R^I is for a collection of three right-handed charged leptons. There is no right-handed neutrinos in the SM framework since at the time the electroweak theory was formulated it was believed that neutrinos are massless particles. However, this is not the case. Due to observations of neutrino oscillations, it implies that neutrinos are actually massive. In addition, the symbol $\not{D} = \gamma^\mu D_\mu$ is called the covariant derivative which is contracted with Dirac gamma matrices γ^μ where μ is a spacetime index running over 0-3. The Dirac gammas in the chiral representation are given by

$$\gamma^0 = \begin{pmatrix} I & 0 \\ 0 & I \end{pmatrix}, \quad \gamma^k = \begin{pmatrix} 0 & \sigma^k \\ -\sigma^k & 0 \end{pmatrix}, \quad \gamma_5 = i\gamma^0\gamma^1\gamma^2\gamma^3 = \begin{pmatrix} 0 & I \\ I & 0 \end{pmatrix}, \tag{1.10}$$

where I is a 2×2 identity matrix. In principle, a 4-component Dirac spinor can be separated into two chiral spinors (left- and right-handed components) as

$$\psi = \begin{pmatrix} \psi_L \\ \psi_R \end{pmatrix}, \tag{1.11}$$

where left- and right-handed chiral fermions are defined by $\psi_L \equiv P_L\psi$ and $\psi_R \equiv P_R\psi$ with $P_L = (1 - \gamma_5)/2$ and $P_R = (1 + \gamma_5)/2$ where the P_L and P_R are left and right chirality projection operators. The covariant derivative describes the interaction between the gauge bosons with other particles if those particles carry charges related to the corresponding symmetry group. For the SM, the generic covariant derivative reads

$$D_\mu = \partial_\mu - ig_s t^a G_\mu^a - ig\tau^i W_\mu^i - ig' Y B_\mu \mathbf{1}, \tag{1.12}$$

where $\partial_\mu = \partial/\partial x^\mu$ and g's are the gauge couplings. The Y is called the hypercharge and $\mathbf{1}$ is the 2×2 identity matrix. However, this covariant derivative is not the same for all SM fields. For example, the explicit form of covariant derivative for the Higgs doublet can be seen in section 1.1.3.

The third line of Eq.(1.1) is called the Yukawa terms in which they describe the interaction of fermions with the Higgs field where Y_ℓ, Y_d and Y_u are called the Yukawa couplings for charged leptons, up-type and down-type quarks, respectively. The Higgs field is the only scalar in the SM and gives masses to all particles (except for neutrinos) in the SM the so-called Higgs mechanism which undergoes the spontaneous symmetry breaking of the SM gauge group. We will discuss the Higgs mechanism and the spontaneous breakdown of the SM symmetry later in this chapter.

The last line of Eq.(1.1) describes the dynamics of the Higgs fields where the first expression is the kinetic term (see the explicit form of D_μ in section 1.1.3) and the second

one is called the scalar potential which is given by

$$V(\Phi) = \mu^2 \Phi^\dagger \Phi + \lambda (\Phi^\dagger \Phi)^2, \tag{1.13}$$

where Φ is the SM Higgs doublet. μ and λ are, respectively, the quadratic and quartic couplings. Also, the quartic coupling has to be positive, otherwise the potential is not bounded from below at large $\Phi^\dagger \Phi$.

1.1.2 The quantum chromodynamics (QCD)

In this section, we discuss the theory of strong interaction based on $SU(3)_c$ which describes the behaviour of hadrons – particles made up of quarks – and gluons. Both quarks and gluons carry the quantum number associated with the strong interaction which is called the colour charge as a label of $SU(3)$. Normally, we use red, green and blue to distinguish each colour of quarks and anti-red, anti-green and anti-blue for anti-quarks. Quarks(antiquarks) and gluons transform as a triplet **3** ($\bar{\mathbf{3}}$) and octet **8** under this group, respectively. Generically hadrons can be categorised into different groups depending on a number of particles forming them, for example, mesons (made up of a pair of a quark and an antiquark) and baryons (made up of three quarks). In the SM, we have 6 quarks and each quark has 3 colours. This means that we have 18 quarks in colour space. The gluons are massless particles because the $SU(3)_c$ is not broken. The Lagrangian of the quantum chromodynamics is given by

$$\mathcal{L} = -\frac{1}{4} G^a_{\mu\nu} G^{a\mu\nu} + i \overline{q}^i \not{D}_{ij} q^j, \tag{1.14}$$

where $G^a_{\mu\nu}$ is defined in Eq.(1.4), $q_i = u, d, c, s, t, b$, the covariant derivative is $(D_\mu)_{ij} = \partial_\mu \delta_{ij} - i g_s (t^a)_{ij} G^a_\mu$. Here the indices $i, j, k, ...$ represents the colour index running over 1-3. The δ_{ij} is the Kronecker delta function and t^a generators in fundamental representation are given by Eqs.(1.6) and (1.9). A quark and an antiquark field in colour space can be written as

$$q = \begin{pmatrix} q^{\text{red}} \\ q^{\text{green}} \\ q^{\text{blue}} \end{pmatrix}, \quad \bar{q} = \begin{pmatrix} \bar{q}^{\text{anti-red}} \\ \bar{q}^{\text{anti-green}} \\ \bar{q}^{\text{anti-blue}} \end{pmatrix}, \tag{1.15}$$

where q stands for a quark flavour u, d, c, s, t, b.

The QCD Lagrangian Eq.(1.14) is invariant under the gauge transformation

$$\begin{aligned} q_i(x) &\to \exp\left(i\theta^a(x) t^a_{ij}\right) q_j(x), \\ t^a G^a_\mu(x) &\to e^{i\theta^a(x) t^a} t^a G^a_\mu(x) e^{-i\theta^a(x) t^a} + \frac{i}{g_s} \left(\partial_\mu e^{i\theta^a(x) t^a}\right) e^{-i\theta^a(x) t^a}, \end{aligned} \tag{1.16}$$

where θ^a is the parameter corresponding to the $SU(3)_c$ generators. The generator t^a in the first and second line of Eq.(1.16) are in the fundamental and adjoint representation, respectively.

1.1.3 The EW sector

The Higgs mechanism is used to describe the origin of the particle masses in the SM. It happens through a process of spontaneously symmetry breaking where the electroweak (EW) group $SU(2)_L \times U(1)_Y$ breaks down into $U(1)_Q$ where Q is the electric charge in the unit of $|e|$. The breakdown of the SM symmetry occurs because the Higgs field acquires the non-zero VEV where the symmetry of the Lagrangian is not that of the vacuum state of the Higgs field. In the SM, the Higgs is a complex scalar field transforming as a doublet of $SU(2)_L \times U(1)_Y$. Generically, we can write it with four real degrees of freedom as

$$\Phi = \begin{pmatrix} \phi^+ \\ \phi^0 \end{pmatrix} = \frac{1}{\sqrt{2}} \begin{pmatrix} \phi_1 + i\phi_2 \\ \phi_3 + i\phi_4 \end{pmatrix}. \tag{1.17}$$

The superscript on ϕ indicates the electric charge and it is consistently determined by the interaction with other particles. For example, the Yukawa term of a lepton doublet. By minimising the scalar potential in Eq.(1.13), we found that

$$|\Phi_0|^2 = (\phi_1^2 + \phi_2^2 + \phi_3^2 + \phi_4^2) = -\frac{\mu^2}{\lambda} \equiv v^2, \tag{1.18}$$

where Φ_0 represents the configuration that minimises the scalar potential and v is the VEV of SM Higgs. Since ϕ_1 and ϕ_2 combine to form a charged state and they cannot acquire the VEV, otherwise they would give mass to photon. In addition, for real v, the ϕ_4 cannot get the VEV because it would generate the complex masses in Yukawa terms. With this argument, the Φ can be recast into

$$\Phi = \frac{1}{\sqrt{2}} \begin{pmatrix} \sqrt{2}w^\pm \\ v + h + iz \end{pmatrix} \tag{1.19}$$

The h is called the Higgs boson and $w^\pm$ and z are the Goldstone bosons [10, 11, 12] which describe the longitudinal component of the $W^\pm$ and Z boson, respectively.

The Lagrangian of Higgs field

As described near the end of section 1.1.1, the dynamics of the scalar field Φ can be explained by the Lagrangian

$$\mathcal{L}_{\text{scalar}} = (D_\mu \Phi)^\dagger (D^\mu \Phi) - V(\Phi). \tag{1.20}$$

It is also explained that if μ^2 in Eq.(1.13) is positive the VEV of SM Higgs is zero and we cannot generate the mass of particles through the spontaneously symmetry breaking mechanism. To get a non-zero VEV, the μ^2 needs to be negative or equivalently the potential needs to be rewritten as

$$V(\Phi) = -\mu^2 \Phi^\dagger \Phi + \lambda (\Phi^\dagger \Phi)^2, \tag{1.21}$$

with positive μ^2. This scalar Lagrangian is invariant under the gauge transformations:

$$\begin{aligned} \Phi &\to \exp\left(i\alpha^i(x)\tau^i + i\beta(x)Y\right)\Phi \quad \text{(onfundamentaltransformation)}, \\ B_\mu &\to B_\mu - \frac{1}{g'}\partial_\mu \beta(x), \\ \tau^i W^i_\mu &\to e^{i\alpha^i(x)\tau^i}\tau^i W^i_\mu e^{-i\alpha^i(x)\tau^i} + \frac{i}{g}\left(\partial_\mu e^{i\alpha^i(x)\tau^i}\right)e^{-i\alpha^i(x)\tau^i}, \end{aligned} \tag{1.22}$$

where $\alpha(x)$ and $\beta(x)$ are the parameter of the gauge transformation related to $SU(2)_L$ and $U(1)_Y$. The first term of Eq.(1.20) will provide masses of gauge bosons which we will discuss later.

Let us minimise the scalar potential by doing derivative of Eq.(1.21) with respect to Φ and set it to be zero

$$0 \equiv \left.\frac{\partial V}{\partial \Phi}\right|_{w^\pm, z, h=0} = v(-\mu^2 + \lambda v^2). \tag{1.23}$$

There are two solutions corresponding to the above equation

$$v_1 = 0 \qquad \text{and} \qquad v_2 = \pm\sqrt{\frac{\mu^2}{\lambda}}. \tag{1.24}$$

For the second derivative of the scalar potential, it implies that

$$\frac{\partial^2 V}{\partial \Phi^\dagger \partial \Phi} = -\mu^2 + 4\lambda \Phi^\dagger \Phi. \tag{1.25}$$

If $\langle \Phi \rangle = v_1$, it gives the local maximum and for $\langle \Phi \rangle = v_2$ it gives the local minimum. With the scalar Lagrangian in terms of component fields

$$\begin{aligned} \mathcal{L}_{\text{scalar}} = {} & \partial_\mu w^- \partial^\mu w^+ + \frac{1}{2}\partial_\mu z \partial^\mu z + \frac{1}{2}\partial_\mu h \partial^\mu h \\ & + \mu^2(w^- w^+ + v^2 + 2vh + h^2 + z^2) - \lambda(w^- w^+ + v^2 + 2vh + h^2 + z^2)^2, \end{aligned} \tag{1.26}$$

we can find the mass of scalar fields by computing second derivative of the potential with respective to the corresponding field

$$\begin{aligned} m_h^2 &= \left.\frac{\partial^2 V}{\partial h^2}\right|_{w^\pm,z,h=0} = 2\lambda v^2, \\ m_{w^\pm}^2 &= \left.\frac{\partial^2 V}{\partial w^+ \partial w^-}\right|_{w^\pm,z,h=0} = 0, \\ m_z^2 &= \left.\frac{\partial^2 V}{\partial z^2}\right|_{w^\pm,z,h=0} = 0. \end{aligned} \tag{1.27}$$

Clearly, the Goldstone bosons for $W^\pm$ and Z bosons are massless particles. The mass of Higgs boson is given by $m_H = \sqrt{2\lambda v^2}$.

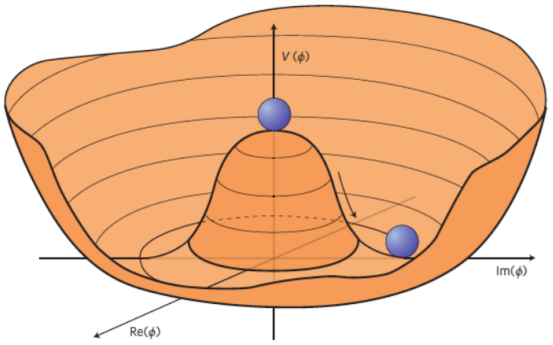

FIGURE 1.1: Higgs potential as a function of Φ.

Gauge boson mass

Additionally, the masses of weak gauge bosons can also be computed. Let us consider the kinetic term of the scalar doublet with hypercharge $Y = 1/2$ in Eq.(1.20) by keeping only the VEV for simplicity, one has

$$\begin{aligned} |D_\mu \Phi|^2 &= \left| \left(\partial_\mu - ig\tau^i W_\mu^i - ig' \frac{1}{2} B_\mu \mathbf{1} \right) \frac{1}{\sqrt{2}} \begin{pmatrix} 0 \\ v \end{pmatrix} \right|^2, \\ &= \left| \left(\partial_\mu - i \begin{pmatrix} \frac{g'}{2} B_\mu + \frac{g}{2} W_\mu^3 & \frac{g}{2}(W_\mu^1 - iW_\mu^2) \\ \frac{g}{2}(W_\mu^1 + iW_\mu^2) & \frac{g'}{2} B_\mu - \frac{g}{2} W_\mu^3 \end{pmatrix} \right) \frac{1}{\sqrt{2}} \begin{pmatrix} 0 \\ v \end{pmatrix} \right|^2, \\ &= \frac{1}{2} \frac{v^2}{4} \left[g^2 (W_\mu^1)^2 + g^2 (W_\mu^2)^2 + (-gW_\mu^3 + g' B_\mu)^2 \right]. \end{aligned} \tag{1.28}$$

We see that W^1 and W^2 are degenerate in their masses. These particles can be redefine to form the $W^\pm$ bosons as follows

$$W_\mu^\pm = \frac{1}{\sqrt{2}} (W_\mu^1 \mp i W_\mu^1). \tag{1.29}$$

Notice that in gauge basis W^3 and B bosons mix and the mass term is given by

$$\mathcal{L}^{\text{mass}}_{\text{gauge}} = \tilde{G}^T \mathcal{M} \tilde{G} = \frac{v^2}{4} \begin{pmatrix} W^3 & B \end{pmatrix} \begin{pmatrix} g^2 & -gg' \\ -gg' & g'^2 \end{pmatrix} \begin{pmatrix} W^3 \\ B \end{pmatrix}. \tag{1.30}$$

This mass matrix has two eigen values: $\lambda_1 = 0$ and $\lambda_2 = v^2\sqrt{g^2 + g'^2}/2$. To diagonalise the mass matrix, assume that the relation between the mass and gauge basis reads

$$G = R(\theta_W)\tilde{G}, \tag{1.31}$$

where

$$G = \begin{pmatrix} Z_\mu \\ A_\mu \end{pmatrix}, \quad R(\theta_W) = \begin{pmatrix} \cos\theta_W & -\sin\theta_W \\ \sin\theta_W & \cos\theta_W \end{pmatrix}, \quad \tilde{G} = \begin{pmatrix} W^3_\mu \\ B_\mu \end{pmatrix}. \tag{1.32}$$

Here θ_W is the so-called Weinberg angle. Thus, the mass term becomes

$$\mathcal{L}^{\text{mass}}_{\text{gauge}} = \tilde{G}^T \mathcal{M} \tilde{G} = G^T \mathcal{M}_{\text{diag}} G = \tilde{G}^T R(\theta_W)^T \mathcal{M} R(\theta_W) \tilde{G}, \tag{1.33}$$

with

$$\mathcal{M}_{\text{diag}} = \begin{pmatrix} v^2\sqrt{g^2 + g'^2}/4 & 0 \\ 0 & 0 \end{pmatrix}. \tag{1.34}$$

By solving Eq.(1.33), we get the relation between gauge and mass basis given by

$$\begin{aligned} Z_\mu &= \frac{1}{\sqrt{g^2 + g'^2}}(gW^3_\mu - g'B_\mu), \\ A_\mu &= \frac{1}{\sqrt{g^2 + g'^2}}(g'W^3_\mu + gB_\mu). \end{aligned} \tag{1.35}$$

We find the relation between $\sin\theta_W(\cos\theta_W)$ and gauge coupling as the following:

$$\cos\theta_W = \frac{g}{\sqrt{g^2 + g'^2}}, \qquad \sin\theta_W = \frac{g'}{\sqrt{g^2 + g'^2}}. \tag{1.36}$$

By substituting Eqs.(1.29), (1.35) into (1.28), we have

$$|D_\mu \Phi|^2 = \frac{1}{2}\frac{v^2}{4}\left(2g^2 W^+_\mu W^{\mu-} + (g^2 + g'^2)Z^2\right). \tag{1.37}$$

Now we see that W^1 and W^2 fields form a complex vector field $W^\pm$. Moreover, the B_μ and W^3 are not the mass eigen states and can be rotated to their mass eigen state by

Eq.(1.31). At the end, the masses of SM gauge bosons read

$$m_{W^\pm} = \frac{g}{2}v, \tag{1.38}$$

$$m_Z = \frac{\sqrt{g^2+g'^2}}{2}v, \tag{1.39}$$

$$m_A = 0. \tag{1.40}$$

Also, the covariant derivative can be written in mass eigen basis as follows

$$\begin{aligned} D_\mu &= \partial_\mu - i\frac{g}{\sqrt{2}}(W^+_\mu T^+ + W^-_\mu T^-) - i\frac{1}{\sqrt{g^2+g'^2}}Z_\mu(g^2T^3 - g'^2Y) \\ &\quad - i\frac{gg'}{\sqrt{g^2+g'^2}}A_\mu(T^3+Y), \\ &= \partial_\mu - i\frac{g}{\sqrt{2}}(W^+_\mu T^+ + W^-_\mu T^-) - i\frac{g}{\cos\theta_W}Z_\mu(T^3 - \sin^2\theta_W Q) - ieA_\mu Q, \end{aligned} \tag{1.41}$$

where $T^\pm = \tau^1 \pm i\tau^2$. In the last line, we use the fact that

$$Q = T^3 + Y, \tag{1.42}$$

$$e = \frac{gg'}{\sqrt{g^2+g'^2}}, \tag{1.43}$$

$$g = \frac{e}{\sin\theta_W}. \tag{1.44}$$

The electron's charge e is a well-measured quantity and is related to the fine structure constant $e = \sqrt{4\pi\alpha}$ given in table 1.2. Morever, we can write the mass ratio of W to Z as

$$\rho \equiv \frac{m_W}{m_Z\cos\theta_W} = 1. \tag{1.45}$$

This ratio holds at tree level but different from one at the higher order correction [13].

The fermion masses and their interactions

Unlike the Higgs and gauge bosons, the mass term of fermions is originated from the Yukawa terms given in the third line of Eq.(1.1) which read

$$\mathcal{L}_Y = -Y_\ell^I \overline{L}_L^I \Phi \ell_R^I - Y_d^{IJ}\overline{Q}_L^I \Phi d_R^J - Y_u^{IJ}\overline{Q}_L^I \tilde{\Phi} u_R^J + h.c, \tag{1.46}$$

where $\tilde{\Phi} = i\sigma_2\Phi^\dagger$ and $h.c.$ stands for the Hermitian conjugate of all previous terms. The first term describes the charged lepton masses. When the Higgs acquires the VEV, the Yukawa terms gives masses as follows

$$\mathcal{L}_Y \supset -m_e\overline{e_L}e_R - m_\mu\overline{\mu_L}\mu_R - m_\tau\overline{\tau_L}\tau_R + h.c, \tag{1.47}$$

where $m_\ell = Y_\ell v/\sqrt{2}$ and $v = (\sqrt{2}G_F)^{-1/2} = 2M_W/g$. With the Fermi coupling in table 1.2, the numerical value of the Higgs VEV is equal to 246.22 GeV. For future reference, we also give the lepton masses in table 1.2.

Unlike the case of leptons, the Yukawa couplings of quarks are 3×3 complex matrices and their mass term read [14]

$$\begin{aligned}\mathcal{L}_Y \supset & -\frac{Y_d^{IJ} v}{\sqrt{2}} \overline{d^I}_L d_R^J - \frac{Y_u^{IJ} v}{\sqrt{2}} \overline{u^I}_L u_R^J + h.c. \\ = & -\frac{Y_d v}{\sqrt{2}} \overline{d}_L d_R - \frac{Y_u v}{\sqrt{2}} \overline{u}_L u_R + h.c.,\end{aligned} \tag{1.48}$$

where $d = (d, s, b)^T$ and $u = (u, c, t)^T$. The matrices Y_u and Y_d can be diagonalised by changing the basis of left- and right-quark as follows

$$u_L \to U_L u_L, \quad u_R \to U_R u_R, \quad d_L \to V_L d_L, \quad d_R \to V_R d_R. \tag{1.49}$$

with $U^\dagger U = UU^\dagger = I$ and $V^\dagger V = VV^\dagger = I$. This implies that $u_{L/R}$ and $d_{L/R}$ are rotated independently. With these rotations, the Yukawa terms for quarks become

$$\mathcal{L}_Y \supset -\overline{d}_L M_d d_R - \overline{u}_L M_u u_R + h.c., \tag{1.50}$$

where $M_d = V_L^\dagger Y_d V_R v/\sqrt{2}$ and $M_u = U_L^\dagger Y_u U_R v/\sqrt{2}$. Therefore, these rotations affect the interaction between quark and weak gauge bosons. To explicitly see this, let us go back to the second line of Eq.(1.1) and rewrite the quarks field in their mass eigenstates. Here we drop the kinetic terms of the SM fermions and consider only the interaction terms which read [4]

$$\mathcal{L}_{fermion} \supset g\left(W_\mu^+ J_W^{\mu+} + W_\mu^+ J_W^{\mu+} + Z_\mu J_Z^\mu\right) + eA_\mu J_{EM}^\mu, \tag{1.51}$$

where

$$\begin{aligned}
J_W^{\mu+} &= \frac{1}{\sqrt{2}}\left(\overline{\nu_L}\gamma^\mu e_L + \overline{u_L}\gamma^\mu V_{\mathrm{CKM}} d_L\right), \\
J_W^{\mu-} &= \frac{1}{\sqrt{2}}\left(\overline{e_L}\gamma^\mu \nu_L + \overline{d_L}\gamma^\mu V_{\mathrm{CKM}}^\dagger u_L\right), \\
J_Z^\mu &= \frac{1}{\cos\theta_W}\left[\overline{\nu_L}\gamma^\mu\left(\frac{1}{2}\right)\nu_L + \overline{e_L}\gamma^\mu\left(-\frac{1}{2} + \sin^2\theta_W\right)e_L + \overline{e_R}\gamma^\mu\left(\sin^2\theta_W\right)e_R\right. \\
&\quad + \overline{u_L}\gamma^\mu\left(\frac{1}{2} - \frac{2}{3}\sin^2\theta_W\right)u_L + \overline{u_R}\gamma^\mu\left(-\frac{2}{3}\sin^2\theta_W\right)u_R \\
&\quad \left. + \overline{d_L}\gamma^\mu\left(-\frac{1}{2} + \frac{1}{3}\sin^2\theta_W\right)d_L + \overline{d_R}\gamma^\mu\left(\frac{1}{3}\sin^2\theta_W\right)d_R\right], \\
J_{EM}^\mu &= \overline{e}\gamma^\mu(-1)\,e + \overline{u}\gamma^\mu\left(\frac{2}{3}\right)u + \overline{d}\gamma^\mu\left(-\frac{1}{3}\right)d.
\end{aligned} \tag{1.52}$$

The V_{CKM} is called the *Cabibbo-Kobayashi-Maskawa* (CKM) matrix which describes the mixing amongst left-handed up and down type quarks. It is a complex 3×3 matrix that can be parameterised by three mixing angles and one CP-violating phase and given by

$$\begin{aligned} V_{\text{CKM}} = U_L^\dagger V_L &= \begin{pmatrix} V_{ud} & V_{us} & V_{ub} \\ V_{cd} & V_{cs} & V_{cb} \\ V_{td} & V_{ts} & V_{tb} \end{pmatrix} \\ &= \begin{pmatrix} 1 & 0 & 0 \\ 0 & c_{23} & s_{23} \\ 0 & -s_{23} & c_{23} \end{pmatrix} \begin{pmatrix} c_{13} & 0 & s_{13}e^{-i\delta} \\ 0 & 1 & 0 \\ -s_{13}e^{i\delta} & 0 & c_{13} \end{pmatrix} \begin{pmatrix} c_{12} & s_{12} & 0 \\ -s_{12} & c_{12} & 0 \\ 0 & 0 & 1 \end{pmatrix}, \\ &= \begin{pmatrix} c_{12}c_{13} & s_{12}c_{13} & s_{13}e^{-i\delta} \\ -s_{12}c_{23} - c_{12}s_{23}s_{13}e^{i\delta} & c_{12}c_{23} - s_{12}s_{23}s_{13}e^{i\delta} & s_{23}c_{13} \\ s_{12}s_{23} - c_{12}c_{23}s_{13}e^{i\delta} & -c_{12}s_{23} - s_{12}c_{23}s_{13}e^{i\delta} & c_{23}c_{13} \end{pmatrix}, \end{aligned} \tag{1.53}$$

where $s_{ij} \equiv \sin\theta_{ij}$ and $c_{ij} \equiv \cos\theta_{ij}$. The numerical value of each element in CKM matrix is given by [9, 13]

$$V_{\text{CKM}} = \begin{pmatrix} 0.97401 \pm 0.00011 & 0.22560 \pm 0.00048 & 0.00361^{+0.00011}_{-0.00009} \\ 0.226360 \pm 0.00048 & 0.97320 \pm 0.00011 & 0.04053^{+0.00083}_{-0.00061} \\ 0.00854^{+0.00023}_{-0.00016} & 0.03978^{+0.00082}_{-0.00060} & 0.999172^{+0.000024}_{-0.000035} \end{pmatrix}. \tag{1.54}$$

One can see that the mixing is strong for quarks in the diagonal terms. Additionally, the CP-violating part of the CKM matrix can be described by the Jarlskog invariant [15]

$$\text{Im}[V_{ij}V_{kl}V_{il}^*V_{kj}^*] \equiv J \sum_{m,n} \epsilon_{ikm}\epsilon_{jln} \tag{1.55}$$

where $J = (3.00^{+0.15}_{-0.09}) \times 10^{-5}$ and ϵ_{ijk} is the rank-3 anti-symmetry tensor. The quantity is very crucial when we try to apply the SM to explain the matter anti-matter problem of the universe. Unfortunately, the SM cannot successfully explain this problem which one of the reason is the smallness of CP-violating phase.

1.1.4 The cross section and decay rate

A *collider* is a machine that physicists use to study the properties of particles in laboratories. The common procedure of collider starts from accelerating initial state particles and then speed them up close to the speed of light. Then, they will be sent into a small tunnel for collision. Normally, we use the stable charged particles because they can be bent by magnets and do not decay during the course of acceleration and collision. Usually, we use electrons, positrons, protons and even some heavy ions as the initial particles for colliding. Properties of some colliders is summarised in table 1.3. Moreover, it is also possible to build the muon collider as proposed in [16].

Name	**Colliding particles**	**started/ended year**	**Length [km]**	**Max. Energy [GeV]**	**Luminosity** $[10^{30}\ \mathbf{cm^{-2}s^{-1}}]$
LEP-I(II)	e^+e^-	1989/2000	26.66	100-104.6	100
SLAC	e^+e^-	1989/1998	1.45 +1.47	50	2.5
HERA	ep	1992/2007	6.336	e: 0.030 p: 0.92	75
TEVATRON	$p\bar{p}$	1987/2011	6.28	0.980	431
RHIC Brookhaven	pp	2001/-	3.834	0.255	160
LHC (CERN)	pp	2009/-	26.659	6.5	160

TABLE 1.3: Specification of some colliders including name, colliding particles, started/ended year, Length, Max. Energy and Luminosity. [9].

The main job of particle theorists is to calculate a *scattering cross section* σ or a *decay rate* Γ of a particular process. Before we compute those quantities we need to evaluate what is called the *amplitude* or *matrix element* which is related to the probability of a system in an initial state $|i\rangle$ to be found in a final state $|f\rangle$ or $\langle f|i\rangle$. For a process of $2 \to n$ scattering, the matrix element [13] is given by

$$\langle p_1', p_2', ...|S-1|p_1, p_2\rangle = i(2\pi)^4\delta^4(p_1+p_2-\sum_{i=1}^{n} p_i')\mathcal{M}(p_1, p_2; p_1', p_2', ...), \tag{1.56}$$

where S is the S-matrix operator that enables the transition from the initial state $|p_1, p_2\rangle$ with momenta p_1, p_2 and $|p_1', p_2', ..., p_n'\rangle$ with momenta $p_1', p_2', ..., p_n'$. The quantity $\mathcal{M}$ is the Lorentz invariant amplitude in momentum space. The Dirac delta function appears to keep the energy-momentum conserved.

Then, the differential scattering cross section reads

$$d\sigma = \frac{(2\pi)^4|\mathcal{M}|^2}{4\sqrt{(p_1\cdot p_2)^2 - m_1^2m_2^2}} d\Phi_n(p_1, p_2; p_1', p_2', ..., p_n'), \tag{1.57}$$

where the measure of n-body phase space is given by

$$d\Phi_n(p_1, p_2; p_1', p_2', ..., p_n') = \delta^4(p_1+p_2-\sum_{i=1}^{n} p_i')\prod_{i=1}^{n}\frac{d^3p_i'}{(2\pi)^3 2E_n'}. \tag{1.58}$$

In the case of 2-2 scattering, there are three possible *topologies* as shown in figure 1.2. For each diagram, there is a corresponding *Mandelstam variable* which describes the momentum transfer of the mediator. Suppose the incoming particles with masses m_1, m_2 and momenta p_1, p_2 collider with each other and create particles with masses m_3, m_4 and

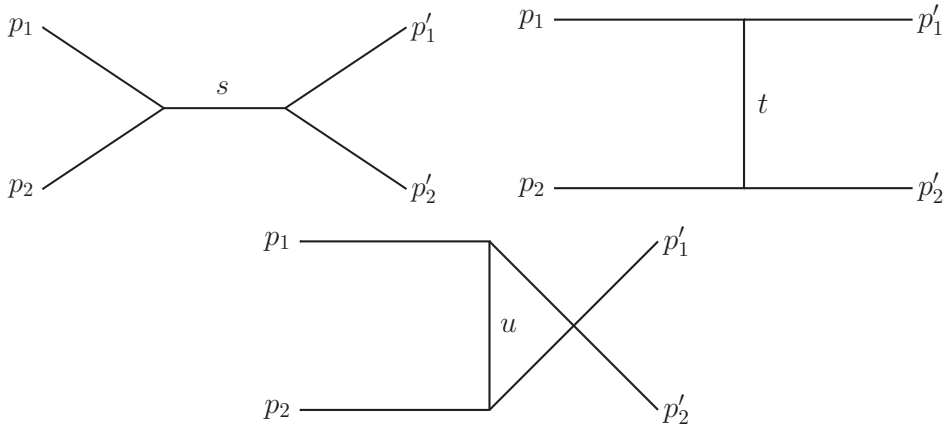

FIGURE 1.2: Different topologies for 2-2 scattering. The momentum transfer for each diagram can be identified by Mandelstam variables: s, t and u.

momenta p_3, p_4 in the final state. The corresponding Mandelstam variables are defined as follows

$$\begin{aligned} s &= (p_1 + p_2)^2 = (p_1' + p_2')^2 \\ &= m_1^2 + 2E_1E_2 - 2\mathbf{p_1} \cdot \mathbf{p_2} + m_2^2, \end{aligned} \tag{1.59}$$

$$\begin{aligned} t &= (p_1 - p_3)^2 = (p_2 - p_4)^2 \\ &= m_1^2 - 2E_1E_3 + 2\mathbf{p_1} \cdot \mathbf{p_3} + m_3^2 \end{aligned} \tag{1.60}$$

$$\begin{aligned} u &= (p_1 - p_4)^2 = (p_2 - p_3)^2 \\ &= m_1^2 - 2E_1E_4 + 2\mathbf{p_1} \cdot \mathbf{p_4} + m_4^2 \end{aligned} \tag{1.61}$$

and the sum of all Mandelstam variables is equal to the sum of all squared masses $s + t + u = m_1^2 + m_2^2 + m_3^2 + m_4^2$.

Two body scattering

After integrating the momenta of outgoing particles, the differential cross section in the centre of mass (CM) frame reads

$$\frac{d\sigma}{d\Omega} = \frac{1}{4E_1E_2} \frac{|\mathbf{p_1}|}{(2\pi)^2 4E_{\text{cm}}} |\mathcal{M}(p_1, p_2 \to p_3, p_4)|^2, \tag{1.62}$$

with

$$E_1 = \frac{s + m_1^2 - m_2^2}{2\sqrt{2}}, \qquad E_2 = \frac{s + m_2^2 - m_1^2}{2\sqrt{2}}. \tag{1.63}$$

The two body decay

For the decay of a particle with mass M and momentum P into particles with masses m_1, m_2 and momenta p_1, p_2, the decay rate reads

$$d\Gamma = \frac{1}{32\pi^2}|\mathcal{M}|^2\frac{|\mathbf{p_1}|}{M^2}d\Omega, \tag{1.64}$$

where

$$\begin{aligned} d\Omega &= d\phi_1 d(\cos\theta_1), \\ E_1 &= \frac{M^2 - m_2^2 + m_1^2}{2M}, \\ |\mathbf{p_1}| = |\mathbf{p_2}| &= \frac{\left[(M^2-(m_1+m_2)^2)(M^2-(m_1-m_2)^2)\right]^{1/2}}{2M}. \end{aligned} \tag{1.65}$$

Here $d\Omega$ is the solid angle of the particle 1. Both Eqs.(1.62) and (1.64) are usually used for calculating theoretical quantities. In experiments at colliders like *Large Electron Positron collider* (LEP) and *Large Hadron Collider* (LHC), physicists measure the number of events that can be registered by the detectors. The performance of a collider depends on multiple factors such as the maximum energy per beam, the luminosity of a particle beam, etc. If the maximum energy per beam is large enough, the collider is likely to create a heavy particle in the collision. The luminosity of two colliding beams with number density n_1, n_2, the beam's cross-sectional area A and they are across each other in the tunnel with frequency f reads

$$heexperimentalists\mathcal{L} = f\frac{n_1 n_2}{A}. \tag{1.66}$$

Then, the experimentalists can calculate the number of events for a particular process by

$$\frac{dN}{dt} = \mathcal{L}\sigma \tag{1.67}$$

or the number of events is given by

$$N = L\sigma \tag{1.68}$$

where $L = \int dt\mathcal{L}$ is the integrated luminosity and the integration is performed over the running time of a collider.

1.2 Particle cosmology

In this section, we summarise some relevant topics of standard cosmology by focusing on the expansion of the universe based on the Friedman-Robertson-Walker (FRW) metric

and thermodynamics of the early universe which are crucial for understanding the DM thermal production which is the key point of section 1.3

1.2.1 The universe in expansion

One of the biggest cosmological discoveries of the 20th century is *the expansion of the universe*. In 1929, Edwin Hubble measured the redshift z of galaxies in the constellation Andromeda versus the luminosity distance d_L where $d_L = (\mathcal{L}/4\pi\mathcal{F})^{1/2}$, $\mathcal{L}$ is the luminosity of object and $\mathcal{F}$ is the released flux. The redshift is measured from the shifted spectrum due to Doppler effect and is defined by [17]

$$z = \frac{\lambda_{\text{obs}} - \lambda_{\text{em}}}{\lambda_{\text{em}}}, \tag{1.69}$$

where λ_{em} and λ_{obs} are the wavelength at the emission point and at the measuring point, respectively. From observations, he found the relation between the distance and radial velocity as [18, 19, 20]

$$v \simeq H_0 d_L, \tag{1.70}$$

where H_0 is the Hubble's constant at present time which its numerical value is given in table 1.4. This equation implies the farther galaxies move away with faster speeds which means that our universe is expanding with acceleration. If the velocity of galaxies is not too large, we can use the approximation that $z \approx v/c$ which leads us to the relation between the redshift and distance

$$z \simeq \frac{H_0}{c} d_L. \tag{1.71}$$

Notice that the larger distance implies the bigger redshift.

Quantity	Symbol	Value
Newtonian constant [$\text{m}^3\ \text{kg}^{-1}\ \text{s}^{-2}$]	G_N	$6.67430(15) \times 10^{-11}$
Planck mass [kg]	M_P	$2.176434(24) \times 10^{-8}$
Hubble constant [$\text{km}\ \text{s}^{-1}\ \text{Mpc}^{-1}$]	H_0	$100h$
scaling factor for Hubble constant	h	$0.674(5)$
baryon density	Ω_b	$0.02237(15)h^{-1}$
dark matter density	Ω_{dm}	$0.1200(12)h^{-1}$
radiation density	Ω_γ	$5.38(15) \times 10^{-5}$
dark energy density	Ω_Λ	$0.685(7)$

TABLE 1.4: Some of the measured values of the cosmological parameters [9, 13, 21].

The observations of the galaxy distributions in the universe at the scale about 100 Mpc^{-1} or so implies that the universe is approximately homogeneous and isotropic. With these properties, the expanding universe can be well described by the FRW metric [19, 22]

$$ds^2 = dt^2 - a^2(t)\left(\frac{dr^2}{1-kr^2} + r^2 d\theta^2 + r^2 \sin^2\theta d\phi^2\right), \tag{1.72}$$

where k is the spacetime curvature and it can be -1, 0 and $+1$ representing the close, flat and open universe. The parameter $a(t)$ is the scale factor which accounts for the expansion at time t. Here (t, r, θ, ϕ) is called *the comoving coordinates* which move along the expansion of the universe or the Hubble flow. If an object is at rest in the comoving coordiates without any external force, it is not moving regardless of the universe expansion. We define the rate of change of the scale as

$$H(t) \equiv \frac{\dot{a}(t)}{a(t)}, \tag{1.73}$$

where $H(t)$ is the Hubble rate or Hubble parameter at a time t. In order to find the equation of motion that describes the spacetime dynamics, we need to make use of the Einstein's equation [22]

$$R_{\mu\nu}(t) - \frac{1}{2}g_{\mu\nu}(t)R(t) + \Lambda(t)g_{\mu\nu}(t) = \frac{T_{\mu\nu}(t)}{M_P^2}, \tag{1.74}$$

where M_P is called the Planck mass. The parameter Λ is the cosmological constant which is a vital component in the standard model of cosmology or ΛCDM. Many models of cosmology describe the cosmological constant in terms of the Dark Energy (DE) and it contributes 68% to the total energy density of the universe. The quantities $R_{\mu\nu}$ and $R = g^{\mu\nu}R_{\mu\nu}$ are the Ricci tensor and scalar, respectively. They are derivatives of $g_{\mu\nu}$. For the metric in Eq.(1.72) they are

$$R_{00}(t) = -\frac{3\ddot{a}(t)}{a(t)}, \qquad R_{ij}(t) = \delta_{ij}\left(2\dot{a}(2)^2 + a(t)\ddot{a}(t)\right). \tag{1.75}$$

If we assume the the energy-momentum tensor $T_{00} = \rho_t$ and $T_{jj} = p_j$ where ρ_t is the total energy density of the universe and p_j is the pressure in jth direction. Then, the Friedmann equation

$$\frac{\dot{a}(t)^2}{a(t)^2} + \frac{k}{a(t)^2} = \frac{\rho_t(t)}{3M_P^2} \tag{1.76}$$

$$\frac{2\ddot{a}(t)}{a(t)} + \frac{\dot{a}(t)^2}{a(t)^2} + \frac{k}{a(t)^2} = -\frac{p(t)}{M_P^2} \tag{1.77}$$

where $\rho_t = \rho_m(t) + \rho_r(t) + \rho_\Lambda(t)$ with $\rho_\Lambda = \Lambda(t)M_P^2 = 3H_0^2 M_P^2 \Omega_\Lambda(t)$. Combining Eq.s(1.76) and (1.77) together, we get

$$\frac{\ddot{a}(t)}{a(t)} = -\frac{\rho_t(t) + 3p(t)}{6M_P^2}. \tag{1.78}$$

By solving this equation, we can identity the scale factor $a(t)$ evolves with time. To this end, we make use of the thermodynamics equation of state

$$p_j(t) = w_j \rho_j(t), \quad \text{with} \quad w_j = \begin{cases} 0 & \text{non-relativistic matter} \\ 1/3 & \text{relativistic radiation} \\ -1 & \text{vacuum energy} \end{cases}. \tag{1.79}$$

From the conservation law of energy-momentum, $dU = -pdV$, we can also write

$$\frac{d}{dt}\left(\rho_j a^3\right) = -p_j \frac{d}{dt} a^3, \tag{1.80}$$

which is just a relation between work and pressure inside a system with volume a^3. By solving a system of Eqs.(1.79) and (1.80), we find the relation between energy density and scale factor

$$\rho_j(a) = C a^{-3(1+w_j)} \propto \begin{cases} a^{-3} & \text{non-relativistic matter} \\ a^{-4} & \text{relativistic radiation} \\ \text{const.} & \text{vacuuuma energy} \end{cases} \tag{1.81}$$

where C is a constant. Substituting Eqs.(1.81) and (1.79) into Eq.(1.78) and writing the solution in terms of power law solution, $a \propto t^\beta$, (this power solution can be used only for $w_j \neq -1$), one finds that

$$\beta = \frac{2}{3 + 3w_j}. \tag{1.82}$$

In the case of cosmological dominated universe, we can find the solution by solving Eq.(1.76) (ignore ρ_m and ρ_r)

$$\frac{\dot{a}(t)^2}{a(t)^2} = \frac{\Lambda(t)}{3}, \tag{1.83}$$

which the solution is just $a(t) \sim e^{(\sqrt{\Lambda(t)/3})t}$. Thus, the time evoluation of scale factor in FRW model can be summarised into

$$a(t) \sim \begin{cases} t^{2/3} & \text{non-relativistic matter} \\ t^{1/2} & \text{relativistic radiation} \\ e^{(\sqrt{\Lambda(t)/3})t} & \text{vacuum energy.} \end{cases} \tag{1.84}$$

Moreover, we can also write the time evolution of the Hubble parameter as in Eq.(1.73) for each case as the following

$$H(t) \sim \begin{cases} \frac{2}{3t} & \text{non-relativistic matter} \\ \frac{1}{2t} & \text{relativistic radiation} \\ \sqrt{\frac{\Lambda(t)}{3}} & \text{vacuum energy.} \end{cases} \tag{1.85}$$

According to cosmological observations [21, 23, 24], at present, we have a fairly complete picture of the components of the universe. They can be divided into 1) non-relativistic matter 2) relativistic radiation and 3) vacuum energy. The fraction of these components of the universe is characterised by a quantity called the density parameter Ω which is a ratio of the energy density of ith component ρ_i to the critical energy density ρ_{crit}.

$$\Omega_i = \frac{\rho_i}{\rho_{\text{crit}}}. \tag{1.86}$$

The critical energy density is a measure of total energy density at a stage that the universe does not expand or collapse. It is defined by

$$\rho_{\text{crit}} = 3H^2 M_P^2, \tag{1.87}$$

where the present Hubble rate and relevant cosmological parameters are summarised in table 1.4

The non-relativistic matter contains baryon matter which is the visible matter around us ranging from atoms to clusters of galaxies, and the dark matter which cannot be understood within the SM framework. We will talk about the the dark matter in some detail in section 1.3. The radiation mainly consists of photons freely propagating from the last scattering surface since the matter and radiation decoupled at $z_{\text{dec}} \sim 1100$. In several models of cosmology, the vacuum energy can be described in form of the cosmological constant Λ. However, we are still puzzled why it has a very tiny value.

1.2.2 Thermodynamics of the early universe

To calculate the Hubble rate in terms of the energy density and other quantities in the early universe, we need to study thermodynamics of particles. The universe at the early stage contains many particle species which interact with each other in a thermal bath. At high temperature, the interaction rate of these particles with thermal bath are high making all particles reach thermal equilibrium. Thus, we can assume that they were in thermal equilibrium to a good approximation. The number density n, energy density ρ

and pressure p for a particle species are given by

$$n_{\rm eq} = g \int \frac{d^3p}{(2\pi)^3} f(\vec{\mathbf{p}}), \tag{1.88}$$

$$\rho_{\rm eq} = g \int \frac{d^3p}{(2\pi)^3} E(\vec{\mathbf{p}}) f(\vec{\mathbf{p}}), \tag{1.89}$$

$$p_{\rm eq} = g \int \frac{d^3p}{(2\pi)^3} \frac{|\vec{\mathbf{p}}|^2}{E} f(\vec{\mathbf{p}}), \tag{1.90}$$

where g is the number of internal degrees of freedom for a particle and the energy satisfies $E^2 = |\vec{\mathbf{p}}|^2 + m^2$. The distribution $f(|\vec{\mathbf{p}}|^2)$ is given by

$$f(\vec{\mathbf{p}}) = \begin{cases} (\exp((E-\mu)/T)+1)^{-1} & \text{for fermions} \\ (\exp((E-\mu)/T)-1)^{-1} & \text{for bosons} \end{cases}, \tag{1.91}$$

which indicates the occupation number in the phase space. The quantity μ is called the chemical potential. If we consider a process $A + B \to C + D$ in chemical equilibrium, the chemical potentials are related through

$$\mu_A + \mu_B = \mu_C + \mu_D. \tag{1.92}$$

After integration of Eq.(1.88) with the distribution function from Eq.(1.91) (assuming that the chemical potential is small compared to the energy term), the number density is given by

$$n_{\rm eq}(T) = \begin{cases} g\left(\frac{mT}{2\pi}\right)^{3/2} e^{-m/T} & \text{non-relativistic particles} \quad T \ll m \\ g\frac{\zeta(3)}{\pi^2}T^3 & \text{relativistic bosons} \quad T \gg m \\ g\frac{3}{4}\frac{\zeta(3)}{\pi^2}T^3 & \text{relativistic fermions} \quad T \gg m \end{cases}, \tag{1.93}$$

where $\zeta(3) \simeq 1.2$ is the Riemann zeta function of 3. Also, the energy density for each case can be computed similarly and is given by

$$\rho_{\rm eq}(T) = \begin{cases} gm\left(\frac{mT}{2\pi}\right)^{3/2} e^{-m/T} & \text{non-relativistic particles} \quad T \ll m \\ g\frac{\pi^2}{30}T^4 & \text{relativistic bosons} \quad T \gg m \\ g\frac{7}{8}\frac{\pi^2}{30}T^4 & \text{relativistic fermions} \quad T \gg m \end{cases}. \tag{1.94}$$

In addition, the pressure is given by

$$p_{\rm eq}(T) = \begin{cases} \rho_{\rm eq}(T) & \text{relativistic particles} \\ n_{\rm eq}T & \text{non-relativistic particles} \end{cases}. \tag{1.95}$$

According to Eq.(1.93), we can calculate the energy density of all species in terms of the photon temperature T as follows

$$\rho_r = \frac{\pi^2}{30} g_*(T) T^4, \tag{1.96}$$

with

$$g_*(T) = \sum_{\text{bosons}} g_b \left(\frac{T_b}{T}\right)^4 + \sum_{\text{fermions}} \frac{7}{8} g_f \left(\frac{T_f}{T}\right)^4 . \tag{1.97}$$

We can try to evaluate the total energy density by assuming that there are only the SM particles in the thermal bath and they are relativistic at the temperature greater than the EW scale ($v = 246.22$ GeV). Thus, the effective number of degrees of freedom for fermion and boson reads

$$\begin{aligned} g_{\text{f}} &= g_{\text{quark}} + g_{\text{lepton}} + g_{\text{neutrino}} = 90, \\ g_{\text{b}} &= g_{\text{gluon}} + g_{\text{weak}} + g_{\text{photon}} + g_{\text{Higgs}} = 28, \\ g_*(T > 246 \ \ \text{GeV}) &= 28 + \frac{7}{8} 90 = 106.75. \end{aligned} \tag{1.98}$$

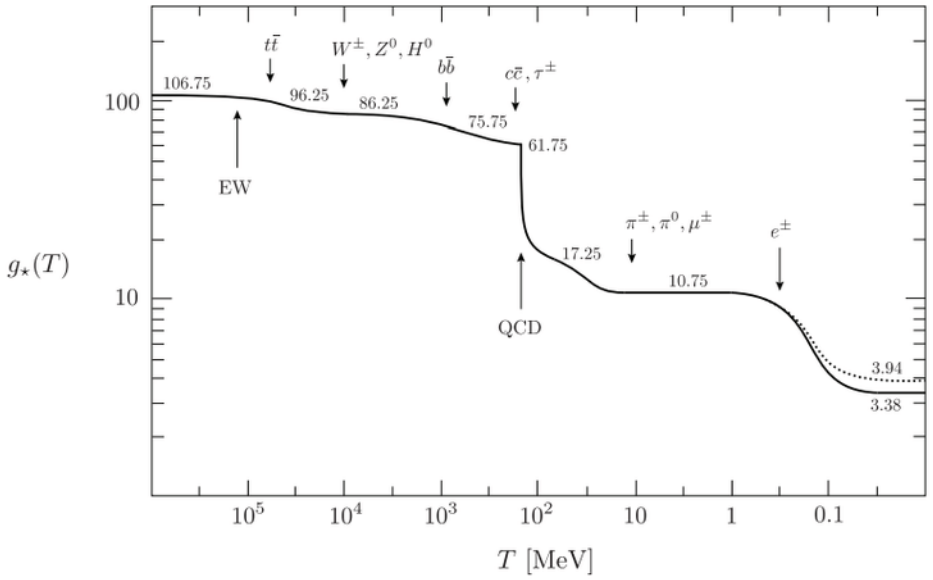

FIGURE 1.3: The time dependence of the effective number. Figure from [25, 26]

Figure 1.3 describes the evolution of the effective number of degrees of freedom with temperature. At the temperature higher than EW scale ($T \approx 246$ GeV), $g_* = 106.75$ as in Eq.(1.98). When temperature drops around the top quark mass, the top quark becomes non-relativistic, the g_* is decreasing. It slightly decreases until the temperature is around the QCD transition scale. The effective degrees of freedom is rapidly dropped because all quarks are hadronised to pions ($\pi^{\pm}, \pi^0$). It is dramatically dropped again when temperature drops to the mass of electron 0.5 MeV. At present, the effective degrees for freedom is equal to 3.6 which contains photons and neutrinos.

At the end, we can find the relation between the time and temperature through the definition of the Hubble rate for radiation-dominated universe as follows

$$H(t)^2 = \left(\frac{1}{2t}\right)^2 = \frac{1}{3M_P^2}\frac{\pi^2}{30}g_*(T)T^4 = \left(\frac{\pi\sqrt{g_*}}{\sqrt{90}}\frac{T^2}{M_P}\right)^2. \tag{1.99}$$

In addition to the number, energy density and pressure, another important quantity is the entropy per comoving volume element which remains unchanged for particle species with the interaction rate much bigger than the Hubble rate. Due to the second law of thermodynamics, we can prove that the entropy density in a comoving volume is given by

$$s \equiv \frac{S}{V} = \frac{\rho + p}{T} \tag{1.100}$$

where S is the entropy in the volume $V = a^3$. Since the relativistic particles dominantly contribute to the entropy density so that we can also write

$$s = \frac{2\pi^2}{45}g_{*S}T^3 \tag{1.101}$$

where

$$g_{*S} = \sum_{\text{b=boson}} g_b \left(\frac{T_b}{T}\right)^3 + \frac{7}{8}\sum_{\text{f=fermion}} g_f \left(\frac{T_f}{T}\right)^3. \tag{1.102}$$

1.3 Dark matter

The dark matter (DM) is one of the long-standing mysteries in cosmology and particle physics. For the review of history of DM, we recommend the reference [27, 28]. The existence of DM has been well established by several independent cosmological and astrophysical observations.

The very first evidence of DM came from the inconsistency between theoretical prediction and measurement of the velocity distribution of stellar object within nearby galaxies. If we assume that the total matter of the universe only comes from the visible component, an object at radius r in a galaxy should orbit around with the rotational velocity $v \propto \sqrt{M(r)/r}$ [9] , where $M(r)$ is the total mass of visible objects. If it is outside the visible part, its velocity should drop like $v \propto 1/\sqrt{r}$. However, in observations it turns out to be that at very large r the velocity is surprisingly constant relative to the distance r. This leads to the idea of dark halo [29] in which the visible parts of universe resides. To explain the constancy of the velocity distribution, the mass density of the halo should scale like $\rho(r) \propto 1/r^2$ or $M(r) \propto r$ but at some point it has to be rapidly falling down to make the total mass of the galaxy finite. In addition, DM is also important to the formation of large scale structure [30, 31], the bullet cluster [32] and gravitational

lensing [33]. These evidences of DM have been solely detected based on its gravitational effect. Therefore, it is the big and long quest for physicists to hunt for DM particle. However, after having been searching for many years, we have not found the direct evidence of DM in laboratories yet. No information on mass, spin and interaction have been measured so far.

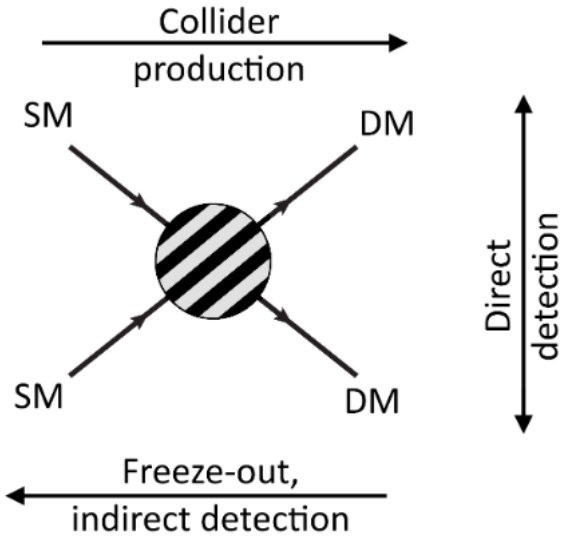

FIGURE 1.4: The interaction between DMs and SM particles can occur in three directions: 1) DM DM → SM SM stands for DM annihilation or indirect detection; 2) DM SM → DM SM for the DM direct detection and 3) SM SM → DM DM for DM production at collider. Figure from [34]

In order to explain the existence of DM in the particle physics point of view, many DM models have been proposed. For example, the DM candidate as the lightest supersymmetric particle (LSP) [35], the sterile neutrinos [36], the axion and axion-like particles [37], the dark photon [38], extended scalar sector of the SM [39]. Amongst various types of models, the most favourite one is called the *weakly-interacting massive particle* (WIMP) which interacts very weakly with the SM particle and has a mass in a range of GeV-TeV scale. The interaction between DM and SM particles that leads to observable signals can be divided into three different types as the following. In a region with dense DM distribution, the DM can annihilate each other and create a pair of SM particles, DM+DM → SM+SM. This mechanism is called indirect detection where the DM signal can be observed via their annihilation products through the gamma-ray telescope (like Fermi-LAT experiment etc.) [40], the neutrino telescope (like IceCube etc.) [41], anti-protons [42], the CMB anisotropies [21] etc. Additionally, the relic DM can also interact with the SM particle through a process of DM+SM → DM+SM which several experiments such as LUX [43], XENON1T [44], PandaX-II [45] etc. have been trying to detect the recoil energy of some heavy nuclei like Xenon as a result of DM scattering. Finally, we can also study phenomenology of DM at colliders like LHC by smashing a pair of SM particles to create a pair of DMs through a process of SM+SM → DM+DM.

In figure 1.4, we summarise three different diagrams representing DM and SM particle interactions.

In this section, we will discuss how to calculate the relic density from theoretical point of view and review the experimental result of the DM relic density measurement by PLANCK[21]. In addition, the direct and indirect searches will be mentioned and the limits from those searches are present. Finally, we will also discuss possible collider signatures of DM which different models can predicts different signatures.

1.3.1 Relic density

The relic abundance of DM in the universe has been precisely measured by studying the temperature fluctuation in the cosmic microwave background (CMB). This CMB mainly consists of photons decoupled when temperature was around 0.32 eV [20]. After the matter-radiation decoupled, they freely propagate through the universe and move towards us which brings very useful information of the universe at early stage. Several experiments have measured the temperature anisotropies in CMB such as COBE [24], WMAP [46] and PLANCK [47, 21]. Today, we have a very precise value of DM abundance which is $\Omega_{\rm DM}h^2 = 0.12 \pm 0.0012$.

The abundance of relic DM can be understood by two different mechanisms. Firstly, it is the so-called *freeze-out mechanism* [48] . Assuming that DM particle was in thermal equilibrium with the SM particles when the universe temperature is far above the DM mass. When the universe temperature dropped around the mass of DM, the interaction rate of DM with SM particle was also decreased so that it was smaller than the Hubble expansion rate, $\Gamma_{\rm DM} \lesssim H$. At this stage, the DM particles started freezing out from the thermal bath. Typically, the DM mass from thermal production mechanism is approximately around the EW scale and its couplings to the SM sector was comparable to the weak coupling, $\alpha_{\rm EW}$. We refer to DM particle with these properties as the WIMP. The second mechanism does not require the DM candidate to be thermally produced in the early universe since the interaction between DM and SM particle is so weak that DM cannot reach thermal equilibrium. The population of DM is essentially generated by the annihilation or decay of other particles into DM. This is called the *freeze-in mechanism* [49]. The typical coupling of DM to SM sector for freeze-in scenario is so tiny, $g \sim 10^{-12} - 10^{-8}$. This kind of DM candidate is called the *feebly-interacting massive particle* (FIMP).

1.3.2 The Boltzmann equation

The number density, energy density and pressure in Eq.(1.93), (1.94) and (1.95) can be applied only for particles in thermal equilibrium. However, when the universe cools

down, some species decouple from the thermal bath since their interaction rates Γ are not strong enough to keep them in thermal equilibrium against the expansion rate of the universe H which leads to the condition for decoupling from the thermal bath

$$\begin{aligned} \Gamma &\gtrsim H \quad \text{coupled}, \\ \Gamma &\lesssim H \quad \text{decoupled}, \end{aligned} \tag{1.103}$$

where the interaction rate can be calculated from

$$\Gamma = n\sigma v, \tag{1.104}$$

where n is the number density of the particle, σ is the scattering cross section of the particles and v is the relative velocity.

In order to keep track of the number density, we need to solve the Boltzmann equation for phase space distribution functions

$$\hat{\mathbf{L}}[f] = \mathbf{C}[f], \tag{1.105}$$

where $\hat{\mathbf{L}}$ is the Liouville operator and $\mathbf{C}$ is the collision operator. The relativistic generalisation of Liouville operator is given by

$$\hat{\mathbf{L}} = p^\alpha \frac{\partial}{\partial x^\alpha} - \Gamma^\alpha_{\beta\gamma} p^\beta p^\gamma \frac{\partial}{\partial p^\alpha}. \tag{1.106}$$

For the FLRW metric in Eq.(1.72), the Liouville operator reads

$$\hat{\mathbf{L}}[f(E,t)] = E\frac{\partial f}{\partial t} - \frac{\dot{a}}{a}|\mathbf{p}|^2 \frac{\partial f}{\partial E}, \tag{1.107}$$

with the time dependent number density

$$n(t) = \frac{g}{(2\pi)^3} \int d^3p f(E,t), \tag{1.108}$$

the Boltzmann equation becomes

$$\frac{dn}{dt} + 3\frac{\dot{a}}{a} n = \frac{g}{(2\pi)^3} \int \mathbf{C}[f] \frac{d^3p}{E}. \tag{1.109}$$

Suppose that we consider the collision term for a process of $\psi + a + b + \cdots \leftrightarrow i + j + \cdots$ is given by

$$\begin{aligned}\frac{g}{(2\pi)^3}\int \mathbf{C}[f]\frac{d^3p}{E} = &-\int d\Pi_\psi d\Pi_a d\Pi_a \cdots d\Pi_i d\Pi_j \cdots \\ &\times (2\pi)^4\delta^4(p_\psi + p_a + p_b + \cdots - p_i - p_j - \cdots) \\ &\times \Big[|\mathcal{M}|^2_{\psi+a+b+\cdots\to i+j+\cdots} f_\psi f_a f_b \cdots (1 \pm f_i)(1 \pm f_j)\cdots \\ &- |\mathcal{M}|^2_{i+j+\cdots\to\psi+a+b+\cdots} f_i f_j \cdots (1 \pm f_\psi)(1 \pm f_a)(1 \pm f_b)\cdots\Big],\end{aligned} \tag{1.110}$$

where the phase space integral is defined as

$$d\Pi = g\frac{d^3p}{(2\pi)^3 2E}. \tag{1.111}$$

The sign in $(1 \pm f)$ is plus for boson while minus for fermion species. Because of the time reversal or T symmetry, the squared matrix element is given by

$$|\mathcal{M}|^2_{\psi+a+b+\cdots\to i+j+\cdots} = |\mathcal{M}|^2_{i+j+\cdots\to\psi+a+b+\cdots} = |\mathcal{M}|^2. \tag{1.112}$$

This is the averaged squared matrix element over initial and final spins. Also, if there are n identical particles in the initial or final state, the matrix element needs to be multiplied by a factor of $1/n!$. In addition, if we consider the freeze-out of a massive particle (assuming that $T < M$), the Fermi-Dirac and Bose-Einstein distribution functions can be replaced by the Maxwell-Boltzmann distribution function $f_i(E_i) = \exp[-(E_i - \mu_i)/T]$ and $(1 \pm f) \simeq 1$. With these changes, the Boltzmann equation for a specific species ψ is given by

$$\begin{aligned}\frac{dn_\psi}{dt} + 3Hn_\psi = &-\int d\Pi_\psi d\Pi_a d\Pi_b \cdots d\Pi_i d\Pi_j \cdots (2\pi)^4|\mathcal{M}|^2 \\ &\times \delta^4(p_\psi + p_a + p_b + \cdots - p_i - p_j - \cdots)\Big[f_\psi f_a f_b \cdots - f_i f_j \cdots\Big],\end{aligned} \tag{1.113}$$

here we use $H = \dot{a}/a$. If the collision term vanishes, the evolution of number density is inversely proportional to the cubic scale factor $(1/a^3)$.

Sometimes it is more convenient to express the Boltzmann equation in terms of the ratio of number density to entropy density $Y \equiv n_\psi/s$. Since the entropy in a comoving volume is constant ($S = sa^3 = \text{constany}$),

$$\frac{d(sa^3)}{dt} = 0 \qquad \longrightarrow \qquad \dot{s} = -3Hs. \tag{1.114}$$

Therefore, we can rewrite

$$\frac{dn_\psi}{dt} + 3Hn_\psi = s\frac{dY}{dt}. \tag{1.115}$$

With this parametrisation, the Boltzmann equation reads

$$s\frac{dY}{dt} = -\int d\Pi_\psi d\Pi_a d\Pi_b \cdots d\Pi_i d\Pi_j \cdots (2\pi)^4 |\mathcal{M}|^2 \times \delta^4(p_\psi + p_a + p_b + \cdots - p_i - p_j - \cdots)\Big[f_\psi f_a f_b \cdots - f_i f_j \cdots\Big],. \tag{1.116}$$

Now we are trying to find the standard form of Boltzmann equation that will be used for calculating the remaining amount of dark matter after decoupling from the thermal bath in section 1.3.

Let us consider the freeze-out of a massive particle ψ which is stable or long-lived compared to the age of the universe. The process of ψ and $\bar{\psi}$ with thermal bath reads

$$\psi + \bar{\psi} \longleftrightarrow X + \bar{X}, \tag{1.117}$$

where X is all particles in thermal bath in which ψ can be annihilate and here $\bar{X}$ is the antiparticle of X. The number density density of ψ is changing during the course of these reactions. We assume that at the time of decoupling of ψ the other particles X are still in thermal equilibrium with thermal bath. We will further assume that they can to a good approximation be explained by the Boltzmann statistics with zero chemical potential for simplicity. Therefore, we can write Eq.(1.113) for a process of $\psi\bar{\psi} \leftrightarrow X\bar{X}$ as

$$s\frac{dY}{dt} = -\int d\Pi_\psi d\Pi_{\bar{\psi}} d\Pi_X d\Pi_{\bar{X}} (2\pi)^4 |\mathcal{M}|^2 \times \delta^4(p_\psi + p_{\bar{\psi}} - p_X - p_{\bar{X}})\Big[f_\psi f_{\bar{\psi}} - f_X f_{\bar{X}}\Big], \tag{1.118}$$

with the equilibrium distributions

$$\begin{aligned} f_X^{\mathrm{eq}} &= \exp(-E_X/T), \\ f_{\bar{X}}^{\mathrm{eq}} &= \exp(-E_{\bar{X}}/T). \end{aligned} \tag{1.119}$$

Because of the energy-momentum conservation in the delta function, it implies that $E_\psi + E_{\bar{\psi}} = E_X + E_{\bar{X}}$. This allows us to write

$$f_X f_{\bar{X}} = \exp\left[-(E_X + E_{\bar{X}})/T\right] = \exp\left[-(E_\psi + E_{\bar{\psi}})/T\right] = f_\psi^{\mathrm{eq}} f_{\bar{\psi}}^{\mathrm{eq}}$$

Therefore, the Boltzmann equation reads

$$\frac{dY}{dt} = -s\langle\sigma_{\psi\bar{\psi}\to X\bar{X}} v\rangle \left(Y^2 - Y_{\mathrm{eq}}^2\right), \tag{1.120}$$

where Y and $Y_{\rm eq}$ are the actual and equilibrium number density over the entropy per comoving volume. Additionally, we also define the thermally-averaged annihilation cross section as

$$\langle \sigma_{\psi\bar{\psi}\to X\bar{X}} v\rangle \equiv (n_{\psi}^{\rm eq})^{-2} \int d\Pi_{\psi} d\Pi_{\bar{\psi}} d\Pi_{X} d\Pi_{\bar{X}} (2\pi)^4 |\mathcal{M}|^2 \times \delta^4(p_{\psi} + p_{\bar{\psi}} - p_X - p_{\bar{X}}) \exp\left(-E_{\psi}/T\right) \exp\left(-E_{\bar{\psi}}/T\right). \quad (1.121)$$

If we include all final states, the Boltzmann equation in terms of the total annihilation cross section is given by

$$\frac{dY}{dt} = -s\langle \sigma_A v\rangle \left(Y^2 - Y_{\rm eq}^2\right). \quad (1.122)$$

This is the Boltzmann equation we need to compute the relic density of dark matter after freezing out from thermal bath and we will use it to estimate the relic abundance of DM in the next section.

The freeze-out mechanism

Since the DM candidate discussed in this thesis is a WIMP[1], it would be good to review how one calculates the DM relic abundance from freeze-out mechanism.

As aforementioned in section 1.3.2 that the out-of-equilibrium number density of a particle species can be evaluated by solving the Boltzmann equation. Let us consider a reaction of DM (χ) and SM (f) particles

$$\chi + \bar{\chi} \longleftrightarrow f + \bar{f}, \quad (1.123)$$

where f represents the SM particles that have interaction with DM through some mediators. At high temperature, the forward and backward interaction rates are equal in size or we say that the system is in chemical equilibrium. The decoupling condition for a generation of a particle species is given by

$$\Gamma(T_{\rm dec}) = H(T_{\rm dec}), \quad (1.124)$$

with

$$\Gamma \equiv n_{\chi} \sigma_{\chi\chi} v_{\rm rel}, \quad (1.125)$$

where $\sigma_{\chi\chi}$ is the scattering cross section of DMs into a pair of SM particle and v is the relative velocity. Since the WIMPs are non-relativistic and their velocities are not

[1]The DM model presented in chapter 2 can also have a DM candiate as a FIMP if the coupling of the dark to SM sectors is very tiny. However, the FIMP scenario has not been yet studied and might be a subject of future study.

constant during the annihilation processes, we need to thermally average the cross section multiplied by velocity. The quantity $T_{\rm dec}$ is the temperature at which the DMs depart from the thermal bath.

Suppose that the incoming momenta are k_χ and $k_{\bar\chi}$, respectively, for χ and $\bar\chi$. The individual velocity can be expressed in terms of Mandelstam variable s as

$$\begin{aligned} s &= (k_\chi + k_{\bar\chi})^2 = 2m_\chi^2 + 2E_\chi E_{\bar\chi} - 2\mathbf{k}_\chi \cdot \mathbf{k}_{\bar\chi} \\ &= 2m_\chi^2 + 2E_\chi^2 + 2|\mathbf{k}_\chi|^2 \\ &= 4m_\chi^2 + 4|\mathbf{k}_\chi|^2 = 4m_\chi^2(1+v_\chi^2). \end{aligned} \tag{1.126}$$

In the last line, we use $E_\chi^2 = m_\chi^2 + |\mathbf{k}_\chi|^2$ and $|\mathbf{k}_\chi| \simeq m_\chi v_\chi$. Therefore, the velocity of DM is given by

$$v_\chi^2 = \frac{s}{4m_\chi^2} - 1. \tag{1.127}$$

It follows that the relative velocity in CM frame is given by

$$v_{\rm rel} = \left| \frac{\mathbf{k}_\chi}{k_\chi^0} - \frac{\mathbf{k}_{\bar\chi}}{k_{\bar\chi}^0} \right| = \frac{2|\vec{k}_\chi|}{k_\chi^0} \simeq 2v_\chi. \tag{1.128}$$

Thus, the relative velocity reads

$$v_{\rm rel} = \sqrt{\frac{s-4m_\chi^2}{m_\chi^2}}. \tag{1.129}$$

Now we compute the thermally averaged cross section as defined in Eq.(1.121),

$$\begin{aligned} \langle \sigma_{\chi\bar\chi\to f\bar f} v_{\rm rel} \rangle &= \frac{\int d^3p_\chi d^3p_{\bar\chi} \sigma_{\chi\bar\chi\to f\bar f} v \exp\left[-(E_\chi + E_{\bar\chi})/T\right]}{\int d^3p_\chi d^3p_{\bar\chi} \exp\left[-(E_\chi + E_{\bar\chi})/T\right]}, \\ &= \frac{2\pi^2 T \int_{4m_\chi^2}^\infty ds \sqrt{s}(s-4m_\chi^2) K_1\left(\frac{\sqrt{s}}{T}\right) \sigma_{\chi\bar\chi\to f\bar f}(s)}{\left(4\pi m_\chi^2 T K_2\left(\frac{m_\chi}{T}\right)\right)^2}, \end{aligned} \tag{1.130}$$

where K_n is the modified Bessel functions of the second kind of order n.

To find the proper solution to the Boltzmann equation, numerical methods are needed. However, the approximated solution can be obtained analytically [50, 51]. Let us go back to Eq.(1.122). It can be written in terms of temperature instead of time by using

$$\frac{dY}{dt} = \frac{3m_\chi H s}{T^2} \frac{dY}{dx} \frac{dT}{ds}, \tag{1.131}$$

Eq.(1.122) becomes

$$\frac{dY}{dx} = -\frac{m_\chi}{3Hx^2} \frac{ds}{dT} \langle \sigma_{\chi\bar\chi} v \rangle \left(Y^2 - Y_{\rm eq}^2\right). \tag{1.132}$$

We assume further that the DM freezing out during the radiation-dominated epoch. Therefore, the Boltzmann equation can be cast into

$$\frac{dY}{dx} = -\frac{m_\chi}{x^2}\sqrt{\frac{\pi g'}{45G}}\langle\sigma_{\chi\bar{\chi}}v\rangle\left(Y^2 - Y_{\rm eq}^2\right), \tag{1.133}$$

or

$$\frac{dY}{dT} = \sqrt{\frac{\pi g'(T)}{45G}}\langle\sigma_{\chi\bar{\chi}}v\rangle\left(Y^2 - Y_{\rm eq}^2\right), \tag{1.134}$$

where

$$\sqrt{g'} = \frac{g_{*S}}{\sqrt{g_*}}\left(1 + \frac{T}{3g_{*S}}\frac{dg_{*S}}{dT}\right), \tag{1.135}$$

and

$$Y_{\rm eq} = \frac{45x^2}{4\pi^2 g_{*S}}\sum_f g_f\left(\frac{m_f}{m_\chi}\right)^2 K_2\left(x\frac{m_f}{m_\chi}\right). \tag{1.136}$$

To obtain the present relic abundance of DM, Y_χ^0, we have to integrate Eq.(1.133) from $x = 0$ ($T = \infty$) to $x = m_\chi/T_0$. However, micrOMEGAs [52] mainly uses Eq.(1.134) with the assumption that $Y \gg Y_{\rm eq}$ such that

$$\frac{1}{Y_0} = \frac{1}{Y_f} + \sqrt{\frac{\pi}{45G}}\int_{T_0}^{T_f}\sqrt{g'}(T)\langle\sigma_{\chi\bar{\chi}}v\rangle dT, \tag{1.137}$$

where Y_0 and Y_f are the abundance at present $T_0 = 2.73$ K and freeze-out temperatures, T_f. At high temperature, $d(Y - Y_{\rm eq})/dT$ is negligible. In addition, at freeze-out, the $Y_f = Y(T_f)$ is very close to $Y_{\rm eq}$, we can estimate $Y_f = (1+\delta)Y_{\rm eq}(T_f)$ where δ is a constant. The freeze-out temperature can be estimated from

$$\frac{d\ln Y_{\rm eq}}{dT} = \sqrt{\frac{\pi g'(T)}{45G}}\langle\sigma_{\chi\bar{\chi}}v\rangle Y_{\rm eq}\delta(\delta+2). \tag{1.138}$$

This equation is used to calculate the freeze-out temperature in micrOMEGAs. It was discussed in [52] that the solution to Eq.(1.137) is not significantly sensitive to the δ and it can vary from 1-2.

The relic density of DM can also be written in terms of dimensionless density parameter $\Omega_\chi = \rho_\chi^0/\rho_{\rm crit}$ where $\rho_{\rm crit} = 3H^2/8\pi G$. Thus, we can write the DM relic abundance as

$$\Omega_\chi h^2 = \frac{\rho_\chi^0 m_\chi h^2}{\rho_{\rm crit}} = 2.755\times10^8\frac{m_\chi}{\rm GeV}Y_0. \tag{1.139}$$

In figure 1.5, the evolution of the DM relic abundance in terms of $Y = n_\chi/s$ as a function of $x = m_\chi/T$ is presented. The dashed line indicates the evolution of $Y_{\rm eq}$ in Eq.(1.136).

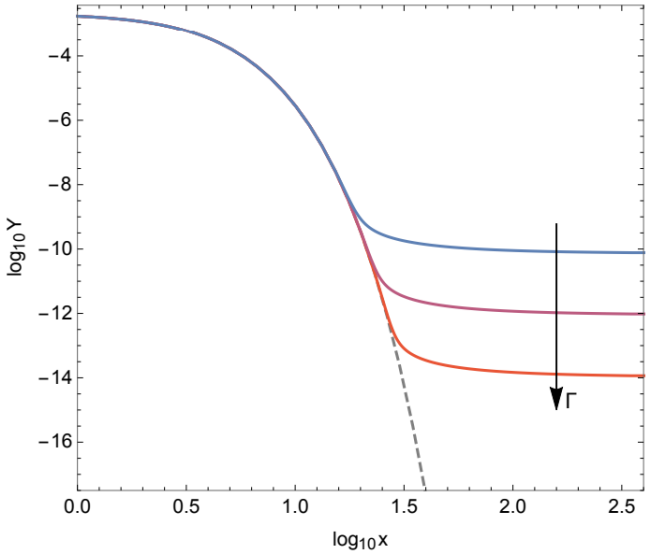

FIGURE 1.5: The evolution of $Y = n_\chi/s$ as a function of $x = m_\chi/T$ for freeze-out mechanisms, figure from [53]

.

The coloured solid lines correspond to the DM abundance due to freeze-out mechanism as a solution to Eq.(1.133). At high temperature or small x, they follow the equilibrium abundance line (black) and then they depart from the thermal bath at $x \sim 20-30$. The blue, pink and orange colours stand for the small to large scattering cross sections.

1.3.3 Indirect detection

In addition to the relic abundance of DM, the DM properties can also be examined through the so-called indirect detection where we are seeking for a signal of possible self annihilation of DM into SM particles as presented by a process of

$$\chi + \bar{\chi} \to \text{SM} + \text{SM}. \tag{1.140}$$

The recent reviews on DM indirect detection can be found in [54, 55, 56]. These self annihilation of DMs could potentially take place within astronomical environments such as the sun, stars, neutron stars, the centre of galaxy and dwarf spheroidal galaxies where the DM is clumpy and dense. The observable products from the DM annihilation could be photons, electrons, protons, neutrinos and their antiparticles. Then, we are trying to detect the excess flux of those particles over the astronomical background. One can expect that the rate of DM annihilation is proportional to the DM density $\Gamma \propto \rho^2_{\text{DM}}$. This means that the flux of annihilation products should be enhanced in a region with very dense DM population, especially at the centre of galaxy where the DM density is bigger than the average.

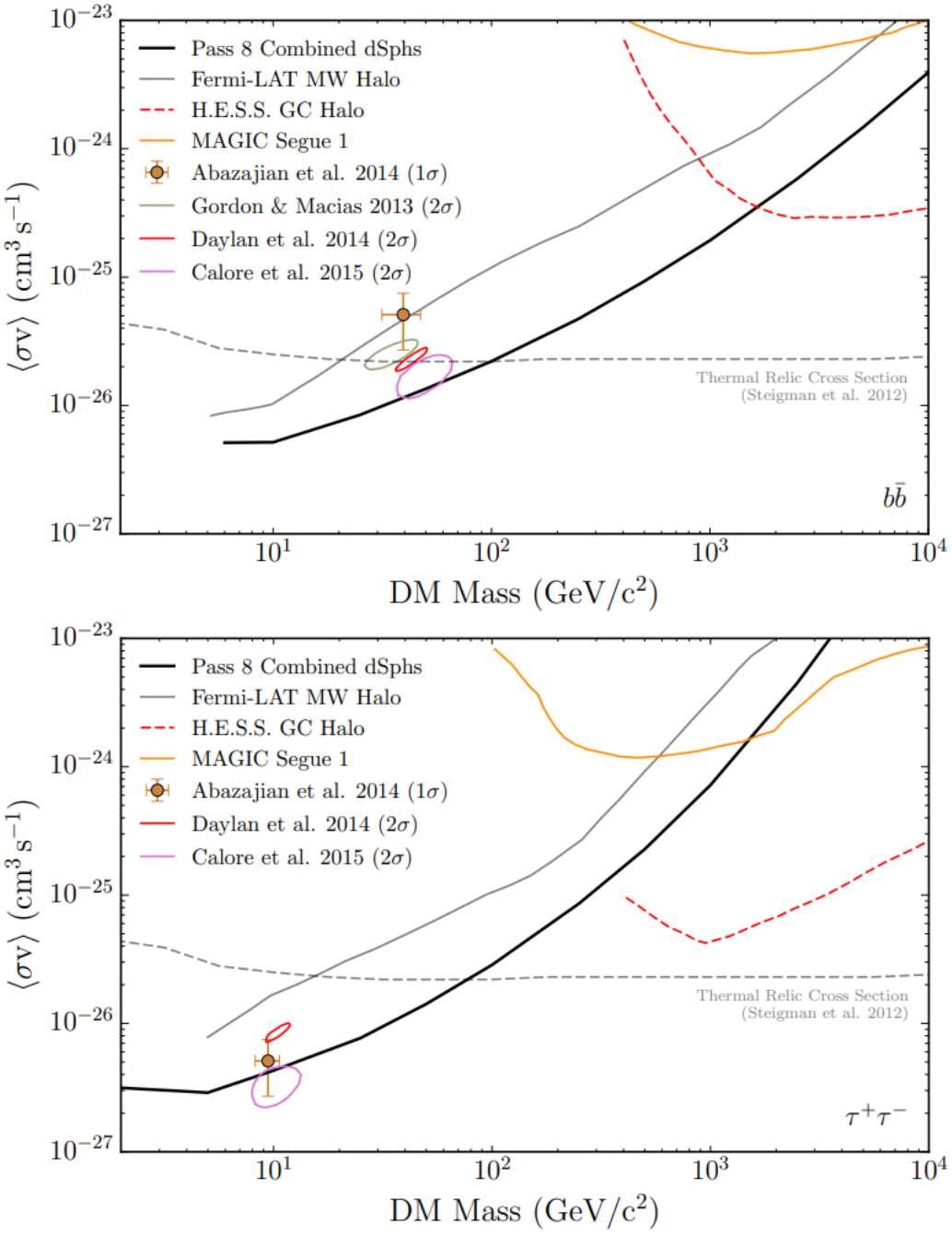

FIGURE 1.6: The upper limit on the WIMP velocity weighted annihilation cross section from various gamma-ray searches. The top(bottom) panel presents a $b\bar{b}$ ($\tau^+\tau^-$) annihilation. Figure from [57]

Gamma ray search

We expect to detect a monochromatic line of γ-rays with energy equal to or less than the DM mass. Since the gamma ray can propagate without deflection we can search for them by pointing detectors to region of dense dark matter such as the galatic centre and dwarf galaxies. However, the DM annihilation rate into photons is too weak [20] leaving us a chance to look for secondary photons produced from primary particles

with a wide energy spectrum. The Fermi-LAT space telescope [40] is able to detect single photons with energy 10 GeV - 10 TeV. In addtion, the Cherenkov telescope like MAGIC or H.E.S.S can cover a wider range from 20 GeV to a few hundred TeV [56]. However, searching for gamma-ray excess at the galactic centre is quite challenging due to the backgrounds from gamma-ray emitting objects. With this reason, the clean structure of dwarf spheroid galaxies are a more favourite sources of the gamma-ray. The search results are interpreted in terms of the WIMP annihilation cross section for various annihilation channels, for example, W^+W^-, ZZ, $q\bar{q}$ and $\ell^+\ell^-$. The most stringent upper limit in the mass range of 0.1-1 TeV has been placed by Fermi-LAT. However, in the mass range above 1 TeV, the most stringent upper bound has been placed by H.E.S.S, as shown in figure 1.6.

Charged cosmic ray search

In addition, the charged cosmic ray – proton, electron, light nuclei and their antiparticles – could be interpreted as a product of DM annihilation or decays via the hadronisation of $q\bar{q}$ or W^+W^- [56]. However, the charged cosmic ray can be easily deflected by the galactic magnetic fields making them travelling to us in a random way. We expect to measure the excess of cosmic ray spectrum over the SM predicted one. Since the large background of electron and proton fluxes from numerous astrophysical objects, the more attractive particles would be positrons and antiprotons. Some positive results on cosmic ray as a probe of DM have been reported by the PAMELA satellite [58] which detected the excess of positron spectrum in the energy range of 1.5-100 GeV . In addition, the ATIC balloon experiment [59] has measured excess of electron flux with energy range of 300-800 GeV. The kind of excess could be generated from the DM annihilation. Later, this result has been confirmed by the Fermi-LAT and AMS-02 satellites (with energy range of 0.5-500 GeV). The limits on the velocity weighted DM annihilation cross section at 95 % confidence level for the $b\bar{b}(W^+W^-)$ channels from cosmic ray excess is presented in figure 1.7.

Neutrino search

Neutrinos can also be used as a probe of DM annihilation. Since they interact only through the weak interaction, they can propagate through space without deflection from the centre of stars. Therefore, one can directly point detectors towards the source of neutrino flux. However, using neutrino as a probe of DM annihilation faces the challenges because of low scattering cross section with matter. This implies that detecting single scattering event needs large detector and long exposure time. Unfortunately, the upper bound on the annihilation cross section is less stringent compared to the

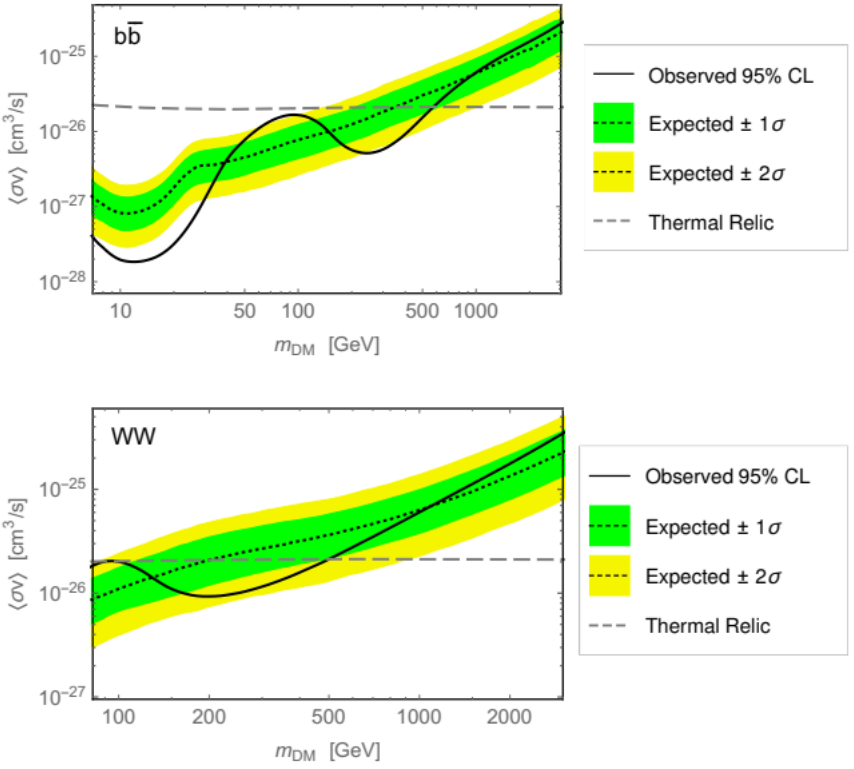

FIGURE 1.7: The upper bounds on the velocity weighted DM annihilation cross section at 95 % confidence level. The top(bottom) panel represent the limits from the $b\bar{b}(W^+W^-)$ channels derived from the antiproton and B/C data of AMS-02. Figure from [60]

limits from gamma-ray search. There are several experiments searching for DM annihilation products as neutrinos such as ANTARES [61, 62], IceCube [41, 63, 64], Super-Kamiokande [65, 66] and etc. The IceCube experiment has detected the very high energy neutrinos around 60 events with energy from 10-1000 TeV. The detected neutrinos are too energetic and not compatible with the atmospheric neutrinos produced in the Earth's atmosphere by cosmic ray scattering. The summary of the velocity weighted annihilation of DM into neutrinos versus the DM mass from various range of searches in the range of $10^{-2} - 10^{7}$ GeV in shown in figure 1.8.

CMB anisotropies

Morever, the CMB anisotropies from the PLANCK collarboration [68, 21] also provides the alternative way for DM indirect searches. The fact that recombination history can be affected by the energy injection from DM annihilation [69] gives us the opportunity to constrain the DM annihilation cross section complementary to other indirect DM searches as previously discussed. The gaseous background can be heated and ionised by different DM annihilation products. The energy fraction that is injected into the gas can be explained by a parameter called the efficiency factor $f(z)$ as a function redshift which ranges from 0.01-1. The rate of energy release from DM annihilation per unit

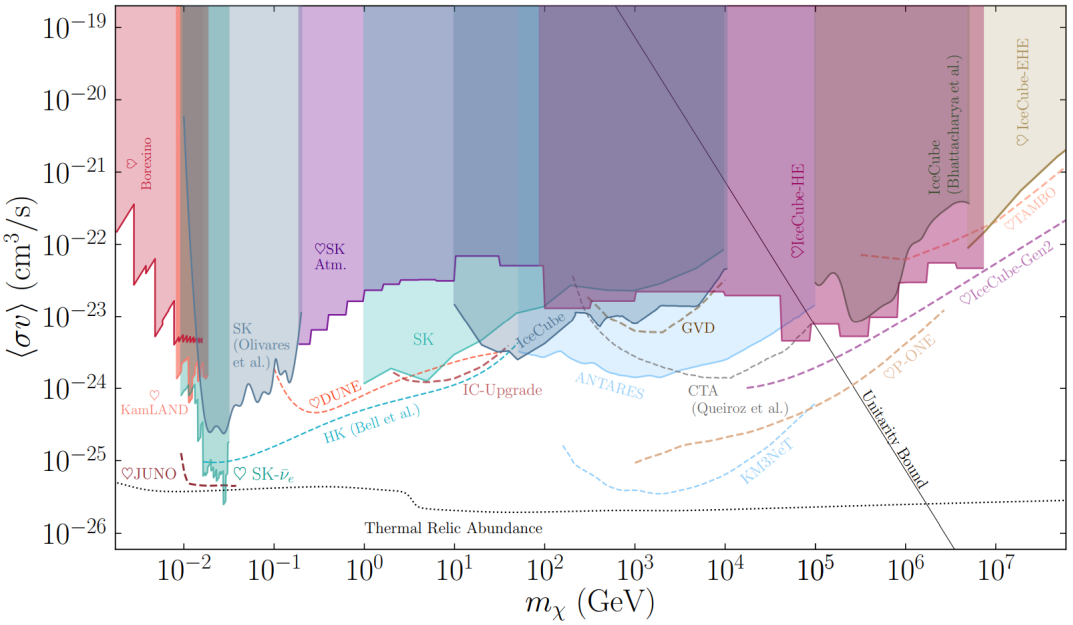

FIGURE 1.8: The upper bounds on the velocity weighted DM annihilation cross section from various experiments. Figure from [67].

volume is given by [68]

$$\frac{dE}{dtdV}(z) = 2\, g\, \rho_{\rm crit}\, c^2\, \Omega_{\rm DM}^2\, (1+z)^6\, p_{\rm ann}(z), \tag{1.141}$$

where

$$p_{\rm ann} \equiv f(z)\frac{\langle\sigma v\rangle}{m_{\rm DM}}. \tag{1.142}$$

The g is a degeneracy factor equal to 1/2 for Majorana particles and 1/4 for Dirac particles, $\Omega_{\rm DM}$ is the DM relic density. The $\langle\sigma v\rangle$ is the thermally-averaged annihilation cross section times the velocity. The $f(z)$ is the efficiency factor depending on the redshift z and provided in [70] for every possible SM particles in the final states. Since the CMB data is sensitive to the energy injection in a range of redshift 1000-600 and the function $f(z)$ peaks at $z \approx 600$ [68]. To a good approximation, the redshift dependence of $f(z)$ can be ignored and replaced by $f_{\rm eff} = f(z = 600)$. The Planck 2018 results [21] gives a constraint on the DM annihilation cross section as shown in figure 1.9. The upper limits for different DM annihilation channels are derived based on $p_{\rm ann} < 3.2 \times 10^{-28}$ cm^3 s^{-1} GeV^{-1}.

1.3.4 Direct detection

The DM direct detection is a powerful way to probe the DM nature by searching for scattering events of DM off SM particles, DM + SM $\rightarrow$ DM + SM. Since DM interacts very weakly with the ordinary matter, the scattering events would occur with very low

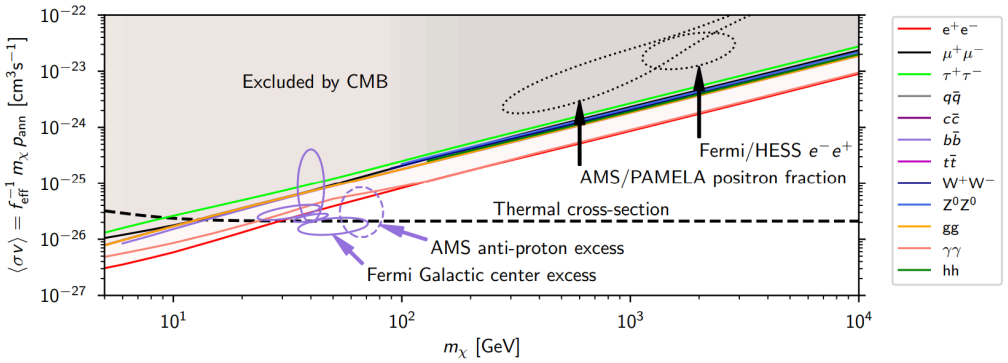

FIGURE 1.9: The upper bounds on the DM annihilation cross section times velocity from different annihilation channels into a pair of SM particles in the final state. Figure from [21].

probability and very small energy deposits because of low DM velocity at the Sun's location ($v \sim 10^{-3}c$). Generally, the scattering process of DM off nucleon can distinguished into the spin-dependent (SD) and spin-independent (SI) one. The best sensitivity of SI search is given by heavy nuclei detectors and for SD one it is offered by light nuclei detectors. However, the most stringent constraint is placed by the SI process. When DMs scatter off heavy nuclei in the detector, the collision energy is transferred and make nuclei slightly recoil. We are trying to measure the recoil energy. Suppose the DM mass is about 100 GeV and the DM velocity at the sun location is estimated to be $v \sim 10^{-3}c$. Then, the maximum recoiling energy of nucleon is given by $E_{\rm DM}^{\rm max} = m_{\rm DM}v^2/2 \sim 100$ keV. This process is very rare. In order to increase the chance to capture DM particles, the size of detectors needs to be very large to get a more or more stringent searching limits. However, the DM direct detection is challenging because neutrons from radioactive decays can also produce the similar signal as they are heavy and neutral. The background signal can be reduced by installing a detector underground or in environment with low radioactivity. The measurement of the recoil energy faces the challenge because of some theoretical uncertainties such as the local energy density of DM at the Earth's position and the DM velocity distribution.

Experimentally, the DM-nucleon scattering cross section can be divided into two groups depending on the interaction nature of DM with nucleons. They are called the spin-dependent and spin-independent ones. However, the spin-dependent cross section is weaker than the spin-independent one. Thus, we will only discuss the spin-independent cross section from now on. There are several experiments trying to find DM direct detection signals which covers a wide range of DM mass from 0.1-1000 GeV as shown in figure 1.10. For example, NEWS-G [72], CDMSLite [73], DarkSide-50 [74] have placed the most stringent upper limits covering light DM mass below 5 GeV. For DM mass range above 5 GeV, the experiments such as PandaX-II [45], LUX [75] and XENON1T [44] have been conducted. The most stringent upper limit has been placed by the XENON1T. However, in 2022, the most stringent upper limit is provided by the LZ experiments [71]

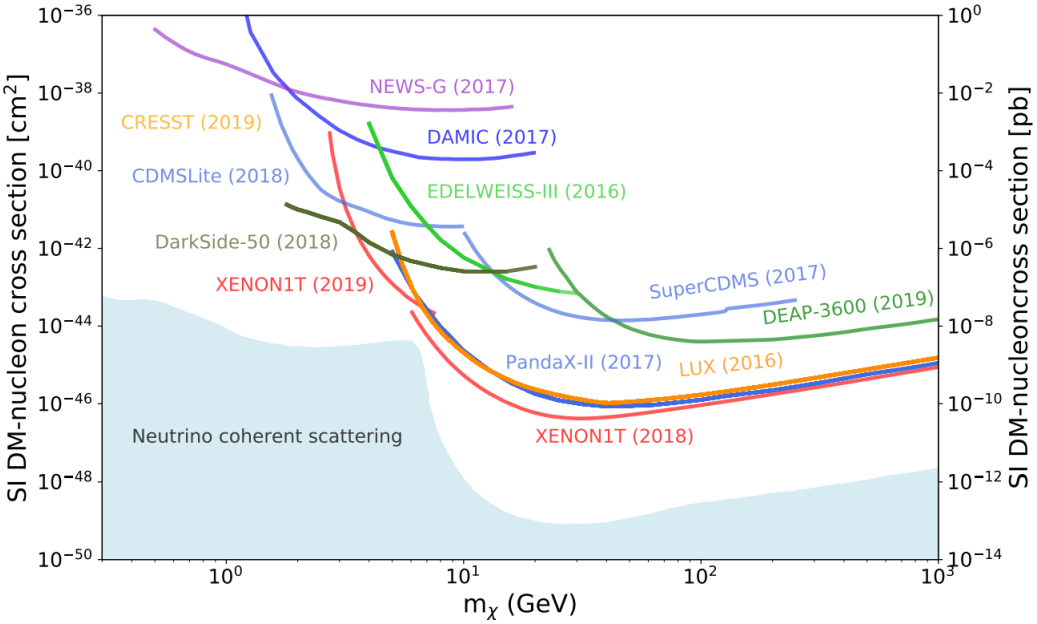

FIGURE 1.10: The upper bounds on the spin-independent DM-nucleon scattering cross section as a function of DM mass in range of 0.1-100 GeV from multiple experiments. Figure from [13].

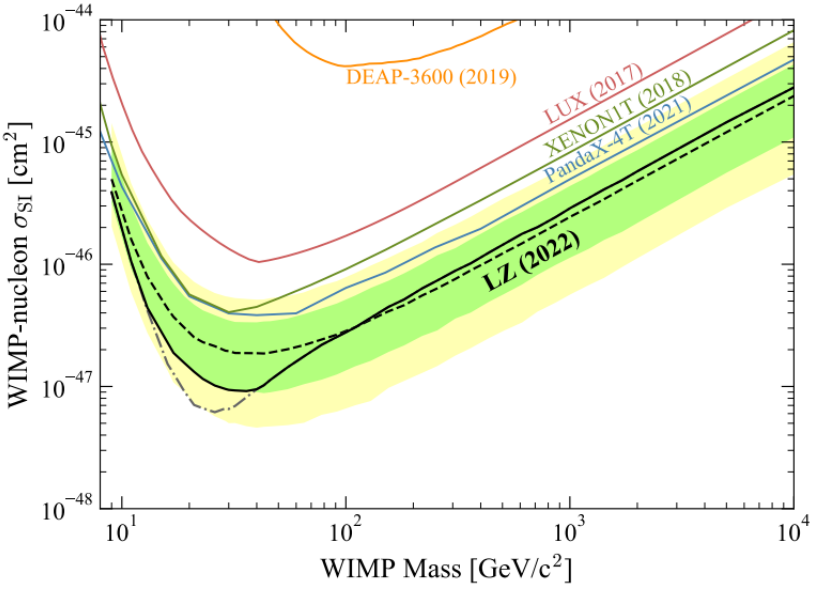

FIGURE 1.11: The upper bounds on the spin-independent DM-nucleon scattering cross section from LZ experiment. Figure from [71].

which is a successor of LUX as shown in figure 1.11. The most strongest limit is at the DM mass around 30 GeV with the DM-nucleon scattering cross section $\sim 10^{-47}$ cm^2.

1.3.5 Collider searches

The production of DM could be possible at collider environments. Various searches for DM signals at LHC [76, 77, 78, 79] with the centre of mass energy of 13 GeV

and the integrated luminosity of 36 fb^{-1} have been conducted by ATLAS and CMS collaborations. The DM signal can manifest in various forms depending on a DM model. In general, the interaction between SM and dark sectors can take place in models with Higgs or Z boson exchange, models with additional mediators and etc. Each model also needs different search strategy. For example, DM might manifest as invisible particles produced by a SM Higgs boson or Z boson or by an exotic resonances or the transverse missing energy produced together with one SM particles or exotic state as a bump in the dijets or dilepton invariant mass distribution [80].

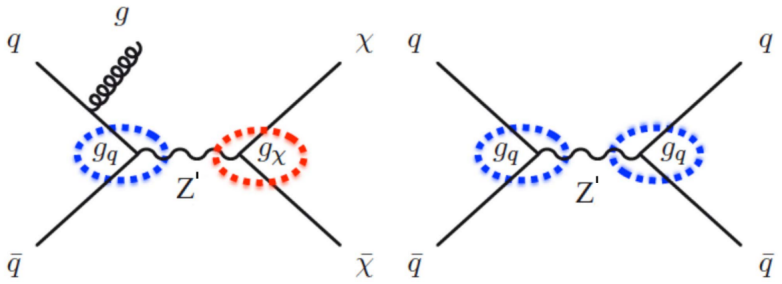

FIGURE 1.12: The representative Feynman diagrams for mono-X and new mediator searches. Figure from [80].

The search strategy at LHC can be divided into mono-X and mediator searches as depicted in figure 1.12. In the former search, a pair of DMs is produced by annihilation of a pair of SM particles like a pair of $q\bar{q}$ and a pair of gg. However, since the DM is blind to the detectors, this kind of signal is not informative as it can be mimicked by neutrinos. Therefore, we need a detectable SM particle produced along with a pair of DMs and then measure the missing transverse energy E_T^{miss} or missing transverse momentum p_T^{miss} for the event. This search at ATLAS and CMS focus on the properties of mediator (a scalar, a pseudo-scalar, a vector, or an axial-vector) and couplings to the SM particles g_q or to DM particle q_χ. The search has placed the upper limits on the production cross section of DM particles as a function of the mediator or DM masses. The possible final states could be mono-jet, mono-γ, mono-Z, mono-Higgs, mono-top and $t\bar{t} + E_T^{\text{miss}}$. The last two final state particles can occur for some models. In the latter search, the annihilation of a pair of SM particles can lead to a creation of new mediator between SM and dark sectors and then it will decay into a pair of SM particles like $q\bar{q}$ or $\ell^+\ell^-$ in the final state. In this search, we look for a bump due to the new resonance in the invariant mass or angular distribution for the final state particles. The limits have been presented as ratio of production cross section of new mediator to that of the SM particle and set the upper bounds on the resonance mass.

Unfortunately, no DM signals have been observed at the LHC experiment [13] so far. However, the limits have been set on masses, couplings and cross section related to dark sector. The latter can be complementary to the DM direct detection searches. Anyway, even though we found a DM signal at LHC but this cannot be a proof of DM discovery.

The signal has to be consistent with other DM searches like relic abundance, direct and indirect detections.

1.4 The muon anomalous magnetic moment

The anomalous magnetic moment experiments of muons or the so-called muon g-2 experiments have implies that a new physics beyond the standard model (BSM) is necessary. The muons are electrically charged particles, like electrons. When entering a region with external magnetic fields they behave like a small magnet. Typically, the magnetic moment of an elementary particle like electron or muon is expressed in terms of the spin magnetic moment which is defined as

$$\vec{\mu} = g\frac{q}{2m}\vec{S}, \tag{1.143}$$

where the dimensionless parameter g is called the g-factor (not the gyromagnetic ratio $\gamma = gq/2m$), q is the particle's charge, m is the mass of a particle and $\vec{S}$ is its spin angular momentum. The magnetic moment of a particle tells us how strong the particle can interact with the external magnetic fields. According to the Dirac equation, the g-factor of Dirac particles is predicted to exactly be 2 according to their two spin states – up and down [81]. The magnetic moment is not only a particle's properties related to the electromagnetic interaction, but it can also imply the departure from a point-like nature a particle of interest as predicted by Dirac's equation. For example, the g-factor of a single proton has been measured to be 5.585 696(50) [82]. However, the experimental value of the muon magnetic moment is slightly greater than 2. Usually, the experimentalists report the deviation of g_μ from 2 in terms of

$$a_\mu \equiv \frac{g_\mu - 2}{2}, \tag{1.144}$$

which indicates the anomalous part of the measured value. This deviation cannot be understoond within the SM framework even though the loop corrections at higher-orders are included in the theoretical prediction. These precise experiments are not only a validation of the SM, but also manifest a sign for new physics.

In this section, we discuss the brief account of the g-2 measurements and the SM prediction. We will see later that the comparison between the averaged experimental result at present and the theoretical prediction within the SM leads to the deviation at the level of 5.0σ.

1.4.1 The $g_\mu - 2$ measurements

After the discovery of muon by Carl D. Anderson and Seth Neddermeyer at Caltech in 1936, physicists still wondered if they were just heavier copy of electrons or other particles. Therefore, the measurement of muon g-2 is one of many experiments had been performed to investigate its properties.

The CERN-I result of muon magnetic moment was published in 1965 [83] with precision of 0.4 % by using a long dipole magnet of 1.6 T. In 1974, the storage ring technique was developed and the relativistic muons was used to increase the observation time. This technique was used in CERN-II and -III experiments with different radii and the precision was improved to 270ppm and 7.3ppm, respectively. After the end of the program on muon g-2 experiment at CERN, the Brookhaven National Laboratory (BNL) was its successor and conducted the g-2 measurement with superconducting storage ring magnet and more uniform magnetic field. This improved the experimental precision to the level of 0.54 ppm. Then, the next experiment was built at Fermilab called the Fermi National Accelerator Laboratory with better precision. The experimental setup for aforementioned measurements is summarised in table 1.5.

Experiment	**Magnet**	**Approach**	γ_μ	$\delta a_\mu / a_\mu$
CERN I (1965)	Long dipole magnet, $B = 1.6$ T	μ injection	1	4000 ppm
CERN II (1974)	$R = 2.5$ m storage ring, $B = 1.71$ T	p injection	12	270ppm
CERN III (1978)	$R = 7.1$ m storage ring, $B = 1.47$ T	π injection	29.3	7.3ppm
BNL (2006)	$R = 7.1$ m storage ring, $B = 1.45$ T	μ injection	29.3	0.54ppm
FNAL Run-1 (2021)	$R = 7.1$ m storage ring, $B = 1.45$ T	μ injection	29.3	0.46ppm
FNAL Run-2/3 (2023)	$R = 7.1$ m storage ring, $B = 1.45$ T	μ injection	29.3	0.21ppm

TABLE 1.5: The summary of various experimental setups for muon g-2. Table from [84].

The precession measurement of muon g-2

Let us consider a muon which is non-relativistically moving on a plane perpendicular to the direction of external magnetic field $\vec{B}$. Then, the muon's momentum rotates around the magnetic field with the cyclotron frequency which is given by

$$\vec{\omega}_c = \frac{e\vec{B}}{m}. \tag{1.145}$$

However, the magnetic moment of the muon is not necessarily aligned with the external magnetic field, there is a precession of its magnetic moment about the $\vec{B}$ field with the

Larmor precession frequency for the muon in its rest frame which is given by

$$\vec{\omega}_L = g\left(\frac{e\vec{B}}{2m}\right) = (1+a_\mu)\left(\frac{e\vec{B}}{m}\right). \tag{1.146}$$

If $g = 2$, these two frequencies are exactly the same. However, from experiment on muon g-2 this is not the case. For $g > 2$, the spin of muon turns faster than its momentum. This difference can be explained by a quantity called the anomalous precession frequency

$$\vec{\omega}_a = \vec{\omega}_L - \vec{\omega}_c = a_\mu \frac{e\vec{B}}{m}. \tag{1.147}$$

The underlying idea behind the experiments is to measure the angle between the spin and the direction of motion of muon as a function of time [85] while moving in a circular orbit under the magnetic field. If the anomalous g-2 is measured to be 10^{-3}, this means that in one cycle on the orbit the relative spin direction turns a thousand rounds under the magnetic field. Therefore, to accurately measure the anomaly the muons need to be stored long enough to make many thousands turns. However, this leads to a problem because the lifetime of muon at rest is short about 2.2 microsecond. The muon's lifetime issue can be leviated by the time dilation effect when it moves with speed close to the speed of light. This means that Eq.(1.145) has to be modified with the Lorentz factor γ

$$\vec{\omega}_c = \frac{e\vec{B}}{\gamma m}, \tag{1.148}$$

where $\gamma = (1-\beta^2)^{-1/2}$ and $\vec{\beta}$ is the muon's velocity in the unit of speed of light.

The motion of the muon on the circular orbit gives rise to a relativistic effect. When viewing from the laboratory frame, its rest frame appears to precess with the frquency

$$\vec{\omega}_T = \left(1 - \frac{1}{\gamma}\right)\frac{e\vec{B}}{m}. \tag{1.149}$$

This fact was discovered by Thomas in the context of electron spin in 1926 [86]. Thus, the total angualar frequency of the spin is given by

$$\vec{\omega}_s \equiv \vec{\omega}_L - \vec{\omega}_T = (1+a_\mu)\left(\frac{e\vec{B}}{m}\right) - \left(1-\frac{1}{\gamma}\right)\left(\frac{e\vec{B}}{m}\right) = \left(a_\mu + \frac{1}{\gamma}\right)\left(\frac{e\vec{B}}{m}\right). \tag{1.150}$$

Eq.(1.150) implies that the relativistic description does not affect the previous conclusion where

$$\vec{\omega}_a = \vec{\omega}_s - \vec{\omega}_c = a_\mu\left(\frac{e\vec{B}}{m}\right), \tag{1.151}$$

which gives the same result as Eq.(1.147).

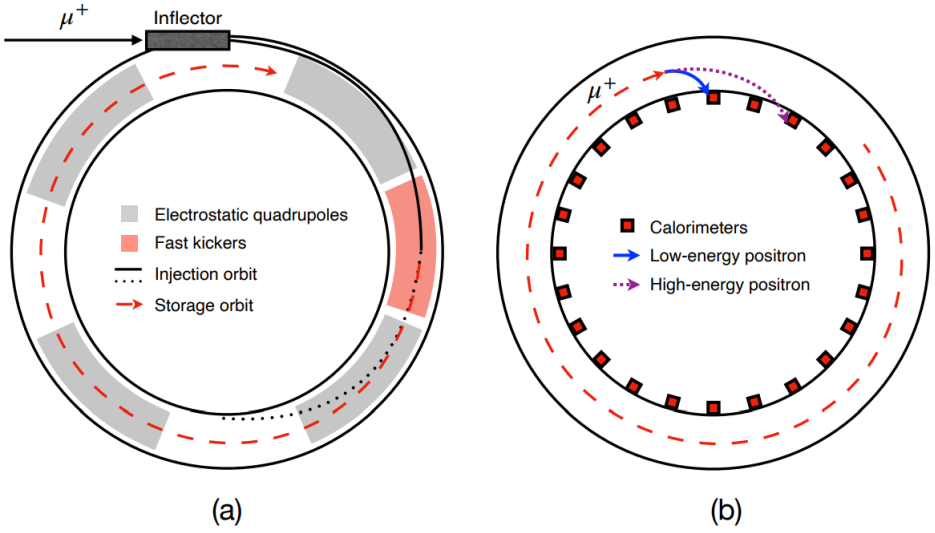

FIGURE 1.13: The schematic setup of the storage ring in FNAL experiment. Figure from [84].

In the modern muon g-2 experiments like BNL and FNAL, the muon beams with chosen spin-polarisation are injected into the storage ring through the inflector as depicted in figure 1.13 and their spin evolution is tracked as they move on the ring. As muons move in the region with uniform magnetic field B and the electric field is absent, assuming that they only on a plane perpendicular to the B field $\vec{\beta}\cdot\vec{B} \approx 0$ where $\vec{\beta}$ is the velocity of muon, the anomalous frequency of muon spin precession is given by Eq.(1.151). However, if the electric field is turned on and the muon beam is not exactly perpendicular to the magnetic field, Eq.(1.151) becomes

$$\vec{\omega}_a \equiv \vec{\omega}_s - \vec{\omega}_c = \frac{e}{m}\left[a_\mu \vec{B} - a_\mu\left(\frac{\gamma}{\gamma+1}\right)(\vec{\beta}\cdot\vec{B})\vec{\beta} - \left(a_\mu - \frac{1}{\gamma^2-1}\right)\vec{\beta}\times\vec{B}\right]. \quad (1.152)$$

When a positive muon travels on a circular ring for a time equal to its lifetime it will decay to a positron and corresponding neutrinos. According parity-violating weak decays, $\mu^+ \to e^+\bar{\nu}_\mu\nu_e$, the muon will preferably inject a high energy positron in the same direction of its spin in the muon rest frame. However, in the lab frame, the angle between muon's spin and momentum can affect the positron energy spectrum. This allows us to measure the evolution of positron energy spectrum as muon beams move around the ring. This energy is measured by many calorimeters placed around the interior of the ring. The energy of positron is the highest when the muon's spin and momentum are pointing in the same direction. Thus, the number of positrons which is detected at time t is given by

$$N(t) = N_0 e^{-t/\tau}[1 + A\cos(\omega_a t + \phi)], \quad (1.153)$$

where N_0 is the normalisation constant, A is the muon decay asymmetry and τ is the lifetime of muon.

The current experimental results from the E821 at BNL for both positive and negative muons were reported to be [13]

$$\begin{aligned} a_{\mu^+}^{\text{exp,BNL}} &= 116\,592\,040(60)(50) \times 10^{-11}, \\ a_{\mu^-}^{\text{exp,BNL}} &= 116\,592\,150(80)(30) \times 10^{-11}, \end{aligned} \tag{1.154}$$

where the numbers in first and second brackets indicate the statistical and systematic errors. In addition, the result at Fermilab from Run I, II and III is combined to be

$$a_{\mu}^{\text{exp,FNAL}} = 116\,592\,055(24) \times 10^{-11}. \tag{1.155}$$

Therefore, the averaged value of the muon anomalous magnetic moment from BNL and FNAL experiments is given by [87]

$$a_{\mu}^{\text{exp}} = 116\,592\,059(22) \times 10^{-11}. \tag{1.156}$$

The current status of the experimental findings from BNL and FNAL Run 1-3 is presented in figure 1.14. The central value for BNL, FNAL Run-1, FNAL Run-2/3 FNAL Run-1 + Run-2/3 and the current experimental average is indicated by the blue triangle, red hollow square, red dot and purple square, respectively. The uncertainties are presented as horizontal lines. The statistical uncertainty is labeled by the small tick on the horizontal lines while the purple band indicates the total uncertainty.

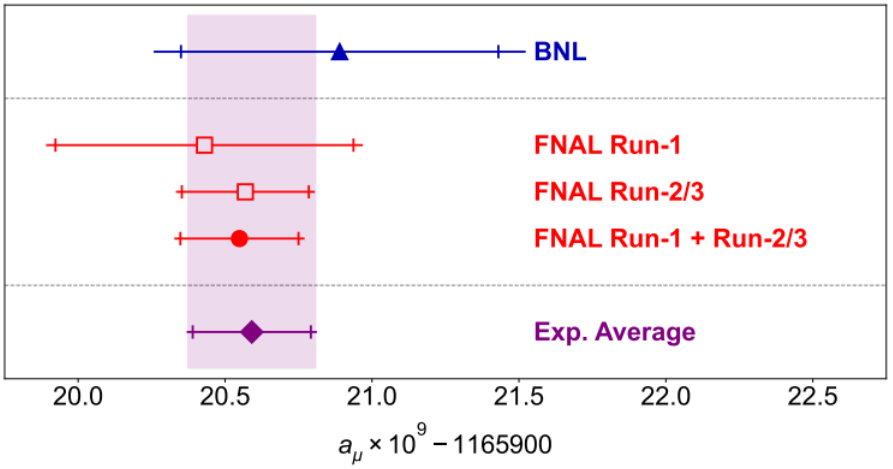

FIGURE 1.14: The comparison of experimental fidings from different muon g-2 measurements. Figure from [87].

1.4.2 The standard model prediction of g-2

Classically, the Dirac equation predicts the g-factor ($g = 2$) for any fermions. However, due to the quantum effect, at higher order correction of $\mu\mu\gamma$ vertex, the vertex function is modified because muon interacts with virtual particles circulating in the loops at higher order. In order to determine the quantum effect on the muon magnetic moment, we need to evaluate the radiative correction of $\mu\mu\gamma$ vertex.

Generically, the vertex function $\Gamma^\mu(p', p)$ can be separated into many parts

$$\begin{aligned}\Gamma^\mu =&\gamma^\mu F_1(q^2) + \frac{i\sigma^{\mu\nu}q_\nu}{2m_\mu}F_2(q^2) + \frac{q^\mu}{m_\mu}F_3(q^2) \\ &+ (\gamma^\mu - \frac{\not{q}q^\mu}{q^2})\gamma_5 G_1(q^2) + \frac{i\sigma^{\mu\nu}q_\nu\gamma_5}{2m_\mu}G_2(q^2) + \frac{q^\mu}{m_\mu}\gamma_5 G_3(q^2).\end{aligned} \tag{1.157}$$

where p and p' represent the momentum of incoming and outgoing muons, respectively. The momentum q is equal to $p - p'$. The quantities F_1, F_2, G_1 and G_2 are called Dirac, Pauli form factor, Anapole and electric dipole moment (EDM), respectively. The only form factor contributing to the anomalous magnetic moment is called the Pauli form factor or $F_2(0)$ and is given by

$$a_\mu = \frac{g_\mu - 2}{2} \equiv F_2(0), \tag{1.158}$$

where g_μ is called the g-factor which tells us how strong the muon can interact with the magnetic field.

At one loop, the $\Gamma^\mu(p', p)$ can be computed by evaluating the relavant Feynmann diagram as shown in figure 1.15. The expression for anomalous magnetic moment of a generic fermion was computed in [88]. Let us consider a model with Lagrangian

$$\mathcal{L}_{\text{int}} = \sum_{F,X} \bar{\mu}[C_V\gamma^\rho + C_A\gamma^\rho\gamma^5]FX_\rho, \tag{1.159}$$

where F and X are a generic fermion and vector boson, respectively. Here C_V and C_A stand for the vector and axial-vector couplings. The result for diagram 1.15(a) and (b)

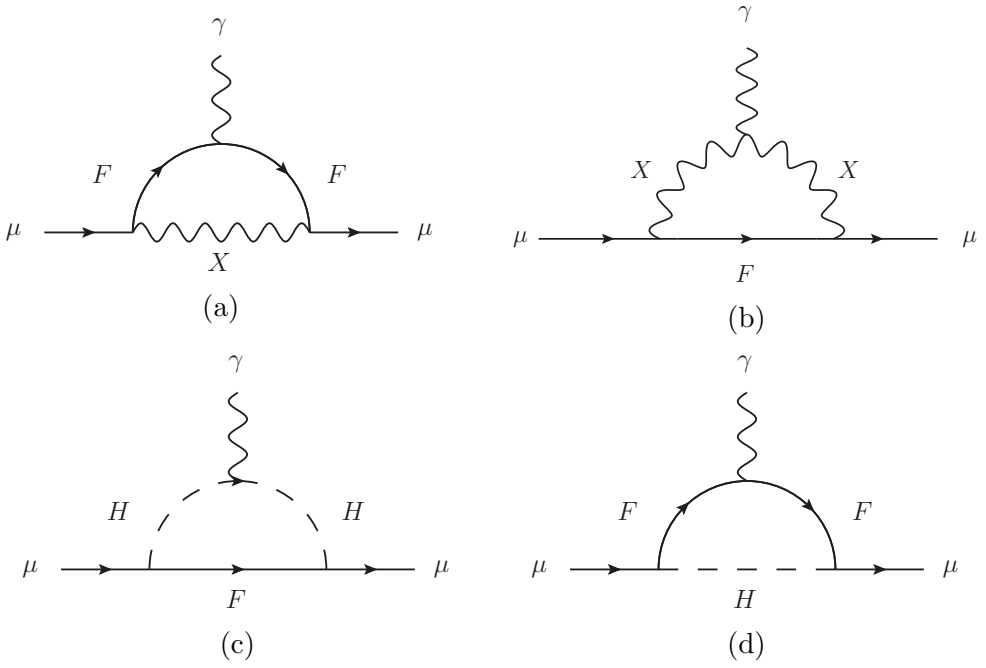

FIGURE 1.15: The contributing diagrams to the $\mu\mu\gamma$ vertex at the leading order from QED and electroweak sectors. Here X, F and H represent generic vector, fermion and scalar fields, respectively.

is given by

$$
\begin{aligned}
a_\mu^{(\mathrm{a})} = -\frac{q_F m_\mu^2}{4\pi^2}\int_0^1 \mathrm{d}x \Bigg[C_V^2 \Bigg\{ (x-x^2)\left(x + \frac{2m_F}{m_\mu} - 2\right) \\
- \frac{1}{2M_X^2}\left(x^3(m_F - m_\mu)^2 + x^2(m_F^2 - m_\mu^2)\left(1 - \frac{m_F}{m_\mu}\right)\right)\Bigg\} \\
+ C_A^2\{m_F \to -m_F\}\Bigg]\Big[m_\mu^2 x^2 + M_X^2(1-x) + x(m_F^2 - m_\mu^2)\Big]^{-1}, \qquad (1.160)
\end{aligned}
$$

$$
\begin{aligned}
a_\mu^{(\mathrm{b})} = \frac{q_X \mu^2}{8\pi^2}\int_0^1 \mathrm{d}x \Bigg[C_V^2 \Bigg\{ \frac{4m_F}{m_\mu}x^2 - 2x^2(1+x) \\
+ \frac{m_\mu^2}{M_X^2}\Bigg[-x^2(x-1) - \frac{m_F}{m_\mu}(-2x^3 + 3x^2 - x) - \frac{m_F^2}{m_\mu^2}(2x - 3x^2 + x^3) \\
+ \frac{m_F^3}{m_\mu^3}(x - x^2)\Bigg]\Bigg\} + C_A^2\{m_F \to -m_F\}\Bigg]\Big[m_\mu^2 x^2 + (M_X^2 - m_\mu^2)x + m_F^2(1-x)\Big]^{-1}, \qquad (1.161)
\end{aligned}
$$

where q_F is the electric charge of F in unit of $|e|$. The m_μ, m_F and M_X are the mass of muon, fermion F and vector boson X, respectively. The term $\{m_F \to -m_F\}$ represents all previous term but with the opposite sign of internal fermion mass. These two results have been cross-validated with the ones I derived in Appendix F.

For the scalar contribution with Lagrangian

$$\mathcal{L}_{\text{Yukawa}} = \sum_{F,H} \bar{\mu}[C_S + C_P\gamma^5]FH, \tag{1.162}$$

the results for diagrams with scalar propagation as depicted in figure 1.15(c) and (d) read

$$a_\mu^{(\text{c})} = -\frac{q_H m_\mu^2}{8\pi^2}\int_0^1 \mathrm{d}x \left[C_S^2\left\{x^3 - x^2 + \frac{m_F}{m_\mu}(x^2 - x)\right\} + C_P^2\{m_F \to -m_F\}\right] \times \left[m_\mu^2 x^2 + (m_H^2 - m_\mu^2)x + m_F^2(1-x)\right], \tag{1.163}$$

$$a_\mu^{(\text{d})} = -\frac{q_F m_\mu^2}{8\pi^2}\int_0^1 \mathrm{d}x \left[C_S^2\left\{x^2 - x^3 + \frac{m_F}{m_\mu}x^2\right\} + C_P^2\{m_F \to -m_F\}\right] \times \left[m_\mu^2 x^2 + (m_F^2 - m_\mu^2)x + m_H^2(1-x)\right], \tag{1.164}$$

where C_S and C_P are the scalar and pseudo-scalar couplings. After integrating over the Feynman parameter x, the result of $a_\mu^{(\text{d})}$ has been checked against Eq.(F.25).

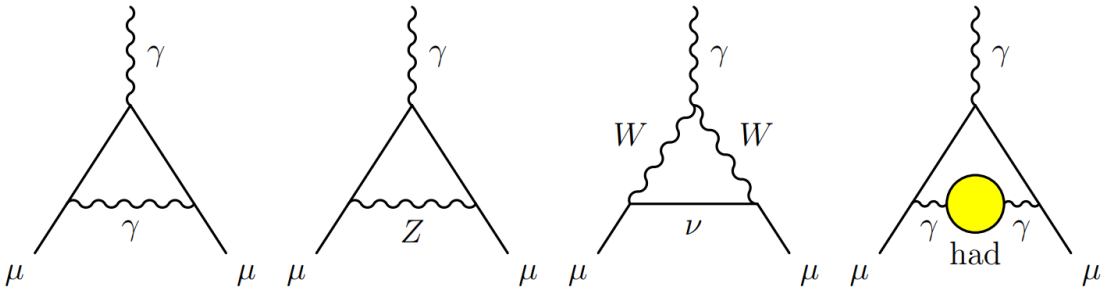

FIGURE 1.16: The SM diagrams contributing to the muon anomalous magnetic moment at one loop. Figure from [13]

In principle, the SM calculation for the muon anomalous magnetic moment can be separated into three parts, which are the pure QED, the electroweak and the hadronic contributions [13]. In the SM, the one loop contributions from QED diagram can be calculated by Eq.(1.160) and is given by

$$a_\mu^{\text{QED}}[\text{1-loop}] = \frac{\alpha}{2\pi}. \tag{1.165}$$

This first expression was originally calculated by Julian Schwinger in his 1948 paper [89]. Nowadays, however, we are able to evaluate the pure QED contribution up to five loops [90] and it reads

$$a_\mu^{\text{QED}} = \frac{\alpha}{2\pi} + 0.765\ 857\ 420(13)\left(\frac{\alpha}{\pi}\right)^2 + 24.050\ 509\ 85(23)\left(\frac{\alpha}{\pi}\right)^3 + 130.8782(60)\left(\frac{\alpha}{\pi}\right)^4 + 751.0(9)\left(\frac{\alpha}{\pi}\right)^5 + \cdots \tag{1.166}$$

$$= 116\ 584\ 718.93(0.10) \times 10^{-11}. \tag{1.167}$$

In addition, the one loop results for EW contributions read

$$a_\mu^{\rm EW}[\text{1-loop}] = \frac{G_F m_\mu^2}{8\sqrt{2}\pi^2}\left[\frac{5}{3} + \frac{1}{3}(1-4\sin^2\theta_W)^2 + \mathcal{O}\left(\frac{m_\mu^2}{M_W^2}\right) + \mathcal{O}\left(\frac{m_\mu^2}{M_H^2}\right)\right], \quad (1.168)$$

$$= 194.8 \times 10^{-11}. \quad (1.169)$$

This result is easily found by substituting the SM couplings into Eq.(1.160), (1.161) and (1.164) and expanding it in the limit of $m_\mu^2/m_W^2 \ll 1$ and $m_\mu^2/m_H^2 \ll 1$[2]. Now we have the EW result up to two loop contribution and it reads

$$a_\mu^{\rm EW} = 153.6(1.0) \times 10^{-11}. \quad (1.170)$$

Note that errors in QED and EW results are small because the parameters used in those expressions are very-well measured.

However, this is not the case for the hadronic contribution because of the large uncertainty. The leading order diagrams from hadronic part is depicted in figure 1.16(d). Traditionally, the data-driven dispersion relation approach is used to compute the leading order contribution by relying on the data of of e^+e^- annihilation cross section into hadrons. The hadronic vaccuum polarisation contribution at leading order is given by [91]

$$a_\mu^{\rm had}[\text{LO}] = \frac{1}{3}\left(\frac{\alpha}{\pi}\right)^2 \int_{m_\pi^2}^{\infty} \mathrm{d}s \frac{K(s)}{s} R^{(0)}(s),$$

$$= 6\,931(40) \times 10^{-11}. \quad (1.171)$$

The function $K(s) \sim 1/s$ is called the QED kernel function at low energy and $R^{(0)}(s)$ is the ratio of cross section of e^+e^- annihilation into hadrons to that into muons which is dominated by the resonance of $\rho(770) \to \pi^+\pi^-$. Recently, the hadronic contribution is calculated up to next to next to leading order (NNLO) and reads

$$a_\mu^{\rm had}[\text{NNLO}] = 6(18) \times 10^{-11}. \quad (1.172)$$

Therefore, the sum of all three contributions leads to

$$a_\mu^{\rm SM} = 116\,591\,810(43) \times 10^{-11}. \quad (1.173)$$

The large uncertainty appears in the SM results mainly originates from the hadronic vacuum polarisation (HVP) contribution [90] based on the data-driven approach. However, there is a different approach for computing this contribution which relies on the lattice QCD simulation. This approach has been used by several groups [93, 94, 95, 96, 97].

[2]The loop function is highly unstable in the region with large mass hierarchy.

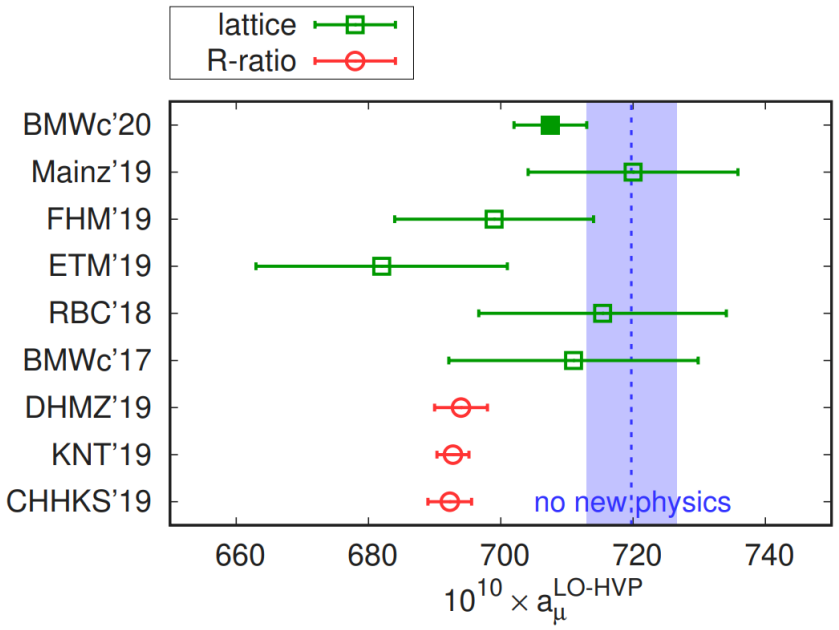

FIGURE 1.17: The comparison between data-driven and lattice QCD approaches as labelled by red and green, respectively. Figure from [92].

However, the lattice simulation results from these collaborations (labelled by BMWc'17, RBC'18, ETM'19, FHM'19, Mainz'19, BMWc'20) gave a large uncertainty and are not comparable to the data-driven or R-ratio results (labelled by CHHKS'19, KNT'19, DHMZ'19) as indicated by figure 1.17. The no new physics blue region in figure 1.17 corresponds to the value of the leading order HVP contribution that would explain the $g_\mu - 2$ experimental result. Recently, the uncertainty from HVP contribution has been considerably reduced according to the BMW result [92] which relaxes a tension between the measurement and SM prediction to the 1.5σ significance. Nevertheless, this result leads to another tension with electroweak global fits which changes the running of fine structure constant $\Delta\alpha^{(5)}_{\text{had}}$ [98]. In addition, the latest BMW result has not yet been confirmed by other groups. Therefore, it is uncertain whether or not their result is correct. Until we can confirm their finding, the result from data-driven approach will be used in this thesis.

When comparing the SM prediction to the experimental result in Eq.(1.156), it follows that

$$\Delta a_\mu = a_\mu^{\text{EXP}} - a_\mu^{\text{SM}} = 249(48) \times 10^{-11}, \tag{1.174}$$

which leads to the 5σ departure from the SM prediction. This number will be used in the chapter 4 when we discuss the phenomenology of the muon portal to vector dark matter scenario.

Chapter 2

Theoretical setup for Vector Dark Matter with Fermionic portal

2.1 Introduction

The Standard Model (SM) of particle physics describes fundamental particle fields and their interactions under strong, Electro-Magnetic (EM) and weak forces using the symmetry principle of gauge invariance. Furthermore, through the so-called Higgs mechanism, triggering Electro-Weak Symmetry Breaking (EWSB), the last two forces are actually unified into a single EW force. Given the particle content and charges under the gauge group of the SM, $SU(3)_C \times SU(2)_L \times U(1)_Y$, some of the particles in it are stable either due to the (unbroken) gauge symmetries themselves (such as the gluons and photon) or due to the fact that they are the lightest ones obeying a conservation law (charge or number conservation) such as the electron and its neutrino. The latter is of some importance here, as the analysis of the gravitational interactions at different scales in the Universe implies the existence of matter without EM interactions, called Dark Matter (DM), for which a particle interpretation is a natural possibility in the framework of the SM. So far, the only viable candidate is the aforementioned neutrino, alas, it is not compliant with corresponding experimental observations. Hence, leaving aside other shortcomings of it, there is an obvious need to surpass the SM.

We consider here DM as a vector (spin-1) gauge particle. Such a theoretical construction is extremely well motivated whilst being constrained in the possible model building choices. The Higgs portal is the simplest and most favoured mechanism to connect a dark sector where the DM is represented by a new gauge boson which gets its mass through a new scalar, that breaks the gauge symmetry through the Higgs mechanism. In this mechanism the quartic interaction involving two new scalars and two Higgs bosons, $|S|^2|H|^2$, is not protected by any symmetry, and is the minimal way of connecting the visible with the invisible sector. The Higgs portal, however, might not be the dominant

connection between the two sectors. It induces a mixing in the scalar sector modifying the Higgs couplings to the SM particles and generating Higgs-DM interactions, which are strongly constrained [99]. The size of the dimensionless coupling of the quartic interaction, which in principle can have any value, is thus constrained to be small to respect the size of the scalar mixing. This makes the detection of signatures from the dark sector extremely challenging. For the non-Abelian case it is also possible to construct kinetic-mixing terms, which are however non-renormalisable and hence suppressed by the scale of new physics. All these scenarios have been extensively studied in literature [100, 101, 102, 103, 104, 105, 106, 107, 108, 109, 110, 111, 112, 113, 114, 115, 116, 117, 118, 119, 120, 121, 122, 123, 124, 125].

Other mediation mechanisms can however be present in case of vector DM, noticeably involving the fermionic sector [126, 125]. The fermionic mediator which was studied in the context of scalar DM is well motivated theoretically [127, 128] and provides interesting phenomenology with well-defined parameter space [129, 130, 131, 132]. The interaction of vector DM with SM fermions is also well motivated from the phenomenological point of view: most of the current anomalies observed in SM measurements are associated with the fermion sector (especially with the lepton one) [133]. Also, the new fermions might also play a role in the radiative shift of the W boson mass, for which a sizeable discrepancy with respect to the SM expectation has been recently reported by [134]. Scenarios with Vector-Like (VL) fermion portals, but for scalar DM candidates, have also been explored in the literature [135, 136]. Some version of a non-Abelian vector DM scenario connected to the SM through the Higgs portal and the fermionic sector was suggested in [126], to explore EM multipole interactions of DM candidates, where the authors introduced two new fermionic multiplets (a doublet Ψ_ℓ and a singlet Ψ_e). Moreover, they assumed a negligibly small Higgs portal, so that the main connection to the SM is at one-loop level via the new fermions. In that paper the authors also assumed vanishing Yukawa terms between new and SM fermions ($y\bar{\Psi}_\ell(i\tau_2\Phi_D^*)\ell_R$) where ℓ_R is the right-handed lepton. However, the new Yukawa terms are introduced due to the mixing between two new fermion multiplets.

In this chapter, we propose a new minimal framework for Fermion Portal Vector DM (FPVDM) (albeit closely related to that of [126]) which incorporates just one dark doublet of VL fermions. The FPVDM scenario relies crucially on the mixing of one of the fermions from the dark doublet with one or more SM fermions sharing the same electric charge, and this mixing provides the tree-level portal connecting dark and SM sectors. Unlike the previous work, we consider the effect of Yukawa terms between new and SM fermions. Also, we include the results from the Z boson propagating diagrams which is not considered in [126]. Therefore, our model is more minimal in the theoretical setup and we further investigate the effect of Z boson propagation together with the photon. In addition we have formulated the complete Lagrangian for this FPVDM framework, together with the necessary conditions and dark charge assignments which

guarantee the stability of vector DM, ensuring the consistency of the new framework suggested in our approach. In our setup the elements of doublet VL fermions have different charges under a new "dark" $SU(2)$ group and are singlets under the $SU(2)_L$ group of the SM. The elements of the fermionic doublet have opposite $\mathbb{Z}_2$ parity. This parity emerges as a subgroup of a new global $U(1)_{Y_D}^{\text{global}}$ symmetry, which has to be imposed to ensure the stability of the dark sector, and for which different members of $SU(2)_D$ multiplets transform differently depending on the third component of their dark-isospin (D-isospin). The $U(1)_{Y_D}^{\text{global}}$ global symmetry can in principle be promoted to a local symmetry and gauged, generating a new massless gauge boson besides the DM candidate.

The plan of this chapter is as follows. In section 2.2 we give a detailed description of the class of models we propose. In the following section 2.3 we further discuss the possibility of gauging the $U(1)_{Y_D}^{\text{global}}$ global symmetry of the model which would provide a natural symmetry behind the stability of DM. In section 3.1 we discuss the case of a particular realisation of our model, in connection with new interesting collider features. In this scenario we invoke a top-quark portal and eliminate any mixing between SM and dark Higgs bosons. We discuss various aspects of phenomenological implications of this specific top-portal scenario (a selection of such results is presented in Ref. [137]). Finally, in chapter 5 we summarise our findings on the new FPVDM framework and our particular realisation of it.

2.2 The dark sector and its interactions with the SM

We start by considering a new dark $SU(2)$ group – the simplest non-Abelian group in terms of number of generators – which we label as $SU(2)_D$. The gauge bosons associated with the $SU(2)_D$ before symmetry breaking are labelled as $V_{D\mu} = \left(V_{D\mu}^+, V_{D\mu}^0, V_{D\mu}^-\right)^T$, where, here and in the following, the superscript identifies the Q_D charge (see the discussion about this charge below)[1]. The full covariant derivative, including the SM terms, is

$$D_\mu = \partial_\mu - \left(i\frac{g}{\sqrt{2}}W_\mu^\pm T^\pm + igW_\mu^3 T_3 + ig'YB_\mu\right) - \left(i\frac{g_D}{\sqrt{2}}V_{D\mu}^\pm T_D^\pm + ig_D V_{D\mu}^0 T_{3D}\right) \ , \quad (2.1)$$

where g and g' are, respectively, the weak and hypercharge coupling constants, g_D is the $SU(2)_D$ coupling constant, T_3 and Y are the weak-isospin and weak-hypercharge, respectively, while T_{3D} is the dark-isospin third component of $SU(2)_D$. The indices of the T_D matrices act only on the $SU(2)_D$ elements and are diagonal with respect to the $SU(2)_L$ ones while the indices of the T matrices act only on the $SU(2)$ elements and are diagonal with respect to $SU(2)_D$. The $SU(2)_D$ symmetry needs to be spontaneously

[1] In order to indicate particles carrying the dark Q_D charge (a superscript), we use a subscript D on them.

broken to generate a mass for its gauge bosons. Two complex scalar doublets are thus needed for the breaking of $SU(2)_L$ and $SU(2)_D$, respectively:

$$\Phi_H = \begin{pmatrix} \phi^+ \\ \phi^0 \end{pmatrix} \longrightarrow \langle \Phi_H \rangle = \frac{1}{\sqrt{2}} \begin{pmatrix} 0 \\ v \end{pmatrix} \quad (\text{breaking } SU(2)_L \times U(1)_Y) \,, \tag{2.2}$$

$$\Phi_D = \begin{pmatrix} \varphi_D^+ \\ \varphi_D^0 \end{pmatrix} \longrightarrow \langle \Phi_D \rangle = \frac{1}{\sqrt{2}} \begin{pmatrix} 0 \\ v_D \end{pmatrix} \quad (\text{breaking } SU(2)_D \times U(1)^{\text{global}}_{Y_D}) \,. \tag{2.3}$$

The full scalar potential has the following form:

$$\begin{aligned} V(\Phi_H, \Phi_D) \;=\; & -\mu^2 \Phi_H^\dagger \Phi_H - \mu_D^2 \Phi_D^\dagger \Phi_D + \lambda (\Phi_H^\dagger \Phi_H)^2 + \lambda_D (\Phi_D^\dagger \Phi_D)^2 \\ & + \lambda_{HD} (\Phi_H^\dagger \Phi_H)(\Phi_D^\dagger \Phi_D) \,, \end{aligned} \tag{2.4}$$

where the last term provides the interaction between Φ_H and Φ_D (the Higgs portal). In the unbroken phase the Lagrangian of Φ_D is invariant under a $SO(4) \sim SU(2) \times SU(2)$ global symmetry. One of the two $SU(2)$ is gauged to be $SU(2)_D$. The Vacuum Expectation Value (VEV) of Φ_D selects a direction in the scalar field space keeping three unbroken generators and leaving an unbroken global symmetry, the custodial symmetry associated with the diagonal $SU(2)$, $SO(4) \to SO(3) \sim SU(2)_{\text{diag}}$. In the absence of new fermions, this custodial symmetry ensures the stability of the new (dark) gauge bosons [101].

We stress here that the quartic term $\Phi_H^\dagger \Phi_H \Phi_D^\dagger \Phi_D$ is in general not protected by any symmetry and therefore cannot be removed altogether from the Lagrangian. A key point of the model, however, is that this portal does not need to play an important role and can indeed be negligible with respect to the other operators of the potential. The connection between the dark sector and the SM is realised via two new VL fermions, singlets of $SU(2)_L$ but with a $U(1)_Y$ hypercharge identical to one of the corresponding right-handed SM fermions. These VL fermions form a doublet under $SU(2)_D$, labelled as $\Psi = (\psi_D,\ F)$. The respective mass terms and Yukawa interactions of the new fermion sector have the following form:

$$-\mathcal{L}_f = M_\Psi \bar{\Psi} \Psi + (y' \bar{\Psi}_L \Phi_D f_R^{\text{SM}} + h.c) \,, \tag{2.5}$$

where f_R^{SM} generically denotes a SM right-handed singlet and y' is a new Yukawa coupling connecting the SM fermion with Ψ through the Φ_D doublet. The absence of an additional Yukawa term $y'' \bar{\Psi}_L \Phi_D^c f_R^{\text{SM}}$, which would violate the stability of DM, is protected by the presence of the unbroken global $U(1)^{\text{global}}_{Y_D}$. Without this symmetry such a term would be compulsory since the scalar doublet, Φ_D, is in the pseudo-real representation. Under this global $U(1)^{\text{global}}_{Y_D} = e^{i\Lambda Y_D}$, the new fields transform non trivially, whilst the SM fields transform into themselves.

In analogy with the SM, where the $SU(2)_L \times U(1)_Y$ symmetry breaks down to the EM $U(1)$, the vacuum state of Φ_D is invariant under a residual $U(1)$, which in this case is global. The invariance of the VEV under the transformation $e^{ig_D\vec{\alpha}\cdot\vec{\tau}}e^{i\Lambda Y_D}$, is ensured if the relations $g_D\alpha_3 = \Lambda$ and $(T_D^3 + Y_D)_{\langle\Phi_D\rangle} = 0$ are satisfied, leading to the assignment $Y_D = 1/2$ for Φ_D. The breaking pattern in the dark sector is therefore $SU(2)_D \times U(1)_{Y_D}^{\text{global}} \to U(1)_{Q_D}^{\text{global}}$ associated with the diagonal generator $SU(2)_D \times U(1)_{Y_D}^{\text{global}}$ with a conserved quantum number $Q_D = T_{3D} + Y_D$, the dark charge of the new particles. For this reason, different elements of $SU(2)_D$ multiplets have different transformation properties under the residual $U(1)_{Q_D}^{\text{global}}$, and with the assignment $Y_D = 1/2$ for doublets and $Y_D = 0$ for triplets, a $\mathbb{Z}_2$ subgroup can be defined as

$$\mathbb{Z}_2 : (-1)^{Q_D} \ , \tag{2.6}$$

under which different members of $SU(2)_D$ multiplets transform differently, guaranteeing the stability of the lightest $\mathbb{Z}_2$ odd state. Specifically, $SU(2)_D$ doublets always contain a $\mathbb{Z}_2$-odd and $\mathbb{Z}_2$-even component, while $SU(2)_D$ triplets have a $(-\ +\ -)$ transformation structure. Clearly, the analogies with the SM EM $U(1)$ can be exploited further by promoting the global $U(1)_{Y_D}^{\text{global}}$ to a local symmetry and gauging it. This leads to the presence of renormalisable kinetic mixing between the SM and dark $U(1)_{Y_D}^{\text{global}}$ groups in the unbroken phase. This aspect will be addressed in section 2.3, but such a construction and its phenomenological consequences is not part of the FPVDM scenario suggested here, and therefore will not be explored in detail.

The particle content of the model is summarised in Table 2.1.

After imposing the dark charge conservation, ensuring the stability of the lightest particle in the dark sector which is odd under $\mathbb{Z}_2$, the most general Lagrangian for this scenario, which is composed of field strength tensors for the vectors (SM and dark), the kinetic and mass terms for the fermions and the scalars, the Yukawa terms and the potential for Φ_H and Φ_D, takes the following form:

$$\begin{aligned}\mathcal{L}_D \ &\supset\ -\frac{1}{4}(V^i_{\mu\nu})^2|_{B,W^i,V_D^{0i},V_D^{\pm}} + \bar{f}^{\text{SM}} i\not{D} f^{\text{SM}} + \bar{\Psi} i\not{D}\Psi + |D_\mu\Phi_H|^2 + |D_\mu\Phi_D|^2 - V(\Phi_H,\Phi_D) \\ &-\ (y\bar{f}_L^{\text{SM}}\Phi_H f_R^{\text{SM}} + y'\bar{\Psi}_L\Phi_D f_R^{\text{SM}} + h.c) - M_\Psi\bar{\Psi}\Psi \ ,\end{aligned} \tag{2.7}$$

with the covariant derivative and scalar potential given in Eq.(2.1) and Eq.(2.4), respectively.

The lightest $\mathbb{Z}_2$-odd particles can be either the $V_{D\mu}^{\pm}$ dark gauge bosons, or ψ_D. If it is ψ_D, it can be either a partner of a) SM quarks, b) charged leptons or c) neutrinos. In case a) the DM candidate would form a stable bound state with SM quarks, in case b) the model would be excluded because the DM would be electrically charge, while in case c) the DM would be a neutrino partner. Conversely, if the lightest $\mathbb{Z}_2$-odd particle is

Scalars	$SU(2)_L$	$U(1)_Y$	Q	$SU(2)_D$	$U(1)_{Y_D}$	Q_D	$\mathbb{Z}_2$
$\Phi_H = \begin{pmatrix}\phi^+\\ \phi^0\end{pmatrix}$	$\mathbf{2}$	$1/2$	$\begin{matrix}1\\0\end{matrix}$	$\mathbf{1}$	0	0	$+$
$\Phi_D = \begin{pmatrix}\varphi_D^+\\ \varphi_D^0\end{pmatrix}$	$\mathbf{1}$	0	0	$\mathbf{2}$	$1/2$	$\begin{matrix}1\\0\end{matrix}$	$\begin{matrix}-\\+\end{matrix}$
Vectors	$SU(2)_L$	$U(1)_Y$	Q	$SU(2)_D$	$U(1)_{Y_D}$	Q_D	$\mathbb{Z}_2$
$W_\mu = \begin{pmatrix}W_\mu^+\\ W_\mu^3\\ W_\mu^-\end{pmatrix}$	$\mathbf{3}$	0	$\begin{matrix}1\\0\\-1\end{matrix}$	$\mathbf{1}$	0	0	$+$
B_μ	$\mathbf{1}$	0	0	$\mathbf{1}$	0	0	$+$
$V_{D\mu} = \begin{pmatrix}V_{D\mu}^+\\ V_{D\mu}^0\\ V_{D\mu}^-\end{pmatrix}$	$\mathbf{1}$	0	0	$\mathbf{3}$	0	$\begin{matrix}1\\0\\-1\end{matrix}$	$\begin{matrix}-\\+\\-\end{matrix}$
Fermions	$SU(2)_L$	$U(1)_Y$	Q	$SU(2)_D$	$U(1)_{Y_D}$	Q_D	$\mathbb{Z}_2$
$f_L^{\rm SM} = \begin{pmatrix}f_{u,\nu}^{\rm SM}\\ f_{d,\ell}^{\rm SM}\end{pmatrix}_L$	$\mathbf{2}$	$\frac{1}{6}, -\frac{1}{2}$	$\begin{matrix}\frac{2}{3} & 0\\ -\frac{1}{3}, & -1\end{matrix}$	$\mathbf{1}$	0	0	$+$
$u_R^{\rm SM}, \nu_R^{\rm SM}$	$\mathbf{1}$	$\frac{2}{3}, 0$	$\frac{2}{3}, 0$	$\mathbf{1}$	0	0	$+$
$d_R^{\rm SM}, \ell_R^{\rm SM}$	$\mathbf{1}$	$-\frac{1}{3}, -1$	$-\frac{1}{3}, -1$	$\mathbf{1}$	0	0	$+$
$\Psi = \begin{pmatrix}\psi_D\\ F\end{pmatrix}$	$\mathbf{1}$	Q	Q	$\mathbf{2}$	$1/2$	$\begin{matrix}1\\0\end{matrix}$	$\begin{matrix}-\\+\end{matrix}$

TABLE 2.1: The quantum numbers under the EW and dark gauge group $SU(2)_D \times U(1)_{Y_D}^{\rm global}$ of the particles of the model, and their $\mathbb{Z}_2$ parity.

$V_{D\mu}^\pm$, the DM is a massive dark gauge boson. It is this this scenario, labelled as Fermion Portal Vector Dark Matter (FPVDM), which we discuss in the rest of this paper.

2.2.1 Kinetic mixing in the unbroken EW and dark phases

We discuss here in more detail the origin of the kinetic mixing at loop level. The two scalar doublets are secluded with respect to one another in the sense that the SM one has no dark quantum numbers (singlet with respect to $SU(2)_D$) and the $SU(2)_D$ one has no SM quantum numbers (transforming as a singlet with respect to the SM). The operators giving rise to kinetic mixing in the effective Lagrangian are of dimension-six for $U(1)_Y$ and dimension-eight for $SU(2)_L$ and, in our case, have the form

$$\mathcal{V}_D^{\mu\nu a}\Phi_{Dk}^\dagger(\sigma^a)_{kl}\Phi_{Dl}\left(\frac{\kappa_W}{\Lambda^4}W_{\mu\nu}^b\Phi_{Hi}^\dagger(\sigma^b)_{ij}\Phi_{Hj} + \frac{\kappa_B}{\Lambda^2}B_{\mu\nu}\right) , \tag{2.8}$$

where σ^a is a Pauli matrix generator of $SU(2)_D$ and σ^b is a generator of $SU(2)_L$. Here, $\mathcal{V}_D^{\mu\nu a}$ is the field strength tensor of $SU(2)_D$ and $W_{\mu\nu}^b$ and $B_{\mu\nu}$ are, respectively, the field strength tensors of $SU(2)_L$ and $U(1)_Y$. The kinetic mixing term is obtained upon inserting the VEVs of the Higgs doublets but, as already indicated, the operator is

suppressed through the fourth power of the large scale Λ. Concerning the origin of this effective operator in our model, the suppression can be estimated with a one-loop two-point function mixing the two types of gauge bosons, $SU(2)_L \times U(1)_Y$ and $SU(2)_D$.

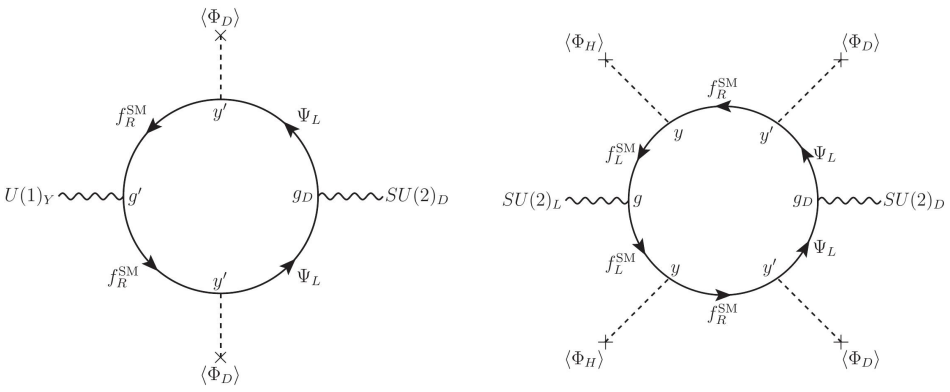

FIGURE 2.1: Loop realisation of the kinetic mixing operators for $U(1)_Y$ and $SU(2)_L$ in the unbroken EW and dark symmetry phases.

The fermion loops with VEV insertions allows the two types of gauge bosons to connect, as shown in figure 2.1, and the interactions are expected to be of order

$$\frac{1}{16\pi^2 M_\Psi^2 m_f^2} y'^2 g' \; g_D v_D^2 \quad (\text{for } U(1)_Y - SU(2)_D \text{ mixing}) \tag{2.9}$$

and

$$\frac{1}{16\pi^2 M_\Psi^2 m_f^4} y^2 y'^2 g \; g_D v^2 v_D^2 \quad (\text{for } SU(2)_L - SU(2)_D \text{ mixing}) \,, \tag{2.10}$$

where M_Ψ is the mass of the VL fermion Ψ with both weak hypercharge and $SU(2)_D$ quantum numbers coupling with a Yukawa type term y' to the Higgs sector.[2] A gauge mixing term is also possible using the quartic term in the scalar potential – $\lambda_{HD} \Phi_H^\dagger \Phi_H \; \Phi_D^\dagger \Phi_D$– but its contribution is more suppressed as it arises at two-loop level. In the broken phase, a kinetic mixing arises between the electrically neutral mass eigenstates [138, 139, 126, 140]. This is described in more detail in section 2.2.3.2 and has important phenomenological consequences.

2.2.2 Electroweak and dark symmetry breaking

The minimum of the potential reads as

$$V(\Phi_H, \Phi_D)_{\rm min} = -\frac{\mu^2}{2} v^2 - \frac{\mu_D^2}{2} v_D^2 + \frac{\lambda}{4} v^4 + \frac{\lambda_D}{4} v_D^4 + \frac{\lambda_{HD}}{4} v^2 v_D^2 \tag{2.11}$$

[2]Notice that the Yukawa parameters determine the masses of both $\mathbb{Z}_2$-even fermions, and their expression is a function of all fermion masses. Therefore, Eq.(2.9),(2.10) are finite in the limit $m_f \to 0$: this can be verified by substituting the explicit expressions of the Yukawa couplings (see Eq.(2.22)) and consider that, in the the same limit, the two elements of the VL fermion doublet become degenerate.

and the minimisation conditions are

$$v(-\mu^2 + \lambda v^2 + \frac{1}{2}\lambda_{HD} v_D^2) = 0 \quad \text{and} \quad v_D(-\mu_D^2 + \lambda_D v_D^2 + \frac{1}{2}\lambda_{HD} v^2) = 0 \tag{2.12}$$

whilst the two non-trivial stationary points are

$$v = \sqrt{\frac{4\lambda_D \mu^2 - 2\lambda_{HD}\mu_D^2}{4\lambda\lambda_D - \lambda_{HD}^2}} \quad \text{and} \quad v_D = \sqrt{\frac{4\lambda\mu_D^2 - 2\lambda_{HD}\mu^2}{4\lambda\lambda_D - \lambda_{HD}^2}} \,, \tag{2.13}$$

where the VEVs are taken to be positive without loss of generality. They are minima if the corresponding Hessian matrix is positive definite (i.e., if its eigenvalues are both positive, being a symmetric matrix),

$$\mathcal{H}|_{v_{\min}, v_{D\min}} = \begin{pmatrix} 3\lambda v^2 - \mu^2 + \frac{\lambda_{HD}}{2} v_D^2 & \lambda_{HD} v v_D \\ \lambda_{HD} v v_D & 3\lambda_D v_D^2 - \mu_D^2 + \frac{\lambda_{HD}}{2} v^2 \end{pmatrix} \,, \tag{2.14}$$

which leads to the following conditions for the Lagrangian parameters:

$$\mu \neq 0 \text{ and } \mu_D \neq 0 \text{ and } \begin{cases} \lambda_{HD} < 0 \text{ and } \lambda > 0 \text{ and } \lambda_D > 0 \text{ and } \lambda_{HD}^2 < 4\lambda\lambda_D \\ \text{or} \\ \lambda_{HD} > 0 \text{ and } 2\lambda\mu_D^2 > \lambda_{HD}\mu^2 \text{ and } 2\lambda_D\mu^2 > \lambda_{HD}\mu_D^2 \end{cases} \tag{2.15}$$

Finally, if the Higgs quartic coupling vanishes, $\lambda_{HD} = 0$, the system simply reduces to two independent potentials, $V(\Phi_H, \Phi_D) = V(\Phi_H) + V(\Phi_D)$, where the two terms have identical structure, corresponding to the SM one, and where the minima are simply defined as:

$$v = \pm\sqrt{\frac{\mu^2}{\lambda}} \quad \text{and} \quad v_D = \pm\sqrt{\frac{\mu_D^2}{\lambda_D}} \,. \tag{2.16}$$

2.2.3 Particle spectrum of the model

The model contains new scalar, fermion and vector states. The scalar and fermion ones can mix with SM objects, while the vectors undergo kinetic and mass mixing in the broken EW and dark phases, potentially affecting observables primarily sensitive to the SM itself. In this section, the structure of each particle sector is thus carefully described.

2.2.3.1 Fermions

The fermion component with $T_{3D} = +1/2$ gets only the VL mass, therefore

$$m_{\psi_D} = M_\Psi \,, \tag{2.17}$$

whereas the other fermion masses are generated after both scalars acquire a VEV. The fermionic mass matrix reads as follows:

$$\mathcal{L}_m^f = (\bar{f}_L^{\rm SM} F_L)\mathcal{M}_F \begin{pmatrix} f_R^{\rm SM} \\ F_R \end{pmatrix}, \quad \text{with} \quad \mathcal{M}_F = \begin{pmatrix} y\frac{v}{\sqrt{2}} & 0 \\ y'\frac{v_D}{\sqrt{2}} & M_\Psi \end{pmatrix} . \tag{2.18}$$

This mass matrix describes the mixing of a VL fermion with a SM fermion but, unlike in well-known VL scenarios where the new states mix with SM fermions via the Higgs boson, in this case the mixing is driven by Φ_D and the non-zero off-diagonal element is proportional to v_D. The mass matrix can be diagonalised by two unitary matrices, $V_{L,R}$, leading to the mass eigenstates f and F, where f identifies the SM fermion and F its heavier partner:

$$\mathcal{L}_m^f = (\bar{f}_L F_L)\mathcal{M}_F^d \begin{pmatrix} f_R \\ F_R \end{pmatrix} = (\bar{f}_L F_L) V_{fL}^\dagger \mathcal{M}_F V_{fR} \begin{pmatrix} f_R \\ F_R \end{pmatrix} . \tag{2.19}$$

The two rotation matrices

$$V_{fL} = \begin{pmatrix} \cos\theta_{fL} & \sin\theta_{fL} \\ -\sin\theta_{fL} & \cos\theta_{fL} \end{pmatrix}, \quad \text{and} \quad V_{fR} = \begin{pmatrix} \cos\theta_{fR} & \sin\theta_{fR} \\ -\sin\theta_{fR} & \cos\theta_{fR} \end{pmatrix}, \tag{2.20}$$

diagonalise the products $\mathcal{M}_F^d \mathcal{M}_F^{d\dagger}$ and $\mathcal{M}_F^{d\dagger} \mathcal{M}_F^d$, respectively, and the mass eigenvalues are:

$$m_{f,F}^2 = \frac{1}{4}\left[y^2 v^2 + y'^2 v_D^2 + 2M_\Psi^2 \mp \sqrt{(y^2 v^2 + y'^2 v_D^2 + 2M_\Psi^2)^2 - 8y^2 v^2 M_\Psi^2} \right] . \tag{2.21}$$

The fermion sector therefore contains the SM fermion with mass m_f, a $\mathbb{Z}_2$-even partner with mass m_F and a $\mathbb{Z}_2$-odd partner with mass m_{ψ_D}. The mass hierarchy is $m_f < m_{\psi_D} \leq m_F$. This is the choice that we make based on the phenomenological reason in which vector-like fermion searches provide the lower limits on mass above the SM partners. Another possible hierarchy is $m_F < m_\Psi < m_f$ which is excluded by collider searches.

It is possible to trade the Yukawa parameters for the masses of the physical fermions $\{m_f, m_{\psi_D}, m_F\}$ as:

$$y = \sqrt{2}\frac{m_f m_F}{m_{\psi_D} v}, \quad y' = \sqrt{2}\frac{\sqrt{(m_F^2 - m_{\psi_D}^2)(m_{\psi_D}^2 - m_f^2)}}{m_{\psi_D} v_D} . \tag{2.22}$$

The mixing angles can also be expressed as function of the masses as:

$$\sin^2\theta_{fL} = \frac{m_f^2}{m_{\psi_D}^2}\frac{m_F^2 - m_{\psi_D}^2}{m_F^2 - m_f^2}, \quad \sin^2\theta_{fR} = \frac{m_F^2 - m_{\psi_D}^2}{m_F^2 - m_f^2} . \tag{2.23}$$

The left-handed mixing angle is suppressed by the $m_f^2/m_{\psi_D}^2$ ratio. This feature is different from the usual scenarios where a $SU(2)_L$-singlet VL fermion is added to the SM and allowed to mix with SM fermions and where the right-handed mixing angle is suppressed [141]. In this case, despite the fact that ψ is a singlet under the SM gauge group, the mixing is driven by the $SU(2)_D$ fermion doublet Ψ and the $SU(2)_D$ scalar doublet Φ_D, the elements of which are also singlets under the EW gauge group and hence involves a right-handed SM fermion.

Finally, the new fermion sector is completely decoupled in the limit $m_F = m_{\psi_D}$, for which $y = y_{\rm SM} = \sqrt{2}\frac{m_f}{v}$, $y' = 0$, $\sin\theta_{fL} = \sin\theta_{fR} = 0$, so that the pure SM scenario is restored.

2.2.3.2 Gauge bosons

The kinetic Lagrangian of Φ_H and Φ_D evaluated at the minimum of the scalar potential reads as follows:

$$\mathcal{L}_S^{\rm kin}|_{v,v_D} \supset (\mathcal{V}^0_{\rm SM})^T \mathcal{M}^2_{\mathcal{V}^0_{\rm SM}} \mathcal{V}^0_{\rm SM} + \frac{1}{4} g^2 v^2 W^+ W^- + \frac{1}{8} g_D^2 v_D^2 (V_D^0)^2 + \frac{g_D^2}{4} v_D^2 V_D^+ V_D^- \ , \quad (2.24)$$

where $\mathcal{V}^0_{{\rm SM}\mu} = (B_\mu \ W^3_\mu)^T$. At tree level, the SM gauge bosons are not affected by the new Φ_D scalar, and therefore their masses correspond to the SM values, while the gauge bosons of $SU(2)_D$ are all degenerate and their masses are

$$m_V \equiv m_{V_D^\pm} = m_{V_D^0} = \frac{g_D}{2} v_D \ . \quad (2.25)$$

The only electrically neutral massive $\mathbb{Z}_2$-odd states of FPVDM scenarios are the $SU(2)_D$ gauge bosons $V_D^\pm$, which are thus identified as DM candidates.

The degeneracy in mass is broken at loop level by different effects. In the following, for making the notation more compact, we will label the two gauge bosons as:

$$\begin{cases} V_{D\pm}^\pm \equiv V_D^{(*)} & \text{with mass } m_{V_D} \\ V_D^0 \equiv V' & \text{with mass } m_{V'} \end{cases} .$$

First of all, in the broken EW and dark gauge symmetry phases, a kinetic mixing arises between V' and both photon and Z boson [138, 139, 126, 140]. Using analogous notation to [140], and assuming only one VL fermion doublet under $SU(2)_D$ exists, the kinetic mixing parameters ϵ_{AV} and ϵ_{ZV} entering the kinetic mixing matrix

$$V^{\rm KM} = \begin{pmatrix} 1 & 0 & -\frac{\epsilon_{AV}}{\sqrt{1-\epsilon_{AV}^2-\epsilon_{ZV}^2}} \\ 0 & 1 & -\frac{\epsilon_{ZV}}{\sqrt{1-\epsilon_{AV}^2-\epsilon_{ZV}^2}} \\ 0 & 0 & \frac{1}{\sqrt{1-\epsilon_{AV}^2-\epsilon_{ZV}^2}} \end{pmatrix} , \quad (2.26)$$

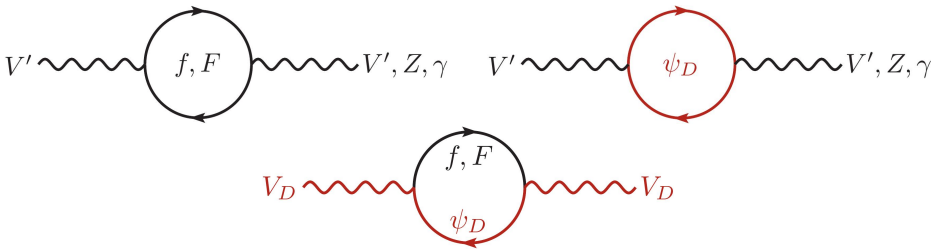

FIGURE 2.2: The Feynman diagrams contributing to mass corrections and mixing of $SU(2)_D$ vector bosons, V', Z, γ (left) and V_D (right) at one loop level. $\mathbb{Z}_2$-odd particles are highlighted in red.

which rotates the $(A_\mu \ Z_\mu \ V'_\mu)$ vector of gauge eigenstates, are determined by loops involving the only three fermions charged under the SM and dark gauge groups, f, F and ψ_D, as shown in figure 2.2. The scalar fields do not contribute due to the fact that neither Φ_H nor Φ_D transform under the SM and dark gauge groups at the same time. These loops can be evaluated separately for the AV and ZV mixings using the general expression of the gauge boson vacuum polarisation tensor provided in [142]. For the AV mixing the tensor is purely transverse and in the $q^2 \to 0$ limit reads $\Pi_T^{AV} \sim q^2 \epsilon_{AV}$, where

$$\begin{aligned}
\epsilon_{AV} &= \frac{g_D e Q_f}{8\pi^2} \sum_{i=f,F,\psi_D} (V_{Li}^2 + V_{Ri}^2) T_{D_i}^3 \ln \frac{m_i^2}{\mu^2} \\
&= \frac{g_D e Q_f}{8\pi^2} \left[-\frac{1}{2}(\sin\theta_{fL}^2 + \sin\theta_{fR}^2) \ln \frac{m_f^2}{\mu^2} - \frac{1}{2}(\cos\theta_{fL}^2 + \cos\theta_{fR}^2) \ln \frac{m_F^2}{\mu^2} + \ln \frac{m_{\psi_D}^2}{\mu^2} \right] \\
&= \frac{g_D e Q_f}{16\pi^2} \left[\frac{m_{\psi_D}^4 - m_f^2 m_F^2}{(m_F^2 - m_f^2) m_{\psi_D}^2} \ln \frac{m_f^2}{m_F^2} + 2 \ln \frac{m_{\psi_D}^2}{m_f m_F} \right] \equiv \frac{g_D e Q_f}{16\pi^2} \mathcal{F}^{AV}(r_f, r_{\psi_D}) \,, \quad (2.27)
\end{aligned}$$

with $\{c, s, t\}_W \equiv \{\cos, \sin, \tan\}\theta_W$, $r_f = m_f/m_{\psi_D}$ and $r_{\psi_D} = m_{\psi_D}/m_F$. The loop function

$$\mathcal{F}^{AV}(r_f, r_{\psi_D}) = \frac{r_{\psi_D}^2 - r_f^2}{1 - r_f^2 r_{\psi_D}^2} \ln(r_f^2 r_{\psi_D}^2) + \ln \frac{r_{\psi_D}^2}{r_f^2} \quad (2.28)$$

does not depend on the specific fermion flavour but only on the ratios between fermion masses, and its numerical values are shown in figure 2.3, where it is possible to see that the contribution of kinetic mixing completely cancels when $r_f = r_{\psi_D}$.

The vacuum polarisation tensor for the ZV mixing, in contrast, is more involved due to the non-vector nature of the couplings on both sides of the loop. Its transverse and longitudinal components in the $q^2 \to 0$ limit read

$$\begin{aligned}
\Pi_T^{ZV}(q^2 \to 0) \ &\sim \ \frac{g g_D}{64\pi^2 c_w} \Big[3 m_f^2 \mathcal{F}_m^{ZV}(r_f, r_{\psi_D}) + q^2 \Big(\mathcal{F}_{qT1}^{ZV}(r_f, r_{\psi_D}) \\
&\qquad + Q_f s_W^2 \mathcal{F}_{qT2}^{ZV}(r_f, r_{\psi_D}) \Big) \Big] \,, \quad (2.29) \\
\Pi_L^{ZV}(q^2 \to 0) \ &\sim \ \frac{g g_D}{64\pi^2 c_w} \Big[3 m_f^2 \mathcal{F}_m^{ZV}(r_f, r_{\psi_D}) + q^2 \mathcal{F}_{qL}^{ZV}(r_f, r_{\psi_D}) \Big] \,, \quad (2.30)
\end{aligned}$$

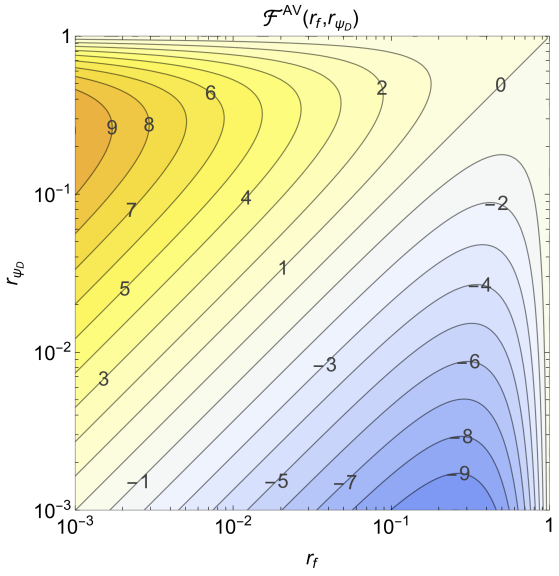

FIGURE 2.3: Numerical values of the loop function $\mathcal{F}^{AV}(r_f, r_{\psi_D})$, with $r_f = m_f/m_{\psi_D}$ and $r_{\psi_D} = m_{\psi_D}/m_F$.

such that the total contribution is

$$\Pi^{ZV}(q^2 \to 0) \sim \frac{g g_D}{64\pi^2 c_w}\Bigg[6m_f^2 \mathcal{F}_m^{ZV}(r_f, r_{\psi_D}) + q^2\left(\mathcal{F}_{qT1+qL}^{ZV}(r_f, r_{\psi_D}) + Q_f s_W^2 \mathcal{F}_{qT2}^{ZV}(r_f, r_{\psi_D})\right)\Bigg], \tag{2.31}$$

where the functions $\mathcal{F}_{m,qT1+qL,qT2}^{ZV}(r_f, r_{\psi_D})$ are provided in Appendix B and their numerical values are shown in figure 2.4.

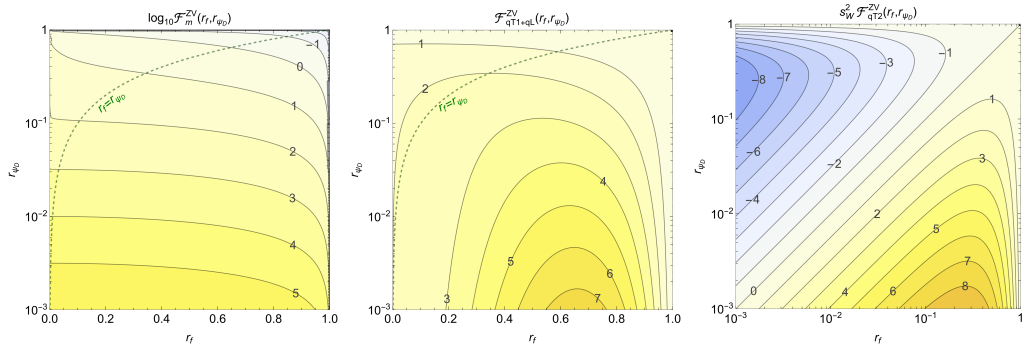

FIGURE 2.4: Numerical values of the loop function $\mathcal{F}_{m,qT1+qL,qT2}^{ZV}(r_f, r_{\psi_D})$, with $r_f = m_f/m_{\psi_D}$ and $r_{\psi_D} = m_{\psi_D}/m_F$.

Besides the kinetic mixing, a mass mixing is thus induced between the SM Z boson and V'. The coefficients of the ZV kinetic and mass mixing read:

$$\epsilon_{ZV} = \frac{g g_D}{64\pi^2 c_w}\left(\mathcal{F}_{qT1+qL}^{ZV}(r_f, r_{\psi_D}) + Q_f s_W^2 \mathcal{F}_{qT2}^{ZV}(r_f, r_{\psi_D})\right), \tag{2.32}$$

$$\Delta m_{ZV}^2 = \frac{3 g g_D}{32\pi^2 c_w} m_f^2 \mathcal{F}_m^{ZV}(r_f, r_{\psi_D}). \tag{2.33}$$

The adimensional function $F_m^{ZV}(r_f, r_{\psi_D})$ appearing in the expression of the mass shift Δm^2_{ZV} is small for $r_{\psi_D} \simeq 1$ (i.e., in the decoupling limit) and rapidly grows as r_{ψ_D} decreases. The function $F^{ZV}_{qT1+qL}(r_f, r_{\psi_D})$ has a similar behaviour but with a milder dependence on r_{ψ_D}. The function $F^{ZV}_{qT2}(r_f, r_{\psi_D})$ has a similar behaviour as $\mathcal{F}^{AV}(r_f, r_{\psi_D})$.

The mass matrix of the $(Z_\mu\ V'_\mu)$ system receives a shift proportional to the mass term in the vacuum polarisation tensor:

$$\tilde{M}^2_{ZV} = \begin{pmatrix} \frac{1}{4}(g^2+g'^2)v^2 & \frac{1}{2}\Delta m^2_{ZV} \\ \frac{1}{2}\Delta m^2_{ZV} & \frac{1}{4}g_D^2 v_D^2 \end{pmatrix} = \begin{pmatrix} \tilde{m}^2_Z & \frac{1}{2}m_f^2\epsilon^m_{ZV} \\ \frac{1}{2}m_f^2\epsilon^m_{ZV} & \tilde{m}^2_{V'} \end{pmatrix} , \tag{2.34}$$

where the adimensional parameter $\epsilon^m_{ZV} = \Delta m^2_{ZV}/m_f^2$ has been introduced, and where loop contributions to the diagonal terms have been neglected because of the non-zero tree-level values. This matrix is rotated by $V^{\rm KM}$ into

$$\begin{aligned} M^2_{ZV} &= \left(V^{\rm KM}\right)^T \tilde{M}^2_{ZV} V^{\rm KM} \\ &= \frac{1}{4}\begin{pmatrix} (g^2+g'^2)v^2 & -\frac{(g^2+g'^2)v^2\epsilon_{ZV} - 2m_f^2\epsilon^m_{ZV}}{\sqrt{1-\epsilon^2_{AV}-\epsilon^2_{ZV}}} \\ -\frac{(g^2+g'^2)v^2\epsilon_{ZV} - 2m_f^2\epsilon^m_{ZV}}{\sqrt{1-\epsilon^2_{AV}-\epsilon^2_{ZV}}} & \frac{g_D^2v_D^2 + (g^2+g'^2)v^2\epsilon^2_{ZV} - 4m_f^2\epsilon_{ZV}\epsilon^m_{ZV}}{1-\epsilon^2_{AV}-\epsilon^2_{ZV}} \end{pmatrix} \end{aligned} \tag{2.35}$$

and diagonalised through a rotation with angle

$$\tan 2\theta_{ZV} = \pm \frac{2\left((g^2+g'^2)v^2\epsilon_{ZV} - 2m_f^2\epsilon^m_{ZV}\right)\sqrt{1-\epsilon^2_{AV}-\epsilon^2_{ZV}}}{(1-\epsilon^2_{AV}-\epsilon^2_{ZV})(g^2+g'^2)v^2 - g_D^2v_D^2 + 4\epsilon_{ZV}\epsilon^m_{ZV}m_f^2} , \tag{2.36}$$

which is positive for $m_{V'} > m_Z$ and negative otherwise, and in the limit of small $\epsilon_{AV}, \epsilon_{ZV}$ and ϵ^m_{ZV} becomes:

$$\tan 2\theta_{ZV} \simeq 2\theta_{ZV} \simeq \pm 2\frac{2m_f^2\epsilon^m_{ZV} - (g^2+g'^2)v^2\epsilon_{ZV}}{g_D^2v_D^2 - (g^2+g'^2)v^2} . \tag{2.37}$$

In the same limit the masses of the Z and V' bosons read:

$$m_Z^2 \simeq \frac{1}{4}(g^2+g'^2)v^2\left[1+\theta^2_{ZV}\left(1-\frac{g_D^2v_D^2}{(g^2+g'^2)v^2}\right)\right] , \tag{2.38}$$

$$m_{V'}^2 \simeq \frac{1}{4}g_D^2v_D^2\left[1+\epsilon^2_{AV}+(\theta_{ZV}-\epsilon_{ZV})^2\left(1-\frac{(g^2+g'^2)v^2}{g_D^2v_D^2}\right)\right] \tag{2.39}$$

The induced modification to the Z boson mass (and an analogous modification to the W boson mass induced by loops involving F and a SM particle, potentially contributing to the W mass anomaly observed by [134])[3] are constrained by EW precision data and depend on specific realisations of the model.

[3]This is not studied yet within our model and it will be done in near future.

Another source of V_D and V' mass split are the different fermionic loop corrections from f, F and ψ_D corresponding to the different $\mathbb{Z}_2$ parities of the $SU(2)_D$ gauge bosons, as shown in figure 2.2. A detailed discussion of the 1-loop calculations is provided in Appendix A. The mass splitting $\Delta m_V = m_{V_D} - m_{V'}$ can be written in a compact form in terms of the parameters

$$\epsilon_1 = \frac{m_F^2 - m_{\psi_D}^2}{m_F^2}, \quad \epsilon_2 = \frac{m_f^2}{m_F^2}, \quad \epsilon_3 = \frac{m_{V_D}^2}{m_F^2} \, . \tag{2.40}$$

In the approximation of $\epsilon_1, \epsilon_2, \epsilon_3 \ll 1$ one has

$$\begin{aligned} \Delta m_V' \equiv \Delta m_V\big|_{\epsilon,\epsilon_2,\epsilon_3 \ll 1} = \frac{1}{640\pi^2 m_{V_D}} \epsilon_1^2 g_D^2 m_F^2 \left[(20 + 3\epsilon_3 - 15\epsilon_2 + 20\epsilon_2\epsilon_3)\right. \\ \left. +10(3\epsilon_2 - \epsilon_3 - 2\epsilon_2\epsilon_3)\log\epsilon_3\right] + o(\epsilon_1^2, \epsilon_2, \epsilon_3) \, . \end{aligned} \tag{2.41}$$

For practical purposes, the expression for Δm_V can be further simplified by neglecting ϵ_2 and ϵ_3 and keeping the leading term in ϵ_1, which leads to the following simple form:

$$\Delta m_V'' \equiv \Delta m_V'\big|_{\epsilon_2,\epsilon_3=0} = \frac{g_D^2 m_F^2}{32\pi^2 m_{V_D}} \epsilon_1^2 = \frac{g_D^2 m_F^2}{32\pi^2 m_{V_D}} \left(\frac{m_F^2 - m_{\psi_D}^2}{m_F^2}\right)^2 . \tag{2.42}$$

The radiative mass splitting between the V_D and V' bosons plays a very important role in the determination of relic density and DM Indirect Detection (ID) rates. The range of validity of the approximations for Δm_V presented above depends on the specific realisation of the FPVDM model and its parameter space. A detailed discussion of the respective numerical results for Δm_V is given in section 3.1 for a specific case study.

Finally, it is important to mention that the covariant derivative is modified by the kinetic mixing as follows:

$$\begin{aligned} D_\mu \simeq \partial_\mu - ieQA_\mu - i\left[\frac{g}{c_w}(T_3 - Qs_W^2) - g_D T_D^3 \theta_{ZV}\right] Z_\mu \\ - i\left[g_D T_D^3 - eQ\epsilon_{AV} + \frac{g}{c_w}(T_3 - Qs_W^2)(\theta_{ZV} - \epsilon_{ZV})\right] V_\mu' \quad , \end{aligned} \tag{2.43}$$

where we have included only leading terms in θ_{ZV} and ϵ_{ZV}.

This modification has certain phenomenological consequences. Among the most relevant ones, the interaction of V' with all charged SM particles via the mixing parameter ϵ_{AV} allows the direct production of V' at the LHC via Drell-Yan topologies, and is therefore constrained by direct searches of heavy resonances. Also, the DM candidate V_D can interact through EM multipoles with atomic matter, contributing to direct detection observables [126]. In the case where only one VL representation is present, the constraints coming from these processes depend only on the fermion charge Q and on the mass ratios r_f and r_{ψ_D}, but not on the specific flavour of the fermion.

2.2.3.3 Scalars

The scalar potential of Eq.(2.4) is constructed starting from the 8 degrees of freedom of all the scalar fields of the theory: 4 for Φ_H and 4 for Φ_D. The theory contains 6 massive gauge bosons: Z, $W^{\pm}$, V' and V_D (with two opposite D-isospin values). Therefore 6 Goldstone bosons are needed to give the corresponding longitudinal components. Thus, 2 degrees of freedom are left, which correspond to physical massive scalars: the SM Higgs boson, h, and a further CP-even scalar, H. Upon expressing the neutral scalars in the interaction eigenstates in terms of their components in the unitary gauge as

$$\phi^0 = \frac{1}{\sqrt{2}}(v + h_1) \,, \tag{2.44}$$

$$\varphi_D^0 = \frac{1}{\sqrt{2}}(v_D + \varphi_1) \,, \tag{2.45}$$

the Lagrangian terms for scalar masses can be written as:

$$\mathcal{L}_m^{\mathcal{S}} = -(h_1 \; \varphi_1) \begin{pmatrix} \lambda v^2 & \frac{\lambda_{HD}}{2} v v_D \\ \frac{\lambda_{HD}}{2} v v_D & \lambda_D v_D^2 \end{pmatrix} \begin{pmatrix} h_1 \\ \varphi_1 \end{pmatrix} . \tag{2.46}$$

The mass eigenvalues are obtained by diagonalising the mass matrix via a rotation matrix $V_S = \begin{pmatrix} \cos\theta_S & \sin\theta_S \\ -\sin\theta_S & \cos\theta_S \end{pmatrix}$ and are

$$m_{h,H}^2 = \lambda v^2 + \lambda_D v_D^2 \mp \sqrt{(\lambda v^2 - \lambda_D v_D^2)^2 + \lambda_{HD}^2 v^2 v_D^2} \tag{2.47}$$

whilst the mixing angle is

$$\sin\theta_S = \sqrt{2\frac{m_H^2 v^2 \lambda - m_h^2 v_D^2 \lambda_D}{m_H^4 - m_h^4}} \,. \tag{2.48}$$

Even in the absence of explicit mixing induced by the quadratic term, i.e., even if $\lambda_{HD} = 0$, h_1 and φ_1 can mix at one-loop via the their interactions with fermions. The consequences of this mixing, which can also affect Higgs-related observables, go beyond the scopes of this analysis, and will be treated in a future work.

2.2.4 Flavour structure and Cabibbo-Kobayashi-Maskawa (CKM) matrix

The previous treatment assumed the presence of one VL $SU(2)_D$ doublet interacting with one SM fermion, without specifying the flavour structure involved. If the full flavour structure of the SM is considered, different possibilities might arise. A VL fermion can interact with one or more SM flavours and there can be multiple VL fermions.

The most general Lagrangian, accounting for the above-mentioned possibilities, is

$$\begin{aligned}\mathcal{L}_m &= M_U^I \bar{U}_I U_I + M_D^J \bar{D}_J D_J + M_E^K \bar{E}_K E_K \\ &+ y_u^i \bar{Q}_{iL}^{\rm SM} \tilde{\Phi}_H u_{iR}^{\rm SM} + y_d^i \tilde{V}_{\rm CKM}^{ij} \bar{Q}_{iL}^{\rm SM} \Phi_H d_{jR}^{\rm SM} + y_l^i \bar{L}_{iL}^{\rm SM} \Phi_H l_{iR}^{\rm SM} + h.c. \\ &+ (y_u')^{Ij} \bar{U}_{IL} \Phi_D u_{jR}^{\rm SM} + (y_d')^{Jj} \bar{D}_{JL} \Phi_D d_{jR}^{\rm SM} + (y_l')^{Kj} \bar{E}_{KL} \Phi_D l_{jR}^{\rm SM} + h.c. \,, \end{aligned} \tag{2.49}$$

where $\tilde{\Phi}_H = i\tau_2 \Phi_H^*$, $i,j = 1,2,3$ are SM flavour indices and I,J,K run over the flavours of the VL partners. The SM Yukawa couplings have been diagonalised exploiting the flavour symmetries and the SM CKM matrix (i.e., the CKM matrix if no VL states were introduced) and $\tilde{V}_{\rm CKM}$ has been introduced to parametrise the misalignment between the flavour and mass eigenstates in the down sector.

The most generic mass matrices read as follows:

$$\begin{aligned}\mathcal{M}_U &= \left(\begin{array}{c|c} y_u^i \frac{v}{\sqrt{2}} & 0^{iI} \\ \hline (y_u')^{Ii} \frac{v_D}{\sqrt{2}} & M_U^I \end{array}\right), \quad \mathcal{M}_D = \left(\begin{array}{c|c} y_d^i \tilde{V}_{\rm CKM}^{ij} \frac{v}{\sqrt{2}} & 0^{iJ} \\ \hline (y_d')^{Ji} \frac{v_D}{\sqrt{2}} & M_D^J \end{array}\right), \\ \mathcal{M}_E &= \left(\begin{array}{c|c} y_l^i \frac{v}{\sqrt{2}} & 0^{iK} \\ \hline (y_l')^{Ki} \frac{v_D}{\sqrt{2}} & M_E^K \end{array}\right). \end{aligned} \tag{2.50}$$

The mass matrices can be diagonalised by two unitary matrices V_L and V_R, with dimension $3 + \{I,J,K\}$ depending on the fermion type. If the same VL fermion interacts with multiple flavours of SM fermions, the most constraining effects are represented by modifications to SM observables, induced by Flavour Changing Neutral Currents (FCNCs) [143, 144]. If for each SM fermion there is a VL partner, the matrix proportional to y' is diagonal as well and no mixing is induced between different SM and VL flavours, thus fermions from the dark sector only interact with the corresponding SM flavour. In the following we will limit the analysis to this simpler scenario.

An important property of this construction is that the CKM matrix of the SM receives contributions from new physics. In fact, the SM charged current is

$$\begin{aligned} J_{W^+}^\mu &= \frac{g}{\sqrt{2}} (\bar{u}_L^{\rm SM\,i}\ \bar{U}_L^I) \gamma^\mu \left(\begin{array}{c|c} 1_{3\times 3} & 0^{3J} \\ \hline 0^{I3} & 0^{IJ} \end{array}\right) \left(\begin{array}{c} d_L^{\rm SM\,i} \\ D_L^J \end{array}\right) \\ &= \frac{g}{\sqrt{2}} (\bar{u}_L^i\ \bar{u}_L'^I) \gamma^\mu V_{uL}^\dagger \left(\begin{array}{c|c} \tilde{V}_{\rm CKM} & 0^{3J} \\ \hline 0^{I3} & 0^{IJ} \end{array}\right) V_{dL} \left(\begin{array}{c} d_L^i \\ d_L'^J \end{array}\right), \end{aligned} \tag{2.51}$$

such that the entries of the measured CKM matrix are given by

$$V_{CKM}^{ij} = (V_{uL}^\dagger)^{ik} \tilde{V}_{\rm CKM}^{kl} V_{dL}^{kj} \,. \tag{2.52}$$

2.2.5 FPVDM parameter space

The Lagrangian parameters of the model are the following:

- gauge couplings: g, g', g_D;
- Scalar potential parameters: $\mu, \lambda, \mu_D, \lambda_D, \lambda_{HD}$;
- Yukawa couplings and VL quark mass: y, y', m_{ψ_D};
- $\tilde{V}_{\rm CKM}$ parameters.

Assuming that the new VL fermion interacts only with one SM flavour, these parameters can be traded for the masses of all the physical states, the weak coupling constant g (or equivalently, the fine structure constant $\alpha_{\rm EM}$), the new gauge coupling g_D, the mixing angle between the scalar fields θ_S and the measured CKM parameters. A complete set of parameters is therefore:

$$\{g, m_W, m_Z\},\ \{g_D, m_{V_D}\},\ \{m_h, m_H, \sin\theta_S\},\ \{m_f, m_F, m_{\psi_D}\} \text{ and } V_{\rm CKM}\ , \tag{2.53}$$

but, since g, m_W, m_Z, m_h, m_f and $V_{\rm CKM}$ are precisely measured SM parameters, we are left with the following six independent new physics parameters, namely:

$$g_D, m_{V_D}, m_H, \sin\theta_S, m_F, m_{\psi_D}\ . \tag{2.54}$$

Approximating the CKM as a diagonal matrix for simplicity, the relations between the Lagrangian parameters connected to the new physics components and the input parameters take a very simple form:

$$v = \frac{2m_W}{g}, \quad v_D = \frac{2m_{V_D}}{g_D}\ , \tag{2.55}$$

$$\lambda = \frac{g^2}{8m_W^2}(m_h^2\cos^2\theta_S + m_H^2\sin^2\theta_S)\ , \tag{2.56}$$

$$\lambda_D = \frac{g_D^2}{8m_{V_D}^2}(m_h^2\sin^2\theta_S + m_H^2\cos^2\theta_S)\ , \tag{2.57}$$

$$\lambda_{HD} = \frac{g\ g_D}{8m_W m_{V_D}}(m_H^2 - m_h^2)\sin 2\theta_S\ , \tag{2.58}$$

$$\mu^2 = \frac{1}{2}\left(m_h^2\cos^2\theta_S + m_H^2\sin^2\theta_S + \frac{1}{2}\frac{g}{g_D}\frac{m_{V_D}}{m_W}(m_H^2 - m_h^2)\sin 2\theta_S\right)\ , \tag{2.59}$$

$$\mu_D^2 = \frac{1}{2}\left(m_h^2\sin^2\theta_S + m_H^2\cos^2\theta_S + \frac{1}{2}\frac{g_D}{g}\frac{m_W}{m_{V_D}}(m_H^2 - m_h^2)\sin 2\theta_S\right)\ , \tag{2.60}$$

$$y = \frac{g\ m_f\ m_F}{\sqrt{2}m_{\psi_D}m_W}\ , \tag{2.61}$$

$$y' = \frac{g_D\sqrt{(m_F^2 - m_{\psi_D}^2)(m_{\psi_D}^2 - m_f^2)}}{\sqrt{2}m_{\psi_D}m_{V_D}}\ . \tag{2.62}$$

The minimisation conditions of the scalar potential in Eq.(2.15) are automatically satisfied. If $\lambda_{HD} < 0$, which corresponds to $m_h > m_H$, the condition $\lambda_{HD}^2 < 4\lambda\lambda_D$ translates into $\frac{1}{16}\frac{g^2 g_D^2}{m_W^2 m_{V_D}^2} m_h^2 m_H^2 > 0$, which is always true, whilst, if $\lambda_{HD} > 0$, the conditions $2\lambda\mu_D^2 > \lambda_{HD}\mu^2$ and $2\lambda_D\mu^2 > \lambda_{HD}\mu_D^2$ translate into $\frac{1}{8}\frac{g^2}{m_W^2} m_h^2 m_H^2 > 0$ and $\frac{1}{8}\frac{g_D^2}{m_{V_D}^2} m_h^2 m_H^2 > 0$, respectively, again automatically satisfied.

For a perturbative analysis of the parameter space we need to identify the regions where coupling parameters do not become too large, in order to make sure that all predictions on the model are reliable. A complete loop description of all the sectors of the model is beyond the scope of this analysis and therefore we assume that perturbativity is achieved by the requirement for all couplings of the FPVDM model to be (optimistically) below 4π. For example, the requirement $\lambda < 4\pi$ defines the maximal value of m_H for a given value of the scalar mixing angle, θ_S, as shown by the blue contour in the left panel of figure 2.5. The same figure presents contours for the g_D/m_{V_D} ratio in the $\{m_H, \theta_S\}$ plane corresponding to $\lambda_D = 4\pi$, which indicates the perturbativity limit on the respective parameters.

The perturbative constraints on the Yukawa couplings y and y' imply that the ratio between the masses of the new fermions F and ψ_D cannot be too large. The condition for y reads as $\frac{m_F}{m_{\psi_D}} < 4\pi\frac{\sqrt{2}m_W}{g m_f}$. At the same time, the $y' < 4\pi$ condition is defined also by the g_D/m_{V_D} ratio, as one can see from Eq.2.62. Both constraints from y and y' perturbativity requirements are presented in the right panel of figure 2.5 in the $(m_{\psi_D}, \frac{m_F}{m_{\psi_D}})$ plane. In our analysis of the parameter space we indicate the respective regions where perturbativity constraints are violated.

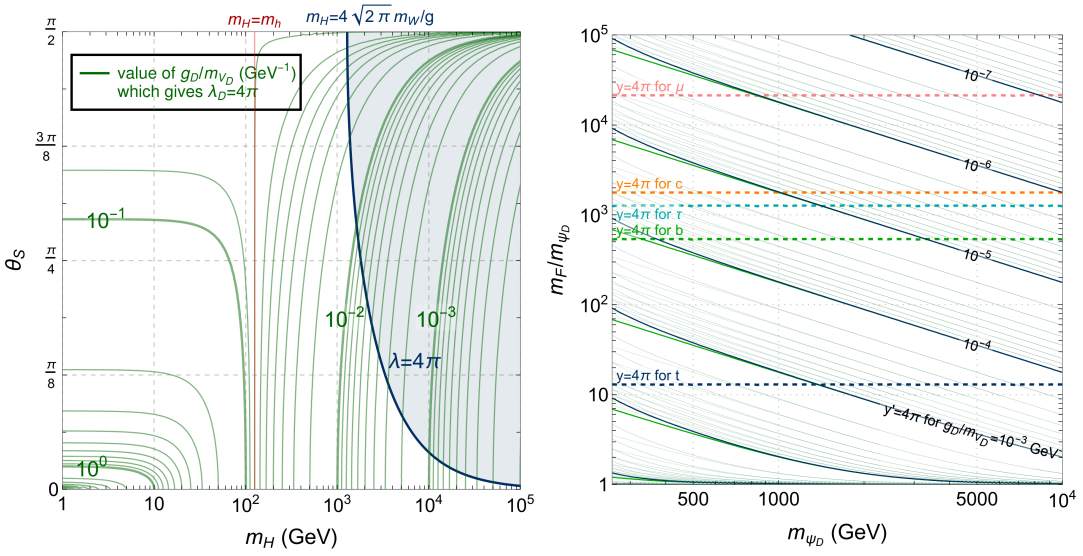

FIGURE 2.5: Left: the maximum value of m_H and minimum value of θ_S for $\lambda < 4\pi$ and $\lambda_D < 4\pi$ as function of $\frac{g_D}{m_{V_D}}$. The regions corresponding to $\lambda_D < 4\pi$ are to the left of the green lines. Right: the maximum value of the m_F/m_{ψ_D} ratio as function of m_{ψ_D} and $\frac{g_D}{m_{V_D}}$, and under different hypotheses about which SM fermion interacts with the $SU(2)_D$ doublet Ψ, to satisfy the perturbativity conditions $\{y, y'\} < 4\pi$.

2.3 On the origin of the global U(1) symmetry

One of the main open questions of the construction presented in this analysis is the origin of the global $U(1)_{Y_D}^{\text{global}}$ symmetry (with its $\mathbb{Z}_2$ parity subset) which has to be imposed to avoid the contemporary presence of two Yukawa interactions involving Φ_D and Φ_D^* which would explicitly break $SU(2)_D$, and therefore spoil the stability of the DM candidate. A theoretical origin of the symmetry would provide a robust ground for the consistency of the model. In this section we explore two options for explaining such origin. The first involves promoting the global $U(1)_{Y_D}^{\text{global}}$ to a local gauge symmetry, $U(1)_{Y_D}$, in the dark sector, which would generate a mirror version of the SM EW sector in the dark sector, the two of which can be connected by the mixed $(\Phi_H^\dagger\Phi_H)(\Phi_D^\dagger\Phi_D)$ quartic term in the full potential and by the gauge kinetic mixing between $U(1)_Y$ and $U(1)_{Y_D}$. In this scenario the $U(1)_{Q_D}$ local symmetry would be associated to a conserved dark-charge completely analogous to the EM charge of QED, thus giving literal meaning to the notation V_D^0 and $V_D^\pm$ for the $SU(2)_D$ gauge bosons in the dark sector.

The second involves the existence of a strongly-coupled sector whose condensates form the particle in the low energy regime, in particular, a residual parity for the composite sector is present due to the specific vacuum alignment present in this kind of models (which would typically also imply an extended Higgs sector). A detailed discussion is given in [145] and further used in [146] for the case of a scalar DM candidate.

2.3.1 A dark electroweak sector

In this scenario the SM is augmented with a dark sector constructed starting from a dark gauge group $\mathcal{G}_D$ with same structure as the EW gauge group of the SM (in this scenario the $U(1)_{Y_D}$ is promoted to be local.). The gauge group is spontaneously broken as:

$$\mathcal{G} = \mathcal{G}_{\text{SM}} \times \mathcal{G}_D = SU(2)_L \times U(1)_Y \times SU(2)_D \times U(1)_{Y_D} \longrightarrow U(1)_Q \times U(1)_{Q_D} \ . \quad (2.63)$$

The gauge boson associated to $U(1)_{Y_D}$ is labelled as $B_{D\mu}$. The full covariant derivative is

$$\begin{aligned} D_\mu = \partial_\mu &- \left(i\frac{g}{\sqrt{2}} W_\mu^\pm T^\pm + igW_\mu^3 T_3 + ig' Y B_\mu \right) \\ &- \left(i\frac{g_D}{\sqrt{2}} V_{\mu D}^\pm T_D^\pm + ig_D V_{\mu D}^0 T_{3D} + ig'_D Y_D B_{D\mu} \right) \ , \end{aligned} \quad (2.64)$$

where g and g' are, respectively, the weak and hypercharge coupling constants, g_D and g'_D are the $SU(2)_D$ and $U(1)_{Y_D}$ coupling constants, T_3 and Y are the weak-isospin and weak-hypercharge, T_{3D} and Y_D are the dark-isospin associated with $SU(2)_D$ and the dark-hypercharge associated with $U(1)_{Y_D}$ and where the indices of the T_D matrices act

only on the $SU(2)_D$ elements and are diagonal with respect $SU(2)_L$ while the indices of the T matrices act only on the $SU(2)$ elements and are diagonal with respect to $SU(2)_D$.

The unbroken $U(1)_{Q_D}$ continuous symmetry is associated to a conserved charge, labelled D-charge, defined as:

$$Q_D = T_{3D} + Y_D \ . \tag{2.65}$$

Notice that *the D-charge is not associated with the electric charge*: electrically neutral particles can be D-charged and vice versa. The only assumption to be made in this scenario is that *all the SM states are neutral under the conserved D-charge* Q_D. This however does not necessarily imply that all the states of new physics are charged under $U(1)_{Q_D}$ or that they must be neutral under the conserved SM charges.

The fields responsible for the breaking of the gauge symmetry are the two scalar doublets Φ_H and Φ_D described in section 2.2. Since Φ_H is singlet with respect to the dark gauge group and Φ_D is singlet with respect to the EW gauge group, given the absence of gauge kinetic mixing terms at tree level, no mixing is induced between the fully neutral gauge bosons W^3_μ, B_μ, $V^0_{D\mu}$ and $B_{D\mu}$. In complete analogy with the SM, by counting the number of bosonic degrees of freedom, one massless gauge boson is predicted in the dark gauge sector and the other dark gauge bosons receive different masses. We can thus define the mass eigenstates γ_D, Z_D and $W^\pm_D$ with values

$$M_{\gamma_D} = 0 \ , \tag{2.66}$$

$$M_{Z_D} = \frac{1}{2}\sqrt{g_D^2 + g_D'^2}\ v_D \ , \tag{2.67}$$

$$M_{W^\pm_D} = \frac{g_D}{2} v_D \ , \tag{2.68}$$

such that the masses of the DM vector $V^\pm_D$ and of the D-charge-neutral gauge boson V^0_D receive a splitting proportional to $\frac{1}{2}g'_D v_D$. The particle content of the model is summarised in Table 2.2. One should note that the presence of the massless dark radiation from the unbroken $U(1)_{Q_D}$ is not necessarily a problem as long as it does not contribute too much to relativistic degrees of freedom at BBN and allows the formation of structures as small scales. As shown in [147], for example, it can be achieved when at the DM decouples from the dark radiation at high redshifts.

The presence of two $U(1)$ gauge groups, however, allows for the existence of a renormalisable and gauge-invariant kinetic mixing term already in the unbroken EW and dark symmetry phases, such that the Lagrangian of the $U(1)_Y \times U(1)_{Y_D}$ sector is

$$-\mathcal{L}_{\rm KM} = \frac{1}{4}B_{\mu\nu}B^{\mu\nu} + \frac{1}{4}B_{D\mu\nu}B_D^{\mu\nu} + \frac{\epsilon}{2}B_{\mu\nu}B_D^{\mu\nu} \ , \tag{2.69}$$

	EW		Dark		Unbroken	
	$SU(2)_L$	$U(1)_Y$	$SU(2)_D$	$U(1)_{Y_D}$	$U(1)_Q$	$U(1)_{Q_D}$
Scalar fields						
$\Phi_H = \begin{pmatrix}\phi^+\\ \phi^0\end{pmatrix}$	$\mathbf{2}$	$1/2$	$\mathbf{1}$	0	$\begin{matrix}1\\0\end{matrix}$	$\begin{matrix}0\\0\end{matrix}$
$\Phi_D = \begin{pmatrix}\varphi_D^+\\ \varphi_D^0\end{pmatrix}$	$\mathbf{1}$	0	$\mathbf{2}$	$1/2$	$\begin{matrix}0\\0\end{matrix}$	$\begin{matrix}1\\0\end{matrix}$
Fermion fields						
$f_L^{\rm SM} = \begin{pmatrix}f_{u,\nu}^{\rm SM}\\ f_{d,\ell}^{\rm SM}\end{pmatrix}_L$	$\mathbf{2}$	$1/6, -1/2$	$\mathbf{1}$	0	$T_{3f}+Y_f$	0
$u_R^{\rm SM}, \nu_R^{\rm SM}$	$\mathbf{1}$	$2/3, 0$	$\mathbf{1}$	0	$T_{3f}+Y_f$	0
$d_R^{\rm SM}, \ell_R^{\rm SM}$	$\mathbf{1}$	$-1/3, -1$	$\mathbf{1}$	0	$T_{3f}+Y_f$	0
$\Psi = \begin{pmatrix}\psi_D\\ F\end{pmatrix}$	$\mathbf{1}$	Q_Ψ	$\mathbf{2}$	$1/2$	Q_Ψ	$\begin{matrix}1\\0\end{matrix}$
Vector fields						
$W_\mu = \begin{pmatrix}W_\mu^+\\ W_\mu^3\\ W_\mu^-\end{pmatrix}$	$\mathbf{3}$	0	$\mathbf{1}$	0	$\begin{matrix}1\\0\\-1\end{matrix}$	$\begin{matrix}0\\0\\0\end{matrix}$
B_μ	$\mathbf{1}$	0	$\mathbf{1}$	0	0	0
$V_{D\mu} = \begin{pmatrix}V_{D\mu}^+\\ V_{D\mu}^0\\ V_{D\mu}^-\end{pmatrix}$	$\mathbf{1}$	0	$\mathbf{3}$	0	$\begin{matrix}0\\0\\0\end{matrix}$	$\begin{matrix}1\\0\\-1\end{matrix}$
$B_{D\mu}$	$\mathbf{1}$	0	$\mathbf{1}$	0	0	0

TABLE 2.2: The quantum numbers under the EW and dark gauge group $SU(2)_D \times U(1)_{Q_D}$ of the particles of the model. The charges of the unbroken local groups $U(1)_Q$ and $U(1)_{Q_D}$ are also provided.

where $B_{D\mu\nu}$ is the field tensor of $U(1)_{Y_D}$ and ϵ is the kinetic mixing parameter. The diagonalisation of the kinetic terms can be obtained through the rotation [148]:

$$\begin{pmatrix} B^\mu \\ B_D^\mu \end{pmatrix} = \begin{pmatrix} \frac{1}{\sqrt{1-\epsilon^2}} & 0 \\ -\frac{\epsilon^2}{\sqrt{1-\epsilon^2}} & 1 \end{pmatrix} \begin{pmatrix} \cos\theta_k & -\sin\theta_k \\ \sin\theta_k & \cos\theta_k \end{pmatrix} \begin{pmatrix} B_1^\mu \\ B_2^\mu \end{pmatrix} \tag{2.70}$$

The kinetic-mixing term induces a modification in the mass mixing matrix of the fully neutral gauge bosons. Upon diagonalisation, two massless eigenstates are obtained, corresponding to the SM photon and to a massless dark photon, and two massive eigenstates, corresponding to the Z boson and to a massive Z' boson. The full expressions of the mass mixing matrix and of the mass eigenstates can be found in Appendix C. Expanding the mass eigenstates of Z and Z' for small ϵ, the lowest order terms assume

a simple form:

$$M_Z^2 = \frac{v^2}{4}\left[g^2+g'^2\left(1+\frac{(g^2+g'^2)v^2-g_D^2v_D^2}{(g^2+g'^2)v^2-(g_D^2+g_D'^2)v_D^2}\epsilon^2\right)\right]+\mathcal{O}(\epsilon^4)\,, \quad (2.71)$$

$$M_{Z'}^2 = \frac{v_D^2}{4}\left[g_D^2+g_D'^2\left(1+\frac{g^2v^2-(g_D^2+g_D'^2)v_D^2}{(g^2+g'^2)v^2-(g_D^2+g_D'^2)v_D^2}\epsilon^2\right)\right]+\mathcal{O}(\epsilon^4)\,, \quad (2.72)$$

which in the $\epsilon \to 0$ limit (no kinetic mixing) reduce to the SM value and Eq.2.67, respectively. Of course, analogously to the FPVDM model with the global $U(1)_{Y_D}^{\text{global}}$ symmetry, after spontaneous breaking of EW and dark symmetries, kinetic and mass mixing terms arise at loop level as illustrated in section 2.2.3.2, involving the four electrically and D-charge neutral gauge bosons. The implications of this scenario and the derivation of its experimental bounds are beyond the scope of this analysis and are reserved for future developments.

2.3.2 A composite origin

In the case of composite models the discrete symmetries allowing the stability of the DM particle depend on the model building details of the composite sector. However, this does not mean that the DM candidate and the corresponding discrete symmetries are an arbitrary choice. The composite effective chiral Lagrangian is invariant under a parity changing the signs of all the pseudo Nambu-Goldstone Bosons (pNGBs), as they appear in bilinear terms in the Lagrangian. Furthermore, these models contain by construction explicit symmetry breaking terms, so more scrutiny is needed to understand if a pNGB can be stable due to a residual parity and therefore be used as a particle describing DM. The origin of the non-invariance with respect to parity (and also charge conjugation) is due to the choice of the vacuum while the strong techni-sector at the origin of these models is instead parity invariant as it is VL with respect to the composite gauge dynamics and the SM gauge group. Once possible parities acting on the pNGBs are identified, these models require a careful check of their invariance, including the Wess-Zumino-Witten terms. In explicit realisations studied in the literature, e.g., in [145, 146], a stable pNGB multiplet allowing the description of DM can indeed be found.

Chapter 3

Phenomenology of the top portal

3.1 A case study: top portal with no mixing between h and H

This section is dedicated to a specific realisation of the model. It is assumed that only one VL partner exists, and interacts exclusively with the SM top quark. Moreover it is further assumed that the Higgs bosons h and H do not mix, i.e., $\theta_S = 0$. These choices significantly simplify the expressions of the Lagrangian parameters (See the full discussion of the theoretical setup in chapter 2), which read:

$$v = \frac{2m_W}{g},\ \mu^2 = \frac{m_h^2}{2},\ \lambda = \frac{g^2 m_h^2}{8m_W^2}, \tag{3.1}$$

$$v_D = \frac{2m_{V_D}}{g_D},\ \mu_D^2 = \frac{m_H^2}{2},\ \lambda_D = \frac{g_D^2 m_H^2}{8m_{V_D}^2},\ \lambda_{\Phi_H \Phi_D} = 0, \tag{3.2}$$

$$y_t = \frac{g\ m_t\ m_T}{\sqrt{2} m_{t_D} m_W} = y_t^{\mathrm{SM}} \frac{m_T}{m_{t_D}}, \quad y_t' = \frac{g_D \sqrt{(m_T^2 - m_{t_D}^2)(m_{t_D}^2 - m_t^2)}}{\sqrt{2} m_{t_D} m_{V_D}}\ , \tag{3.3}$$

where the $\mathbb{Z}_2$-even(-odd) partner of the top quark has been labelled $T(t_D)$, the SM Higgs sector is left unaffected by the new scalar, and Φ_D has a potential completely analogous to the Higgs potential. The hierarchy between the masses in the fermion sector is the same as that discussed in section 2.2.3.1, i.e., $m_t < m_{t_D} \leq m_T$, but H can have any mass allowed by experimental bounds, including, in principle, being lighter than the SM Higgs boson.

The new physics parameter space for this model is five-dimensional:

$$g_D, m_{V_D}, m_H, m_{t_D}, m_T\ . \tag{3.4}$$

In the following, we will denote this scenario as TPVDM – a specific case of top portal in the FPVDM framework. We chose this realisation as a case study since, on the

one hand, it is minimal whilst, on the other hand, it allows us to explore a scenario where a non-Abelian dark sector is not connected to the SM via a Higgs portal at tree level. Furthermore, connecting the dark sector only with the SM top quark allows for an exploration of several interesting collider physics signatures, whilst reducing the impact of constraints from direct detection.

Many other realisations are also very attractive. For example, the dark sector could be connected to SM leptons. The collider constraints on new VL leptons would then be milder, making the scenarios potentially less restricted, but the impact on the cosmological observables would not qualitatively change.[1] These kind of realisations are potentially interesting for a study of anomalies in the lepton sector, for example in connection with the muon anomalous magnetic moment, which is the subject of the chapter 4.

As anticipated in section 2.2.3.2, the mass splitting between m_{V_D} and $m_{V'}$, $\Delta m_V = m_{V_D} - m_{V'}$, plays an important role for DM phenomenology. First of all, we have found that $\Delta m_V > 0$ in the whole parameter space of the model, with the approximate expressions for Δm_V given by Eq.(2.41) and (2.42). Since $m_{V_D} > m_{V'}$, the $V_D V_D^* \to V'V'$ process for DM annihilation will *always* take place for any point in the parameter space to contribute crucially to the list of processes affecting the relic density and to extend the viable parameter space compatible with constraints imposed by the relic density. The $V_D V_D^* \to V'V'$ process also contributes to the DM indirect detection signals.

Numerically, the value of Δm_V varies over a very wide range, since it scales as g_D^2 and it is proportional to $m_T^2 - m_{t_D}^2$. One should also note that Δm_V does not depend on m_H, as explained in appendix A. In figure 3.1 (left) we present the iso-contours for Δm_V in the $\{m_{t_D}, m_{V_D}\}$ plane for $g_D = 0.1$ and $m_T = 1600$ GeV, whilst in figure 3.1 (right) we show how Δm_V evolves as function of m_{V_D} for the specific value of $m_{t_D} = 1590$ GeV, all other parameters being the same. The value of m_T is chosen to be safely above the current upper limit on VL top partners at the LHC [149]. For our particular choice of g_D and m_T, Δm_V can be as large as 1 GeV, while its minimal value reaches zero for a vanishing value of $m_T - m_{t_D}$. In both frames we present a comparison of the exact one-loop result for Δm_V and its approximations given by Eq.(2.41) and (2.42). It is possible to see from figure 3.1 (right) that the approximate formulae are very accurate for a small $m_T - m_{t_D}$ splitting, but break down for m_{V_D} close to the $m_t + m_{t_D}$ threshold, where the one-loop corrections are highly non-linear in the expansion parameters used in approximate expressions for Δm_V. Moreover, for small values of m_{V_D}, the one-loop mass corrections can be large, making the evaluation of Δm_V perturbatively unstable. Therefore, we indicate by the hatched area the region where one-loop corrections to the

[1] This is true except when the mass difference between DM and VL fermion mediator is small. In that case DM co-annihilation will be less intense in comparison with strong co-annihilation with the t_D quark.

masses of V_D and/or V' become larger than 50% of the corresponding tree level masses.

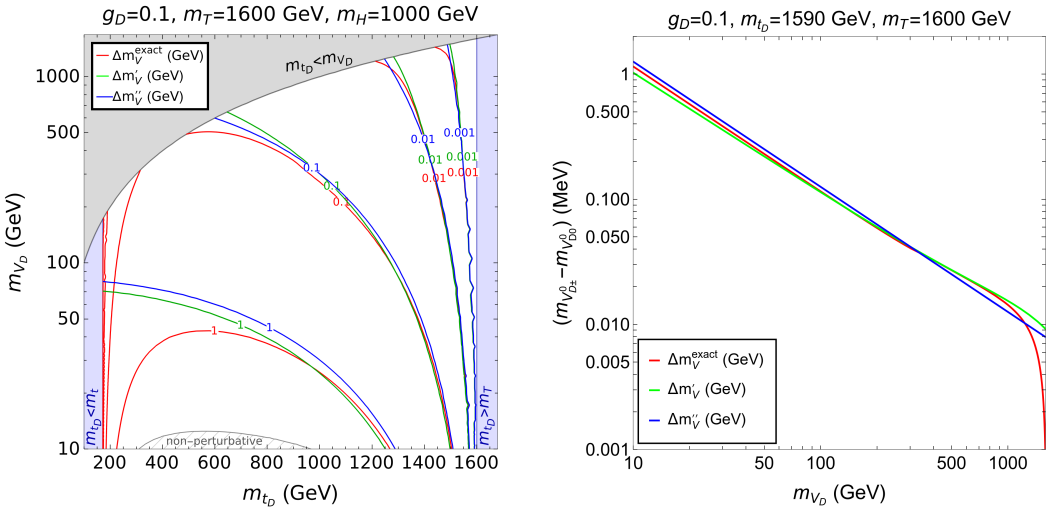

FIGURE 3.1: Values of the mass splitting $\Delta m_V = m_{V_D} - m_{V'}$ in the (m_{t_D}, m_{V_D}) plane for a specific choice of g_D, m_T and m_H (left panel) and as a function of m_{V_D} for a specific value of m_{t_D} (right panel). The red, green and blue curves correspond to results from exact expression, approximated formulae Eq.(2.41) and (2.42), respectively. The region where one-loop corrections to the masses of V_D or V' become larger than 50%, so that a perturbative treatment is questionable, is also highlighted.

The lifetime of V' does not directly depend on Δm_V. However, the $\mathbb{Z}_2$-even $SU(2)_D$ gauge boson can also be long lived, if the DM is light enough. The only tree-level interaction of V' with SM particles is with top quarks, due to its mixing with T. If the mass of V' drops below the $t\bar{t}$ threshold, it can only decay directly to a three-body or four-body final state with W bosons and b quarks via the off-shell top quarks, or decay to a $b\bar{b}$ final state at one-loop, see the Feynman diagrams in figure 3.2 (left). The latter, although only present at the one-loop level, becomes dominant due to the reduced phase space for the four-body final state. This is shown in figure 3.2 (centre and right). These loop-induced diagrams prevent V' from having a sufficiently long lifetime to spoil Big Bang Nucleosynthesis (BBN). However, when the g_D coupling is small, the t_D mass approaches the decoupling limit ($m_{t_D} = m_T$) and the DM is light, V' becomes long lived at colliders. Therefore, it could provide a signal for searches of long-lived neutral bosons decaying into $b\bar{b}$ pairs.

As mentioned in section 2.2.3.3, even if TPVDM scenario does not contain a tree-level mixing, a loop-induced mixing between h and H still occurs, via SM top and the $\mathbb{Z}_2$-even top (T) loops. This contribution is eventually suppressed. A scenario with tree-level scalar mixing is more constrained and can exhibit the following signatures: 1) the heavy scalar H can decay also to any final state accessible to the Higgs boson, and therefore the model predicts further signatures at collider; 2) if the mass of the DM is small enough, the Higgs boson will decay into the DM itself or the $\mathbb{Z}_2$-even gauge boson V', affecting its width and branching ratios. From the cosmological point of view, additional

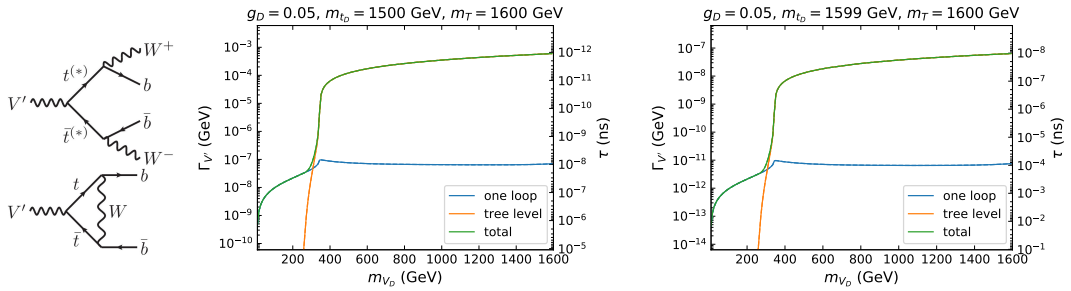

FIGURE 3.2: Left: Tree-level and one-loop diagrams for V' decay. Center and right: decay width and lifetime of V' at tree and one-loop level for $g_D = 0.05$, $m_T = 1600$ GeV and different values of m_{t_D}.

interactions from the tree-level scalar mixing will affect the relic density, and direct and indirect detection observables.

Since there is no h-H mixing in TPVDM scenario, DM scattering off the nuclei is induced only at loop-level. The Feynman diagrams for DM-gluon interactions with quark box and triangle topologies are shown in figure 3.3(a) and (b), while the DM-quark diagrams generated by the loop-induced $V' - \gamma/Z$ kinetic mixing and triangle diagrams are shown in figure 3.3(c) and (d), respectively. The detailed evaluation of the triangle loop of fermions connected to gauge boson propagators is given in appendix D. As it will become clear in section 3.1.3, the KM and triangle contributions play a crucial role in constraining the parameter space of the model through Direct Detection (DD) limits on DM.

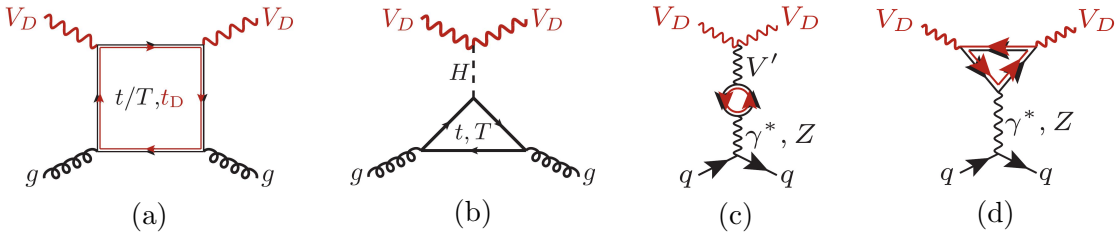

FIGURE 3.3: Representative diagrams for direct detection processes. H is the $\mathbb{Z}_2$-even scalar in the dark sector. $\mathbb{Z}_2$-odd particles are highlighted in red.

In the following sections, this model is tested against multiple observables from cosmology (relic abundance, direct and indirect DM detection rates) and LHC searches. For this analysis we implemented the Lagrangian of the model in the LANHEP [150] and FEYNRULES [151] packages whilst model files have been generated in CALCHEP [152], FEYNARTS [153] and UFO [154] formats.[2] We used MICROMEGAS v5.2.7 [51] for calculating DM observables and for setting the corresponding limits (see section 3.1.1) as well as for the evaluation of some LHC processes. The model implementation in UFO format has been used in MG5_AMC [156] for the determination of the complete set of

[2]The model implementations are available in the HEPMDB [155] repository in CALCHEP (https://hepmdb.soton.ac.uk/hepmdb:0322.0335) and UFO (https://hepmdb.soton.ac.uk/hepmdb:0322.0336) formats.

LHC constraints (see section 3.1.2). The FeynArts model files from LanHEP were used to generated one-loop corrections to masses of $SU(2)_D$ gauge bosons by FeynCalc [157], FeynHelpers [158] and Package-X [159]. A simplified version of the model has been implemented to calculate cross-sections at one-loop level in MG5_aMC and FormCalc9.8 [160].

3.1.1 Cosmological constraints

There are many non-collider experiments dedicated to searching for signals of DM, both in space and on Earth which play a very important role in limiting the DM parameter space and in the identification of viable DM models. These experiments are devoted to the precise determination of the DM relic density as well as to DD and ID of DM.

3.1.1.1 DM relic density

In particular, the PLANCK experiment has measured the relic density with a precision better than 1% [21]:

$$\Omega_{\rm DM}^{\rm Planck} h^2 = 0.12 \pm 0.0012\,. \tag{3.5}$$

In our analysis, we will select points that satisfy this constraint, bearing in mind that points which predict a relic density below the PLANCK constraint could still be allowed if new sources of DM exist besides V_D.

3.1.1.2 DM direct detection

For DM DD we use the limits from XENON1T [44]. The XENON1T experiment provides the most stringent upper limit (compared to LUX (2017) and Panda-X (2017), see figure 5 in the reference [44]). XENON1T provides the limit on DM-nucleon's cross-section vs DM mass at 90% C.L. together with the detector's efficiency as a function of nuclear recoil energy. We have evaluated the DM-nucleon scattering cross section and converted it into the number of events by taking in account the efficiency of the XENON1T detector. This allowed us to find the corresponding p-value for the signal. The calculation was performed using a modified version of micrOMEGAs package which allowed us to correctly evaluate DM DD rates from the loop-induced $\gamma(Z)$-V_D-V_D interactions.

The modified code of micrOMEGAs

The standard routine `CDM_NUCLEON` of micrOMEGAs cannot be used to calculate the DM DD rate for diagrams of virtual photon with zero momentum transfer as it causes

divergence. To this end, we use the special code implemented by Alexander Pukhov (one of the authors of MICROMEGAs package).

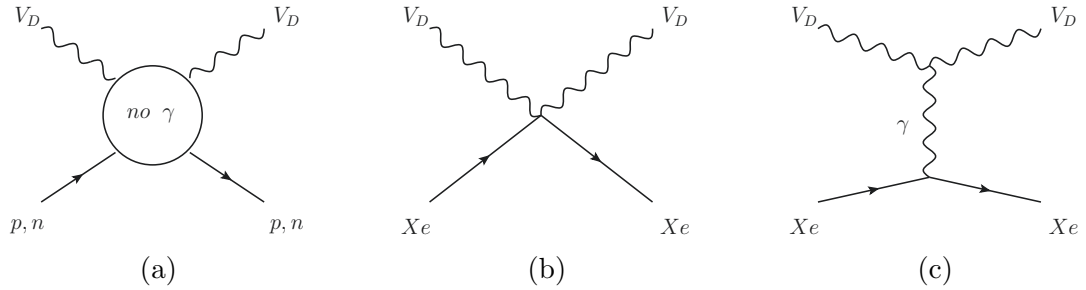

FIGURE 3.4: The diagrams describing the interaction between DM and (a) nucleons without virtual photon, (b) xenon as point-like and (c) xenon with virtual photon.

We use the following trick to calculate the DM DD rate. Firstly, we calculate the spin-independent amplitudes of DM-nucleon scattering excluding the photon propagating diagrams as depicted in figure 3.4 (a). Then, we implement the 4-point vertex of V_D, V_D, Xe, Xe with the following effective Lagrangian

$$\mathcal{L}^{\text{eff}}_{\text{4-point}} = g_{\text{eff}} \overline{Xe}\, Xe\, V_D^{\alpha}(p_3)\, V_D^{\beta}(p_4), \tag{3.6}$$

where

$$g_{\text{eff}} = 4m_{V_D}(54A_p^S + (130-54)A_n^S)g_{\alpha\beta} + 2(54A_p^A + (130-54)A_n^A(\not{p}_3 - \not{p}_4))g_{\alpha\beta}. \tag{3.7}$$

The factor 54 and (130-54) are the number of protons and neutrons, respectively, inside xenon nuclei. The quantities $A_p^S(A_n^S)$ and $A_p^A(A_n^A)$ are the symmetric and asymmetric amplitudes of DM scattering on proton(neutron), respectively. They are defined by

$$\begin{aligned} A_p^S &= \frac{1}{2}(A_p^{V_D} + A_p^{V_D^*}), \\ A_p^A &= \frac{1}{2}(A_p^{V_D} - A_p^{V_D^*}), \end{aligned} \tag{3.8}$$

where $A_p^{V_D}$ is the amplitude of DM and proton and $A_p^{V_D^*}$ is the amplitude of anti-DM and proton. After that, we sum the amplitude from diagram 3.4 (b) and (c) and then calculate the scattering cross section for $V_D, Xe \to V_D, Xe$ process.

In the code, the differential scattering cross section in terms of the squared matrix element $|\mathcal{M}|^2$, the detector efficiency ϵ_{eff} and nuclear form factor F is given by

$$\frac{d\sigma_{\text{EM}}}{d\sin(\theta/2)} = 4\sin\left(\frac{\theta}{2}\right)|\mathcal{M}|^2\,\epsilon_{\text{eff}}\,F^2. \tag{3.9}$$

The scattering cross section reads

$$\sigma_{\text{EM}} = \frac{1}{32\pi s}\int_a^1 \frac{d\sigma_{\text{EM}}}{d\sin(\theta/2)} d\sin(\theta/2), \tag{3.10}$$

where

$$a = \sqrt{\frac{E_{\rm min}}{2p_{\rm cm}}},$$
$$p_{\rm cm} = \left(\frac{m_{\rm DM}\, m_{\rm N}}{m_{\rm DM} + m_{\rm N}}\right) v. \tag{3.11}$$

Finally, we calculate the number of events by

$$N_{\rm event} = \frac{\rho_{\rm DM}}{m_{\rm DM}}\, t\, N_{\rm Xe}\, \sigma_{\rm EM} \int_0^{v_{\rm esc}+v_{\rm Earth}} v f_{\rm Maxwell}(v) dv, \tag{3.12}$$

where ρ_{DM} is the local DM density, t the exposure time and $N_{\rm Xe}$ the number of xenon nuclei. The parameter $v_{\rm esc}$ is the maximal DM velocity around the sun and $v_{\rm Earth}$ is the Earth velocity in the galactic rest frame, respectively.

We have scaled the number of registered events if the corresponding relic density is less than the measured value as follows:

$$\hat{N}_{\rm event} \;=\; \begin{cases} \left(\frac{\Omega_{\rm DM}}{\Omega_{\rm DM}^{\rm Planck}}\right) N_{\rm event}, & \text{if } \Omega_{\rm DM}h^2 < 0.12 \\ N_{\rm event}, & \text{otherwise} \end{cases}, \tag{3.13}$$

and have defined the p-value, $\hat{p}$, as

$$\hat{p} \;=\; \exp(-\hat{N}_{\rm event})\,. \tag{3.14}$$

The exclusion of parameter space is imposed on the points where $\hat{p} < 0.1$, which corresponds to the exclusion limit at 90% C.L.

3.1.1.3 DM indirect detection

ID DM searches are being performed by many experiments, including Fermi-LAT [161], IceCube [64], ANTARES [62], etc. However, these experiments rely on the DM local density and velocity distribution as well as the propagation of the particles in the galactic plane. Therefore, the respective predictions are affected by various uncertainties of an astronomical nature. To be independent of these uncertainties, in this study we use the Cosmic Microwave Background (CMB) limit on DM ID based on PLANCK data. We consider the product of the DM-self annihilation or the DM decay into SM particles. By studying the effect of energy injection from DM annihilation products (electrons, positrons, gamma-ray, neutrinos and anti-protons) on the galactic medium which is sensitive to the CMB anisotropies, the upper limit on the energy injection measured by PLANCK is:

$$P_{\rm ann} < 3.2 \times 10^{-28}\, \frac{\rm cm^3}{\rm s\,GeV} \quad \text{at } 95\% \text{ C.L.}, \tag{3.15}$$

with

$$P_{\rm ann} = \sum_j \frac{f_j^{\rm eff} \langle \sigma v \rangle_j}{M_{\rm DM}} \left(\frac{\Omega_{\rm DM}}{\Omega_{\rm DM}^{\rm Planck}} \right)^2 , \tag{3.16}$$

where $\langle \sigma v \rangle_j$ is the thermally averaged partial annihilation cross-section for the j channel whilst $f_j^{\rm eff}$ is the energy fraction of DM annihilation transferring to the plasma for the jth channel. $P_{\rm ann}$ To construct the quantity $P_{\rm ann}$, we use MICROMEGAs to calculate $\langle \sigma v \rangle_j$ for all possible channels and neglect those that contribute to the total annihilation cross-section less than 0.1%. The effective fraction of energy $f_j^{\rm eff}$ was thoroughly studied and provided for almost all DM annihilation processes into two SM particles in the final state in [70, 162]. For non-SM particles in the final state of $2 \to 2$ processes, for example $V_D, V_D^* \to V', V'/V', H/H, H$, we make the approximation $f_{\text{non-SM}}^{\rm eff} \sim f_{q\bar{q}}^{\rm eff}$. This approximation is reasonable because each V_D/H eventually decays into 3 pairs of quarks anti-quarks and the energy fractions stored in each quark anti-quark pair (u, d, s, c, b, t) are not significantly different. The annihilation cross-section in eq. (3.16) is rescaled by $(\Omega_{\rm DM}/\Omega_{\rm DM}^{\rm Planck})^2$ due to the two DM particles in the initial state.

Finally, we have checked that the model does not spoil the predictions from BBN. When the lifetime of V' is too long, such that it decays during or after BBN, it would spoile the observed neutron to proton density ratio. For $m_{V'} \lesssim 2m_W$, the dominant decay to $b\bar{b}$ via the loop-induced process discussed above makes V' lifetime much shorter than the value excluded by BBN. So, in this respect, BBN does not exclude any region of the parameter space of our model that is allowed by relic density constraints.

3.1.2 Collider constraints

In the scenario under consideration the top quark is the only SM particle which interacts with the dark sector. Processes involving top quarks in propagators or final states are therefore affected by new physics contributions. The model contains a complex vector DM candidate but two different kind of mediators: the VL and $\mathbb{Z}_2$-odd top partner t_D and the two $\mathbb{Z}_2$-even bosons H and V', which however can only be produced at the LHC via interactions with the top quark or its $\mathbb{Z}_2$-even partner t'.

A list of relevant signatures for the scenario are provided in Table 3.1. A mono-jet signature can only arise at loop level, while the $t\bar{t} + E_T^{\rm miss}$ and $t\bar{t}t\bar{t}$ one can receive both tree- and loop-level contributions, which might be of similar size depending on the regions of parameter and phase space. Given the preliminary and explorative nature of this analysis, in the following we perform a recast of current LHC searches only for the tree-level processes to obtain constraints on the parameter space of the model.

The simulations are performed at Leading Order (LO) with MG5_AMC [156] in the 4-flavour scheme using the NNPDF3.0 LO set [163] through the LHAPDF 6 library [164]

Process	Representative diagrams
mono-jet (only loop)	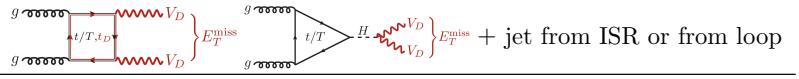 + jet from ISR or from loop
$t\bar{t} + E_T^{\text{miss}}$	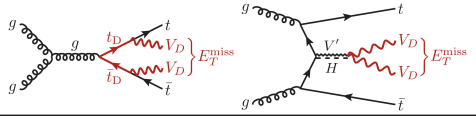
$t\bar{t}t\bar{t}$	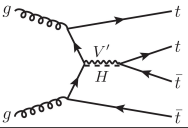
hV' and $V'V'$ (only loop)	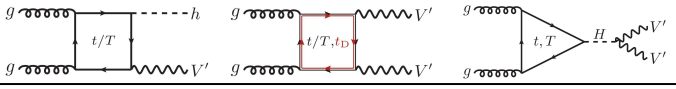

TABLE 3.1: List of relevant processes at the LHC. $\mathbb{Z}_2$-odd particles are highlighted in red. Due to its purely VL nature, t_D cannot interact with the scalars.

(LHA index 262400). No resonant propagation of new particles is imposed, to allow for the inclusion of interference and off-shellness effects when relevant. For the $t\bar{t} + E_T^{\text{miss}}$ signature, in the region of a small mass gap between t_D and V_D, where $m_{t_D} - m_{V_D} < m_t$, simulations are performed for the $2 \to 6$ process $pp \to W^+bW^-\bar{b}V_DV_D$. The recast is done through the MADANALYSIS 5 framework and the searches considered for the recast are different depending on the process:

- for the $t\bar{t} + E_T^{\text{miss}}$ processes we used a CMS search for top squark pair production decaying to DM, in final states with opposite sign leptons and missing transverse energy E_T^{miss} [165], recast in [166].
- for the $t\bar{t}t\bar{t}$ processes we used a CMS search for four top quarks in final states with either a pair of same-sign leptons or at least three leptons, in addition to multiple jets [167], recast in [168].

In both cases, the searches target the very same final states predicted by our model, and are therefore ideal for determining constraints from collider.

The model also predicts a signal from pair production of the $\mathbb{Z}_2$-even partners of the SM top-quark, $T\bar{T}$, which is constrained by ATLAS and CMS searches and only needs to be rescaled for different branching ratios. However, the T-quark primarily decays into $Wb/Zt/ht$ final state with a 50%/25%/25% branching ratio pattern, and the contribution of decays to new states is very small in the whole parameter space. Therefore, current LHC bounds leave the region of parameter space with $m_T \gtrsim 1.5$ TeV unconstrained [169, 170]. Bounds from single T production are more model-dependent, but less tight, as the production cross-section is driven by the $T - t$ mixing which is small.

The loop-level diagrams can be relevant especially when the particles which decay to the final states are produced at resonance : in this case the loop suppression can be compensated by the lower multiplicity in the phase space. For the hV' and $V'V'$ processes

we have only computed cross-sections using a simplified version of the model suitable for one-loop calculations in MG5_aMC, to estimate if they can be tested against data from current searches.

3.1.3 Combined bounds

3.1.3.1 Full parameter scan

We explore the viable parameter space of our model as well as the effect of the cosmological and collider constraints by performing a comprehensive scan over the 5D parameter space in the following ranges:

$$\begin{cases} 10^{-3} < g_D < 4\pi \\ 10 \text{ GeV} < m_{V_D} < m_{t_D} \\ 1.5 \text{ TeV} < m_T \\ m_t < m_{t_D} \leq m_T < 10 \text{ TeV} \\ 10 \text{ GeV} < m_H < 20 \text{ TeV} \end{cases} . \tag{3.17}$$

In figure 3.5 we present the results of this scan showing projections into various planes: (m_{V_D}, g_D) (a), (m_H, m_{V_D}) (b), (m_{t_D}, m_{V_D}) (c) and (m_{t_D}, g_D) (d).

The allowed parameter space is indicated by the green, cyan and blue regions, corresponding to generic DM annihilation (via $V_D V_D \to V'V'$ and t-channel $V_D V_D \to t\bar{t}$ processes), resonant (H) annihilation and DM $- t_D$ co-annihilation regions respectively. The representative Feynman diagrams for these channels are shown in figure 3.6.

In these regions the relic density constraint from PLANCK is satisfied to within 5%. The grey colour indicates the under-abundant DM relic density region. From figure 3.5(a) one can see that the generic DM annihilation (diagrams (a)–(c) of figure 3.6) determines a narrow strip in the (g_D, m_{V_D}) plane indicating the correlation between g_D and m_{V_D} required to arrange the right amount of DM. For values of g_D below this band these processes cannot provide large enough cross-section for DM annihilation and this leads to the excluded over-abundant DM region indicated by the red colour. One can clearly see this region in all panels of figure 3.5 for large DM masses. However, there are additional processes which provide an effective DM annihilation low DM relic density respectively, consistent with PLANCK data. One of them is $V_D V_D \to H$ resonant annihilation, a representative diagram of which is shown in figure 3.6(d). This process allows one to extend the viable parameter space into the lower region of g_D (by up to two orders of magnitude) indicated by the cyan colour. This can be clearly seen in figure 3.5(b), which presents the cyan H resonant band which goes across the whole parameter space in the (m_H, m_{V_D}) plane.

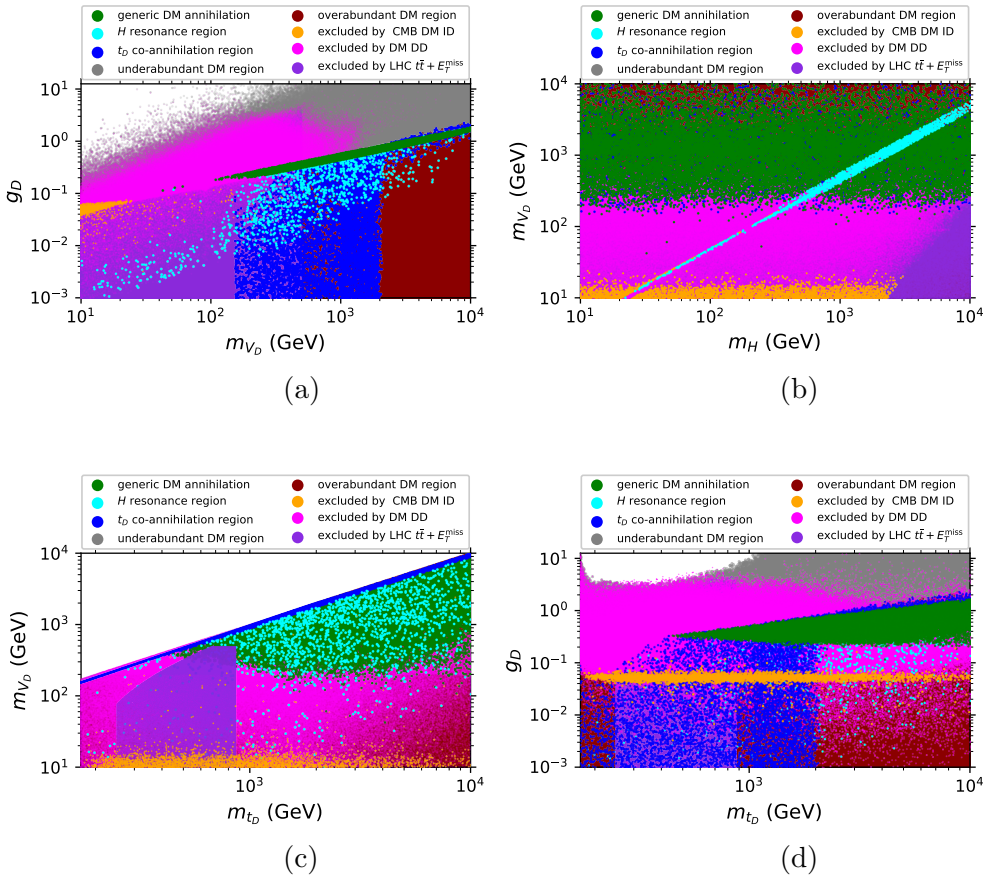

FIGURE 3.5: Excluded and allowed region of the parameter space of the model from the full five-dimensional scan of the parameter space projected into (m_{V_D}, g_D), (m_H, m_{V_D}), (m_{t_D}, m_{V_D}) and (m_{t_D}, g_D) planes. The white areas represent: top-left corner of panel (a) and bottom-right corner of panel (c) – non-perturbative region of the parameter space; upper part of panel (c) – kinematically inaccessible $m_{V_D} > m_{t_D}$ region.

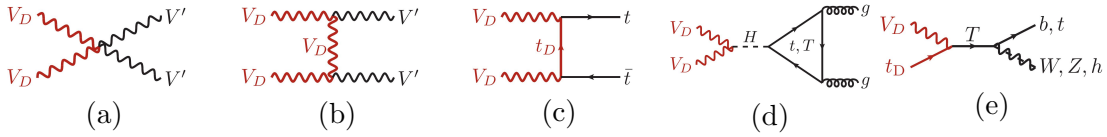

FIGURE 3.6: Representative contributions to relic density. From left to right: 4-leg; t-channel DM annihilation; DM annihilation via resonant H (the $\mathbb{Z}_2$-even scalar in the dark sector); DM-mediator co-annihilation. $\mathbb{Z}_2$-odd particles are highlighted in red.

Another process, the DM-t_D co-annihilation channel (see representative diagram in figure 3.6(e)), provides viable parameter space even for lower values of g_D for $m_{V_D} > m_t$ and m_{t_D} values below 2 TeV. The respective region is indicated by the blue colour, which can be clearly seen especially in (m_{t_D}, m_{V_D}) as a narrow resonance band. At the same time, when m_{V_D} is above 2 TeV, neither DM-t_D co-annihilation nor H-resonant annihilation are effective enough to provide low enough relic density for g_D values below the generic DM annihilation region. Therefore, the region with low g_D and large m_{V_D} is excluded due to the over-abundant relic density indicated by the red colour.

Furthermore, notice that the regions with low m_{V_D} and large g_D values are partly excluded by DD and/or ID experiments as indicated by magenta and orange points, respectively. The region of DM masses which can be tested and excluded by the LHC is presented by the violet region. This parameter space, which can be seen in all panels of figure 3.5, is related to constraints on the $t\bar{t}+E_T^{\text{miss}}$ signal at the LHC coming from $t_D\bar{t}_D$ pair production. For masses of t_D below about 900 GeV this signal would be observed if there is enough phase space for $t_D \to V_D t$ decay. This process is important in setting one of the main collider constraints on the model under study.

The four projections presented in figure 3.5 reveal the non-trivial shapes of the allowed and excluded regions over the 5D parameter space of the model. For example, the orange colour, which presents the DM ID exclusion region, takes place for $m_{V_D} < 20$ GeV (figure 3.5(a,b,c)), $g_D \lesssim 0.06$ (figure 3.5(a,d)) and $m_H \lesssim 3$ TeV(figure 3.5(b)). In figure 3.5 (b), one can see that DM ID exclusion takes place (besides the low m_{V_D} region discussed above) and also along the very middle of the cyan band, where $m_{V_D} = m_H/2$. Indeed, in this case, DM effectively annihilates through the H state into $t\bar{t}$, $V'V'$ or gg, distorting precise CMB data, which therefore also limits the model parameter space. This region cannot be clearly seen in other panels, where it is presented just by randomly scattered points.

3.1.3.2 Benchmark analysis

In order to assess the relative role of the different constraints in identifying the allowed region of parameter space of our model we identify different benchmarks, characterised by fixed values for the masses of the $\mathbb{Z}_2$-even top partner, $m_T = 1600$ GeV, and of the new scalar, $m_H = 1000$ GeV, as well as different values of the new gauge coupling $g_D = \{0.05, 0.1, 0.3, 0.5\}$. These choices have the following rationale: 1) the gauge coupling can either assume a small value for which constraints from over-abundant relic density only allow tiny regions of the parameter space or a larger value for which such constraints become weaker; 2) the $\mathbb{Z}_2$-even partner of the top (T) is heavy enough to evade current LHC bounds based on pair production and considering decays into SM final states; 3) the mass of the H state is large enough for it to decay into a top-quark pair. This affects the relative contribution of the diagrams mediated by H in table 3.1.

The complementarity of cosmological and collider constraints can be represented in the $\{m_{t_D}, m_{V_D}\}$ or $\{m_{t_D}, 1 - \frac{m_{V_D}}{m_{t_D}}\}$ planes. The former, shown in figure 3.7, allows us to highlight the low m_{V_D} region while the latter, shown in figure 3.8, emphasises the small mass gap region between t_D and the DM particle.

The interplay between cosmological and collider bound is largely driven by the relative roles of relic density and DD bounds as function of the gauge coupling value, while indirect detection plays a role only for small coupling values.

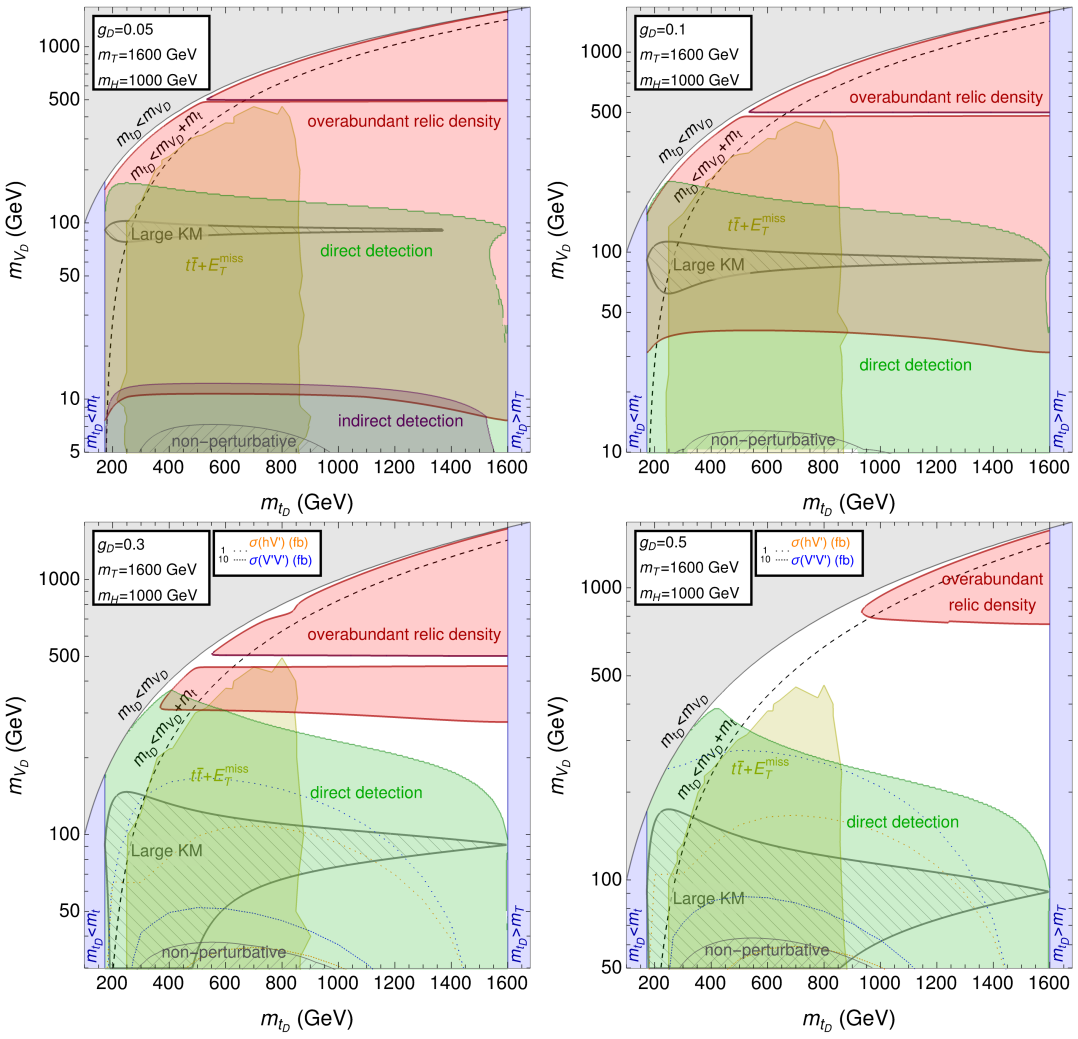

FIGURE 3.7: Combination of constraints from LHC, relic density, ID and DD in the $\{m_{t_D}, m_{V_D}\}$ plane for $m_T = 1600$ GeV, $m_H = 1000$ GeV and different values of g_D. The coloured regions are excluded. The measured relic density value is reconstructed on the borders of the excluded region. When constraints from ID are absent, cross-sections for hV' and $V'V'$ production processes are shown. The non perturbative region corresponds to corrections to the gauge boson masses larger than 50%. An estimate of the region of large KM is shown as a hatched area where at least one of the adimensional KM parameters $\{\epsilon_{AV}, \epsilon_{ZV}, \theta_{ZV}\}$ becomes larger than 10%.

For smaller values of the gauge coupling, $g_D = 0.05$ and $g_D = 0.1$, the measured amount of relic density is reconstructed only for light DM masses, $m_{V_D} \sim \mathcal{O}(10)$ GeV, and in a narrow region where the mass splitting between t_D and the DM is small, less than $\sim 10\%$ of m_{t_D}. In the co-annihilation region, where the mass gap between V_D and t_D is small, as well as in the H-resonant region around $m_{V_D} = m_H/2$, where H is produced near resonance, the relic density is drastically reduced, becoming under-abundant.

The small bell-shaped area visible in the middle of each panel of figure 3.8 with $g_D < 0.5$ corresponds to the process in which T is produced resonantly and decays into SM final states Wb, Zt or ht, (see figure 3.6). If the gauge coupling becomes large enough, it eventually becomes impossible to reconstruct the measured value of the relic density and

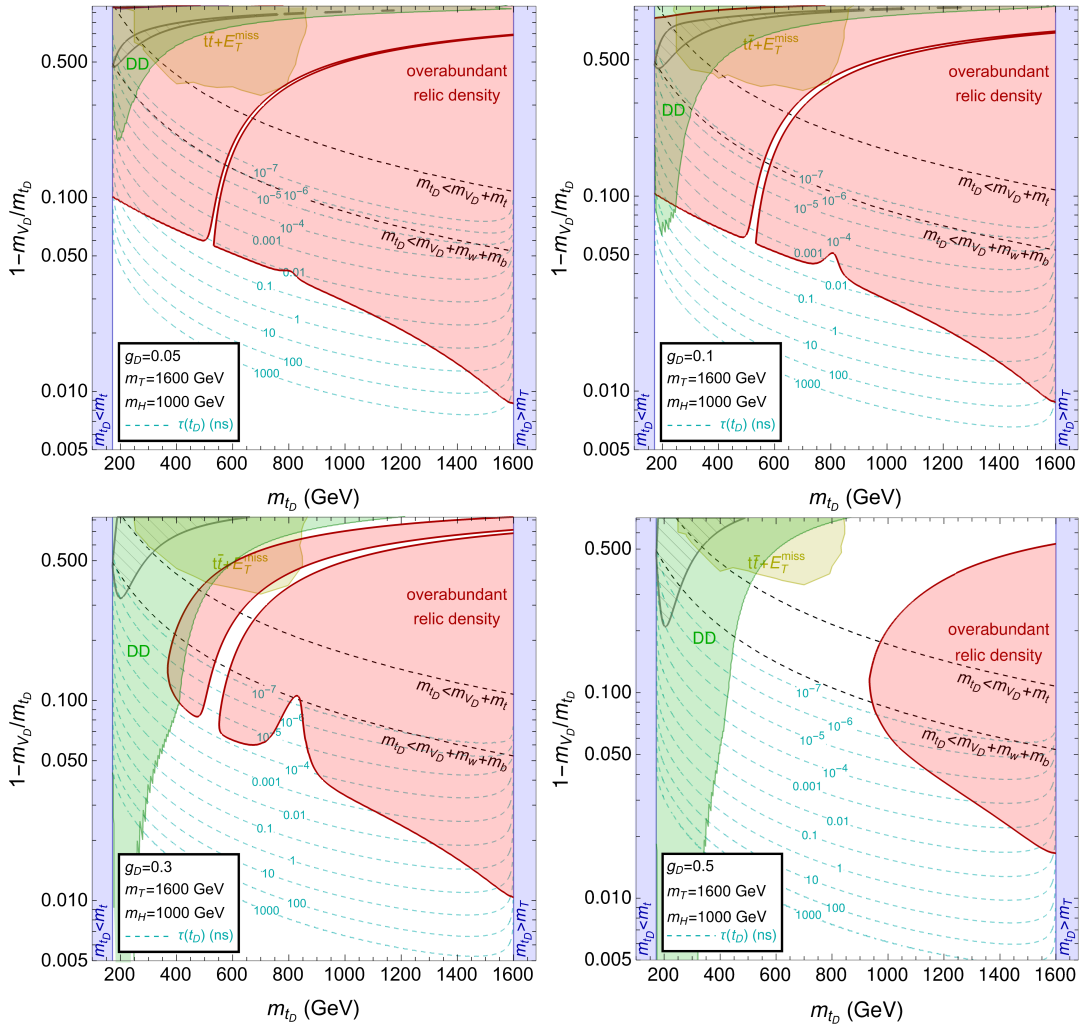

FIGURE 3.8: Same as figure 3.7 in the plane $\{m_{t_D}, 1-\frac{m_{V_D}}{m_{t_D}}\}$, to highlight the region where the DM and t_D have a small mass splitting. Contours corresponding to the lifetime of t_D (in a region where it can be long-lived) are also shown.

the entire allowed parameter space of the model corresponds to an under-abundant relic density. In this case, the theory would not be able to explain the whole observed DM content of the universe and other sources of DM would be needed.

In the small m_{V_D} region, strong constraints from ID limit the allowed parameter space to m_{t_D} values approaching m_T, i.e., the region where the mixing between T and t becomes small. ID constraints however disappear for increasing values of g_D, corresponding to a reduction of relic density values, owing to the scaling reported in eq.(3.16).

However, the constraints from DD always exclude the region with small m_{V_D} regardless of the gauge coupling value. The contribution of DM-gluon topologies is limited to the region with either minimal or maximal mixing in the fermion sector, corresponding to dominant contributions of the topologies (a) or (b) of figure 3.3, respectively. These contributions destructively interfere for generic mixing otherwise, reducing the impact of this process in driving the DD bounds. But the main contributions to DM DD is

driven by the topologies with kinetic mixing induced by gauge boson self-energies, see figure 3.3(c), and by loop-induced effective couplings V_D-V_D-Z/γ which lead to DM-quark interactions through multipole moments, see figure 3.3(d). The evaluation of the amplitudes for triangle diagrams leading to V_D-V_D-Z/γ multipole interactions is given in detail in figure D.[3] For DM masses below about ∼400 GeV, the kinetic mixing with Z-boson plays dominant role for DM DD constraints. In the hatched region of figure 3.7, one can see that the KM contribution becomes strongest when the DM mass is comparable to the mass of Z boson (i.e., dominated by the mass mixing between Z and V'). As the gauge coupling increases, the effect of KM becomes strong also when the DM mass is small and the ratio between t_D and T is small (compatibly with the behaviour of the KM functions in figure 2.4. On the other hand, for heavier DM and sufficiently large y'_t coupling, triangle diagrams, defining multipole DM interactions with the photon can play a dominant role. Therefore, taking into account of the complete set of Feynman diagrams and their interference is an important element for the consistent and correct estimation of DM DD rates and constraints in the FPVDM framework.

The LHC bound comes exclusively from the $t\bar{t} + E_T^{\text{miss}}$ signature, dominated by the pair production of t_D states. The bound is almost independent of the mass of t_D and constrains the region 250 GeV $\lesssim m_{t_D} \lesssim$ 850 GeV, independently of g_D, until the mass difference between t_D and the DM becomes small: in this case the missing energy component of the events decreases and the sensitivity of the relevant CMS search reduces, allowing the small mass gap region. Effects coming from the width of t_D are negligible, as the t_D is narrow in the whole parameter space for each choice of g_D. The 4-top-quark search does not show any sensitivity over the whole parameter space, regardless of the value of g_D. The loop processes of hV' associate production and $V'V'$ pair production are not testable at current luminosities, as their cross-sections are always well below $\sigma \gtrsim \mathcal{O}(10\text{ fb})$ in the region where the relic density is reproduced. Higher luminosities and/or higher energies would be needed to be sensitive to such final states.

A very interesting feature of this scenario emerges for small values of g_D in the small region where the DM and t_D have a small mass gap: the decay width of t_D becomes significantly small, such that t_D becomes long-lived (its lifetime in the small mass gap region is shown in figure 3.8) and can be probed by dedicated searches at the LHC or future colliders. Different T or H masses would not modify this qualitative picture.

One should also note that the model predicts that the tth Yukawa coupling, y_t is always bigger than the SM one (see eq. 3.3). This happens due to the the presence of a non-zero y' coupling – the key point of the model, which provides the portal between the SM and dark sectors. The current direct constraints on y_t are quite weak (of the order of 50%) from $pp \to ttH$ production at the LHC. We have checked that

[3] The role of multipole contributions in DM DD has also been studied in [126]. In our study, however, we took into account also KM topologies and the interference between them.

imposing even 10% constraint on y_t, e.g., requiring $\delta y_t/y_t < 0.1$ does not qualitatively change our results. On the other hand, the y_t constraint will play a very important role at future e^+e^- colliders, which will measure y_t to within an accuracy of one percent. The importance of such a constraint as future colliders is the subject of a separate study.

As a general conclusion, the combination of cosmology and LHC bounds always favours the region with a small mass splitting between t_D and the DM. Other regions can be accessed depending on the value of other model parameters. This specific realisation of the model is in any case an example dictated by its simple features. Including mixing in the scalar sector, further VL partners or further interactions of the same VL representation would enlarge the possible signatures and change the complementarity between different observables in constraining the model, potentially opening up further new interesting signatures.

Chapter 4

Phenomenology of the muon portal and muon $g_\mu - 2$

The precise measurements of the muon anomalous magnetic moment, $a_\mu \equiv (g_\mu - 2)/2$, from Brookhaven National Laboratory (BNL) [171, 172, 173] and Fermilab National Accelerator Laboratory (FNAL) [174, 175, 176, 87] implies the departure from the Standard Model (SM) prediction. Thanks to a more stable beam and improved magnetic field at Fermilab, the systematic error is decreased by more than a factor of 2 [87]compared to its previous result [176] which leads to a smaller uncertainty in the combined result from BNL and FNAL measurements

$$a_\mu^{\mathrm{EXP}} = 116592059(22) \times 10^{-11}. \tag{4.1}$$

In the near future, this error is expected to be further improved by the upcoming Fermilab and J-PARC experiments based on a different measurement technique [177, 178]. On the theoretical side, however, the prediction of the SM [179, 180, 181, 182, 183, 184, 185, 186, 187, 188, 189, 190, 191, 192, 193, 194, 195, 196, 197] gives

$$a_\mu^{\mathrm{SM}} = 116591810(43) \times 10^{-11}. \tag{4.2}$$

It is a well-known fact that the contribution from the Leading Order Hadronic Vacuum Polarisation (LO-HVP) [90] is mainly responsible for the large uncertainty in the SM prediction which relies on the data-driven dispersion relation approach [186, 187, 198, 199] using data from the ratio of e^+e^- annihilation cross section into hadrons to a pair of muons. Despite, a different approach has been used to compute this contribution which relies on the lattice QCD simulation. The lattice simulation approach has been applied by several groups [92, 93, 94, 95, 96, 97]. In the past, the lattice QCD results were not reliable because of large uncertainty compared to the data-driven approach. However, the recent result by BMW group in 2020 [92] has considerably reduced this uncertainty. The result massively reduces a tension between the measurement and SM prediction to

1.5σ significance level. However, it is still unclear that this result is correct as it leads to the tension with electroweak global fits which changes the running of fine structure constant $\Delta\alpha^{(5)}_{\rm had}$ [98] and it has not yet been confirmed by other groups. Therefore, until the dust settles we will not consider the result from the lattice QCD but adopt the value from data-driven approach in this thesis. By comparing Eq.(4.1) and (4.2), it leads to

$$\Delta a_\mu^{\rm EXP} = a_\mu^{\rm EXP} - a_\mu^{\rm SM} = 249(48) \times 10^{-11}, \tag{4.3}$$

which implies the positive excess of experimentally averaged result over the SM prediction at the level of 5σ significance. The excess obviously manifests a need for physics beyond the Standard Model (BSM) to successfully accommodate the deviation. More precisely, we need new particles that interact with the SM muon and/or photon.

In addition to the $g_\mu - 2$ anomaly, the existence of DM is also a long-standing and compelling issue in particle physics since there is no suitable particle in the SM that can consistently explain its particle nature as a Cold Dark Matter (CDM). Recently, the dedicated observations of the Cosmic Microwave Backgroud (CMB) anisotropies by PLANCK measurement implies a large amount of DM about five greater than that of the baryonic matter [21]. In spite of that, for many years we have been searching for DM signal in terrestrial laboratories but it still evades our sight. Therefore, the hunting for DM might be one of the long and biggest quest for particle physicists and cosmologists nowadays.

The $g_\mu - 2$ anomaly and DM problem is a sensible motivation for us to seek for beyond the SM (BSM). Nowadays, there are several models purposed to simultaneously describe the these issues: the Scalar DM (SDM) models [200, 201, 202, 203, 204], the SDM with Vector-Like Leptons (VLLs) [205, 206, 207, 208, 209, 210], the Vector Dark Matter (VDM) with scalar portal [211, 212], the VDM with VLL portal [122].

In the previous chapter, we have thoroughly studied the scenario in which the VL fermion double is a VL top quarks in both cosmological and collider phenomenology. In this chapter, we study a possibility to explain the DM problem and muon anomalous magnetic moment at the same time with the MPVDM scenario. The theoretical framework of the MPVDM is still similar to our previous articles. The connection between SM and D sectors is established via the Yukawa interaction of SM and VL muons. In additional to the SM particles in the loop, a_μ receives contributions from new gauge bosons, scalars and fermions from MPVDM which we abbreviate as "New Physics" (NP) contribution. Therefore, the MPVDM has a potential to address the $g_\mu - 2$ and DM problems at the same time.

This chapter is organised as follows: In section 4.2, we display the relevant expressions for a_μ and present the parameter space that is allowed by the existing limits. In section 4.3, we consider the DM candidate for our model and the surviving parameter space

after application of a series of cosmological bounds (relic density, direct and indirect detections). In section 4.4, we discuss the collider limits from $pp \to \mu^+\mu^- + E_T^{miss}$ which is important to constrain the masses of VL muons. In addition, our model predicts unique and novel multi-lepton signature. Also, we study the interplay between the $(g-2)_\mu$, collider and DM limits that narrows down our parameter space to region where all aforementioned bounds are satisfied at the same time. Finally, we summarise our findings on the MPVDM scenario in section 5 and propose future outlooks.

4.1 The MPVDM model

In this thesis, we explore the potential of FPVDM to explain the DM observables and experimental excess of g-2 over the SM prediction [179]. The combined result from BNL and FNAL experiments indicates the 5σ discrepancy from the SM prediction $\Delta a_\mu^{\rm EXP} = 249(48) \times 10^{-11}$. In order to explain the Muon anomalous magnetic moment we need a D fermionic doublet which mixes wtih the SM muon and this D fermionic doublet can naturally be a doublet of VL muon $\Psi = (\mu_D, \mu')^T$. The mixing of SM and D muons is obviously given by the Yukawa term of y'. Therefore, the additional contributions to the $g_\mu - 2$ result from the NP diagrams including H_D , $V', V_D^{(*)}$ and μ_D, μ'. [1]

The most general Lagrangian for this scenario takes the following form

$$\begin{aligned}\mathcal{L} \supset & -\frac{1}{4}(V^i_{\mu\nu})^2|_{B,W^i,V^i_D} + \bar{f}^{\rm SM} i\not{D} f^{\rm SM} + \bar{\Psi} i\not{D}\Psi + |D_\mu \Phi_H|^2 + |D_\mu \Phi_D|^2 - V(\Phi_H, \Phi_D) \\ & - (y\bar{f}^{\rm SM}_L \Phi_H f^{\rm SM}_R + y'\bar{\Psi}_L \Phi_D f^{\rm SM}_R + h.c) - M_{\mu_D}\bar{\Psi}\Psi \ , \end{aligned} \tag{4.4}$$

where $V(\Phi_H, \Phi_D)$ is the scalar potential and is given by

$$\begin{aligned} V(\Phi_H, \Phi_D) = & -\mu^2 \Phi_H^\dagger \Phi_H - \mu_D^2 \Phi_D^\dagger \Phi_D + \lambda (\Phi_H^\dagger \Phi_H)^2 + \lambda_D (\Phi_D^\dagger \Phi_D)^2 \\ & + \lambda_{HD} (\Phi_H^\dagger \Phi_H)(\Phi_D^\dagger \Phi_D) \ . \end{aligned} \tag{4.5}$$

The quartic term of Φ_H and Φ_D (the Higgs portal) mixes and will play an vital role in studying the phase transition and gravitational waves. However, we are considering a mininal scenario in which the quartic coupling λ_{HD} is negligibly small.

4.1.1 MPVDM parameter space

Even though there are a number of parameters in the Lagrangian but those are fixed by the experimental results. In general, the model contains free six parameters.

$$g_D, m_{V_D}, m_{H_D}, m_{\mu'}, m_{\mu_D}, \sin\theta_S \ . \tag{4.6}$$

[1] In this chapter, we change a notation to label scalars. The SM Higgs and new scalar are presented by H and H_D, respectively.

However, in this thesis we would like to consider the effect of the fermionic portal to dark sector without scalar portal at tree level which mean that $\sin\theta_S = 0$. Therefore, the dependent parameters can be written in terms of input parameters as follows

$$v = \frac{2m_W}{g}, \quad v_D = \frac{2m_{V_D}}{g_D}\,, \tag{4.7}$$

$$\lambda = \frac{g^2 m_H^2}{8m_W^2}\,, \lambda_D = \frac{g_D^2 m_{H_D}^2}{8m_{V_D}^2}\,, \lambda_{HD} = 0\,, \tag{4.8}$$

$$\mu^2 = \frac{m_H^2}{2}\,, \mu_D^2 = \frac{m_{H_D}^2}{2}, \tag{4.9}$$

$$y = \frac{g\, m_\mu}{\sqrt{2} m_W}\frac{m_{\mu'}}{m_{\mu_D}}\,, y' = \frac{g_D\sqrt{(m_{\mu'}^2 - m_{\mu_D}^2)(m_{\mu_D}^2 - m_\mu^2)}}{\sqrt{2} m_{\mu_D} m_{V_D}}\,. \tag{4.10}$$

4.2 The analytical and numerical results

As we have mentioned at the beginning of the introduction that the averagedly combined experimental measure of the anomalous magnetic moment of the muon, $a_\mu \equiv (g_\mu - 2)/2$, from BNL and FNAL leads to $a_\mu^{\rm EXP} = 116592059(22) \times 10^{-11}$. However, the prediction of this quantity within the framework of SM gives $a_\mu^{\rm SM} = 116591810(43) \times 10^{-11}$ provided by the Muon g-2 Theory Initiative in 2020 [179]. In general, the SM prediction can be divided into 3 catergories: 1) the pure QED contribution $a_\mu^{\rm QED} = 116\,584\,718.93(0.10) \times 10^{-11}$, 2) the Electro-Weak (EW) contribution $a_\mu^{\rm EW} = 153.6(1.0) \times 10^{-11}$ and 3) the Hadronic Vacuumn Polarisation (HVP) contribution $a_\mu^{\rm Had} = 6\,931(40) \times 10^{-11}$ [2] . The theoretical uncertainties from the QED and EW sectors are negligibly small. The most difficult part is the hadronic one which is responsible for the large contribution in uncertainty of the SM prediction. The discrepancy between experimental results and SM prediction leads to $\Delta a_\mu^{\rm EXP} = a_\mu^{\rm EXP} - a_\mu^{\rm SM} = 249(48) \times 10^{-11}$ which indicates the 5.2σ deviation from the SM prediction.

This experimental excess over the theoretical prediction could be explained by the MPVDM framework. As we mentioned before that the model does not require the Higgs portol to connect to dark sector. Therefore, we will not consider diagrams with scalar mixing ($\sin\theta_S = 0$) in this thesis. In the next section, we present the complete analytical results of $g_\mu - 2$ for our model.

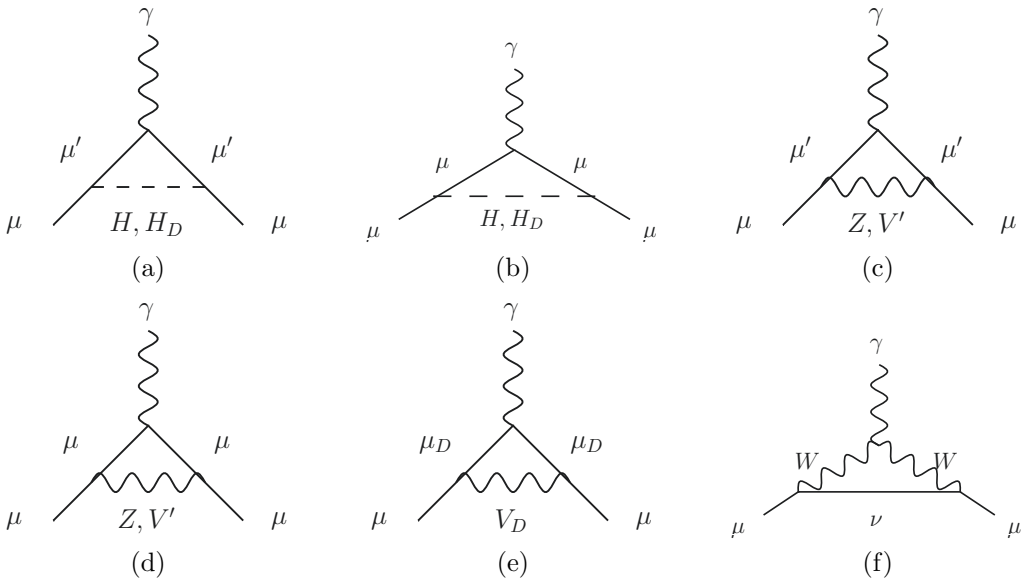

FIGURE 4.1: A set of diagrams contributing to the a_μ in addition to the pure SM ones. The pure QED and hadronic diagrams are not represented here.

4.2.1 Analytical results

It has been shown in [88] that analytical expressions for a_μ for generic diagrams and internal particles are gauge-independent and divergent free. In order to ensure that the results in [88] are reliable, we have also calculated the contributions to the a_μ with generic couplings and mediators in the limit of $R_\xi \to 0$ (in the Unitary gauge) and cross-validated with their results. We found that our results on a_μ agree with theirs. The detail of our calculations can be found in Appendix F. Moreover, our results have been crossed validated against the pre-existing in [88, 213, 214]. Indeed, the one-loop results could be extensively complicated and highly unstable. The instability in loop functions originates from the fact that the mass of muon is much smaller than that of other particles which means that we cannot naively use the results. Fortunately, the instability can be coped with the approximation formulae which give us the more simplified and compact expressions. The loop diagrams from MPVDM at the leading order are depicted in figure 4.1. Note that we do not present the pure QED and HVP diagrams here since they are similar to the SM scenario at the leading order. In the following sections, we discuss the analytical results from diagrams with scalar, vector with Neutral Current (NC) and Charged Current (CC), respectively.

[2]We use the result due to a data-driven dispersion relation approach. However, there are several groups evaluating the HVP contribution using the lattice QCD approach. The recent result from the BMW collaboration [92] is $a_\mu^{\rm BWM} = 7075(55) \times 10^{-11}$. The difference between two approaches might be explained by new physics contributions

4.2.1.1 The scalar diagram

As aforementioned, the instability in loop functions happens if the mass of muon is much smaller than that of other particles. Therefore, in order to get a reliable result we expand the scalar contribution in the limit of $m_\mu \ll m_f$ where m_μ and m_f are the mass of muon and VL muons, respectively. After doing expansion and keeping only the leading order, the analytical result for figure 4.1 (a) reads

$$a_\mu^S = \frac{(C_S^2 - C_P^2)}{16\pi^2} \frac{m_\mu m_f}{(m_f^2 - m_s^2)^3} \left(m_f^4 - 4m_f^2 m_s^2 + 3m_s^4 - 2m_s^4 \log\left(\frac{m_s^2}{m_f^2}\right)\right) + \mathcal{O}\left(\frac{m_\mu^2}{m_f^2}\right), \tag{4.11}$$

where m_s is the mass of scalar fields. The C_S and C_P are the scalar and pseudo-scalar components of a generic coupling of a scalar-fermion-fermion vertex, respectively. The full analytical expression in terms of integral for scalar case is given by Eq.(F.4). In addition, in the regime that $m_s \ll m_f$ and $m_\mu \ll m_f$, the result for figure 4.1 (a) is much more simplified to

$$a_\mu^S = \frac{(C_S^2 - C_P^2)}{16\pi^2} \frac{m_\mu}{m_f} + \mathcal{O}\left(\frac{m_\mu^2}{m_f^2}\right) + \mathcal{O}\left(\frac{m_s^2}{m_f^2}\right) \tag{4.12}$$

Note these results are evaluated at the leading orders of the expansion. Of course, the higher order results are much more complicated.

In the case of the internal fermions are SM muons and $m_\mu \ll m_s$, the result reads

$$a_\mu^S = \frac{m_\mu^2}{48\pi^2 m_s^2} \left((11C_P^2 - 7C_S^2) + (C_S^2 - C_P^2) 6 \log\left(\frac{m_s^2}{m_\mu^2}\right)\right) + \mathcal{O}\left(\frac{m_\mu^4}{m_s^4}\right) \tag{4.13}$$

In our framework after substituting the C_S and C_P couplings (see table E.1 and E.2), the NP contributions from H_D propagating diagrams in figure 4.1(a) and (b) can be reduced to

$$a_\mu^{(a),H} \approx \frac{g_W^2}{64\pi^2} \frac{m_\mu^2}{m_W^2} \frac{\Delta M^2}{M_{\mu'}^2} \frac{m_\mu^2}{(m_{\mu'}^2 - m_H^2)^3} \left[3m_H^4 - 4m_H^2 m_{\mu'}^2 + m_{\mu'}^4 + 4m_H^4 \log\frac{m_{\mu'}}{m_H}\right] \tag{4.14}$$

$$a_\mu^{(a),H_D} \approx \frac{g_D^2}{96\pi^2} \frac{m_\mu^2}{m_{V_D}^2} \left[\frac{1}{4} \frac{\Delta M^2}{m_{\mu'}^2} \left(-1 + \frac{7\Delta M^2}{m_{\mu'}^2}\right)\right] \tag{4.15}$$

$$a_\mu^{(b),H_D} \approx \frac{g_D^2}{96\pi^2} \frac{m_\mu^2}{m_{V_D}^2} \left[\frac{1}{2} \frac{m_\mu^2}{m_{H_D}^2} \frac{\Delta M^4}{m_{\mu'}^4} \left(-7 + 12 \log\frac{m_{H_D}}{m_\mu}\right)\right], \tag{4.16}$$

respectively, where $\Delta M^2 = m_{\mu'}^2 - m_{\mu_D}^2$. One can see that the $a_\mu^{(a),H}$ contribution is very suppressed because of m_μ^2/m_W^2 and $\Delta M^2/m_{\mu'}^2$. The $a_\mu^{(a),H_D}$ and $a_\mu^{(b),H_D}$ contribution

obviously depends on three quantities: 1) the squared coupling constant g_D^2, 2) the square of the ratio of muon's mass to DM's mass $(m_\mu/m_{V_D})^2$ and 3) the mass squared difference between two VL muons over $m_{\mu'}^2$. This fact is also true for the contributions from NC and CC diagrams as we will see later. More specifically, one can clearly see that Eq.(4.15) can give a positive contribution if $(m_{\mu'}/m_{\mu_D})^2 > 7/6$ and it is negative if $1 < (m_{\mu'}/m_{\mu_D})^2 < 7/6$. Eq.(4.16) is positive and negative if $m_{H_D} > m_\mu$ and $m_{H_D} < m_\mu$, respectively. The contributions involving the SM-Higgs can be neglected due to the suppression in the mixing of SM and D fermions.

4.2.1.2 The NC diagram

The contributions from the vector propagating diagrams can be divided into 2 groups: 1) the diagrams with NC and 2) the diagrams with CC. Starting with a contribution from NC diagram, the result for figure 4.1 (c)-(e) at the leading order of the expansion in the limit of $m_\mu \ll m_f$ is given by

$$a_\mu^{\rm NC} = \frac{(C_V^2 - C_A^2)}{16\pi^2} \frac{m_\mu m_f}{m_v^2(m_f^2 - m_v^2)^3} \left(m_f^6 + 3m_f^2 m_v^4 - 4m_v^6 + 6m_f^2 m_v^4 \log\left(\frac{m_v^2}{m_f^2}\right)\right) + \mathcal{O}\left(\frac{m_\mu^2}{m_f^2}\right), \tag{4.17}$$

where the C_V and C_A are a vector and axial-vector couplings of a vector-fermion-fermion vertex. The full analytical integral for NC case is given by Eq.(F.59). Here the m_f is the masses of VL muons (μ_D, μ') and m_v is the masses of neutral gauge bosons (Z, V', V_D). When $m_\mu \ll m_f$ and $m_v \ll m_f$, the analytical expression reads

$$a_\mu^{\rm NC} = \frac{(C_V^2 - C_A^2)}{16\pi^2} \frac{m_\mu(m_f^2 + 3m_v^2)}{m_f m_v^2} + \mathcal{O}\left(\frac{m_\mu^2}{m_f^2}\right) + \mathcal{O}\left(\frac{m_v^2}{m_f^2}\right). \tag{4.18}$$

When the internal fermions are SM muons and if $m_\mu \ll m_v$, the contribution from NC diagram reads

$$a_\mu^{\rm NC} = \frac{(C_V^2 - 5C_A^2)}{12\pi^2} \frac{m_\mu^2}{m_v^2} + \mathcal{O}\left(\frac{m_\mu^4}{m_v^4}\right), \tag{4.19}$$

This result is consistent with the Eq. (2.5) in [215] and we have checked that it can reproduced the SM prediction found in [13].

Substituting the relevant couplings from tabletable E.1 and E.2, the NP contributions of new gauge bosons propagating diagrams from figure 4.1(c), (d) and (e) reads

$$a_\mu^{(c),V'} \approx \frac{g_D^2}{96\pi^2}\frac{m_\mu^2}{m_{V_D}^2}\left[\frac{1}{4}\frac{\Delta M^2}{m_{\mu'}^2}\left(1+\frac{5\Delta M^2}{m_{\mu'}^2}\right)\right], \tag{4.20}$$

$$a_\mu^{(d),V'} \approx \frac{g_D^2}{96\pi^2}\frac{m_\mu^2}{m_{V_D}^2}\left[-2\frac{\Delta M^4}{m_{\mu'}^4}\right], \tag{4.21}$$

$$a_\mu^{(e),V_D} \approx \frac{g_D^2}{96\pi^2}\frac{m_\mu^2}{m_{V_D}^2}\left[\frac{1}{2}\frac{\Delta M^2}{m_{\mu'}^2}\right], \tag{4.22}$$

respectively. One can clearly see the key features of these results are still similar to what we have commented for the scalar contribution. The NP contributions from figure 4.1(c), (d) and (e) give the positive, negative and positive results, respectively.

4.2.1.3 The charged current diagram

The last contribution is originated from the CC diagrams which the result we present here is from the full integral in Eq.(F.73). Expanding in the limit of $m_\mu \ll m_v$, the expression for figure 4.1 (f) is given by

$$a_\mu^{\rm CC} = \frac{5(C_V^2+C_A^2)}{24\pi^2}\frac{m_\mu^2}{m_v^2} + \mathcal{O}\left(\frac{m_\mu^4}{m_v^4}\right) \tag{4.23}$$

where $m_v = m_W$. This result is used for the figure 4.1(f) and is always positive. After substituting the C_V and C_A according to table E.1 and E.2, we numerically found that the result is equal to that of the pure SM. Notice that this result has been computed under the assumption that mass of internal fermion is zero which is consistent to the SM and the MPVDM cases in which the neutrinos are massless. The more general result can be found in [88], Eq.(4). The extensive detail for one-loop contributions to g-2 from S, NC and CC digrams are given in the Appendx F. The validation of Eq.(4.19) and (4.23) can be done by considering the SM results from the Z and W boson diagrams and we found that they provide the consistent results with Eq.(14) and (15) in [216].

As we see above, the contributions from all NP diagrams can give both positive and negative results. In order to explain the experimental results we need the total positive contribution. The MPVDM model has a potential to accommodate the $\Delta a_\mu^{\rm EXP}$ discrepany through new contributions from VL muons (μ_D and μ'), a dark scalar (H_D) and two new gauge bosons (V_D and V'). In order to explain this discrepancy, we define the NP contributions as the difference between MPVDM and SM ones as follows

$$\Delta a_\mu^{\rm NP} = a_\mu^{\rm MPVDM} - a_\mu^{\rm SM} \tag{4.24}$$

where $a_\mu^{\rm MPVDM}$ is the contributions according to the diagrams (a-f) in figure 4.1 and $a_\mu^{\rm SM}$ is merely the contributions from diagrams a, c and f with pure SM particles and

couplings combining the pure QED, EW and Had contribution as mentioned in the begining of section 4.2. Thus, the $\Delta a_\mu^{\rm NP}$ give purely NP contributions.

4.2.2 The $g_\mu - 2$ results

In order to understand a comprehensive picture of the full 5-Dimensional (5D) parameter space of $\{g_D, m_{V_D}, m_{\mu_D}, m_{\mu'}, m_{H_D}\}$, we have scanned over the 5D parameter space with the following ranges

$$\begin{aligned} 10^{-4} &\leq g_D \leq 4\pi, \\ 0.01 &\leq m_{V_D}/\text{GeV} \leq 10000, \\ 100 &\leq m_{\mu_D}/\text{GeV} \leq 10000, \\ 100 &\leq m_{\mu'}/\text{GeV} \leq 10000, \\ 0.01 &\leq m_{H_D}/\text{GeV} \leq 10000. \end{aligned} \tag{4.25}$$

The upper limit on the coupling is chosen according to the perturbativity condition while the lower one should not be too small because it will not be relevant to the collider search for new signature (see the discussion of the multi-leptons signatures in section 4.4). The maximum values of the masses are limited at 10^4 GeV whilst the minimum values of masses are set at 10 MeV. The lower limit on the VL muons was set based on the obvious limit from LEP experiment which has searched for exotic unstable neutral and charged heavy leptons at the L3 detector. We use the results in 2000 which corresponds to the centre of mass energy 200-208 GeV with a total integrated luminosity 450 pb^{-1}. The heavy charged leptons $L^\pm$ are pair-produced through the Dell-Yan processes $e^+\, e^- \to \gamma,\ Z \to L^+\, L^-$ then they can decay into a pair of neutrinos with W bosons $L^\pm \to \nu_\ell\, W^\pm$ or a pair of SM charged leptons with Z bosons $L^\pm \to \ell^\pm\, Z$. The bovious lower limit on $L^\pm$ is placed around 100 GeV [217]. For the actual limits on masses of VL muons, we derive in section 4.4.1 by using the data on $\mu^+\mu^- + E_T^{\rm miss}$ from LHC.

In the 5D scan, we have collected only data that satisfies the perturbativity constraints which is defined as follows

$$\lambda_H \leq 4\pi, \quad \lambda_D \leq 4\pi, \quad y \leq 4\pi, \quad y' \leq 4\pi, \quad \frac{m_{V_D} - m_{V'}}{m_{V_D}} < 0.5, \tag{4.26}$$

where m_{V_D} and $m_{V'}$ are the renormalised masses at one loop for V_D and V', respectively.

In order to visualise the region of good a_μ within experimental limits, we have defined the $\Delta\hat{a}_\mu$ which describes the deviation of the NP contributions $\Delta a_\mu^{\rm NP}$ from the $\Delta a_\mu^{\rm EXP}$

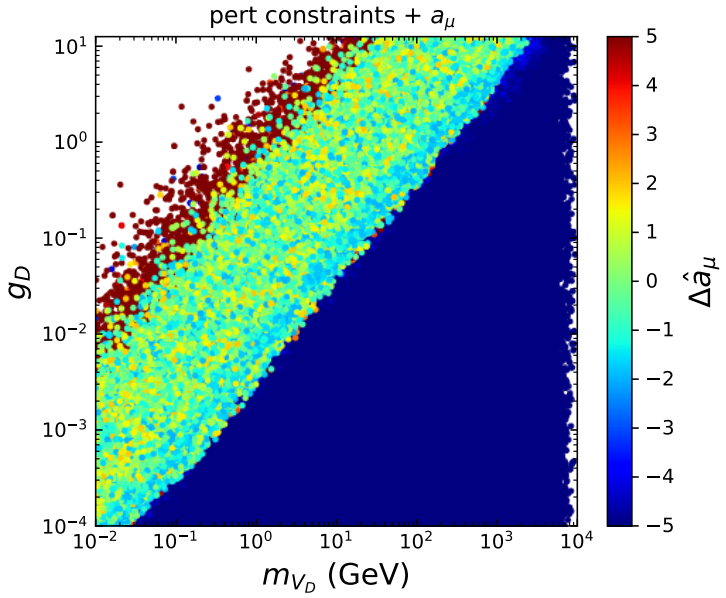

FIGURE 4.2: The colour bar plot of $\Delta\hat{a}_\mu$ from 5D scan projected on the (g_D, m_{V_D}) plane. The perturbativity constraints Eq.(4.26) is imposed on the plot. The varying spectrum illustrates the deviation of the $\Delta a_\mu^{\rm NP}$ from $\Delta a_\mu^{\rm EXP}$. The spectrum ranges from dark blue to dark red which corresponds to $-5.0\sigma \leq \Delta\hat{a}_\mu \leq 5.0\sigma$. The region with $a_\mu \pm 2\sigma$ is highlighted by a spectrum from light blue to bright orange which corresponds to $-2\sigma \leq \Delta\hat{a}_\mu \leq 2\sigma$.

as follows

$$\Delta\hat{a}_\mu = \frac{(\Delta a_\mu^{\rm NP} - \Delta a_\mu^{\rm EXP})}{\sigma} \tag{4.27}$$

where $\Delta a_\mu^{\rm EXP}$ is given by Eq.(4.3) and $\Delta a_\mu^{\rm NP}$ by Eq.(4.24), and $\sigma = 48 \times 10^{-11}$ from the recent averaged value [87].

The figure 4.2 represents the projection of 5D data onto the (g_D, m_{V_D}) plane. The colour bar on the right of the plot shows the varying colour sprectrum from dark blue to dark red for $-5.0 \leq \Delta\hat{a}_\mu \leq 5.0$. The points with a_μ within 95% C.L. or $\pm 2\sigma$ are highlighted with the spectrum from ligth blue to bright orange. The white region is excluded by the perturbativity constraint Eq.(4.26). As we have mentioned in the analytical results sector that the a_μ is proportional to the squared coupling g_D^2 and inversely proportional to the squared mass of DM $m_{V_D}^2$. From figure 4.2, it is obvious that the greater g_D the bigger a_μ while it is smaller if the DM mass gets heavier. As we have seen from Eqs.(4.15), (4.16), (4.20), (4.21), (4.22), when the ratio $\Delta M^2/m_{\mu'}^2$ is small , the contributions from the diagram (a), (c) and (e) are dominant. However, if the ratio $\Delta M^2/m_{\mu'}^2$ is large , the contributions from the diagram (b) and (d) are dominant. The contributions from other diagrams are highly suppressed by the mixing between SM and VL muons, especially for the diagram involving SM Higgs, Z and W bosons. Even

if SM and VL muon mix, the SM-like contributions are very slightly changed compared to the SM prediction.

In order see clearly in which region we can reproduce the experimental result of $g_\mu - 2$, we present the 1 dimensional plots of $(m_{V_D}, \Delta a_\mu^{\rm NP})$ in figure 4.3. In each panel, the mass of DM varies from 0.01-100 GeV. The dotted, solid and dashed blue lines correspond to the $\Delta a_\mu^{\rm NP} = \Delta a_\mu^{\rm EXP} - 2\sigma$, $\Delta a_\mu^{\rm NP} = \Delta a_\mu^{\rm EXP}$ and $\Delta a_\mu^{\rm NP} = \Delta a_\mu^{\rm EXP} + 2\sigma$, respectively. In figure 4.3 (a), we fix $m_{\mu_D} = 800$ GeV, $m_{\mu'} = 850$ GeV and $m_{H_D} = 0.5$ GeV and vary $g_D \in \{0.001, 0.0025, 0.005\}$ which are labeled by the solid red, green and orange lines, respectively. One can see that the points where the blue line intersects with the red, green and orange ones can reproduce the experimentally measured value of $g_\mu - 2$ and correspond to $m_{V_D} \in \{0.0475, 0.119, 0.236\}$ GeV. If g_D is large we also need large m_{V_D} to balance the $g_D^2/m_{V_D}^2$. However, the a_μ is not sensitive to m_{H_D} as one can in figure 4.3 (b). The curves slightly changes with respect to m_{H_D} even though we vary $m_{H_D} \in \{0.01, 0.1, 1\}$ GeV. This is because, at the leading order of expansion, amongst the NP contributions the scalar contributions are less relevant compared to the NC and CC contribution. Numerically, it contributes at most only a few percent to the $\Delta a_\mu^{\rm NP}$. In figure 4.3 (c), it is obvious that a_μ is proportional to $\Delta M^2/m_{\mu'}^2$. To get the measured value of $g_\mu - 2a$, if $\Delta M^2/m_{\mu'}^2$ is large the large m_{V_D} is needed to compensate.

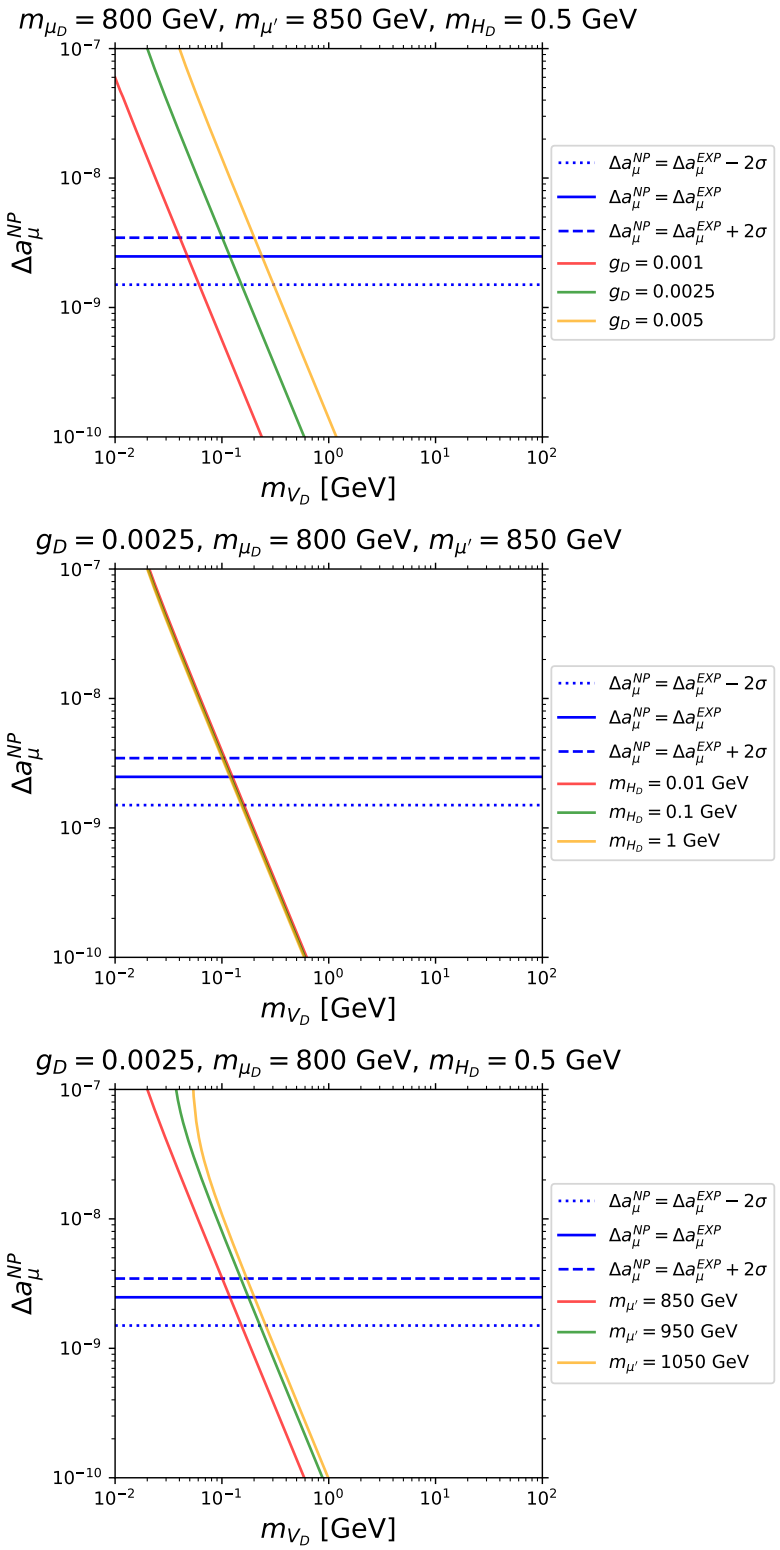

FIGURE 4.3: The 1 dimensional plots of $(m_{V_D}, \Delta a_\mu)$. In each panel, the mass of DM is varied from 0.01-100 GeV. The dotted, solid and dashed blue lines correspond to the $\Delta a_\mu^{\rm NP} = \Delta a_\mu^{\rm EXP} - 2\sigma$, $\Delta a_\mu^{\rm NP} = \Delta a_\mu^{\rm EXP}$ and $\Delta a_\mu^{\rm NP} = \Delta a_\mu^{\rm EXP} + 2\sigma$, respectively.

4.3 Cosmological probes of MPVFM model

4.3.1 The cosmological limits

We have already discussed the cosmological bounds in section 3.1.1. Here we only present the result for MPVDM scenario after applying those constraints.

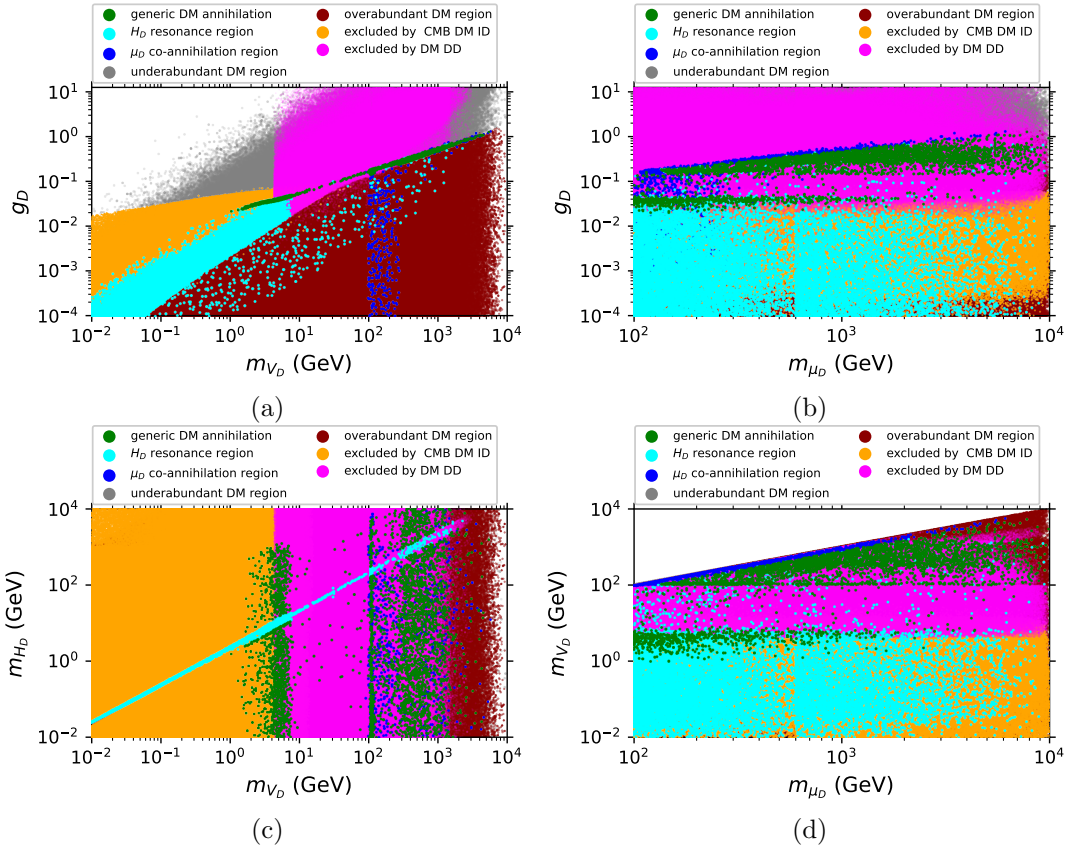

FIGURE 4.4: The data from 5D scan projecting on various scatter plots: a) (m_{V_D}, g_D), b) (m_{μ_D}, g_D), c) (m_{V_D}, m_{H_D}) and d) (m_{μ_D}, m_{V_D}) planes, respectively. The perturbativity and cosmological constraints have been applied on each individual panel. The cosmological limits contain 1) the DM relic density, 2) the DM DD and 3) the DM ID. The allowed region are coloured by green, cyan, blue and grey while the excluded ones are highlighted by dark red, orange and magneta. The white region corresponds to the perturbativity exclusion region.

In figure 4.4, the allowed regions are coloured by green, cyan, blue and grey while the excluded ones are labeled by dark red, orange and magenta. The green, cyan and blue regions are allowed by perturbativity constraint, DD and ID, and they have the relic density $\Omega_{DM}^{\text{Planck}} h^2 \pm 0.012$. The grey region also satisfies the same constraints as green, cyan and blue ones but has the under-abundant relic density. On the other hand, the dark red, orange and magenta regions are not allowed by the relic density, CMB ID and DD limits, respectively. More precisely, the green region as labelled by *generic DM annihilation* appears as a small diagonal strip in figure 4.4(a) where the dominant annihilation channels are $V_D\ V_D^* \to V'\ V'$. However, the generic DM annihilation

processes are not effective and is excluded by DM ID constraint in a region of small DM mass below 1 GeV and small coupling g_D below 0.02. One can see that the green strip is not uniform over a range $1 < m_{V_D}/\text{GeV} < 10000$, especially in the region with $10 < m_{V_D}/\text{GeV} < 100$ in which the DM DD constraint becomes relatively stronger. The regions above(below) the green one corresponds to the region with under(over) relic abundance which they are labelled in grey and dark red. The cyan region is identified by the H_D *resonance region* where the main annihilation channel is $V_D\, V_D^* \to H_D \to V'\, V'$. This can happen when the DM mass gets close to a half of m_{H_D}. One can clearly see a region of the resonance as a diagonal cyan strip of figure 4.4(c). Finally, the blue region corresponds to the μ_D *co-annihilation region* and this happens when the DM mass gets close to m_{μ_D} as in figure 4.4(b) and (d) panels. The co-annihilation process becomes visible on the parameter space when the DM mass goes to 100 GeV (the lower limit of VLM from LEP). For small coupling $g_D < 0.1$, the co-annihilation region is effectively produced by a process of $\mu_D, \mu_D \to q\bar{q}, \ell^+\ell^-, \nu\bar{\nu}$ via photon and Z exchange which does not depend on the coupling g_D and happens in region of $100 < m_{V_D}/\text{GeV} < 300$. When the coupling g_D becomes larger, the dominant process shifts to $V_D\mu_D \to \gamma\mu, \gamma\mu'$ via μ, μ' exchange.

4.3.2 The combined bounds: cosmological and a_μ limits

In previous sections, we have discussed the cosmological and a_μ constraints seperately. In this section, we try to combine these bounds together and find a allowed region where it satisfies the cosmological and a_μ bounds simultaneously.

In figure 4.5 and 4.6, the grey region is allowed by the perturbativity constraint. The green(cyan) region is allowed by the DM DD, ID and has the correct(underabundant) relic density. The dark red labels a region with a_μ within 2σ from the averaged value Eq.(4.1). The starred magenta and orange indicate a region allowed by $a_\mu \pm 2\sigma$, DM DD, ID with the relic density $\Omega_{DM}^{\text{Planck}}h^2$ and $15\%\Omega_{DM}^{\text{Planck}}h^2$, respectively. The white region in the figure 4.5 (a) panel violates the perturbativity constraint while the white region in figure 4.6 (b), (c) and (d) panels is excluded by the mass hierarchy condition $m_{V_D} < m_{\mu_D} < m_{\mu'}$.

In figure 4.5 (a) the (m_{V_D}, g_D) panel, one can clearly see that the dark red and green bands have different slopes. They intersect in a region of $10^{-4} < g_D < 10^{-1}$ and $0.01 < m_{V_D}/\text{GeV} < 10$. However, the CMB ID constraint becomes strong and enormously excludes a region of $1 < m_{V_D}/\text{GeV} < 10$ and $0.01 < g_D < 0.1$. At the largest coupling $g_D = 4\pi$, the $(g_\mu - 2)/2$ is below $\Delta a_\mu^{\text{EXP}} - 2\sigma$ in a region with $m_{V_D} > 2000$, $m_{\mu_D} > 3000$, $m_{\mu'} > 4000$ and $m_{H_D} > 2000$ GeV as one can see clearly from figure 4.5 (a), (b), (c) and (d) panels, respectively. A region which is allowed by cosmological and $g_\mu - 2$ limits corresponds to the H_D resonance region and it appears as a diagonal strip in figure 4.6 (a).

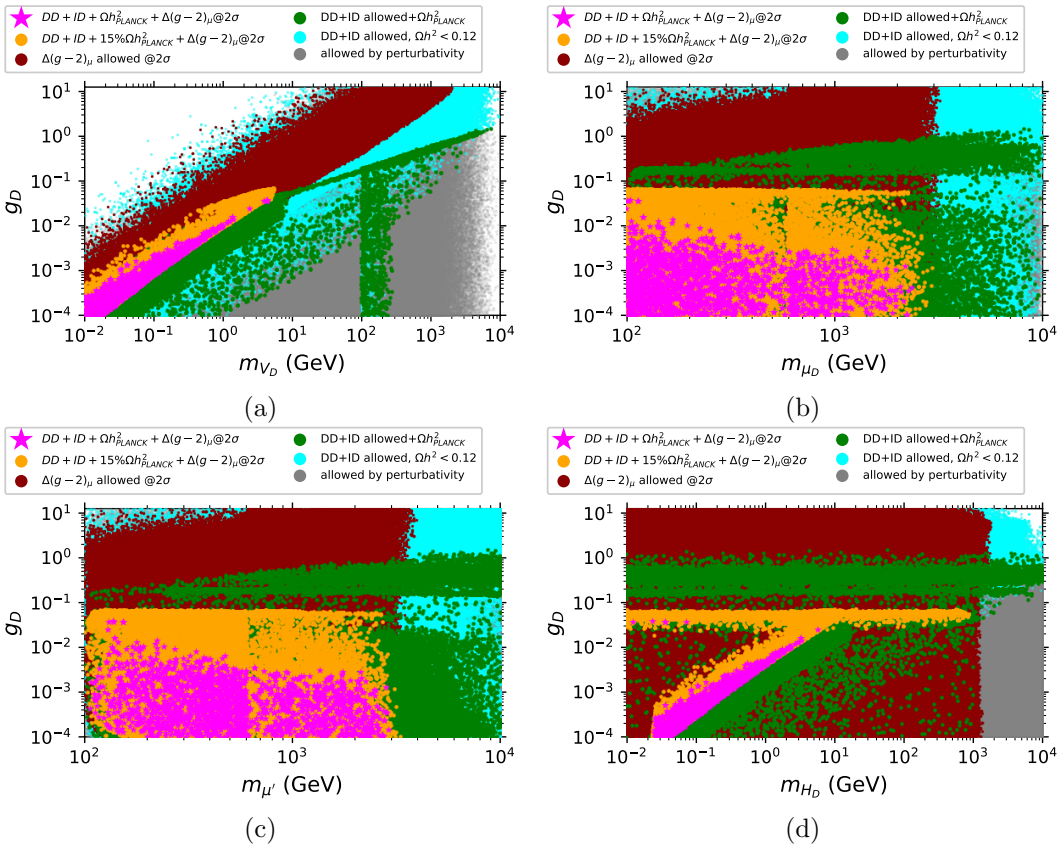

FIGURE 4.5: The scatter plots from 5D data projected on various planes: (m_{V_D}, g_D), (m_{μ_D}, g_D), $(m_{\mu'}, g_D)$ and (m_{H_D}, m_{μ_D}), respectively. The combined constraints on perturbativity (Eq.(4.26)), cosmology, VLM masses and a_μ have been applied on each plot. The VLM search has put a lower limits on m_{μ_D} and $m_{\mu'}$ around 600 GeV from LHC data. The constraint on $(g_\mu - 2)/2$ is within 2σ.

In figure 4.7, we consider the 2D plots of (m_{V_D}, g_D) plane with $m_{\mu_D} = 650, 700, 750$ GeV, $m_{\mu'} = 800$ GeV, $m_{H_D} = 0.5$ GeV. In figure 4.8, we change $m_{\mu_D} = 700, 800, 900$ GeV and $m_{\mu'} = 1000$ GeV while keep $m_{H_D} = 0.5$ GeV. In those plots, the red, orange and magenta regions are excluded by the DM relic density, DM ID and perturbativity constraints, respectively. The solid red line corresponds to the PLANCK relic density $\Omega_{\rm DM}h^2 = 0.12$. The solid orange one means the $P_{\rm ann} = 3.2 \times 10^{-28}$ cm^{3}s^{-1} GeV^{-1}. The dashed, solid and dotted blue lines indicate the curves with $\Delta\hat{a}_\mu = -2\sigma$, $\Delta\hat{a}_\mu = 0$ and $\Delta\hat{a}_\mu = +2\sigma$, respectively. In parameter space we present in figure 4.7 and 4.8, the DM DD limit is not relevant as the DM mass and coupling g_D are too small. The allowed region by cosmological and $g_\mu - 2$ limits resides in the white region, and only between dashed and dotted blue lines. In figure 4.7 (a), the allowed region has $0.21 < m_{V_D} < 0.24$ GeV and $0.002 < g_D < 0.004$. As one can see that the a_μ increases depending on the larger coupling g_D. However, it decreases as DM mass increases. If the mass splitting of VL muons decreases the slope of the blue lines increases to get the a_μ with 2σ as one can see from the figure 4.7 (b) and (c). In figure 4.8, the allowed region by cosmological and $g_\mu - 2$ resides between $0.0015 < g_D < 0.0035$ with the same range of m_{V_D} as in

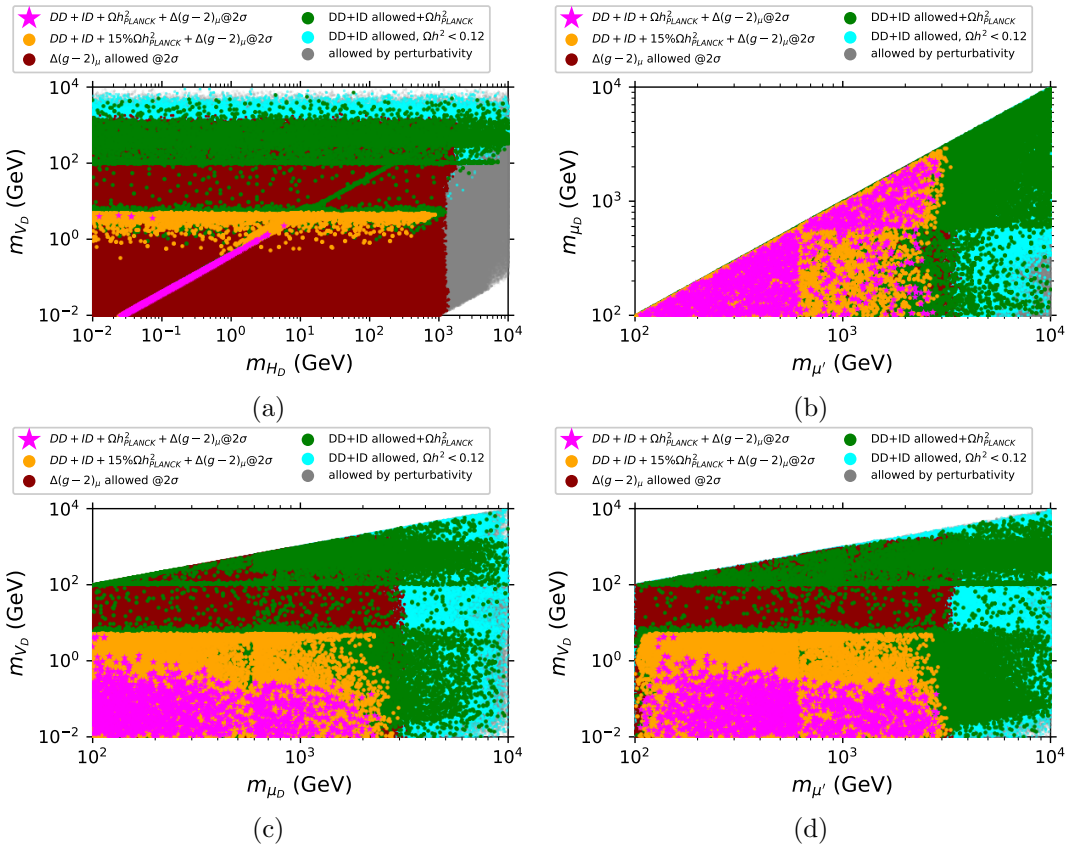

FIGURE 4.6: (Cont.) The scatter plots from 5D data projected on various planes: (m_{H_D}, m_{V_D}), $(m_{\mu'}, m_{\mu_D})$, $(m_{\mu'}, m_{V_D})$ and $(m_{\mu'}, m_{V_D})$, respectively. The combined constraints on perturbativity (Eq.(4.26)), cosmology, VLM masses and a_μ have been applied on each plot. The VLM search has put a lower limits on m_{μ_D} and $m_{\mu'}$ around 600 GeV from LHC data. The constraint on $(g_\mu - 2)/2$ is within 2σ.

figure 4.7 because m_{H_D} does not change. However, the allowed range of g_D is slightly smaller compared to those in figure 4.7 because of large mass splitting of VL masses.

Another 2D plane can be found in figure 4.9. We present the 2D plots on (m_{μ_D}, m_{V_D}) plane with $g_D = 0.001, 0.0025, 0.005, 0.0075$, $m_{\mu'} = 1000$ GeV and $m_{H_D} = 0.5$ GeV. According to the combined limits from cosmology and $g_\mu - 2$, one can see that the allowed region appears only in figure 4.9 (b) where $g_\mu = 0.0025$, $0.21 < m_{V_D} < 0.24$ GeV and $750 < m_{\mu_D} < 800$ GeV.

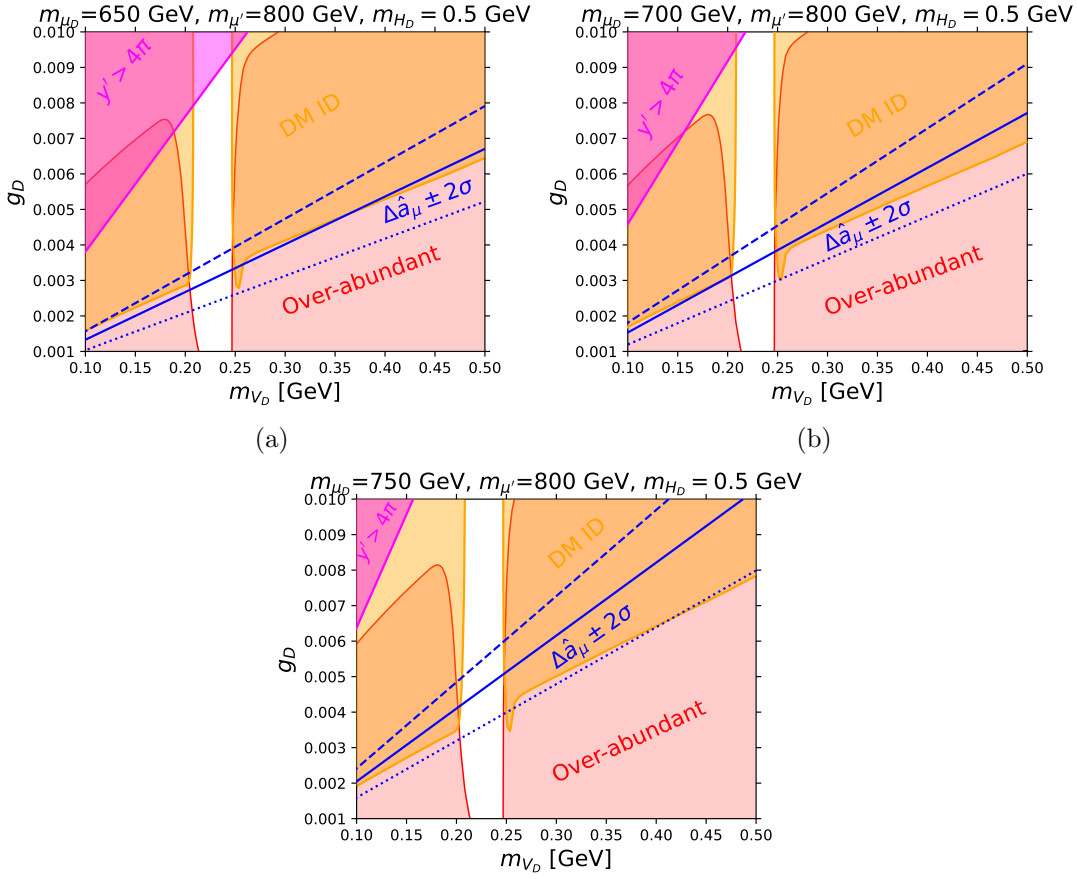

FIGURE 4.7: The 2D parameter space of (m_{V_D}, g_D) plane with $m_{\mu_D} = 650, 700, 750$ GeV, $m_{\mu'} = 800$ GeV and $m_{H_D} = 0.5$ GeV. The magenta, orange and red regions are excluded by the perturbativity, DM ID and relic density constraints, respectively. The solid red line corresponds to the relic density $\Omega_{\rm DM}h^2 = 0.12$. The solid orange line indicates the $P_{\rm ann} = 3.2 \times 10^{-28}$ cm^{3}s^{-1} GeV^{-1}. The dotted, solid and dashed blue lines represent the $\Delta\hat{a}_\mu = -2\sigma$, $\Delta\hat{a}_\mu = 0$ and $\Delta\hat{a}_\mu = 2\sigma$, respectively.

Inputs/Observables	BP1	BP2	BP3
g_D	0.0025	0.0025	0.0025
m_{V_D} [GeV]	0.206	0.206	0.206
m_{μ_D} [GeV]	650	740	850
$m_{\mu'}$ [GeV]	800	1000	1000
m_{H_D} [GeV]	0.5	0.5	0.5
$(g_\mu - 2)/2$	2.04×10^{-9}	2.461×10^{-9}	1.76×10^{-9}
$\Omega_{\rm DM}h^2$ (Relic density)	0.105	0.098	0.105
$N_{\rm event}$ (DD)	1.016×10^{-8}	2.014×10^{-8}	7.254×10^{-9}
$\hat{p}$ (DD)	1	1	1
$P_{\rm ann}$ [cm^3 s^{-1}GeV^{-1}] (ID)	2.38×10^{-28}	3.17×10^{-28}	2.43×10^{-28}

TABLE 4.1: The representative benchmark points that are allowed by $g_\mu - 2$ and cosmological bounds.

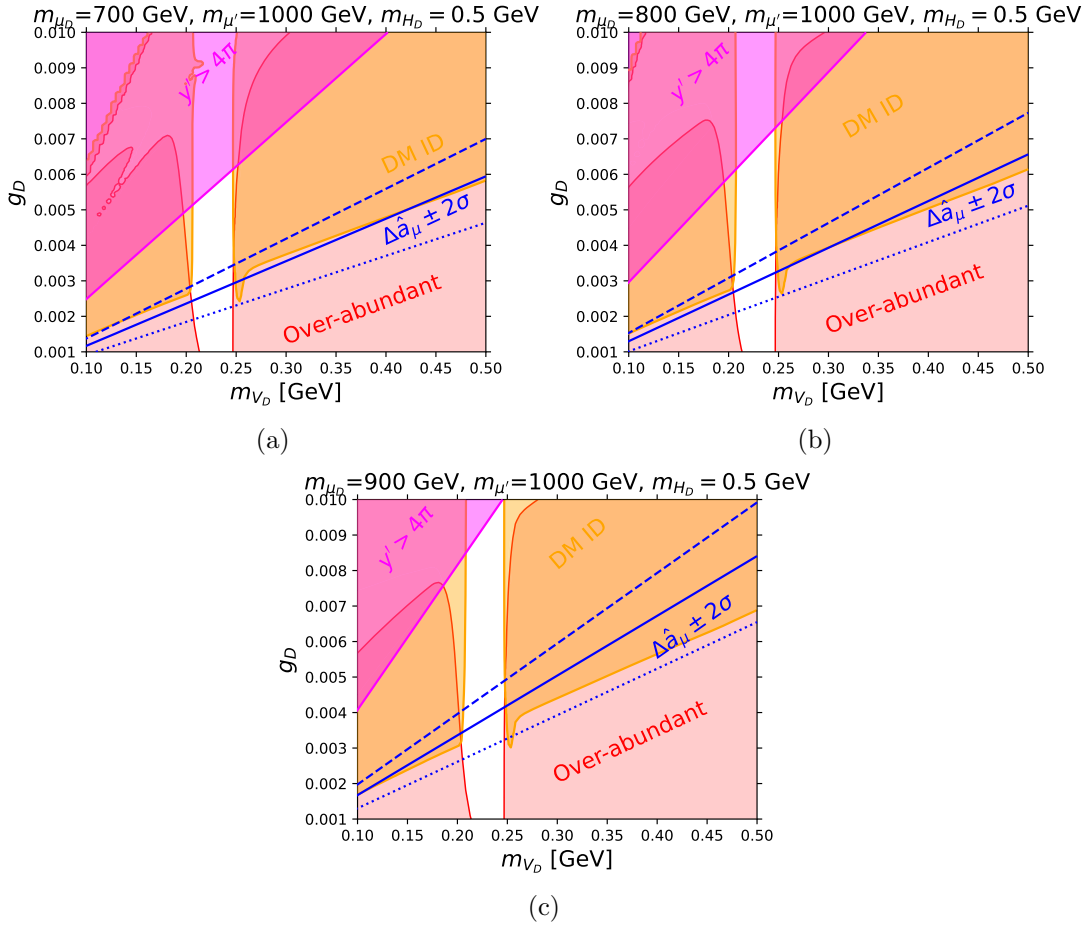

FIGURE 4.8: The 2D parameter space of (m_{V_D}, g_D) plane with $m_{\mu_D} = 700, 800, 900$ GeV, $m_{\mu'} = 1000$ GeV and $m_{H_D} = 0.5$ GeV. The magenta, orange and red regions are excluded by the perturbativity, DM ID and relic density constraints, respectively. The solid red line corresponds to the relic density $\Omega_{\rm DM}h^2 = 0.12$. The solid orange line indicates the $P_{\rm ann} = 3.2 \times 10^{-28}$ cm^{3}s^{-1} GeV^{-1}. The dotted, solid and dashed blue lines represent the $\Delta\hat{a}_\mu = -2\sigma$, $\Delta\hat{a}_\mu = 0$ and $\Delta\hat{a}_\mu = 2\sigma$, respectively.

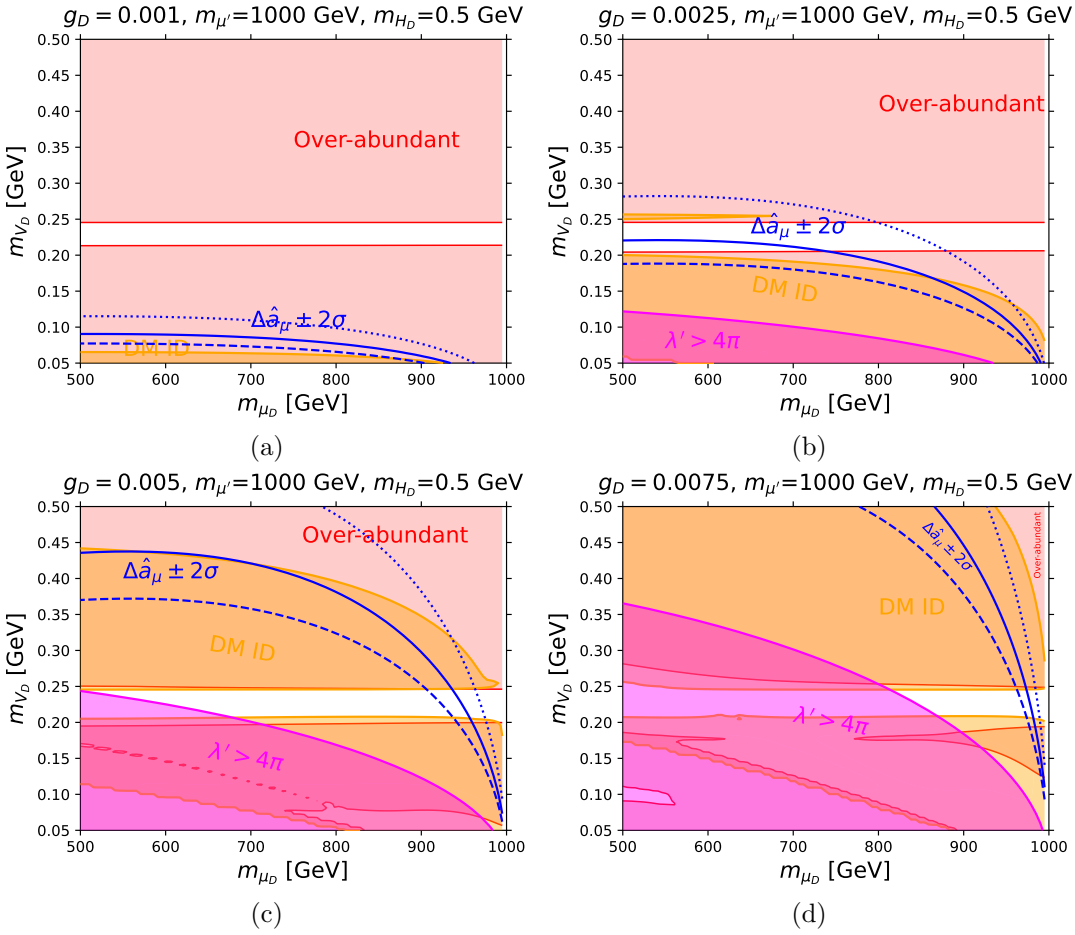

FIGURE 4.9: The 2D parameter space of (m_{μ_D}, m_{V_D}) plane with $g_D = 0.001, 0.0025$,-$0.005, 0.0075$, $m_{\mu'} = 1000$ GeV and $m_{H_D} = 0.5$ GeV. The magenta, orange and red regions are excluded by the perturbativity, DM ID and relic density constraints, respectively. The solid red line corresponds to the relic density $\Omega_{\rm DM}h^2 = 0.12$. The solid orange line indicates the $P_{\rm ann} = 3.2 \times 10^{-28}$ cm^{3}s^{-1} GeV^{-1}. The dotted, solid and dashed blue lines represent the $\Delta\hat{a}_\mu = -2\sigma$, $\Delta\hat{a}_\mu = 0$ and $\Delta\hat{a}_\mu = 2\sigma$, respectively.

4.4 Collider Constraints

In this section, we discuss collider limits for DM searches from LHC data where the ATLAS collaboration is looking for a signal of a pair production of sleptons produced in proton-proton collision and then they finally decay into a pair of SM muons and missing transverse momentum $pp \to \tilde{\ell}\tilde{\ell} \to \ell\ell + E_{\rm T}^{\rm miss}$. Additionally, we discuss novel signatures of multi-leptons with at least six muon in the final state predicted by our model. Then, we provide some benchmark points (BPs) with information of relevant branching ratios, production cross sections of multi-leptons and the corresponding number of events. These representative BPs are allowed by $g_\mu - 2$, cosmological bounds and collider limits from $pp \to \ell\ell + E_{\rm T}^{\rm miss}$. Moreover, the parameter space from 5D scan projecting onto different planes of input parameters are presented after successively applying all aforementioned limits.

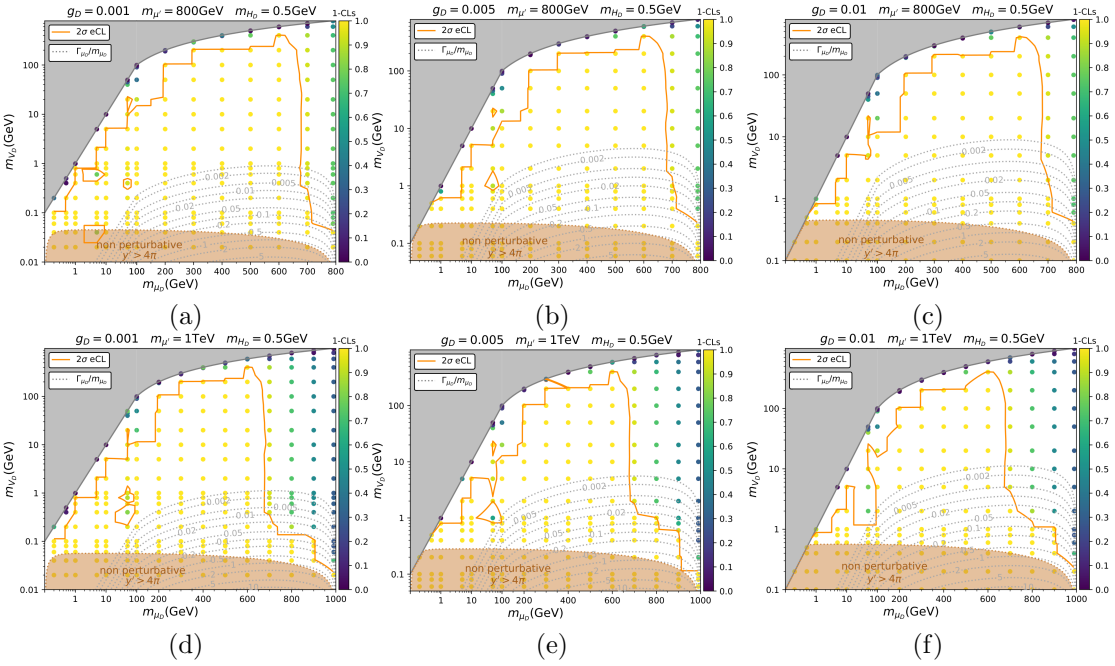

FIGURE 4.10: The recasting limits on the (m_{μ_D}, m_{V_D}) plane for $pp \to \mu_D^+\mu_D^- + E_{\rm T}^{\rm miss}$ based on the combined limits from ALTAS and CMS searches. The recast is simulated for $g_D = 0.001, 0.005, 0.01$, $m_{\mu'} = 800, 1000$ GeV and $m_{H_D} = 0.5$ GeV. The orange line indicates the exclusion limit at 95 % C.L. and the dotted lines show the ratio of the μ_D decay width over its mass.

4.4.1 The lower masses of VL muons from $pp \to \mu^+\mu^- + E_{\rm T}^{\rm miss}$

The production of a pair of VL muons $\mu_D^+\mu_D^-$ can be made through proton-proton collision via γ, Z, V' exchange. The first two processes are evidently dominant since μ_D carries the same hypercharge as SM muon while the V' involving process is highly suppressed by the KM effect. After the pair production of $\mu_D^+\mu_D^-$, a μ_D will entirely decay into a V_D and a SM muon due to the mixing between SM and VL muons through the

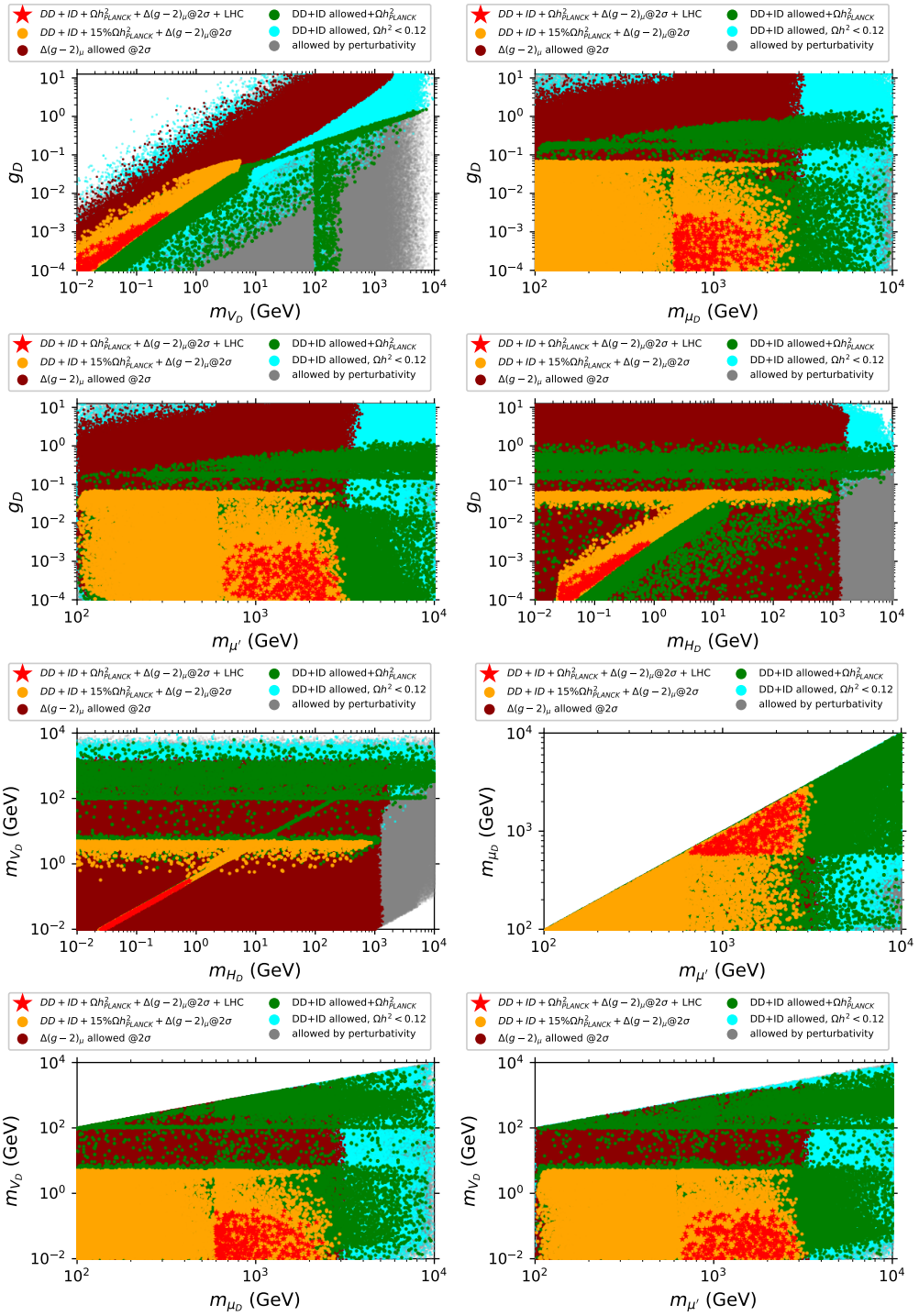

FIGURE 4.11: The scatter plots from 5D data projected on various planes: (m_{V_D}, g_D), (m_{H_D}, m_{V_D}) and $(m_{\mu'}, m_{\mu_D})$, respectively. The combined constraints on perturbativity (Eq.(4.26)), cosmology, VLM masses and a_μ have been applied on each plot. The VLM search has put a lower limits on m_{μ_D} and $m_{\mu'}$ around 600 GeV from LHC data. The constraint on $(g_\mu - 2)/2$ is within 2σ.

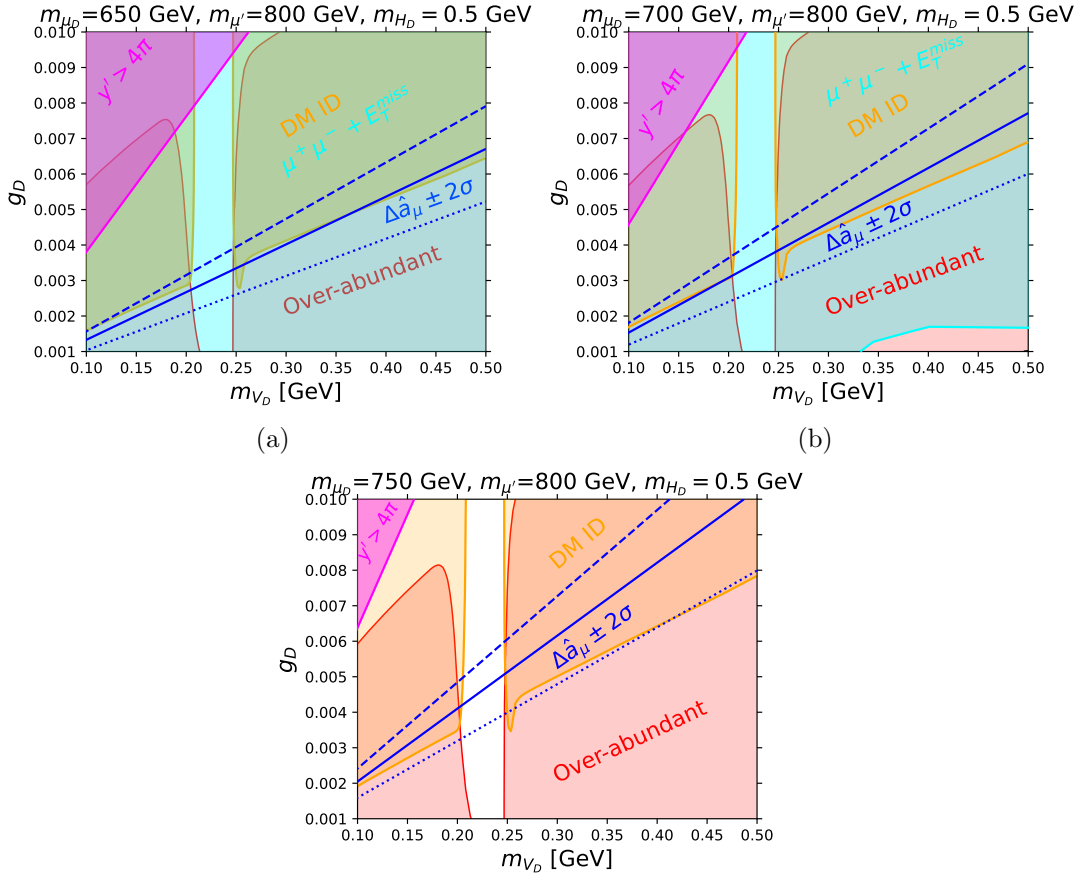

FIGURE 4.12: The 2D parameter space of (m_{V_D}, g_D) plane with $m_{\mu_D} = 650, 700, 750$ GeV, $m_{\mu'} = 800$ GeV and $m_{H_D} = 0.5$ GeV. The magenta, orange, red and cyan regions are excluded by the perturbativity, DM ID, relic density, collider constraints, respectively. The solid red line corresponds to the relic density $\Omega_{\rm DM}h^2 = 0.12$. The solid orange line indicates the $P_{\rm ann} = 3.2 \times 10^{-28}$ cm^{3}s^{-1} GeV^{-1}. The dotted, solid and dashed blue lines represent the $\Delta\hat{a}_\mu = -2\sigma$, $\Delta\hat{a}_\mu = 0$ and $\Delta\hat{a}_\mu = 2\sigma$, respectively. The solid cyan line shows the LHC exclusion limit at 95 % C.L.

Yukawa terms. In this section, we use collider limits from the ATLAS and CMS searching for a pair of production of sleptons decaying into two SM muons and transverse missing energy through the process of $pp \to \tilde{\ell}\tilde{\ell} \to \mu^+\mu^- + E_{\rm T}^{\rm miss}$. In our model, a similar process can be produced by $pp \to \mu_D^+\mu_D^- \to \mu^+\mu^- + E_{\rm T}^{\rm miss}$. By recasting the limit from this process, we can derive the exclusion region at 95 % confident level which can be used to set a lower bound on masses of VL muons. The list of searches are the following: atlas-susy-2018-32 [218], cms-sus-16-039 [219] and cms-exo-19-010 [220]. The recast is based on these searches can be found in figure 4.10 and the results are presented in the (m_{μ_D}, m_{V_D}) plane with varying parameters: $g_D = 0.001, 0.005, 0.01$, $m_{\mu'} = 800, 1000$ GeV and $m_{H_D} = 0.5$ GeV. One can see that in the region of interest where $m_{V_D} < 1$ GeV the lower limit on m_{μ_D} by recasting is around 700 GeV. In figure 4.11, we apply this limit on the various projections of 5D scan and one can see that the allowed region (indicated by red stars) reside exactly in the resonance region of H_D with $g_D < 0.003$,

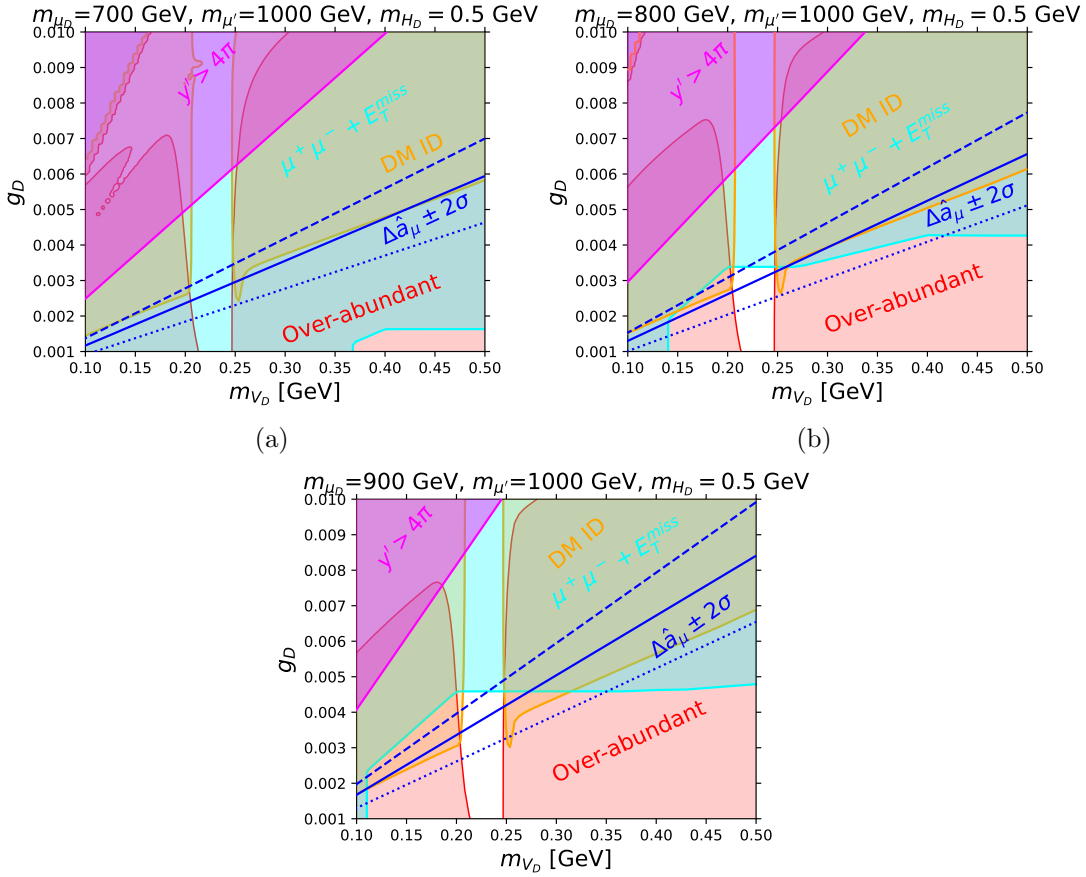

FIGURE 4.13: The 2D parameter space of (m_{V_D}, g_D) plane with $m_{\mu_D} = 700, 800, 900$ GeV, $m_{\mu'} = 1000$ GeV and $m_{H_D} = 0.5$ GeV. The magenta, orange, red and cyan regions are excluded by the perturbativity, DM ID, relic density, collider constraints, respectively. The solid red line corresponds to the relic density $\Omega_{\rm DM}h^2 = 0.12$. The solid orange line indicates the $P_{\rm ann} = 3.2 \times 10^{-28}$ cm^{3}s^{-1} GeV^{-1}. The dotted, solid and dashed blue lines represent the $\Delta\hat{a}_\mu = -2\sigma$, $\Delta\hat{a}_\mu = 0$ and $\Delta\hat{a}_\mu = 2\sigma$, respectively. The solid cyan line shows the LHC exclusion limit at 95 % C.L.

$m_{V_D} < 0.5$ GeV, $m_{H_D} < 1$ GeV and $700 < m_{\mu_D}, m_{\mu'} < 2000$ GeV.

In addition, we also apply the recast results at 95% to the 2D plots as in figures 4.12, 4.13 and 4.14. In figure 4.12 (c), the parameter space is not excluded by LHC constraint and the allowed region for $m_{\mu_D} = 750$ GeV, $m_{\mu'} = 800$ GeV and $m_{H_D} = 0.5$ GeV is in range of $0.005 < g_D < 0.003$ and $0.21 < m_{V_D} < 0.24$ GeV, while parameter space in figure 4.12 (a) and (b) is not survived by the LHC constraint. In figure 4.13, the parameter space in panel (a) is excluded by LHC constraint. The allowed region by cosmological, $g_\mu - 2$ and LHC constraints for $m_{\mu_D} = 800$ GeV, $m_{\mu'} = 1000$ GeV and $m_{H_D} = 0.5$ GeV has $0.002 < g_D < 0.003$ (panel (b)) while for $m_{\mu_D} = 900$ GeV, $m_{\mu'} = 1000$ GeV and $m_{H_D} = 0.5$ GeV the region with $0.0025 < g_D < 0.004$ is allowed (panel (c)).

The 2D parameter space of (m_{μ_D}, m_{V_D}) plane is shown in figure 4.14. One can see that the allowed region is depicted by figure 4.14 (b) where $g_D = 0.0025$, $m_{\mu_D} = 1000$ GeV,

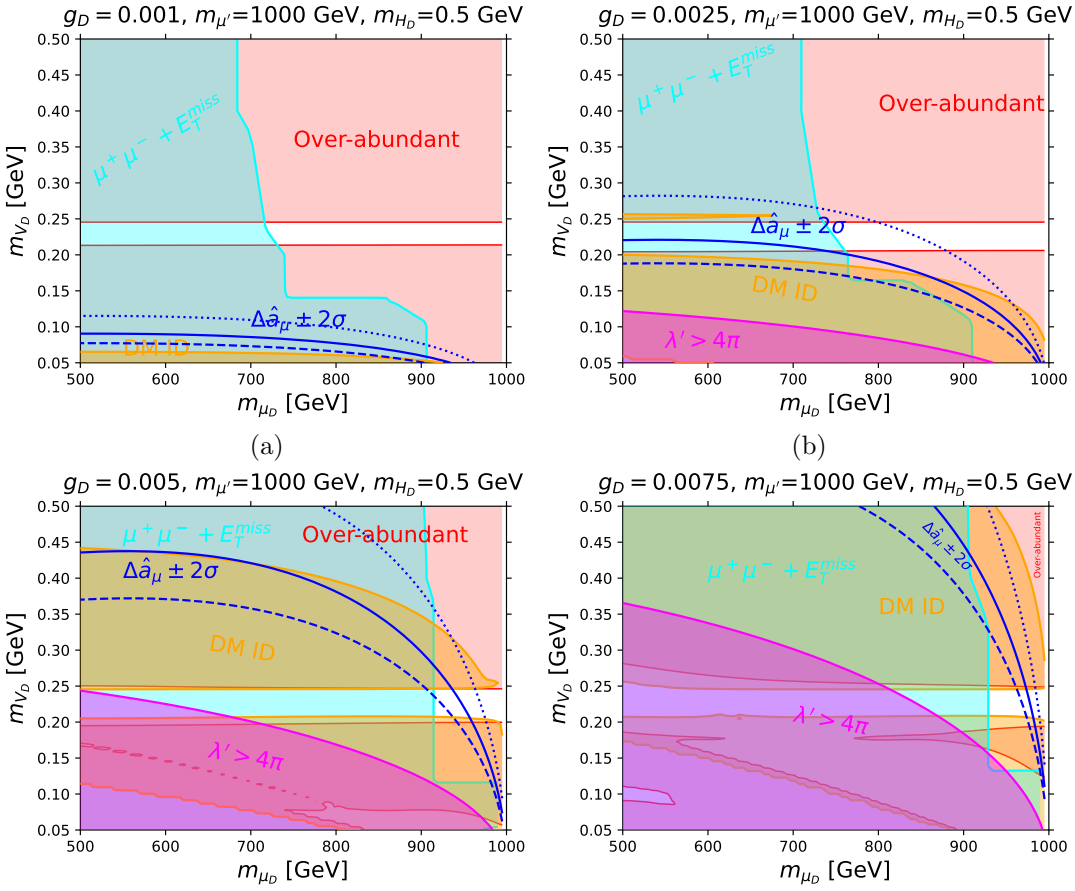

FIGURE 4.14: The 2D parameter space of (m_{μ_D}, m_{V_D}) plane with $g_D = 0.001, 0.0025$,-$0.005, 0.0075$, $m_{\mu'} = 1000$ GeV and $m_{H_D} = 0.5$ GeV. The magenta, orange and red regions are excluded by the perturbativity, DM ID and relic density constraints, respectively. The solid red line corresponds to the relic density $\Omega_{\rm DM}h^2 = 0.12$. The solid orange line indicates the $P_{\rm ann} = 3.2 \times 10^{-28}$ cm^{3}s^{-1} GeV^{-1}. The dotted, solid and dashed blue lines represent the $\Delta\hat{a}_\mu = -2\sigma$, $\Delta\hat{a}_\mu = 0$ and $\Delta\hat{a}_\mu = 2\sigma$, respectively.

$m_{H_D} = 0.5$ GeV and $750 < m_{\mu_D} < 800$ GeV.

4.4.2 The signatures: multilepton in final states

In this section, we discuss the novel and characteristic collider signatures predicted by the MPVDM. In our model, the multi-lepton processes can be produced by proton-proton collisions through a pair production of $\mu'^+\mu'^-$ and then a μ' will decay into one of these channels: 1) $\mu_D V_D$, 2) μH_D and 3) $\mu V'$. One H_D decays into $V_D V_D^*$, $V'V'$ and $\mu^+\mu^-$ and then V' decays into a pair of two muons which the decay rate and branching ratios of H_D is determined by g_D, m_{H_D} and the mass splitting ratio of two VL fermions, $(m^2_{\mu'} - m^2_{\mu_D})/m^2_{\mu'}$. The information about decay channels and corresponding branching ratios for relevant particles is given in table 4.2. Therefore, a process of pair production of $\mu'^+\mu'^-$ ends up with at least six muons in the final state. In table 4.2, we provide a few Benchmark Points (BPs) that produce the measured relic density and passed DM

Inputs/Observables	BP1	BP2	BP3
g_D	0.0025	0.0025	0.0025
m_{V_D} [GeV]	0.22	0.22	0.22
m_{μ_D} [GeV]	600	600	600
$m_{\mu'}$ [GeV]	650	850	1000
m_{H_D} [GeV]	0.5	0.5	0.5
$Br(\mu' \to V'\mu)$	0.48	0.3	0.22
$Br(\mu' \to H_D\mu)$	0.48	0.28	0.2
$Br(\mu' \to \tilde{V}\mu_D)$	0.045	0.43	0.59
$Br(H_D \to V_D V_D^*)$	0.66	0.608	0.551
$Br(H_D \to V'V')$	0.334	0.36	0.402
$Br(H_D \to \mu^+\mu^-)$	0.003	0.032	0.047
$Br(V' \to \mu^+\mu^-)$	$\sim$1	$\sim$1	$\sim$1
$Br(\mu' \to V'\mu \to 3\mu)$	0.48	0.3	0.22
$Br(\mu' \to H_D\mu \to 5\mu)$	0.16	0.1	0.076
$\sigma_{\rm tot}(pp \to \mu'\mu')$	0.85	0.22	0.088
$N_{\rm event}(pp \to 6\mu)$	58.75	5.94	1.28
$N_{\rm event}(pp \to 8\mu)$	19.58	1.98	0.44
$N_{\rm event}(pp \to 10\mu)$	6.53	0.66	0.15

TABLE 4.2: The decay channels and corresponding branching ratios of μ', V' and H_D for three representative BPs. The number of events is computed assuming that the integrated luminosity is equal to 300 fb^{-1}. Here the branching ratios of H_D is determined by g_D, H_D and the ratio $(m^2_{\mu'} - m^2_{\mu_D})/m^2_{\mu'}$.

DD and ID constraints, and have $(g_\mu - 2) \pm 2\sigma$. For the representative BPs, we evaluate the production cross section at $\sqrt{s} = 13.6$ TeV and 300 fb^{-1} integrated luminosity for six, eight and ten muons in the final state, and corresponding number of events for each BP.

One can see that probability for having six, eight and ten muons from $\mu'^+\mu'^-$ production is in the range of 5-20%, 2-8%, and 1-3%, respectively. This spectacular signature would give between 60 (for $m_{\mu_D} = 650$ GeV) and 1 (for $m_{\mu'} = 1000$ GeV) events. Since H_D and its respective decay products $H_D \to V'V'$ will be boosted, it will give four merged boosted muons, which requires a dedicated study. For very heavy μ', however, for example $m_{\mu'} > 1$ TeV and $m_{\mu_D} = 600$ GeV, the radiative corrections bring down the mass of V' below twice the mass of muon, $m_{V'} < 2m_\mu$, so V' becomes long-lived and decays to e^+e^- and three pairs of $\nu_\ell\bar{\nu}_\ell$ almost equally in branchings providing even more intriguing signature, which looks like the flavour violation one – more precisely, the lepton flavour violation occurs because of KM effect. In general, the model exhibits the following unique signatures

1) one isolated prompt muon + four merged boosted muons

2) pair of isolated muons + pair of four merged boosted muons

3) one isolated muon + four merged electrons from displaced vertex (10 muons in total)

4) pair of isolated muons + pair of four merged boosted displaced electrons (2 muons+8 electrons in total)

These novel signatures are very characteristic for this model.

Finally, the parameter space from 5D scan are present in figure 4.11 after sequentially applying the $g_\mu - 2$, cosmological and collider constraints, respectively. After imposing the LHC costraint, one can see from (g_D, m_{V_D}) panel that the DM mass and g_D are limited in a range of $0.01 < m_{V_D}/\text{GeV} < 4$ and $10^{-4} < g_D < 5 \times 10^{-3}$. In the (g_D, m_{H_D}) panel, the H_D mass consistently varies from 0.001-4 GeV. The m_{V_D} and m_{H_D} masses are constrained to the region of H_D resonance in (m_{V_D}, m_{H_D}) panel. According to the (g_D, m_{μ_D}), $(g_D, m_{\mu'})$ and $(m\mu_D, m_{\mu'})$ panels, the mass of μ_D and μ' are allowed by LHC bounds within 600-2500 and 650-300 GeV, respectively.

Chapter 5

Conclusions

In this thesis, we explore a new class of models which is proposed in the publications [1, 2]. This framework relies on the new mechanism that connects the SM and dark sector together called the Fermionic Portal to Vector Dark Matter (FPVDM). The model has an additional $SU(2)_D$ gauge group and $U(1)_{Y_D}$ global symmetry. Two of the new gauge bosons from $SU(2)_D$ group play a role as a DM candidate while global $U(1)_{Y_D}$ symmetry is introduced to stabilise the DM. The portal to the SM sector is constructed by the Yukawa term between the SM and its VL partners. As such, this scenario does not necessarily require a Higgs portal mediating the interactions between the dark sector and the standard one. This framework has a rich phenomenology which depends on the nature of VL partners and the form of the scalar potential.

Here we investigated the DM phenomenology based on a simple scenario of FPVDM models where the SM and dark scalars do not mix and the portal is purely from the Yukawa. Therefore, only five parameters are needed to define the model. In addition, the VL fermions mix with only one SM flavour. Our first study is called the Top Portal to Vector Dark Matter (TPVDM) where the VL top quarks (t_D and T) are added and mix with the SM top quark. Since this scenario does not provide the interaction between DM and nucleons at tree level, we calculated the loop-induced vertices of DM-DM-Z/γ and provided the generic expressions in terms of vector (v) and axial-vector (a) couplings. This is a very crucial result for evaluating the DM DD rate. We applied the DM ID constraint from CMB anisotropies observation which has less uncertainty than conventional measurements. For collider limits, we used the LHC bound for VL top search which does not allow the mass of T below 1.5 TeV. We also used the LHC constraint for $t\bar{t} + E_{\mathrm{T}}^{\mathrm{miss}}$ searches by recasting which excludes the parameter space with $225 < m_{t_D} < 825$ GeV and $m_{V_D} < 500$ GeV. The interplay between cosmological and collider limits play a crucial role in constraining the parameter space of the model. Here we presented the 5D scatter plots after applying those bounds and clearly showed the allowed regions with different mechanisms of generic, co-annihilating and H_D resonant DM annihilation. We also gave the 2D plots to highlight the specific region where the

H_D resonance and co-annihilation regions happen. In addition, More importantly, this specific scenario predicts two long-lived particles (t_D and V') which makes this class of model is more attractive and is possible to test it in the current and future colliders.

The second study is based on the Muonic Portal to Vector Dark Matter (MPVDM) where we have, instead of VL top quark, the VL muons (μ_D and μ'). In this scenario, we have a possibility to describe the muon anomalous magnetic moment $g_\mu - 2$ and DM issue simultaneously. We also rederived the generic expressions of $g_\mu - 2$ contribution and crossed-validated against the existing results. Here we still used the same cosmological constraints as in the case of TPVDM. However, for collider constraint, we did recasting for $\mu^+\mu^- + E_{\rm T}^{\rm miss}$ based on the ATLAS and CMS searches for a pair of sleptons. We used this result to set up the lower limit on the VL muons where it is slightly above 700 GeV. Applying the combined limits from cosmology, $g_\mu - 2$ and collider on the parameter space, we found that the allowed region is clearly on the resonance region of new scalar H_D. Moreover, we presented the 5D scatter and 2D plots which showed the allowed parameter space. The key feature of this scenario is that it predicts the multi-leptons signatures with 6-10 muons in the final state which makes this scenario very interesting to experimentalists to test it.

The material that I presented in this thesis is based on my publications [1, 2] discussed in chapter 2 and 3 and upcoming article entitled "the muon anomalous magnetic moment $g_\mu - 2$ from Fermionic Portal to Vector Dark Matter" [3] discussed in chapter 4.

The studies in this thesis are only two realisations of the FPVDM framework which can be extended to explain many problems in the SM, not only the DM and $g_\mu - 2$. Here I will give an outline for future studies that can be explored. For example, if the Yukawa coupling and new gauge coupling are so tiny that DM cannot be in thermal bath with SM particles. It allows us to study the another DM production mechanism called the freeze-in scenario. Instead of VL top quarks and muons, we can introduce the VL neutrinos which mix with the SM neutrinos. This scenario could explain the smallness of SM neutrino masses and also provide the fermionic DM instead of Vector DM which makes really intriguing. Moreover, a recent anomaly on W boson mass could be explained by new VL states propagating in the loop. The first order phase transition (FOPT) can be created in $SU(2)_D$ breaking and leads to the gravitational waves (GW). Another interesting scenario can happen with a non-zero scalar mixing ($\lambda_{HD} \neq 0$). This setup modifies the scalar potential and gives an crucial ingredient to create the FOPT at the early universe which is very important to baryogenesis. In addition, if we have both non-zero scalar mixing and VL neutrinos in the same scenario. It could lead to a model of leptogenesis which is another way to explain to the baryon asymmetry of the universe (BAU) apart from the baryogenesis. In the framwork we presented here, it is assumed that VL fermions mix with only one SM particle. So if we allow these VL fermions mix with more than one SM fermions this could explain the flavour anomalies in the SM. Now one can see a big picture of the FPVDM framework that it does not

only explain the DM problem but many problems in the SM could be explained by this framework and it needs further studies in future.

Appendix A

Mass splitting at one loop

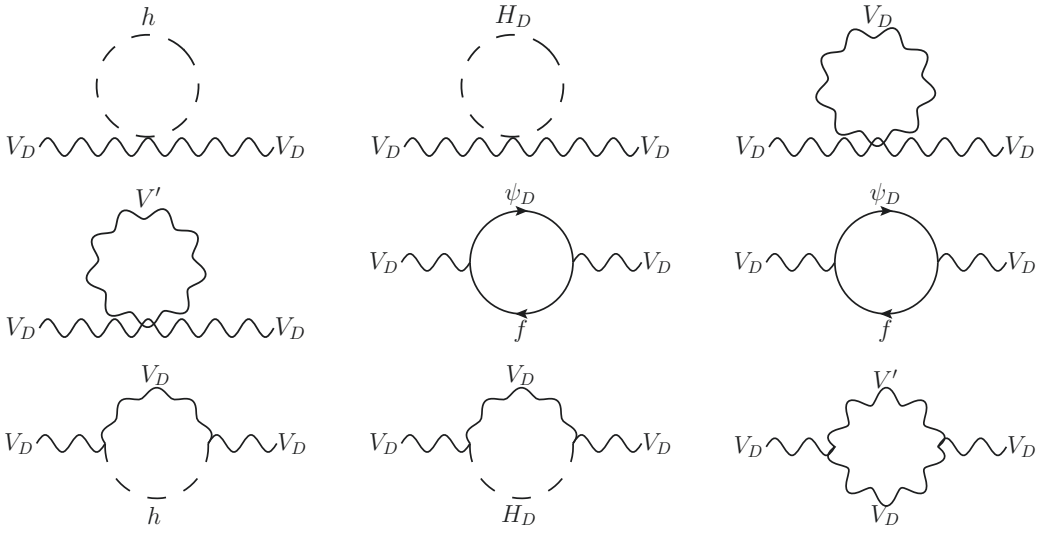

FIGURE A.1: The complete set of Feynman diagams contributing to the mass correction of the V_D.

At tree level, the neutral and charged components of $SU(2)_D$ gauge triplet are degenerate in mass as one can see in eq. (2.25). Nevertheless, the radiative correction at one-loop level obviously breaks their mass degeneracy. The difference between m_{V_D} and $m_{V'}$ takes place due to the F-f mixing and the different $\mathbb{Z}_2$ parities of the members of the $SU(2)_D$ fermion doublet, which results in distinct particles circling in the loops. In figure A.1 and A.2, the complete contributions to the mass correction of V_D and V' are depicted. In the limit of $m_F \to m_{\psi_D}$, Eq.(2.23) implies no mixing mixing between the F-f fermions. Thus, the mass degeneracy of V_D and V' is still not broken. The mass splitting occurs when m_F is different from m_{ψ_D}. The scalar contributions from h and H_D mediation are non-zero separately. However, they are identical for V_D and V' and will play any role in the mass difference.

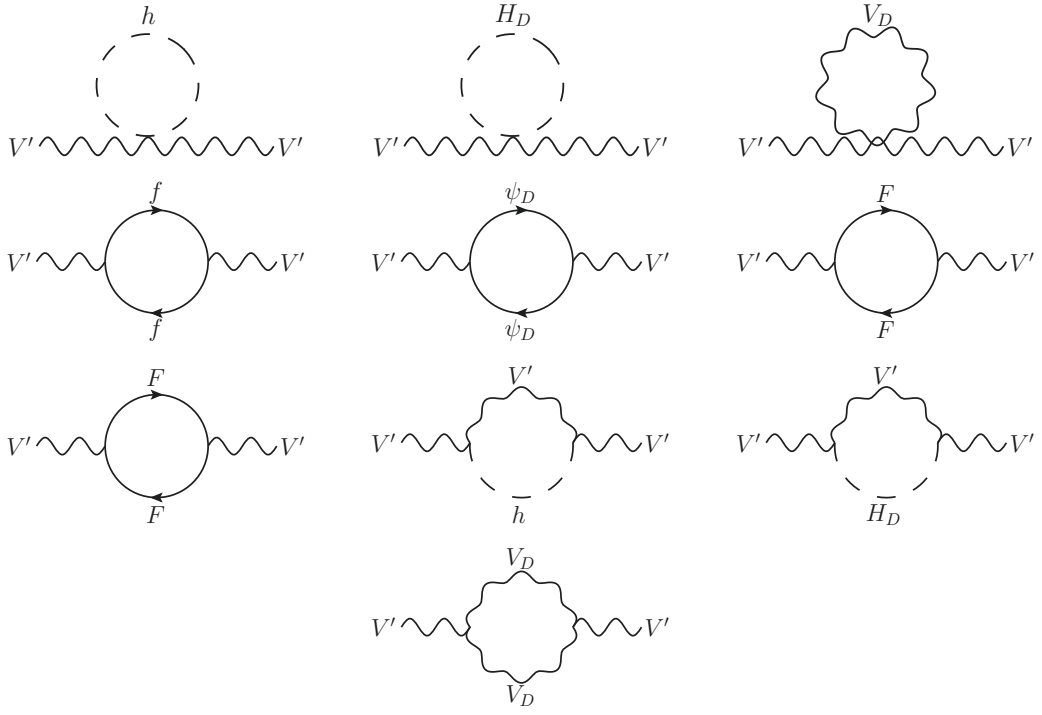

FIGURE A.2: The complete set of Feynman diagams contributing to the mass correction of the V'.

Self-energy diagrams with fermionic loops for V_D and V' are shown in figure 2.2. Generally, the self-energy function of a vector boson can be decomposed into two components:

$$i\Pi_V^{\mu\nu}(p^2) = \left(g^{\mu\nu} - \frac{p^\mu p^\nu}{p^2}\right) i\Pi_V^{\mathrm{T}}(p^2) + \left(\frac{p^\mu p^\nu}{p^2}\right) i\Pi_V^{\mathrm{L}}(p^2)\ , \tag{A.1}$$

where Π_V^{T} and Π_V^{L} are the transverse and longitudinal amplitudes, respectively. Here we use a symbol V to indicate either V_D or V'. To get the transverse and longitudinal components of the self-energy amplitude, we extract each part by using the following operators

$$\begin{aligned} \Pi_V^{\mathrm{T}}(p^2) &= \frac{1}{3-2\epsilon}\left(g_{\mu\nu} - \frac{p_\mu p_\nu}{p^2}\right)\Pi_V^{\mu\nu}(p^2), \\ \Pi_V^{\mathrm{L}}(p^2) &= \frac{p_\mu p_\nu}{p^2}\Pi_V^{\mu\nu}(p^2). \end{aligned} \tag{A.2}$$

We work in d-dimensions where $d = g_{\mu\nu}g^{\mu\nu} = 4 - 2\epsilon$. The physical mass, m_V, is defined as the position of the propagator's pole and is given by

$$m_V^2 \equiv (m_V^{\mathrm{pole}})^2 = m_{V,\mathrm{tree}}^2 + \mathrm{Re}(\Pi_V^{\mathrm{T}})\ , \tag{A.3}$$

where $m_{V,\mathrm{tree}}$ is the bare mass at tree level, which is the same for both V_D and V', and $\mathrm{Re}(\Pi_V^{\mathrm{T}})$ stands for the real part of Π_V^{T} function. We use the physical (one-loop corrected)

mass of DM (V_D) as an input parameter of the model. The mass of V' is given by

$$\begin{aligned} m^2_{V'} &= m^2_{V_D} - \Pi^{\rm T}_{V'} + \Pi^{\rm T}_{V_D}, \\ m_{V'} &= m_{V_D}\sqrt{1 - \frac{\left(\Pi^{\rm T}_{V'} - \Pi^{\rm T}_{V_D}\right)}{m^2_{V_D}}} \\ &= m_{V_D} - \frac{\left(\Pi^{\rm T}_{V'} - \Pi^{\rm T}_{V_D}\right)}{2m_{V_D}} + \dots . \end{aligned} \tag{A.4}$$

We have expanded the square root assuming that $\Delta\Pi \equiv (\Pi^{\rm T}_{V'} - \Pi^{\rm T}_{V_D})/m^2_{V_D} \ll 1$. After cutting the expansion up to the g^2_D order, the $V_D - V'$ mass splitting at one-loop reads:

$$\Delta m_V = m_{V_D} - m_{V'} = \frac{1}{2}\left(\frac{\Pi^{\rm T}_{V_D} - \Pi^{\rm T}_{V'}}{m_{V_D}}\right) . \tag{A.5}$$

The sign of mass splitting is very important to the calculation of relic density and DM annihilation rate. If it is positive the cross section of $V_D V_D \to V'V'$ is enhanced and vice versa.

The transverse component of the self-energy function $\Pi^{\rm T}_V(p^2)$ of gauge bosons with fermion F_1 and F_2 in the loop is given by

$$\begin{aligned} \Pi^T_{F_1,F_2}(p^2) = \frac{1}{16\pi^2}\Big[& 2(v^2_{12} + a^2_{12})(A_0(m^2_1) + A_0(m^2_2)) \\ & - 8(v^2_{12} + a^2_{12})B_{00}(p^2, m^2_1, m^2_2) + 2(v^2_{12}(m_1 - m_2)^2 + a^2_{12}(m^2_1 + m^2_2) \\ & - p^2(v^2_{12} + a^2_{12}))B_0(p^2, m^2_1, m^2_2)\Big], \end{aligned} \tag{A.6}$$

where the v_{12} and a_{12} are the vector and axial-vector couplings of F_1F_2V vertices, respectively. The A_0, B_0 and B_{00} are the standard one- and two-point Veltman-Passarino functions. The one-loop function for V' and V_D are defined as

$$\begin{aligned} \Pi^{\rm T}_{V_D} &= \Pi^{\rm T}_{f,\psi_D} + \Pi^{\rm T}_{F,\psi_D}, \\ \Pi^{\rm T}_{V'} &= \Pi^{\rm T}_{f,f} + \Pi^{\rm T}_{F,F} + \Pi^{\rm T}_{f,F} + \Pi^{\rm T}_{\psi_D,\psi_D}, \end{aligned} \tag{A.7}$$

where $\Pi^{\rm T}_{F_1,F_2}$ is the transverse component of self-energy function in which the fermions F_1 and F_2 are circulating.

We have evaluated Eq.(A.5) by using Eq. (A.6), the expressions for couplings from table E.1 and E.2, and then set the square incoming momentum and the renormalisation scale equal to the mass of DM, $\mu^2 = p^2 = m^2_{V_D}$, which leads to the following simple

expression

$$\Delta m'_V = \frac{g_D^2}{640\pi^2}\frac{m_F^2}{m_{V_D}}\epsilon_1^2\Big[(20+3\epsilon_3-15\epsilon_2+20\epsilon_2\epsilon_3) + 10(3\epsilon_2-\epsilon_3-2\epsilon_2\epsilon_3)\log\epsilon_3\Big]\,. \tag{A.8}$$

where

$$\epsilon_1 = \frac{m_F^2 - m_{\psi_D}^2}{m_F^2}, \quad \epsilon_2 = \frac{m_f^2}{m_F^2}, \quad \epsilon_3 = \frac{m_V^2}{m_F^2}\,. \tag{A.9}$$

This formula was derived in the approximation $\epsilon_1, \epsilon_2, \epsilon_3 \ll 1$. Keeping only the leading term of ϵ_1 provides the following very simple expression for the V_D-V' mass splitting:

$$\Delta m''_V = \frac{g_D^2}{32\pi^2}\frac{m_F^2}{m_{V_D}}\epsilon_1^2 = \frac{g_D^2}{32\pi^2}\frac{m_F^2}{m_{V_D}}\left(\frac{m_F^2 - m_{\psi_D}^2}{m_F^2}\right)^2\,. \tag{A.10}$$

Appendix B

Kinetic mixing functions

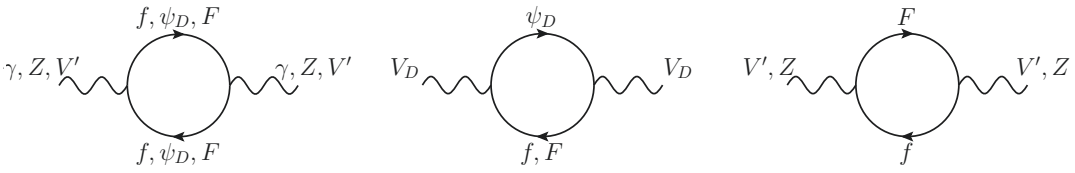

FIGURE B.1: The complete set of Feynman diagams contributing to the mass correction of the V_D.

The neutral gauge bosons like γ, Z and V' cannot mix at tree level. However, this is not the case at one loop or higher order loops. They do mix via the fermionic propagation in the loop as one can in figure B.1.

The kinetic mixing (KM) is thoroughly explained in section 2.2.3.2 and the KM functions for the Z-V mixing are given by

$$\begin{aligned} F^{ZV}_{qT1+qL}(r_f, r_{\psi_D}) = \frac{2(r_f^2-1)(r_{\psi_D}^2-1)}{3(r_f^2 r_{\psi_D}^2-1)^4}\Bigg[&3r_f^6 r_{\psi_D}^6 - 5r_f^6 r_{\psi_D}^4 - 21 r_f^4 r_{\psi_D}^4 \\ &+ 22 r_f^4 r_{\psi_D}^2 - 21 r_f^2 r_{\psi_D}^2 - 5r_f^2 + 3 \\ &+ 6\frac{\left(r_f^8 r_{\psi_D}^6 - 3r_f^6 r_{\psi_D}^4 + 12 r_f^4 r_{\psi_D}^4 - 3 r_f^4 r_{\psi_D}^2 + r_f^2\right)}{r_f^2 r_{\psi_D}^2 - 1}\log\left(r_f r_{\psi_D}\right)\Bigg], \end{aligned} \tag{B.1}$$

$$F^{ZV}_{qT2}(r_f, r_{\psi_D}) = 8\left[\log\left(\frac{r_f}{r_{\psi_D}}\right) + \frac{(r_{\psi_D}^2 - r_f^2)\log\left(r_f r_{\psi_D}\right)}{r_f^2 r_{\psi_D}^2 - 1}\right], \tag{B.2}$$

$$\begin{aligned} F^{ZV}_{m}(r_f, r_{\psi_D}) = \frac{(r_f^2-1)(r_{\psi_D}^2-1)}{(r_f^2 r_{\psi_D}^2-1)^2}\Bigg[&\frac{1 - 4r_{\psi_D}^2 + r_f^2 r_{\psi_D}^2}{r_{\psi_D}^2} \\ &+ \frac{4(r_f^2 r_{\psi_D}^2 - r_f^2 + 1)\log\left(r_f r_{\psi_D}\right)}{(r_f^2 r_{\psi_D}^2 - 1)}\Bigg], \end{aligned} \tag{B.3}$$

where $r_f = m_f/m_{\psi_D}$ and $r_{\psi_D} = m_{\psi_D}/m_F$.

Appendix C

Mixing structure in the dark EW sector

Defining $\mathcal{V}^0_{D0\mu} = (B_\mu, W^3_\mu, B^0_{D0\mu}, V^0_{D0\mu})^T$ and using analogous notation as Eq.(2.24) for the fully neutral gauge boson Lagrangian term after EW and dark symmetry breaking,

$$\mathcal{L}^{\rm kin}_{\mathcal{V}^0_{D0}}|_{v,v_D} \supset (\mathcal{V}^0_{D0})^T \mathcal{M}^2_{\mathcal{V}^0_{D0}} \mathcal{V}^0_{D0} \,, \tag{C.1}$$

the entries of the mass mixing matrix in the gauge sector are:

$$\begin{aligned}
\mathcal{M}^2_{\mathcal{V}^0_{D0}}|_{11} &= \frac{1}{8\left(1-\epsilon^2\right)}\Big[\left(g'^2v^2 + g'^2_D v_D^2\epsilon^2\right)\cos^2\theta_k - g'^2_D\epsilon\sqrt{1-\epsilon^2}\sin 2\theta_k v_D^2 \\
&\quad + g'^2_D\left(1-\epsilon^2\right)\sin^2\theta_k v_D^2\Big] && \text{(C.2)}\\
\mathcal{M}^2_{\mathcal{V}^0_{D0}}|_{12} &= \mathcal{M}^2_{\mathcal{V}^0_{D0}}|_{21} = -\frac{gg'v^2\cos\theta_k}{8\sqrt{1-\epsilon^2}} && \text{(C.3)}\\
\mathcal{M}^2_{\mathcal{V}^0_{D0}}|_{13} &= \mathcal{M}^2_{\mathcal{V}^0_{D0}}|_{31} = \frac{1}{16\left(1-\epsilon^2\right)}\Big[g'^2_D v_D^2\left(\left(1-2\epsilon^2\right)\sin 2\theta_k - 2\epsilon\sqrt{1-\epsilon^2}\cos 2\theta_k\right) \\
&\quad - g'^2\sin 2\theta_k v^2\Big] && \text{(C.4)}\\
\mathcal{M}^2_{\mathcal{V}^0_{D0}}|_{14} &= \mathcal{M}^2_{\mathcal{V}^0_{D0}}|_{41} = \frac{1}{8}g_D g'_D v_D^2\left(\frac{\epsilon\cos\theta_k}{\sqrt{1-\epsilon^2}} - \sin\theta_k\right) && \text{(C.5)}\\
\mathcal{M}^2_{\mathcal{V}^0_{D0}}|_{22} &= \frac{g^2v^2}{8} && \text{(C.6)}\\
\mathcal{M}^2_{\mathcal{V}^0_{D0}}|_{23} &= \mathcal{M}^2_{\mathcal{V}^0_{D0}}|_{32} = \frac{gg'v^2\sin\theta_k}{8\sqrt{1-\epsilon^2}} && \text{(C.7)}\\
\mathcal{M}^2_{\mathcal{V}^0_{D0}}|_{24} &= \mathcal{M}^2_{\mathcal{V}^0_{D0}}|_{42} = 0 && \text{(C.8)}\\
\mathcal{M}^2_{\mathcal{V}^0_{D0}}|_{33} &= \frac{1}{8\left(1-\epsilon^2\right)}\Big[g'^2_D\left(1-\epsilon^2\right)\cos^2\theta_k v_D^2 + g'^2_D\epsilon\sqrt{1-\epsilon^2}\sin 2\theta_k v_D^2 \\
&\quad + \left(g'^2v^2 + g'^2_D v_D^2\epsilon^2\right)\sin^2\theta_k\Big] && \text{(C.9)}\\
\mathcal{M}^2_{\mathcal{V}^0_{D0}}|_{34} &= \mathcal{M}^2_{\mathcal{V}^0_{D0}}|_{43} = -\frac{1}{8}g_D g'_D v_D^2\left(\cos\theta_k + \frac{\epsilon\sin\theta_k}{\sqrt{1-\epsilon^2}}\right) && \text{(C.10)}
\end{aligned}$$

$$\mathcal{M}^2_{\mathcal{V}^0_{D0}}|_{44} = \frac{g_D^2 v_D^2}{8}\,, \tag{C.11}$$

where ϵ is the KM parameter defined in Eq.(2.69). The mass eigenstates corresponding to the eigenvalues of the mixing matrix are γ, γ_D, Z and Z'. Their masses do not depend on the rotation angle θ_k and read:

$$m_\gamma = m_{\gamma_D} = 0 \tag{C.12}$$

$$\begin{aligned} M^2_{Z,Z'} = \frac{1}{8}\Big[&g^2v^2 + g_D^2 v_D^2 \\ &+ \frac{1}{1-\epsilon^2}\left(g'^2v^2 + g_D'^2 v_D^2 \mp \sqrt{\mathcal{K}_0 + \mathcal{K}_2\epsilon^2 + \mathcal{K}_4\epsilon^4}\right)\Big] \end{aligned} \tag{C.13}$$

where the $\mathcal{K}$ functions are defined as:

$$\mathcal{K}_0 = \left(\left(g^2+g'^2\right)v^2 - \left(g_D'^2+g_D^2\right)v_D^2\right)^2 \tag{C.14}$$

$$\begin{aligned} \mathcal{K}_2 = -2\Big[&g^2(g^2+g'^2)v^4 + g_D^2(g_D^2+g_D'^2)v_D^4 \\ &- \left(g^2(2g_D^2+g_D'^2) + g'^2\left(g_D^2+2g_D'^2\right)\right)v^2v_D^2\Big] \end{aligned} \tag{C.15}$$

$$\mathcal{K}_4 = (g^2v^2 - g_D^2v_D^2)^2 \tag{C.16}$$

and the sign in front of the square root is chosen to reconstruct the SM value of the Z mass for $\epsilon \to 0$ and $\left(g^2+g'^2\right)v^2 > \left(g_D'^2+g_D^2\right)v_D^2$.

Appendix D

Fermion loop contributions to DM DD

In micrOMEGAs package [51], the computation of the direct detection rate is usually done at tree level. However, in the case that the interaction between nucleons and DM does not exist at tree level. The one loop box and triangle (scalar propagating) diagrams in figure 3.3 (c) and (d) will be evaluated. These contributions only give a mild effect on the parameter space where the mixing between F and f is optimum at $m_F \to m_{\psi_D}$ or $m_{\psi_D} \to m_f$. In addition to those diagrams, there are also two additional vertices, $V^0_{D+}V^0_{D-}\gamma$ and $V^0_{D+}V^0_{D-}Z$, which can also contribute to the direct detection limit. In figure D.1, additional contributions of the fermionic triangle diagrams are shown. Here the momenta for $V^0_{D+\alpha}$, $V^0_{D-\beta}$ and V_μ are p_1, p_2 and q, respectively. They are all pointing towards the vertex and satisfy $0 = q + p_1 + p_2$. The figure D.1 (a) and (b) describe the clockwise (CW) directions of fermionic lines but with interchange of m_2 and m_3.

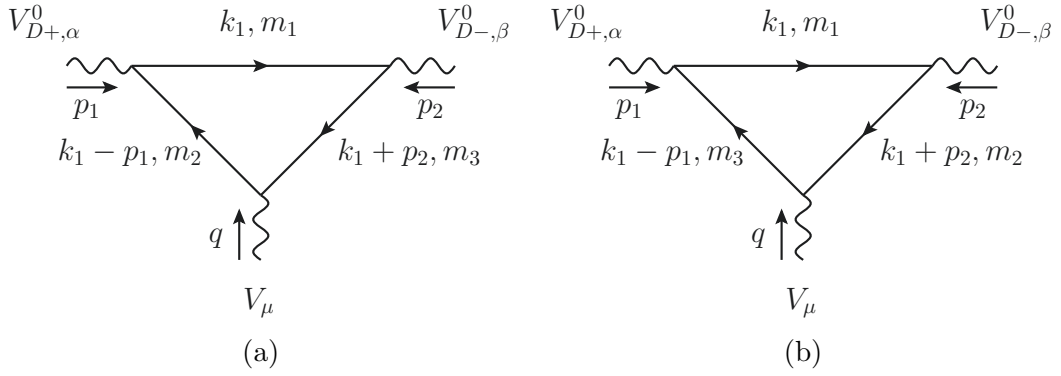

FIGURE D.1: The generic triangle diagrams for $V^0_{D+\alpha}V^0_{D-\beta}V_\mu$ where V_μ stands for either photon and Z-boson. The ingoing momenta for V^0_{D+}, V^0_{D-} are p_1, p_2 and q, respectively, and they safisfy $0 = q + p_1 + p_2$. Diagrams (a) and (b) represent the clockwise directions of fermionic lines with interchange of m_2 and m_3.

The most general (CP conserving) effective Lagrangian [126, 221] for on-shell DM $V^0_{D\pm}$ interacting with neutral vector bosons γ/Z is given by

$$\begin{aligned}\mathcal{L}^{\text{eff}}_{V^0_{D+}V^0_{D-}V} &= \lambda_1^V\left[(\partial_\mu V^0_{D+\nu}-\partial_\nu V^0_{D+\mu})V^{0\mu}_{D-}V^\nu-(\partial_\mu V^0_{D-\nu}-\partial_\nu V^0_{D-\mu})V^{0\mu}_{D+}V^\nu\right]\\ &-\lambda_2^V V^0_{D+\mu}V^0_{D-\nu}(\partial^\mu V^\nu-\partial^\nu V^\nu)\\ &+\frac{\lambda_3^V}{M^2_{V\pm}}(\partial_\lambda V^0_{D+\mu}-\partial_\mu V^0_{D+\lambda})(\partial^\mu V^0_{D-\nu}-\partial_\nu V^0_{D-\mu})(\partial^\nu V^\lambda-\partial^\lambda V^\nu)\\ &-i\lambda_5^V\epsilon^{\mu\nu\rho\sigma}(V^0_{D+\mu}\partial_\rho V^0_{D-\nu}-V^0_{D-\nu}\partial_\rho V^0_{D+\mu})V_\sigma\\ &-i\lambda_6^V\epsilon^{\mu\nu\rho\sigma}(V^0_{D+\mu}\partial_\rho V^0_{D-\nu}-V^0_{D-\nu}\partial_\rho V^0_{D+\mu})\partial^\lambda\partial_\sigma(\partial^2)^{-1}V_\lambda,\end{aligned}\tag{D.1}$$

where V can be either γ or Z and λs are the effective couplings. The DM vector particles $V^0_{D\pm}$ are taken to be on-shell with mass $M_{V^\pm}$. Since in the direct detection process, the momentum transferred from DM particles to nucleons is much smaller than the masses of the DM particles, the form factors can be estimated in limit of $q^2\to 0$.

The effective Lagrangian (in momentum space) Eq.(D.1) can be expressed in terms of the vertex function $V(p_1,p_2,q)$ which is a function of all incoming momenta

$$\mathcal{L}^{\text{eff}}_{V^0_{D+}V^0_{D-}V}=-iV_V^{\alpha\beta\mu}(p_1,p_2,q)V^0_{D+\alpha}(p_1)V^0_{D-\beta}(p_2)V_\mu(q),\tag{D.2}$$

where the vertex function reads

$$\begin{aligned}V_V^{\alpha\beta\mu}(p_1,p_2,q) &= f_1^V(p_1-p_2)^\mu g^{\alpha\beta}+\frac{f_2^V}{M^2_{V\pm}}(p_1-p_2)^\mu q^\alpha q^\beta\\ &+f_3^V(q^\alpha g^{\mu\beta}-q^\beta g^{\mu\alpha})+if_5^V\epsilon^{\alpha\beta\mu\rho}(p_1-p_2)_\rho\\ &+i\frac{f_8^V}{M^2_{V\pm}}(p_1-p_2)_\rho q_\sigma(\epsilon^{\mu\alpha\rho\sigma}q^\beta-\epsilon^{\mu\beta\rho\sigma}q^\beta).\end{aligned}\tag{D.3}$$

The CP-conserving[1] form factors, f_i, are related to the couplings λ_i of Eq.(D.1) by

$$f_1^V = \lambda_1^V+\frac{q^2}{2M^2_{V\pm}}\lambda_3^V,\tag{D.4}$$

$$f_2^V = -\lambda_3^V,\tag{D.5}$$

$$f_3^V = \lambda_1^V+\lambda_2^V+\frac{1}{2}\lambda_3^V,\tag{D.6}$$

$$f_5^V = \lambda_6^V-\lambda_5^V,\tag{D.7}$$

$$f_8^V = -\frac{M^2_{V\pm}}{q^2}\lambda_6^V.\tag{D.8}$$

We explicitly calculate the form-factors of the $V^0_{D+}V^0_{D-}V$ vertex according to the diagrams in figure D.1 where p_1,p_2 and q are the momenta of V^0_{D+}, V^0_{D-} and V_μ, respectively.

[1]The more general vertex function found in appendix A of [221] includes additional CP-violating form-factors f_4, f_6, f_7 and f_9. However, these are irrelevant for direct detection of DM in this model, and are therefore omitted.

The vector and axial coupling constants for the vertex between a vector particle and fermions F_i annd F_j (with masses m_i and m_j) are denoted by v_{ij} and a_{ij}, respectively.

For the diagrams in figure D.1 (a) and (b), the corresponding amplitudes read

$$iV_{(a)}^{\mu\alpha\beta} = (-1)(-i)^3(i)^3 \int \frac{d^dk}{(2\pi)^d} \frac{N_{(a)}^{\mu\alpha\beta}}{\left(k^2-m_1^2\right)\left((k-p_1)^2-m_2^2\right)\left((k+p_2)^2-m_3^2\right)}, \tag{D.9}$$

$$iV_{(b)}^{\mu\alpha\beta} = (-1)(-i)^3(i)^3 \int \frac{d^dk}{(2\pi)^d} \frac{N_{(b)}^{\mu\alpha\beta}}{\left(k^2-m_1^2\right)\left((k-p_1)^2-m_3^2\right)\left((k+p_2)^2-m_2^2\right)}, \tag{D.10}$$

where the factor (-1) is the Feynman rules for the fermion loop. The factor $(-i)^3$ for three vertices and $(i)^3$ for three fermion propagator factor. The numerators of these integrals are defined by

$$\begin{aligned} N_a =& \mathrm{Tr}\Big[\gamma^\mu(v_{23}-a_{23}\gamma_5)(\not{k}+\not{p}_2+m_3)\gamma^\beta(v_{13}-a_{13}\gamma_5) \\ & \cdot(\not{k}+m_1)\gamma^\alpha(v_{12}-a_{12}\gamma_5)(\not{k}-\not{p}_1+m_2)\Big], \end{aligned} \tag{D.11}$$

$$\begin{aligned} N_b =& \mathrm{Tr}\Big[\gamma^\mu(v_{23}-a_{23}\gamma_5)(\not{k}+\not{p}_2+m_2)\gamma^\beta(v_{12}-a_{12}\gamma_5) \\ & \cdot(\not{k}+m_1)\gamma^\alpha(v_{13}-a_{13}\gamma_5)(\not{k}-\not{p}_1+m_2)\Big]. \end{aligned} \tag{D.12}$$

We compute the loop integrals by using the Package-X [159] and use a set of appropriate Schouten identities.

$$p_2^\alpha\epsilon^{\nu\rho\mu\beta} = p_2^\nu\epsilon^{\alpha\rho\mu\beta} + p_2^\rho\epsilon^{\nu\alpha\mu\beta} + p_2^\mu\epsilon^{\nu\rho\alpha\beta} + p_2^\beta\epsilon^{\nu\rho\mu\alpha}, \tag{D.13}$$

$$p_1^\beta\epsilon^{\nu\rho\mu\alpha} = p_1^\nu\epsilon^{\beta\rho\mu\alpha} + p_2^\rho\epsilon^{\nu\beta\mu\alpha} + p_2^\mu\epsilon^{\nu\rho\beta\alpha} + p_2^\alpha\epsilon^{\nu\rho\mu\beta}. \tag{D.14}$$

Then, we use the on-shell condition

$$p_1\cdot p_1 = p_2\cdot p_2 = m_V^2, \tag{D.15}$$

and the zero momentum transfer

$$(p_1+p_2)^2 = q^2 = 0 \quad \rightarrow \quad p_1\cdot p_2 = -m_V^2. \tag{D.16}$$

Since the $V_{D+,\alpha}^0$ and $V_{D-,\beta}^0$ are external particles so that the polarisation vectors are orthogonal to their momenta

$$p_1\cdot\epsilon(p_1) = 0 \quad \text{and} \quad p_2\cdot\epsilon(p_2) = 0, \tag{D.17}$$

this is equivalent to imposing

$$p_1^\alpha = 0 \quad \text{and} \quad p_2^\beta = 0. \tag{D.18}$$

After doing Feynman integrals and matching the coefficients of Eq.(D.3), we find the following expressions for the form-factors:

$$
\begin{aligned}
f_1^V &= \frac{(v_{23}v_{12}v_{13}+v_{23}a_{12}a_{13}+a_{23}v_{12}a_{13}+a_{23}a_{12}v_{13})}{4\pi^2} \\
&\times\left[1-(m_2^2+m_3^2)\bar{C}_1-(m_3^2-m_2^2)\Delta C_1+8\bar{C}_{001}\right] \\
&+\frac{(v_{23}v_{12}v_{13}-v_{23}a_{12}a_{13}+a_{23}v_{12}a_{13}-a_{23}a_{12}v_{13})}{4\pi^2}m_1m_2\left[\bar{C}_0+2\bar{C}_1\right] \\
&+\frac{(v_{23}v_{12}v_{13}-v_{23}a_{12}a_{13}-a_{23}v_{12}a_{13}+a_{23}a_{12}v_{13})}{4\pi^2}m_1m_3\left[\bar{C}_0+2\bar{C}_1\right] \\
&-\frac{(v_{23}v_{12}v_{13}+v_{23}a_{12}a_{13}-a_{23}v_{12}a_{13}-a_{23}a_{12}v_{13})}{4\pi^2}m_2m_3\left[2\bar{C}_1\right]\ , \qquad \text{(D.19)} \\
f_2^V &= -\frac{(v_{23}v_{12}v_{13}+v_{23}a_{12}a_{13}+a_{23}v_{12}a_{13}+a_{23}a_{12}v_{13})}{4\pi^2}M_{V^\pm}^2\left[8\bar{C}_{112}+4\bar{C}_{12}\right]\ , \qquad \text{(D.20)} \\
f_3^V &= \frac{(v_{23}v_{12}v_{13}+v_{23}a_{12}a_{13}+a_{23}v_{12}a_{13}+a_{23}a_{12}v_{13})}{4\pi^2}\left[-2-2m_1^2(\bar{C}_0+2\bar{C}_1)\right. \\
&\left.+(m_3^2+m_2^2)\bar{C}_1+(m_3^2-m_2^2)\Delta C_1+8\bar{C}_{00}+8\bar{C}_{001}\right] \\
&-\frac{(v_{23}v_{12}v_{13}-v_{23}a_{12}a_{13}+a_{23}v_{12}a_{13}-a_{23}a_{12}v_{13})}{4\pi^2}m_1m_2\left[\bar{C}_0+2\Delta C_1\right] \\
&+\frac{(v_{23}v_{12}v_{13}-v_{23}a_{12}a_{13}-a_{23}v_{12}a_{13}+a_{23}a_{12}v_{13})}{4\pi^2}m_1m_3\left[2\Delta C_1-\bar{C}_0\right] \\
&+\frac{(v_{23}v_{12}v_{13}+v_{23}a_{12}a_{13}-a_{23}v_{12}a_{13}-a_{23}a_{12}v_{13})}{4\pi^2}m_2m_3\left[2\bar{C}_1\right]\ , \qquad \text{(D.21)} \\
f_5^V &= -\frac{(a_{23}a_{12}a_{13}+a_{23}v_{12}v_{13}+v_{23}a_{12}v_{13}+v_{23}v_{12}a_{13})}{4\pi^2} \\
&\times\left[(m_2^2+m_3^2)\bar{C}_1+(m_3^2-m_2^2)\Delta C_1\right] \\
&-\frac{(a_{23}a_{12}a_{13}-a_{23}v_{12}v_{13}+v_{23}a_{12}v_{13}-v_{23}v_{12}a_{13})}{4\pi^2}m_1m_2\left[\bar{C}_0+2\bar{C}_1\right] \\
&-\frac{(a_{23}a_{12}a_{13}-a_{23}v_{12}v_{13}-v_{23}a_{12}v_{13}+v_{23}v_{12}a_{13})}{4\pi^2}m_1m_3\left[\bar{C}_0+2\bar{C}_1\right] \\
&-\frac{(a_{23}a_{12}a_{13}+a_{23}v_{12}v_{13}-v_{23}a_{12}v_{13}-v_{23}v_{12}a_{13})}{4\pi^2}m_2m_3\left[2\bar{C}_1\right]\ , \qquad \text{(D.22)} \\
f_8^V &= \frac{(a_{23}a_{12}a_{13}+a_{23}v_{12}v_{13}+v_{23}a_{12}v_{13}+v_{23}v_{12}a_{13})}{4\pi^2}M_{V^\pm}^2[2\bar{C}_{12}]\ . \qquad \text{(D.23)}
\end{aligned}
$$

The average and difference of three-point Passarino-Veltman C-functions are defined as

$$
\begin{aligned}
\bar{C}_{\{i\}} &\equiv \frac{1}{2}\left(C_{\{i\}}^{(a)}+C_{\{i\}}^{(b)}\right), \\
\Delta C_{\{i\}} &\equiv \frac{1}{2}\left(C_{\{i\}}^{(a)}-C_{\{i\}}^{(b)}\right). \qquad \text{(D.24)}
\end{aligned}
$$

where $C^r_{\{i\}}$, $(r = a, b)$ are given in terms of to one-loop triangle Feynman integrals

$$\begin{aligned}
\frac{1}{i\pi^2}\int d^4k\ \frac{1}{D^{(r)}} &= C_0^{(r)}\ , \\
\frac{1}{i\pi^2}\int d^4k\ \frac{k^\mu}{D^{(r)}} &= -p_1^\mu C_1^{(r)} + p_2^\mu C_2^{(r)}\ , \\
\frac{1}{i\pi^2}\int d^4k\ \frac{k^\mu k^\nu}{D^{(r)}} &= g^{\mu\nu} C_{00}^{(r)} + p_1^\mu p_1^\nu C_{11}^{(r)} + p_2^\mu p_2^\nu C_{22}^{(r)} - \left(p_1^\mu p_2^\nu + p_1^\nu p_2^\mu\right) C_{12}^{(r)}\ , \\
\frac{1}{i\pi^2}\int d^4k\ \frac{k^\mu k^\nu k^\rho}{D^{(r)}} &= -\left(p_1^\mu g^{\nu\rho} + p_1^\nu g^{\mu\rho} + p_1^\rho g^{\mu\nu}\right) C_{001}^{(r)} \\
&\quad + \left(p_2^\mu g^{\nu\rho} + p_2^\nu g^{\mu\rho} + p_2^\rho g^{\mu\nu}\right) C_{002}^{(r)} \\
&\quad + \left(p_1^\mu p_1^\nu p_2^\rho + p_1^\mu p_1^\rho p_2^\nu + p_1^\nu p_1^\rho p_2^\mu\right) C_{112}^{(r)} \\
&\quad - \left(p_1^\mu p_2^\nu p_2^\rho + p_1^\nu p_2^\mu p_2^\rho + p_1^\rho p_2^\mu p_2^\nu\right) C_{122}^{(r)} \\
&\quad - p_1^\mu p_1^\nu p_1^\rho C_{111}^{(r)} + p_2^\mu p_2^\nu p_2^\rho C_{222}^{(r)}.
\end{aligned} \tag{D.25}$$

The denominators of the Feynman integrals are

$$\begin{aligned}
D^{(a)} &= \left(k^2 - m_1^2\right)\left((k-p_1)^2 - m_3^2\right)\left((k+p_2)^2 - m_2^2\right). \\
D^{(b)} &= \left(k^2 - m_1^2\right)\left((k-p_1)^2 - m_2^2\right)\left((k+p_2)^2 - m_3^2\right).
\end{aligned} \tag{D.26}$$

Both the graphs in figure D.1, have the fermion direction in the clockwise (CW) direction. Diagrams for which the fermion line is in the counter-clockwise direction (CCW) give contributions to the the form-factors, which are related to the clockwise form-factor contributions by

$$\begin{aligned}
f_1^{\rm CCW} &= -f_1^{\rm CW}, \\
f_2^{\rm CCW} &= -f_2^{\rm CW}, \\
f_3^{\rm CCW} &= -f_3^{\rm CW}, \\
f_5^{\rm CCW} &= f_5^{\rm CW}, \\
f_8^{\rm CCW} &= f_8^{\rm CW}.
\end{aligned} \tag{D.27}$$

For the direct detection calculation, we need to evaluate the triangle integrals that correspond to the Feynman diagrams shown in figure D.2. The vertex $V^0_{D+}V^0_{D-}\gamma$ receives the contributions from figure D.2 (a)-(d), while The vertex $V^0_{D+}V^0_{D-}Z$ from figure D.2 (a)-(f). The complete set vertex couplings required to evaluate these triangle graphs is provided in table E.1 and E.2 in section E.

For the numerical evaluation of triangle loops, we have created our own code written in C and PYTHON for computing the necessary Passarino-Veltman (PV) functions, as LoopTools [222] does not provide stable and reliable results for small momentum

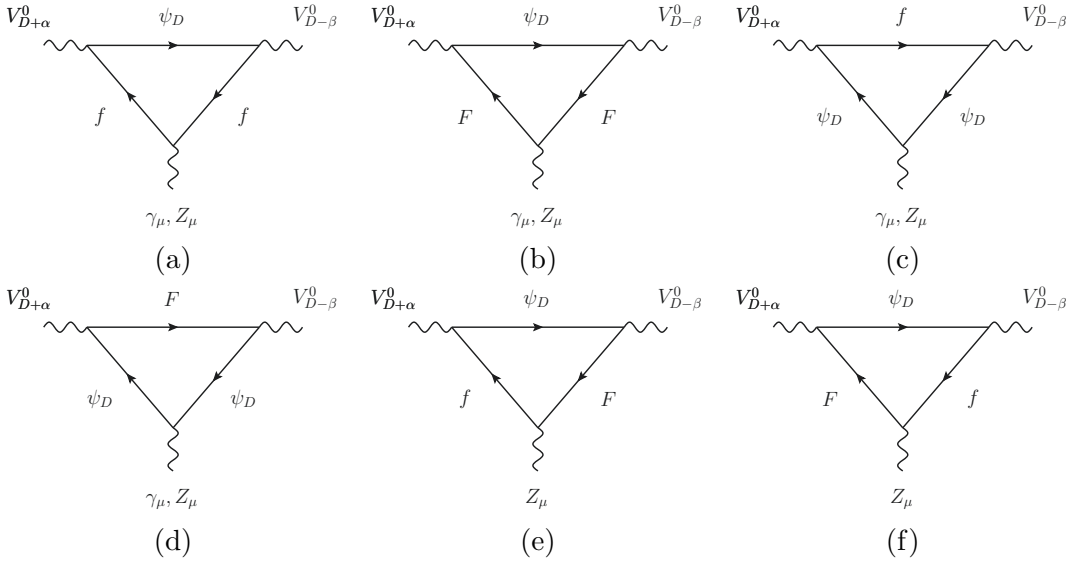

FIGURE D.2: The complete set of Feynman graphs for $V^0_{D+}V^0_{D-}\gamma$ and $V^0_{D+}V^0_{D-}Z$ form factor calculations. The diagram (a)-(d) contribute to the $V^0_{D+}V^0_{D-}\gamma$ vertex and (a)-(f) to the $V^0_{D+}V^0_{D-}Z$ vertex.

$q^2 \to 0$.[2].

[2]These codes are available together with the model files in the HEPMDB [155] repository at the following link `https://hepmdb.soton.ac.uk/hepmdb:0322.0335`

Appendix E

The relevant Feynman rules for FPVDM

Here we have summarised all vertices relevant for the calculation of the KM, fermionic triangle contributions and new physics contributions of g-2. For a generic scalar-fermion-fermion vertex, we separate couplings into $C_S - \gamma_5 C_P$ where the C_S and C_P are the scalar and pseudo-scalar components. Similarly, a generic vector-fermion-fermion coupling can be divided to $\gamma^\mu(C_V - \gamma_5 C_A)$ where C_V and C_A are the vector and axial-vector components. The spacetime index μ must be contracted with the Lorentz index on a vector field.

In table E.1 and E.2, we present Feynman rules for some relevant vertices which are necessary to calculation of KM, fermionic triangle and g-2 contributions. Here Q_f is the electric charge of the SM partner which mixes with F fermion. The coupling $g_W \equiv e/s_W$ and s_W are the weak coupling and sine of weak mixing angle, respectively. The T_3^f is the isospin of third component for the SM partner. The fermionic mixing angles ($\sin\theta_{fL}$ and $\sin\theta_{fR}$) are defined in Eq.(2.23).

Vertices	**Vector couplings** (C_V)	**Axial couplings** (C_A)
$A_\mu \overline{f} f$	eQ_f	0
$A_\mu \overline{\psi}_D \psi_D$	eQ_f	0
$A_\mu \overline{F} F$	eQ_f	0
$Z_\mu \overline{f} f$	$\frac{g_W}{s_W}\left(\frac{1}{2}\cos^2\theta_{fL}\, T_3^f - Q_f s_W^2\right)$	$\frac{g_W}{s_W}\frac{1}{2}\cos^2\theta_{fL}\, T_3^f$
$Z_\mu \overline{\psi}_D \psi_D$	$-\frac{g_W}{c_W} Q_f s_W^2$	0
$Z_\mu \overline{F} F$	$\frac{g_W}{c_W}\left(\frac{1}{2}\sin^2\theta_{fL}\, T_3^f - Q_f s_W^2\right)$	$\frac{g_W}{c_W}\frac{1}{2}\sin^2\theta_{fL}\, T_3^f$
$Z_\mu \overline{f} F$	$\frac{g_W}{c_W}\frac{1}{2}\sin\theta_{fL}\cos\theta_{fL}\, T_3^f$	$\frac{g_W}{c_W}\frac{1}{2}\sin\theta_{fL}\cos\theta_{fL}\, T_3^f$
$V_{D\mu} \overline{\psi}_D f$	$-\frac{g_D}{2\sqrt{2}}\left(\sin\theta_{fL} + \sin\theta_{fR}\right)$	$-\frac{g_D}{2\sqrt{2}}\left(\sin\theta_{fL} - \sin\theta_{fR}\right)$
$V_{D\mu} \overline{\psi}_D F$	$\frac{g_D}{2\sqrt{2}}\left(\cos\theta_{fL} + \cos\theta_{fR}\right)$	$\frac{g_D}{2\sqrt{2}}\left(\cos\theta_{fL} - \cos\theta_{fR}\right)$
$V'_\mu \overline{f} f$	$-\frac{g_D}{4}\left(\sin^2\theta_{fR} + \sin^2\theta_{fL}\right)$	$\frac{g_D}{4}\left(\sin^2\theta_{fR} - \sin^2\theta_{fL}\right)$
$V'_\mu \overline{F} F$	$-\frac{g_D}{4}\left(\cos^2\theta_{fR} + \cos^2\theta_{fL}\right)$	$\frac{g_D}{4}\left(\cos^2\theta_{fR} - \cos^2\theta_{fL}\right)$
$V'_\mu \overline{f} F$	$\frac{g_D}{4}\left(\sin\theta_{fR}\cos\theta_{fR} + \sin\theta_{fL}\cos\theta_{fL}\right)$	$-\frac{g_D}{4}\left(\sin\theta_{fR}\cos\theta_{fR} - \sin\theta_{fL}\cos\theta_{fL}\right)$
$V'_\mu \overline{\psi}_D \psi_D$	$\frac{g_D}{2}$	0

TABLE E.1: The vector (C_V) and axial-vector (C_A) components of a coupling in the form of $\gamma^\mu(C_V - C_A\gamma_5)$ and μ is the Lorentz index of a vector field.

Vertices	**Scalar couplings** C_S	**Pseudo-scalar couplings** C_P
$h \overline{f} f$	$-\frac{Y_\mu}{\sqrt{2}}\cos\theta_{fL}\cos\theta_{fR}$	0
$H_D \overline{f} f$	$\frac{Y'_\mu}{\sqrt{2}}\sin\theta_{fL}\cos\theta_{fR}$	0
$h \overline{F} F$	$-\frac{Y_\mu}{2\sqrt{2}}(\sin\theta_{fR}\cos\theta_{fL} + \sin\theta_{fL}\cos\theta_{fR})$	$-\frac{Y_\mu}{2\sqrt{2}}(\sin\theta_{fR}\cos\theta_{fL} - \sin\theta_{fL}\cos\theta_{fR})$
$H_D \overline{F} F$	$-\frac{Y_\mu}{2\sqrt{2}}(\cos\theta_{fL}\cos\theta_{fR} - \sin\theta_{fL}\sin\theta_{fR})$	$-\frac{Y_\mu}{2\sqrt{2}}(\cos\theta_{fL}\cos\theta_{fR} + \sin\theta_{fL}\sin\theta_{fR})$
$h \overline{F} f$	$-\frac{Y_\mu}{2\sqrt{2}}(\sin\theta_{fR}\cos\theta_{fL} + \sin\theta_{fL}\cos\theta_{fR})$	$\frac{Y_\mu}{2\sqrt{2}}(\sin\theta_{fR}\cos\theta_{fL} - \sin\theta_{fL}\cos\theta_{fR})$
$H_D \overline{F} f$	$-\frac{Y'_\mu}{2\sqrt{2}}(\cos\theta_{fL}\cos\theta_{fR} - \sin\theta_{fL}\sin\theta_{fR})$	$\frac{Y'_\mu}{2\sqrt{2}}(\sin\theta_{fL}\sin\theta_{fR} + \cos\theta_{fL}\cos\theta_{fR})$

TABLE E.2: The scalar and pseudo-scalar components of a coupling in the form of $C_S - C_P\gamma_5$.

Appendix F

The g-2 calculation

The general vertex function for a F-$\bar{F}$-γ vertex is given by

$$\begin{aligned}\Gamma^{\mu} =&\gamma^{\mu}F_1(q^2) + \frac{i\sigma^{\mu\nu}q_{\nu}}{2m}F_2(q^2) + \frac{q^{\mu}}{m}F_3(q^2) \\ &+ (\gamma^{\mu} - \frac{\not{q}q^{\mu}}{q^2})\gamma_5 G_1(q^2) + \frac{i\sigma^{\mu\nu}q_{\nu}\gamma_5}{2m}G_2(q^2) + \frac{q^{\mu}}{m}\gamma_5 G_3(q^2).\end{aligned} \tag{F.1}$$

where F_1, F_2, G_1 and G_2 are called Dirac, Pauli form factor, Anapole and electric dipole moment (EDM), respectively. The only form factor that is relevant to the anomalous magnetic moment is the Pauli one $F_2(0)$. It is defined by

$$a_{\ell} = \frac{g-2}{2} \equiv F_2(0), \tag{F.2}$$

where g is the g-factor which tells us how strong the lepton interact with the external electromagnetic field. In quantum mechanics, the g-factor is the magnetic moment measured in unit of $e\hbar/2m_{\ell}$

$$\vec{M} = g\frac{e}{2m_{\ell}}\vec{S}. \tag{F.3}$$

At one loop, there are kinds of diagrams that contribute to the vertex function $\Gamma^{\mu}(p', p)$.

Vertices	**Vector couplings** (v_{ij})	**Axial couplings** (a_{ij})
$\gamma\mu^+\mu^-$	$-e$	0
$\gamma\mu_D^+\mu_D^-$	$-e$	0
γM^+M^-	$-e$	0
$Z\mu^+\mu^-$	$-\frac{g_W}{c_W}\left(\frac{\cos^2\theta_L}{4}-s_W^2\right)$	$-\frac{g_W}{c_W}\frac{\cos^2\theta_L}{4}$
$ZM^+\mu^-$	$-\frac{g_W}{c_W}\frac{\sin\theta_L\cos\theta_L}{4}$	$-\frac{g_W}{c_W}\frac{\sin\theta_L\cos\theta_L}{4}$
ZM^+M^-	$-\frac{g_W}{c_W}\left(\frac{\sin^2\theta_L}{4}-s_W^2\right)$	$-\frac{g_W}{c_W}\frac{\sin^2\theta_L}{4}$
$Z\mu_D^+\mu_D^-$	$\frac{g_W s_W^2}{c_W}$	0
$V_0\mu^+\mu^-$	$-\frac{g_D}{4}(\sin^2\theta_L+\sin^2\theta_R)$	$-\frac{g_D}{4}(\sin^2\theta_L-\sin^2\theta_R)$
$V_0M^+\mu^-$	$\frac{g_D}{4}(\sin\theta_L\cos\theta_L+\sin\theta_R\cos\theta_R)$	$\frac{g_D}{4}(\sin\theta_L\cos\theta_L-\sin\theta_R\cos\theta_R)$
$V_D\mu_D^+\mu^-$	$-\frac{g_D}{2\sqrt{2}}(\sin\theta_L+\sin\theta_R)$	$-\frac{g_D}{2\sqrt{2}}(\sin\theta_L-\sin\theta_R)$
$V_DM_D^+M^-$	$\frac{g_D}{2\sqrt{2}}(\cos\theta_L+\cos\theta_R)$	$\frac{g_D}{2\sqrt{2}}(\cos\theta_L-\cos\theta_R)$
$W^-\mu^+\nu$	$\frac{g_W}{2\sqrt{2}}\cos\theta_L$	$\frac{g_W}{2\sqrt{2}}\cos\theta_L$
$H\mu^+\mu^-$	$-\frac{Y_\mu}{\sqrt{2}}\cos\theta_L\cos\theta_R$	0
$H_D\mu^+\mu^-$	$\frac{Y'_\mu}{\sqrt{2}}\sin\theta_L\cos\theta_R$	0
HM^+M^-	$-\frac{Y_\mu}{2\sqrt{2}}(\sin\theta_R\cos\theta_L+\sin\theta_L\cos\theta_R)$	$-\frac{Y_\mu}{2\sqrt{2}}(\sin\theta_R\cos\theta_L-\sin\theta_L\cos\theta_R)$
$H_DM^+M^-$	$-\frac{Y_\mu}{2\sqrt{2}}(\cos\theta_L\cos\theta_R-\sin\theta_L\sin\theta_R)$	$-\frac{Y_\mu}{2\sqrt{2}}(\cos\theta_L\cos\theta_R+\sin\theta_L\sin\theta_R)$
$HM^+\mu^-$	$-\frac{Y_\mu}{2\sqrt{2}}(\sin\theta_R\cos\theta_L+\sin\theta_L\cos\theta_R)$	$\frac{Y_\mu}{2\sqrt{2}}(\sin\theta_R\cos\theta_L-\sin\theta_L\cos\theta_R)$
$H_DM^+\mu^-$	$-\frac{Y'_\mu}{2\sqrt{2}}(\cos\theta_L\cos\theta_R-\sin\theta_L\sin\theta_R)$	$\frac{Y'_\mu}{2\sqrt{2}}(\sin\theta_L\sin\theta_R+\cos\theta_L\cos\theta_R)$

TABLE F.1: The vector and axial part of coupling in the form of $\gamma^\mu\,(v-a\gamma_5)$ where v is the vector part, a the axial part and μ is the Lorentz index of a vector field. Here we suppress the $SU(2)_D$ charge of V^+/V^- and write them as V.

F.1 The scalar diagram

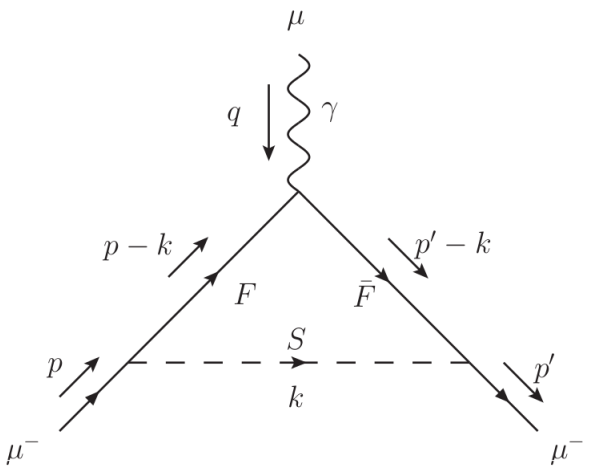

FIGURE F.1: The scalar diagram contributing to the $g_\mu - 2$ calculation. The generic internal fermion and scalar are labelled by F and S.

Let us start with the simplest calculation, the diagram with scalar propagation, fig. F.1 in which the general vertex function is given by[1]

$$\begin{aligned}
&\bar{u}(p')\Gamma^\mu_a u(p) = \\
&\quad i\int \frac{d^dk}{(2\pi)^d}\bar{u}(p')\left[\frac{(Y_V+Y_A\gamma_5)(\not{p}'-\not{k}+m_F)\gamma^\mu(\not{p}-\not{k}+m_F)(Y_V-Y_A\gamma_5)}{\left[(p'-k)^2-m_F^2\right]\left[(p-k)^2-m_F^2\right]\left[k^2-m_S^2\right]}\right]u(p), \\
&=i\int \frac{d^dk}{(2\pi)^d}\bar{u}(p')\frac{1}{\left[(p'-k)^2-m_F^2\right]\left[(p-k)^2-m_F^2\right]\left[k^2-m_S^2\right]}\Bigg[\\
&\quad Y_V^2\left(\not{p}'-\not{k}+m_F\right)\gamma^\mu\left(\not{p}-\not{k}+m_F\right)+Y_VY_A\gamma_5\left(\not{p}'-\not{k}+m_F\right)\gamma^\mu\left(\not{p}-\not{k}+m_F\right) \\
&\quad -Y_VY_A\left(\not{p}'-\not{k}+m_F\right)\gamma^\mu\left(\not{p}-\not{k}+m_F\right) \\
&\quad -Y_A^2\gamma_5\left(\not{p}'-\not{k}+m_F\right)\gamma^\mu\left(\not{p}-\not{k}+m_F\right)\gamma_5\Bigg]u(p),
\end{aligned} \tag{F.4}$$

where

$$\begin{aligned}
den &= \left[(p'-k)^2-m_F^2\right]\left[(p-k)^2-m_F^2\right]\left[k^2-m_S^2\right] \\
\mathcal{N}_1 &= Y_V^2\left(\not{p}'-\not{k}+m_F\right)\gamma^\mu\left(\not{p}-\not{k}+m_F\right), \\
\mathcal{N}_2 &= Y_VY_A\gamma_5\left(\not{p}'-\not{k}+m_F\right)\gamma^\mu\left(\not{p}-\not{k}+m_F\right), \\
\mathcal{N}_3 &= -Y_VY_A\left(\not{p}'-\not{k}+m_F\right)\gamma^\mu\left(\not{p}-\not{k}+m_F\right)\gamma_5, \\
\mathcal{N}_4 &= -Y_A^2\gamma_5\left(\not{p}'-\not{k}+m_F\right)\gamma^\mu\left(\not{p}-\not{k}+m_F\right)\gamma_5
\end{aligned} \tag{F.5}$$

[1]Notice that the coupling at $\bar{\mu}FS$ has the opposite sign to the coupling at $\bar{F}\mu S$.

Using the Dirac equation and the relation between Dirac matrices

$$\not{p}u(p) = m_\mu u(p), \qquad \bar{u}(p')\not{p}' = \bar{u}(p')m_\mu, \qquad \gamma^\mu\gamma^\nu + \gamma^\nu\gamma^\mu = 2g^{\mu\nu}, \tag{F.6}$$

we can simplify the numerator as

$$\begin{aligned}\bar{u}(p')Nu(p) =&\bar{u}(p')\Bigg[Y_V^2\Big\{(m_\mu + m_F)^2\gamma^\mu + \not{k}\gamma^\mu\not{k} - 2k^\mu(m_\mu + m_F)\Big\} \\ &+ Y_V Y_A\Big\{2(m_\mu^2 - m_F^2)\gamma^\mu\gamma_5 - 2\not{k}\gamma^\mu\not{k}\gamma_5 + 4m_\mu k^\mu\gamma_5 - 4m_\mu\not{k}\gamma^\mu\gamma_5\Big\} \\ &- Y_A^2\Big\{-(m_\mu - m_F)^2\gamma^\mu - \not{k}\gamma^\mu\not{k} + 2k^\mu(m_\mu - m_F)\Big\}\Bigg]u(p).\end{aligned} \tag{F.7}$$

Consider the integral denominator. Having used the Feynman parameters, it followds that

$$\frac{1}{[(p'-k)^2 - m_F^2][(p-k)^2 - m_F^2][k^2 - m_S^2]} = 2\int_0^1 dx \int_0^{1-x} dy \frac{1}{D^3} \tag{F.8}$$

where

$$D = x[(p'-k)^2 - m_F^2] + y[(p-k)^2 - m_F^2] + z[k^2 - m_S^2] \tag{F.9}$$

The denominator can be simplified further by using on-shell condition $p\cdot p = p'\cdot p' = m_\mu^2$ and the fact that $x + y + z = 1$. Thus, it is reduced to

$$D = k^2 - 2p'\cdot kx - 2p\cdot ky + (m_\mu^2 - m_F^2)(x+y) - m_S^2(1-x-y). \tag{F.10}$$

In order to make the integral possible to integrate, we want to get rid of the scalar product, $p\cdot k$ and $p'\cdot k$, by shifting the integration variable $k^\mu \to \ell^\mu + xp_2^\mu + yp_1^\mu$. It follows that

$$\begin{aligned}D &= \ell^2 - p'^2x^2 - 2p\cdot p'xy - p^2y^2 + (m_\mu^2 - m_F^2)(x+y) - m_S^2(1-x-y), \\ &= \ell^2 - m_\mu^2(x+y)^2 + (m_\mu^2 - m_F^2)(x+y) - m_S^2(1-x-y) + xyq^2, \\ &= \ell^2 - \Delta,\end{aligned} \tag{F.11}$$

where $\Delta = m_\mu^2(x+y)^2 - (m_\mu^2 - m_F^2)(x+y) + m_S^2(1-x-y) - xyq^2$. Note that we replace $p\cdot p' = m_\mu^2 - q^2/2$ in the second line.

Now let us go back to the numerator of the integral eq. (F.7). After replacing $k^\mu \to \ell^\mu + xp'^\mu + yp^\mu$, we found that

$$\begin{aligned}\bar{u}(p')Nu(p) =&\bar{u}(p')\Bigg[Y_V^2\Big\{(m_\mu + m_F)^2\gamma^\mu + (\not{\ell} + \not{p}'x + \not{p}y)\gamma^\mu(\not{\ell} + \not{p}'x + \not{p}y) \\ &- 2(\ell^\mu + p'^\mu x + p^\mu y)(m_\mu + m_F)\Big\} + Y_V Y_A\Big\{\cdots\Big\}\gamma_5 \\ &- Y_A^2\Big\{-(m_\mu - m_F)^2\gamma^\mu - (\not{\ell} + \not{p}'x + \not{p}y)\gamma^\mu(\not{\ell} + \not{p}'x + \not{p}y)\end{aligned}$$

$$
\begin{aligned}
&+ 2(\ell^\mu + p'^\mu x + p^\mu y)(m_\mu - m_F)\Big\}\Big] u(p),\\
=&\bar{u}(p')\Big[Y_V^2\Big\{(m_\mu + m_F)^2\gamma^\mu + \not{\ell}\gamma^\mu\not{\ell} + (\not{p}'x + \not{p}y)\gamma^\mu(\not{p}'x + \not{p}y)\\
&- 2(p'^\mu x + p^\mu y)(m_\mu + m_F)\Big\} + Y_V Y_A\Big\{\cdots\Big\}\gamma_5\\
&- Y_A^2\Big\{-(m_\mu - m_F)^2\gamma^\mu - \not{\ell}\gamma^\mu\not{\ell} - (\not{p}'x + \not{p}y)\gamma^\mu(\not{p}'x + \not{p}y)\\
&+ 2(p'^\mu x + p^\mu y)(m_\mu - m_F)\Big\}\Big] u(p). \qquad \text{(F.12)}
\end{aligned}
$$

Notice that we wrote $\cdots$ as the coefficient γ_5 because it is not related to the magnetic moment. Thus, we do not need to write it explicitly. However, this term contribute to the electric dipole moment (EDM) of muon. In the second line, we have dropped the terms proportional to ℓ^μ because

$$
\int \frac{d^d\ell}{(2\pi)^d}\frac{\ell^\mu}{D^3} = 0. \qquad \text{(F.13)}
$$

We can simplify it further by using

$$
\begin{aligned}
\int \frac{d^d\ell}{(2\pi)^d}\frac{\ell^\mu\ell^\nu}{D^3} &= \int \frac{d^d\ell}{(2\pi)^d}\frac{\frac{1}{4}g^{\mu\nu}\ell^2}{D^3},\\
\int \frac{d^d\ell}{(2\pi)^d}\frac{\not{\ell}\gamma^\mu\not{\ell}}{D^3} &= \int \frac{d^d\ell}{(2\pi)^d}\frac{1}{D^3}\left(-\frac{1}{2}\gamma^\mu\ell^2\right),\\
\bar{u}(p')(\not{p}'x + \not{p}y)\gamma^\mu(\not{p}'x + \not{p}y)u(p) &= \bar{u}(p')\Big[-m_\mu^2(x+y)^2\gamma^\mu + 2m_\mu(x+y)^2p'^\mu\\
&\quad - 2m_\mu y(x+y)q^\mu + xyq^2\gamma^\mu\Big]u(p). \qquad \text{(F.14)}
\end{aligned}
$$

Then, eq. (F.12), after doing a bit of maths, becomes

$$
\begin{aligned}
\bar{u}(p')Nu(p) =&\bar{u}(p')\Bigg[Y_V^2\Bigg\{\gamma^\mu\left(-\frac{\ell^2}{2} + (m_\mu + m_F)^2 - m_\mu^2(x+y)^2 + xyq^2\right)\\
&+ 2m_\mu(x+y)^2p'^\mu - 2m_\mu y(x+y)q^\mu - 2(p'^\mu x + p^\mu y)(m_\mu + m_F)\Bigg\}\\
&+ Y_V Y_A\Big\{\cdots\Big\} - Y_A^2\Bigg\{\gamma^\mu\left(\frac{\ell^2}{2} - (m_\mu - m_F)^2 + m_\mu^2(x+y)^2 - xyq^2\right)\\
&- 2m_\mu(x+y)^2p'^\mu + 2m_\mu y(x+y)q^\mu + 2(p'^\mu x + p^\mu y)(m_\mu - m_F)\Bigg\}\Bigg]u(p),\\
=&\bar{u}(p')\Bigg[Y_V^2\Bigg\{\gamma^\mu\left(-\frac{\ell^2}{2} + (m_\mu + m_F)^2 - m_\mu^2(x+y)^2 + xyq^2\right)\\
&+ 2m_\mu(x+y)^2\left(\frac{P^\mu + q^\mu}{2}\right) - 2m_\mu y(x+y)q^\mu
\end{aligned}
$$

$$
\begin{aligned}
&- 2\left[\left(\frac{P^\mu+q^\mu}{2}\right)x+\left(\frac{P^\mu-q^\mu}{2}\right)y\right](m_\mu+m_F)\Bigg\}+Y_VY_A\Big\{\cdots\Big\}\\
&- Y_A^2\Bigg\{\gamma^\mu\left(\frac{\ell^2}{2}-(m_\mu-m_F)^2+m_\mu^2(x+y)^2-xyq^2\right)\\
&- 2m_\mu(x+y)^2\left(\frac{P^\mu+q^\mu}{2}\right)+2m_\mu y(x+y)q^\mu\\
&+ 2\left[\left(\frac{P^\mu+q^\mu}{2}\right)x+\left(\frac{P^\mu-q^\mu}{2}\right)y\right](m_\mu-m_F)\Bigg\}\Bigg]u(p). \qquad \text{(F.15)}
\end{aligned}
$$

We have replaced $p'^\mu=(P^\mu+q^\mu)/2$ and $p^\mu=(P^\mu-q^\mu)/2$ in the last line.

Let us recall the Gordon identity which states that

$$
\bar u(p')\gamma^\mu u(p)=\bar u(p')\left[\frac{P^\mu}{2m_\mu}+\frac{i\sigma^{\mu\nu}q_\nu}{2m_\mu}\right]u(p). \qquad \text{(F.16)}
$$

So we can write P^μ in terms of γ^μ and $\sigma^{\mu\nu}$ by using eq. (F.16). Finally, the integral numerator for the scalar diagram is given by

$$
\begin{aligned}
\bar u(p')Nu(p)=&\bar u(p')\Big[\gamma^\mu(\cdots)+q^\mu(\cdots)+\frac{i\sigma^{\mu\nu}q_\nu}{2m_\mu}2m_\mu\Big(Y_V^2\left[(m_\mu+m_F)(x+y)\right.\\
&\left.-m_\mu(x+y)^2\right]+Y_A^2\left[(m_\mu-m_F)(x+y)-m_\mu(x+y)^2\right]\Big)\Big]u(p). \qquad \text{(F.17)}
\end{aligned}
$$

Comparing with

$$
\Gamma^\mu(p',p)=\gamma^\mu F_1(q^2)+\frac{i\sigma^{\mu\nu}q_\nu}{2m_\mu}F_2(q^2), \qquad \text{(F.18)}
$$

the Pauli form factor $F_2(0)$ for the scalar diagram reads

$$
\begin{aligned}
F_2(0)=&\,i\int\frac{d^d\ell}{(2\pi)^d}\,2\int_0^1dx\int_0^{1-x}dy\frac{1}{(\ell^2-\Delta)^3}2m_\mu\Big(Y_V^2\left[(m_\mu+m_F)(x+y)\right.\\
&\left.-m_\mu(x+y)^2\right]+Y_A^2\left[(m_\mu-m_F)(x+y)-m_\mu(x+y)^2\right]\Big),\\
=&\,2i\int_0^1dx\int_0^{1-x}dy\,2m_\mu\Big(Y_V^2\left[(m_\mu+m_F)(x+y)-m_\mu(x+y)^2\right]\\
&+Y_A^2\left[(m_\mu-m_F)(x+y)-m_\mu(x+y)^2\right]\Big)\int\frac{d^d\ell}{(2\pi)^d}\frac{1}{(\ell^2-\Delta)^3}. \qquad \text{(F.19)}
\end{aligned}
$$

Now $\Delta = m_\mu^2(x+y)^2-(m_\mu^2-m_F^2)(x+y)+m_S^2(1-x-y)$. The integration over spacetime is referred to eq.(A.44) in Peskin book where

$$\int \frac{d^d\ell}{(2\pi)^d}\frac{1}{(\ell^2-\Delta)^n} = \frac{(-1)^n i}{(4\pi)^{d/2}}\frac{\Gamma(n-\frac{d}{2})}{\Gamma(n)}\left(\frac{1}{\Delta}\right)^{n-\frac{d}{2}}, \tag{F.20}$$

$$\left(\frac{1}{\Delta}\right)^{2-\frac{d}{2}} = 1-\left(2-\frac{d}{2}\right)\log\Delta+\cdots \tag{F.21}$$

$$\Gamma(x) = \frac{1}{x}-\gamma_E+\mathcal{O}(x) \tag{F.22}$$

In the case that $n=3$, we found

$$\int \frac{d^d\ell}{(2\pi)^d}\frac{1}{(\ell^2-\Delta)^3} = \frac{-i}{2(4\pi)^2}\frac{1}{\Delta}. \tag{F.23}$$

Therefore, we arrive at

$$\begin{aligned} F_2(0) = {} & \frac{1}{16\pi^2}\int_0^1 dx\int_0^{1-x} dy\ \left[m_\mu^2(x+y)^2-(m_\mu^2-m_F^2)(x+y)+m_S^2(1-x-y)\right]^{-1} \\ & \times 2m_\mu\Big(Y_V^2\left[(m_\mu+m_F)(x+y)-m_\mu(x+y)^2\right] \\ & + Y_A^2\left[(m_\mu-m_F)(x+y)-m_\mu(x+y)^2\right]\Big) \end{aligned} \tag{F.24}$$

$$\begin{aligned} F_2(0) = {} & \frac{2(Y_V^2+Y_A^2)m_F^2+2(Y_V^2-Y_A^2)m_\mu m_F-(Y_V^2+Y_A^2)(m_\mu^2+2m_S^2)}{16\pi^2 m_\mu^2} \\ & -\frac{1}{16\pi^2 m_\mu^4}\Big((Y_V^2+Y_A^2)m_F^4+(Y_V^2-Y_A^2)m_\mu m_F^3+(Y_V^2+Y_A^2)m_S^4 \\ & -(Y_V^2-Y_A^2)(m_\mu^3 m_F+m_\mu m_F m_S^2)-(Y_V^2+Y_A^2)(m_\mu^2 m_F^2+2m_F^2 m_S^2)\Big)\log\left[\frac{m_F^2}{m_S^2}\right] \\ & +\frac{1}{8\pi^2 m_\mu^4}\Big((Y_V^2+Y_A^2)m_F^6+(Y_V^2-Y_A^2)m_\mu m_F^5+(Y_V^2+Y_A^2)m_S^4(m_\mu^2-m_S^2) \\ & -2(Y_V^2-Y_A^2)m_\mu m_F^3(m_\mu^2+m_S^2)-(Y_V^2+Y_A^2)m_F^4(2m_\mu^2+3m_S^2) \\ & +(Y_V^2-Y_A^2)m_\mu m_F(m_\mu^4+m_S^4)+(Y_V^2+Y_A^2)m_F^2(m_\mu^4+m_\mu^2 m_S^2+3m_S^4)\Big) \\ & \times\frac{1}{\sqrt{\lambda}}\log\left[\frac{\sqrt{\lambda}-m_\mu^2+m_F^2+m_S^2}{2m_F m_S}\right] \end{aligned} \tag{F.25}$$

where $\lambda = m_\mu^4 + m_F^4 + m_S^4 - 2m_\mu^2 m_F^2 - 2m_\mu^2 m_S^2 - 2m_F^2 m_S^2$. In order to get the result, these identities have been applied

$$\tan^{-1}(iz) = i\tanh^{-1}(z), \tag{F.26}$$

$$\tanh^{-1}(x) - \tanh^{-1}(y) = \tanh^{-1}\left(\frac{x-y}{1-xy}\right), \tag{F.27}$$

$$\tanh^{-1}(x) = \frac{1}{2}\log\left(\frac{1+x}{1-x}\right). \tag{F.28}$$

F.2 The NC diagram

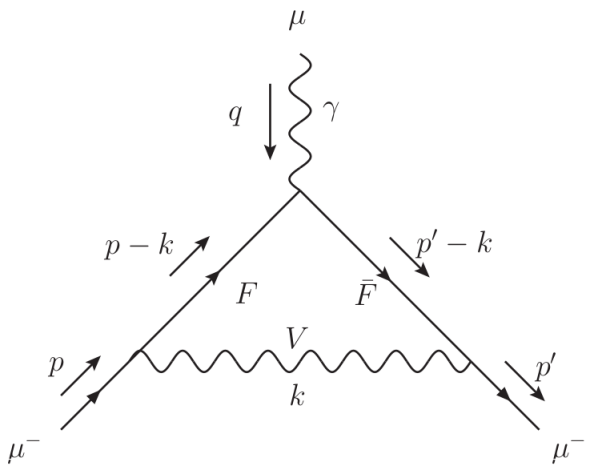

FIGURE F.2: The NC diagram contributing to the $g_\mu - 2$ calculation. The generic internal fermion and vector are labelled by F and V.

For vector diagram, fig. F.2, the loop integral is given by

$$\begin{aligned}
&\bar{u}(p')\Gamma_b^\mu u(p) = \\
&\quad - i\int \frac{d^D k}{(2\pi)^D}\bar{u}(p')\Big[\gamma^\rho(v - a\gamma_5)\frac{(\not{p}' - \not{k} + m_F)}{(p'-k)^2 - m_F^2}\gamma^\mu\frac{(\not{p} - \not{k} + m_F)}{(p-k)^2 - m_F^2} \\
&\times \gamma^\nu(v - a\gamma_5)\frac{\left(g_{\nu\rho} - \frac{k_\nu k_\rho}{m_V^2}\right)}{k^2 - m_V^2}\Big]u(p)
\end{aligned} \tag{F.29}$$

Let us separate the numerator as

$$\bar{u}(p')\Gamma_V^\mu u(p) = -i\int \frac{d^D k}{(2\pi)^D}\bar{u}(p')\frac{[N_1 + N_2]}{[(p'-k)^2 - m_F^2][(p-k)^2 - m_F^2][k^2 - m_V^2]}u(p), \tag{F.30}$$

where

$$N_1 = \gamma^\nu(v - a\gamma_5)(\not{p}' - \not{k} + m_F)\gamma^\mu(\not{p} - \not{k} + m_F)\gamma_\nu(v - a\gamma_5), \tag{F.31}$$

$$N_2 = -\frac{1}{m_V^2}\not{k}(v - a\gamma_5)(\not{p}' - \not{k} + m_F)\gamma^\mu(\not{p} - \not{k} + m_F)\not{k}(v - a\gamma_5). \tag{F.32}$$

Consider $\bar{u}(p')N_1u(p)$

$$\begin{aligned}
\bar{u}(p')N_1u(p) =&\bar{u}(p')\Big[v^2\gamma^\nu(\not{p}' - \not{k} + m_F)\gamma^\mu(\not{p} - \not{k} + m_F)\gamma_\nu \\
&+ a^2\gamma^\nu\gamma_5(\not{p}' - \not{k} + m_F)\gamma^\mu(\not{p} - \not{k} + m_F)\gamma_\nu\gamma_5 + (\cdots)\gamma_5\Big]u(p) \\
=&\bar{u}(p')\Big[v^2\gamma^\nu(\not{p}' - \not{k} + m_F)\gamma^\mu(\not{p} - \not{k} + m_F)\gamma_\nu \\
&+ a^2\gamma^\nu\gamma_5(\not{p}' - \not{k} - m_F)\gamma^\mu(\not{p} - \not{k} - m_F)\gamma_\nu\gamma_5 + (\cdots)\gamma_5\Big]u(p) \\
=&\bar{u}(p')\Big[(v^2 + a^2)\gamma^\nu(\not{p}' - \not{k})\gamma^\mu(\not{p} - \not{k})\gamma_\nu + (v^2 - a^2)m_F\gamma^\nu(\not{p}' - \not{k})\gamma^\mu\gamma_\nu \\
&+ (v^2 - a^2)m_F\gamma^\nu\gamma^\mu(\not{p} - \not{k})\gamma_\nu + (v^2 + a^2)m_F^2\gamma^\nu\gamma^\mu\gamma_\nu + (\cdots)\gamma_5\Big]u(p)
\end{aligned} \tag{F.33}$$

eq. (F.33) can be simplified by using these identities

$$\gamma^\nu\gamma^\alpha\gamma^\mu\gamma^\beta\gamma_\nu = -2\gamma^\beta\gamma^\mu\gamma^\alpha, \tag{F.34}$$

$$\gamma^\nu\gamma^\alpha\gamma^\mu\gamma_\nu = 4g^{\alpha\mu}, \tag{F.35}$$

$$\gamma^\nu\gamma^\mu\gamma_\nu = -2\gamma^\mu. \tag{F.36}$$

It follows that

$$\begin{aligned}
\bar{u}(p')N_1u(p) =&\bar{u}(p')\Big[-2(v^2 + a^2)(\not{p} - \not{k})\gamma^\mu(\not{p}' - \not{k}) + 4m_F(v^2 - a^2)\left(p^\mu + p'^\mu - 2k^\mu\right) \\
&- 2m_F^2(v^2 + a^2)\gamma^\mu + (\cdots)\gamma_5\Big]u(p).
\end{aligned} \tag{F.37}$$

The above equation can be further simplified by replacing $p^\mu = p'^\mu - q^\mu$ and $p'^\mu = p^\mu + q^\mu$ and using Dirac equation. With these, we get

$$\begin{aligned}
\bar{u}(p')N_1u(p) =&\bar{u}(p')\Big[-2(v^2 + a^2)(m_\mu - \not{q} - \not{k})\gamma^\mu(m_\mu + \not{q} - \not{k}) \\
&+ 4m_F(v^2 - a^2)\left(p^\mu + p'^\mu - 2k^\mu\right) - 2m_F^2(v^2 + a^2)\gamma^\mu + (\cdots)\gamma_5\Big]u(p), \\
=&\bar{u}(p')\Big[-2(v^2 + a^2)\Big\{m_\mu^2\gamma^\mu + m_\mu(\gamma^\mu\not{q} - \not{q}\gamma^\mu) - m_\mu(\gamma^\mu\not{k} + \not{k}\gamma^\mu) - \not{q}\gamma^\mu\not{q} \\
&+ \not{q}\gamma^\mu\not{k} - \not{k}\gamma^\mu\not{q} + \not{k}\gamma^\mu\not{k}\Big\} + 4m_F(v^2 - a^2)\left(p^\mu + p'^\mu - 2k^\mu\right) \\
&- 2m_F^2(v^2 + a^2)\gamma^\mu + (\cdots)\gamma_5\Big]u(p).
\end{aligned} \tag{F.38}$$

The second and third terms are written by using anti-commutation and commutation properties of Dirac matrices.

$$\begin{aligned}\gamma^\mu\gamma^\nu - \gamma^\nu\gamma^\mu &= \frac{2}{i}\sigma^{\mu\nu},\\ \gamma^\mu\gamma^\nu + \gamma^\nu\gamma^\mu &= 2g^{\mu\nu}\end{aligned} \tag{F.39}$$

eq. (F.38) becomes

$$\begin{aligned}\bar{u}(p')N_1u(p) =&\bar{u}(p')\Big[-2(v^2+a^2)\Big\{-2m_\mu i\sigma^{\mu\nu}q_\nu - 2m_\mu k^\mu\\ &- \not{q}\not{k}\gamma^\mu + \not{k}\not{q}\gamma^\mu + \not{k}\gamma^\mu\not{k}\Big\} + 4m_F(v^2-a^2)\left(p^\mu + p'^\mu - 2k^\mu\right)\\ &+ (\cdots)\,\gamma^\mu + (\cdots)\,q^\mu + (\cdots)\,\gamma_5\Big]u(p).x\end{aligned} \tag{F.40}$$

Notice that we have written terms proportional to γ^μ, q^μ and γ_5 implicitly because they do not contribute to the Pauli form factor. We also need the following results. Their derivations are quite straightforward. So I claim that

$$\begin{aligned}\bar{u}(p')\left[\not{k}\not{q}\gamma^\mu - \not{q}\not{k}\gamma^\mu\right]u(p) &= \bar{u}(p')\left[-4\not{k}p^\mu + (\cdots)\,\gamma^\mu\right]u(p),\\ \bar{u}(p')\left[\not{k}\gamma^\mu\not{k}\right]u(p) &= \bar{u}(p')\left[m_\mu(x+y)^2(p^\mu+p'^\mu) + (\cdots)\,q^\mu + (\cdots)\,\gamma^\mu\right]u(p)\end{aligned} \tag{F.41}$$

eq. (F.40) becomes

$$\begin{aligned}\bar{u}(p')N_1u(p) =&\bar{u}(p')\Big[-2(v^2+a^2)\Big\{-2m_\mu i\sigma^{\mu\nu}q_\nu - 2m_\mu k^\mu\\ &- 4\not{k}p^\mu + m_\mu(x+y)^2(p^\mu+p'^\mu)\Big\} + 4m_F(v^2-a^2)\left(p^\mu + p'^\mu - 2k^\mu\right)\\ &+ (\cdots)\,\gamma^\mu + (\cdots)\,q^\mu + (\cdots)\,\gamma_5\Big]u(p).\end{aligned} \tag{F.42}$$

Now we shift the momentum $k^\mu \to \ell^\mu + p'^\mu x + p^\mu y$ together with rewriting $p'^\mu = \left(P^\mu + q^\mu\right)/2$ and $p^\mu = \left(P^\mu - q^\mu\right)/2$. We get

$$\begin{aligned}\bar{u}(p')N_1u(p) =&\bar{u}(p')\Big[-2(v^2+a^2)\Big\{-2m_\mu i\sigma^{\mu\nu}q_\nu + \left(-3m_\mu(x+y) + m_\mu(x+y)^2\right)P^\mu\Big\}\\ &+ 4m_F(v^2-a^2)\left(1-x-y\right)P^\mu + (\cdots)\,\gamma^\mu + (\cdots)\,q^\mu + (\cdots)\,\gamma_5\Big]u(p).\end{aligned} \tag{F.43}$$

By using the Gordon's identity eq. (F.16), We can write

$$\begin{aligned}\bar{u}(p')N_1u(p) =&\bar{u}(p')2m_\mu\Big[m_\mu(v^2+a^2)\left(4-6(x+y)+2(x+y)^2\right)\\&+m_F(v^2-a^2)\left(-4+4(x+y)\right)\Big]\frac{i\sigma^{\mu\nu}q_\nu}{2m_\mu}u(p),\\=&\bar{u}(p')2m_\mu\Big[v^2\Big\{(4m_\mu-4m_F)+(4m_F-6m_\mu)(x+y)+2m_\mu(x+y)^2\Big\}\\&+a^2\{m_F\to-m_F\}\Big]\frac{i\sigma^{\mu\nu}q_\nu}{2m_\mu}u(p).\end{aligned}\tag{F.44}$$

Now let us turn back to the N_2 part

$$\begin{aligned}\bar{u}(p')N_2u(p) =&-\frac{1}{m_V^2}\bar{u}(p')\not{k}(v-a\gamma_5)(\not{p}'-\not{k}+m_F)\gamma^\mu(\not{p}-\not{k}+m_F)\not{k}(v-a\gamma_5)u(p)\\=&-\frac{1}{m_V^2}\bar{u}(p')\Big[v^2\not{k}(\not{p}'-\not{k}+m_F)\gamma^\mu(\not{p}-\not{k}+m_F)\not{k}\\&+a^2\not{k}\gamma_5(\not{p}'-\not{k}+m_F)\gamma^\mu(\not{p}-\not{k}+m_F)\not{k}\gamma_5+(\cdots)\gamma_5\Big]u(p)\\=&-\frac{1}{m_V^2}\bar{u}(p')\Big[v^2\not{k}(\not{p}'-\not{k}+m_F)\gamma^\mu(\not{p}-\not{k}+m_F)\not{k}\\&+a^2\not{k}(\not{p}'-\not{k}-m_F)\gamma^\mu(\not{p}-\not{k}-m_F)\not{k}+(\cdots)\gamma_5\Big]u(p)\\=&-\frac{1}{m_V^2}\bar{u}(p')\Big[\left(v^2+a^2\right)\not{k}(\not{p}'-\not{k})\gamma^\mu(\not{p}-\not{k})\not{k}+\left(v^2-a^2\right)m_F\not{k}(\not{p}'-\not{k})\gamma^\mu\not{k}\\&+\left(v^2-a^2\right)m_F\not{k}\gamma^\mu(\not{p}-\not{k})\not{k}+\left(v^2+a^2\right)m_F^2\not{k}\gamma^\mu\not{k}+(\cdots)\gamma_5\Big]u(p)\end{aligned}\tag{F.45}$$

In the third line, we have swapped γ_5 through all γ^μ from the left to the right with the use of $\{\gamma_5,\gamma^\mu\}=0$, until it meets with another γ_5 then we used $\gamma_5^2=I$. Next, we can move the exterior $\not{k}$ into the bracket and use $\not{k}\not{k}=k^2$. As a result, we get

$$\begin{aligned}\bar{u}(p')N_2u(p) =&-\frac{1}{m_V^2}\bar{u}(p')\Big[\left(v^2+a^2\right)(\not{k}\not{p}'-k^2)\gamma^\mu(\not{p}\not{k}-k^2)+\left(v^2-a^2\right)m_F(\not{k}\not{p}'-k^2)\gamma^\mu\not{k}\\&+\left(v^2-a^2\right)m_F\not{k}\gamma^\mu(\not{p}\not{k}-k^2)+\left(v^2+a^2\right)m_F^2\not{k}\gamma^\mu\not{k}+(\cdots)\gamma_5\Big]u(p),\\=&-\frac{1}{m_V^2}\bar{u}(p')\Big[\left(v^2+a^2\right)\Big\{\not{k}\not{p}'\gamma^\mu\not{p}\not{k}-k^2\not{k}\not{p}'\gamma^\mu-k^2\gamma^\mu\not{p}\not{k}+k^4\gamma^\mu\Big\}\\&+\left(v^2-a^2\right)\Big\{m_F\not{k}\not{p}'\gamma^\mu\not{k}-m_Fk^2\gamma^\mu\not{k}+m_F\not{k}\gamma^\mu\not{p}\not{k}-m_Fk^2\not{k}\gamma^\mu\Big\}\\&+\left(v^2+a^2\right)m_F^2\not{k}\gamma^\mu\not{k}+(\cdots)\gamma_5\Big]u(p).\end{aligned}\tag{F.46}$$

We would like to move $\not{p}'$ and $\not{p}$ to the very left and right side, respectively, so we can use Dirac equation. It follows that

$$\begin{aligned}\bar{u}(p')N_2u(p) =&-\frac{1}{m_V^2}\bar{u}(p')\Big[\left(v^2+a^2\right)\Big\{\left(2k\cdot p'-\not{p}'\not{k}\right)\gamma^\mu\left(2k\cdot p-\not{k}\not{p}\right)-k^2\left(2k\cdot p'-\not{p}'\not{k}\right)\gamma^\mu\\&-k^2\gamma^\mu\left(2k\cdot p-\not{k}\not{p}\right)+k^4\gamma^\mu\Big\}\\&+\left(v^2-a^2\right)\Big\{m_F\left(2k\cdot p'-\not{p}'\not{k}\right)\gamma^\mu\not{k}-m_Fk^2\left(\gamma^\mu\not{k}+\not{k}\gamma^\mu\right)\end{aligned}$$

$$
\begin{aligned}
&+ m_F \not{k}\gamma^\mu \left(2k\cdot p - \not{k}\not{p}\right) \Big\} \\
&+ \left(v^2+a^2\right) m_F^2 \not{k}\gamma^\mu \not{k} + (\cdots)\,\gamma_5 \Big] u(p), \\
=& -\frac{1}{m_V^2}\bar{u}(p')\Big[\left(v^2+a^2\right) \Big\{ \left(2k\cdot p' - m_\mu \not{k}\right)\gamma^\mu \left(2k\cdot p - m_\mu \not{k}\right) - k^2 \left(2k\cdot p' - m_\mu \not{k}\right)\gamma^\mu \\
&- k^2 \gamma^\mu \left(2k\cdot p - m_\mu \not{k}\right) + k^4 \gamma^\mu \Big\} \\
&+ \left(v^2-a^2\right) \Big\{ m_F \left(2k\cdot p' - m_\mu \not{k}\right)\gamma^\mu \not{k} - 2m_F k^2 k^\mu \\
&+ m_F \not{k}\gamma^\mu \left(2k\cdot p - m_\mu \not{k}\right) \Big\} \\
&+ \left(v^2+a^2\right) m_F^2 \not{k}\gamma^\mu \not{k} + (\cdots)\,\gamma_5 \Big] u(p), \\
=& -\frac{1}{m_V^2}\bar{u}(p')\Big[\left(v^2+a^2\right) \Big\{ 4k\cdot p k\cdot p' \gamma^\mu - 2m_\mu k\cdot p' \gamma^\mu \not{k} - 2m_\mu k\cdot p \not{k}\gamma^\mu + m_\mu^2 \not{k}\gamma^\mu \not{k} \\
&- 2k^2 k\cdot p' \gamma^\mu + m_\mu k^2 \left(\not{k}\gamma^\mu + \gamma^\mu \not{k}\right) - 2k^2 k\cdot p \gamma^\mu + k^4 \gamma^\mu \Big\} \\
&+ \left(v^2-a^2\right) \Big\{ 2m_F k\cdot p' \gamma^\mu \not{k} - 2m_\mu m_F \not{k}\gamma^\mu \not{k} - 2m_F k^2 k^\mu + 2m_F k\cdot p \not{k}\gamma^\mu \Big\} \\
&+ \left(v^2+a^2\right) m_F^2 \not{k}\gamma^\mu \not{k} + (\cdots)\,\gamma_5 \Big] u(p). \qquad \text{(F.47)}
\end{aligned}
$$

On the sixth term, we can use $\not{k}\gamma^\mu + \gamma^\mu \not{k} = 2k^\mu$ and write the terms proportional to γ^μ implicitly because they do not contribute to a_μ. We have

$$
\begin{aligned}
\bar{u}(p')N_2 u(p) =& -\frac{1}{m_V^2}\bar{u}(p')\Big[\left(v^2+a^2\right) \Big\{ -2m_\mu k\cdot p' \gamma^\mu \not{k} - 2m_\mu k\cdot p \not{k}\gamma^\mu + \left(m_\mu^2 + m_F^2\right) \not{k}\gamma^\mu \not{k} \\
&+ 2m_\mu k^2 k^\mu \Big\} \\
&+ \left(v^2-a^2\right) \Big\{ 2m_F k\cdot p' \gamma^\mu \not{k} - 2m_\mu m_F \not{k}\gamma^\mu \not{k} - 2m_F k^2 k^\mu + 2m_F k\cdot p \not{k}\gamma^\mu \Big\} \\
&+ (\cdots)\,\gamma^\mu + (\cdots)\,\gamma_5 \Big] u(p), \\
=& -\frac{1}{m_V^2}\bar{u}(p')\Big[v^2 \Big\{ (-2m_\mu + 2m_F)(k\cdot p' \gamma^\mu \not{k} + k\cdot p \not{k}\gamma^\mu) \\
&+ (2m_\mu - 2m_F) k^2 k^\mu + (m_\mu - m_F)^2 \not{k}\gamma^\mu \not{k} + a^2 \left\{ m_F \to -m_F \right\} \Big\} \Big] \qquad \text{(F.48)}
\end{aligned}
$$

Having shifted the momentum $k^\mu \to \ell^\mu + p'^\mu x + p^\mu y$, we found that

$$
\begin{aligned}
\bar{u}(p')(k\cdot p' \gamma^\mu \not{k} + k\cdot p \not{k}\gamma^\mu)(p) &= \bar{u}(p')\Big[\frac{2}{d}\ell^2 (p^\mu + p'^\mu) + 2m_\mu^2 (x+y)(p'^\mu x + p^\mu y) + (\cdots)\gamma^\mu \Big] u(p), \\
\bar{u}(p')k^2 k^\mu u(p) &= \bar{u}(p')\Big[\Big(1 + \frac{2}{d}\Big)\ell^2 (p'^\mu x + p^\mu y) + m_\mu^2 (x+y)^2 (p'^\mu x + p^\mu y) \Big] u(p), \\
\bar{u}(p')\not{k}\gamma^\mu \not{k} u(p) &= \bar{u}(p')\Big[\frac{1}{d}\ell^2 \gamma^\mu + m_\mu (x+y)(p'^\mu x + p^\mu y) \Big] u(p) \qquad \text{(F.49)}
\end{aligned}
$$

On substituting eq. (F.49) into eq. (F.48), we get

$$\begin{aligned}\bar{u}(p')N_2u(p) =& -\frac{1}{m_V^2}\bar{u}(p')\Big[v^2\Big\{(-2m_\mu+2m_F)\Big(\frac{2}{d}\ell^2(p^\mu+p'^\mu)+2m_\mu^2(x+y)(p'^\mu x+p^\mu y)\Big)\\ &+(2m_\mu-2m_F)\Big(\Big(1+\frac{2}{d}\Big)\ell^2(p'^\mu x+p^\mu y)+m_\mu^2(x+y)^2(p'^\mu x+p^\mu y)\Big)\\ &+(m_\mu-m_F)^2\Big(\frac{1}{d}\ell^2\gamma^\mu+m_\mu(x+y)(p'^\mu x+p^\mu y)\Big)\\ &+a^2\left\{m_F\to -m_F\right\}\Big\}\Big] \end{aligned} \tag{F.50}$$

In the above results, we have dropped the term proportional to ℓ^μ, γ^μ and q^μ. Those terms do not contribute to $g-2$. By substituting $p^\mu = (P^\mu - q^\mu)/2$ and $p'^\mu = (P^\mu + q^\mu)/2$, we arrive at

$$\begin{aligned}\bar{u}(p')N_2u(p) =& -\frac{1}{m_V^2}\bar{u}(p')\Bigg[v^2\Big\{(m_\mu-m_F)\big((d+2)(x+y)-4\big)\frac{\ell^2}{d}\\ &+m_\mu^2(m_\mu-m_F)(x+y)^3+m_\mu(m_F^2-m_\mu^2)(x+y)^2\Big\}\\ &+a^2\left\{m_F\to -m_F\right\}\Bigg]P^\mu u(p). \end{aligned} \tag{F.51}$$

Now we use the Gordon identity eq. (F.16) to write P^μ in terms of γ^μ and $i\sigma^{\mu\nu}q_\nu$. We get

$$\begin{aligned}\bar{u}(p')N_2u(p) =& \frac{2m_\mu}{m_V^2}\bar{u}(p')\Bigg[v^2\Big\{(m_\mu-m_F)\big((d+2)(x+y)-4\big)\frac{\ell^2}{d}\\ &+m_\mu^2(m_\mu-m_F)(x+y)^3+m_\mu(m_F^2-m_\mu^2)(x+y)^2\Big\}\\ &+a^2\left\{m_F\to -m_F\right\}\Bigg]\left(\frac{i\sigma^{\mu\nu}q_\nu}{2m_\mu}\right)u(p). \end{aligned} \tag{F.52}$$

At this point, we are done with the numerator part. The denominator part is given by

$$\frac{1}{[(p'-k)^2-m_F^2][(p-k)^2-m_F^2][k^2-m_V^2]} = 2\int_0^1 dx\int_0^{1-x} dy\frac{1}{D^3} \tag{F.53}$$

where

$$D=\ell^2-\Delta,\quad \Delta = m_\mu^2(x+y)^2-(m_\mu^2-m_F^2)(x+y)+m_V^2(1-x-y)-xyq^2. \tag{F.54}$$

Notice that we have terms proportional to ℓ^2 in eq. (F.52). Let us consider this integral first.

$$\int\frac{d^d\ell}{(2\pi)^d}\frac{\ell^2}{(\ell^2-\Delta)^n} = \frac{(-1)^{n-1}i}{(4\pi)^{d/2}}\frac{d}{2}\frac{\Gamma(n-\frac{d}{2}-1)}{\Gamma(n)}\left(\frac{1}{\Delta}\right)^{n-\frac{d}{2}-1}. \tag{F.55}$$

Here we use $d = 4 - 2\epsilon$. In the case of $n = 3$, the integral becomes

$$\int \frac{d^d\ell}{(2\pi)^d} \frac{\ell^2}{(\ell^2 - \Delta)^3} = \frac{i}{16\pi^2} \frac{d}{4} \Gamma(\epsilon) \left(\frac{4\pi}{\Delta}\right)^{\epsilon}. \tag{F.56}$$

Now we can do the momentum integration as follow

$$\begin{aligned}
&\int \frac{d^d\ell}{(2\pi)^d} \frac{((d+2)(x+y)-4)}{d} \frac{\ell^2}{(\ell^2-\Delta)^3} \\
&\qquad = \frac{((4-2\epsilon+2)(x+y)-4)}{d} \frac{i}{16\pi^2} \frac{d}{4} \Big(\frac{1}{\epsilon} - \log\left(\frac{\Delta}{4\pi e^{-\gamma_E}}\right) + \mathcal{O}(\epsilon) \Big) \\
&\qquad = \frac{i}{16\pi^2} \left\{ \left(\frac{3(x+y)-2}{2}\right) \frac{1}{\epsilon} - \left(\frac{3(x+y)-2}{2}\right) \log\left(\frac{\Delta}{4\pi e^{-\gamma_E}}\right) - \frac{(x+y)}{2} \right\}.
\end{aligned} \tag{F.57}$$

The divergent term is vanishing because of

$$\int_0^1 dx \int_0^{1-x} dy \frac{i}{16\pi^2} \left(\frac{3(x+y)-2}{2}\right) \frac{1}{\epsilon} = 0. \tag{F.58}$$

Thus, the $F_2(0)$ is free from divergent. From eqs. (F.44), (F.52) and (F.57), the Pauli form factor $F_2(0)$ is given by

$$\begin{aligned}
F_2(0) = -\frac{m_\mu}{8\pi^2} \int_0^1 dx \int_0^{1-x} dy \Bigg[v^2 \Bigg\{ &\Big((4m_\mu - 4m_F) + (4m_F - 6m_\mu)(x+y) + 2m_\mu (x+y)^2 \Big) \frac{1}{\Delta_0} \\
&+ \frac{1}{m_V^2} \Bigg((m_\mu - m_F) \Big((3(x+y)-2) \log \Delta_0 + x + y \Big) \\
&+ \Big(m_\mu^2 (m_\mu - m_F)(x+y)^3 + m_\mu (m_F^2 - m_\mu^2)(x+y)^2 \Big) \frac{1}{\Delta_0} \Bigg) \Bigg\} \\
&+ a^2 \left\{ m_F \to -m_F \right\} \Bigg]
\end{aligned} \tag{F.59}$$

where

$$\Delta_0 = \Delta(q^2 \to 0) = m_\mu^2 (x+y)^2 - (m_\mu^2 - m_F^2)(x+y) + m_V^2 (1-x-y) \tag{F.60}$$

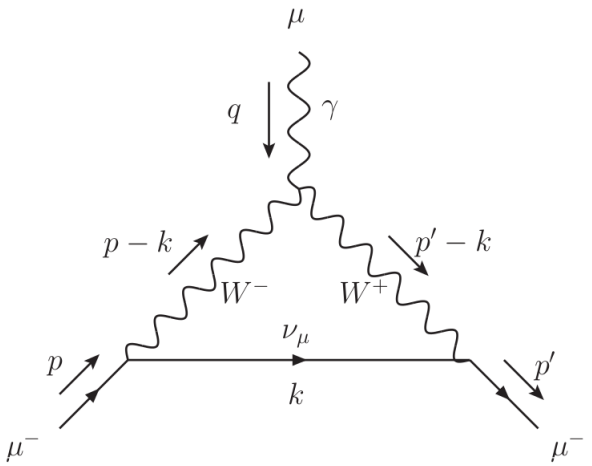

FIGURE F.3: The CC diagram contributing to the $g_\mu - 2$ calculation. The generic internal fermion and vector are labelled by F and V.

F.3 The CC diagram

Now let us consider fig. F.3. We can write the vertex function as[2]

$$\bar{u}(p')\Gamma_c^\mu u(p) =$$
$$i\int \frac{d^Dk}{(2\pi)^D}\bar{u}(p')\Big[\gamma^\nu(v-a\gamma_5)\frac{\not{k}}{k^2}\gamma^\rho(v-a\gamma_5)\frac{\left(g_{\rho\alpha}-\frac{(p-k)_\rho(p-k)_\alpha}{m_W^2}\right)}{(p-k)^2-m_W^2}\frac{\left(g_{\beta\nu}-\frac{(p'-k)_\beta(p'-k)_\nu}{m_W^2}\right)}{(p'-k)^2-m_W^2}$$
$$\times\left[g^{\alpha\beta}(2k-p-p')^\mu+g^{\beta\mu}(2p'-p-k)^\alpha+g^{\mu\alpha}(2p-p'-k)^\beta\right]\Big]u(p). \tag{F.61}$$

The denominator can be rewritten in terms of Feynman parameters

$$\frac{1}{\left[(p'-k)^2-m_W^2\right]\left[(p-k)^2-m_W^2\right]\left[k^2\right]} = 2\int dx\,dy\,\frac{1}{D^3}, \tag{F.62}$$

where

$$D=\ell^2-\Delta,\quad \Delta=(m_W^2-m_\mu^2)(x+y)+m_\mu^2(x+y)^2-xyq^2. \tag{F.63}$$

We have shifted the momentum $k^\mu \to \ell^\mu + p'^\mu x + p^\mu y$. Now let us consider the numerator of eq. (F.61).

$$\begin{aligned}\bar{u}(p')Nu(p) = \bar{u}(p')&\left[\gamma^\nu(v-a\gamma_5)\not{k}\gamma^\rho(v-a\gamma_5)\right]\\ &\times\left(g_{\rho\alpha}-\frac{(p-k)_\rho(p-k)_\alpha}{m_W^2}\right)\left(g_{\beta\nu}-\frac{(p'-k)_\beta(p'-k)_\nu}{m_W^2}\right)\\ &\times\left[g^{\alpha\beta}(2k-p-p')^\mu+g^{\beta\mu}(2p'-p-k)^\alpha+g^{\mu\alpha}(2p-p'-k)^\beta\right]u(p).\end{aligned} \tag{F.64}$$

[2]Please pay attention to the sign of $W^-\gamma W^+$ vertex. For the standard Feynman rules for loop calculation we need to go against the fermion line in fig. F.3 we will first encounter W^- that is why we use the Feynman rule of $W^-\gamma W^+$ vertex, not the $W^+\gamma W^-$ one.

In order to make our calculation less complicated. We can split the numerator into 3 parts.

$$\begin{aligned}
\bar{u}(p')N_1u(p) &= \bar{u}(p')\left[\gamma^\nu(v-a\gamma_5)\not{k}\gamma^\rho(v-a\gamma_5)\right]g_{\rho\alpha}g_{\beta\nu}\\
&\quad\times\Big[g^{\alpha\beta}(2k-p-p')^\mu+g^{\beta\mu}(2p'-p-k)^\alpha+g^{\mu\alpha}(2p-p'-k)^\beta\Big]\,u(p),\\
\bar{u}(p')N_2u(p) &= \bar{u}(p')\left[\gamma^\nu(v-a\gamma_5)\not{k}\gamma^\rho(v-a\gamma_5)\right]\\
&\quad\times\left(-g_{\rho\alpha}\frac{(p'-k)_\beta(p'-k)_\nu}{m_W^2}-g_{\beta\nu}\frac{(p-k)_\rho(p-k)_\alpha}{m_W^2}\right)\\
&\quad\times\Big[g^{\alpha\beta}(2k-p-p')^\mu+g^{\beta\mu}(2p'-p-k)^\alpha+g^{\mu\alpha}(2p-p'-k)^\beta\Big]\,u(p),\\
\bar{u}(p')N_3u(p) &= \bar{u}(p')\left[\gamma^\nu(v-a\gamma_5)\not{k}\gamma^\rho(v-a\gamma_5)\right]\frac{(p-k)_\rho(p-k)_\alpha}{m_W^2}\frac{(p'-k)_\beta(p'-k)_\nu}{m_W^2}\\
&\quad\times\Big[g^{\alpha\beta}(2k-p-p')^\mu+g^{\beta\mu}(2p'-p-k)^\alpha+g^{\mu\alpha}(2p-p'-k)^\beta\Big]\,u(p).
\end{aligned}\tag{F.65}$$

We start with the N_1

$$\begin{aligned}
\bar{u}(p')N_1u(p) &= \bar{u}(p')\left[\gamma^\nu(v-a\gamma_5)\not{k}\gamma^\rho(v-a\gamma_5)\right]g_{\rho\alpha}g_{\beta\nu}\\
&\quad\times\Big[g^{\alpha\beta}(2k-p-p')^\mu+g^{\beta\mu}(2p'-p-k)^\alpha+g^{\mu\alpha}(2p-p'-k)^\beta\Big]\,u(p),\\
&= \bar{u}(p')\left[v^2\gamma^\nu\not{k}\gamma^\rho+a^2\gamma^\nu\gamma_5\not{k}\gamma^\rho\gamma_5\right]g_{\rho\alpha}g_{\beta\nu}\\
&\quad\times\Big[g^{\alpha\beta}(2k-p-p')^\mu+g^{\beta\mu}(2p'-p-k)^\alpha+g^{\mu\alpha}(2p-p'-k)^\beta\Big]\,u(p),\\
&= \bar{u}(p')(v^2+a^2)\gamma^\nu\not{k}\gamma^\rho g_{\rho\alpha}g_{\beta\nu}\\
&\quad\times\Big[g^{\alpha\beta}(2k-p-p')^\mu+g^{\beta\mu}(2p'-p-k)^\alpha+g^{\mu\alpha}(2p-p'-k)^\beta\Big]\,u(p),\\
&= \bar{u}(p')(v^2+a^2)\left[(2k-p-p')^\mu\gamma^\alpha\not{k}\gamma_\alpha+\gamma^\mu\not{k}(2\not{p}'-\not{p}-\not{k})+(2\not{p}-\not{p}'-\not{k})\not{k}\gamma^\mu\right]u(p),\\
&= \bar{u}(p')(v^2+a^2)\Big[(2k-p-p')^\mu(2-d)\not{k}+2m_\mu k^\mu-4(p^\mu+p'^\mu)\not{k}+(\cdots)\gamma^\mu\Big]u(p),\\
&= \bar{u}(p')(v^2+a^2)\Big[(2-d)(2(\ell^\mu+p'^\mu x+p^\mu y)-p^\mu-p'^\mu)+2m_\mu(\ell^\mu+p'^\mu x+p^\mu y)\\
&\quad-4(p^\mu+p'^\mu)(\not{\ell}+\not{p}'x+\not{p}y)\Big]u(p),\\
&= \bar{u}(p')(v^2+a^2)\Big[(2-d)\left(2m_\mu(x+y)(p'^\mu x+p^\mu y)-m_\mu(x+y)(p^\mu+p'^\mu)\right)\\
&\quad+2m_\mu(p'^\mu x+p^\mu y)-4m_\mu(p^\mu+p'^\mu)(x+y)+(\cdots)\gamma^\mu\Big]u(p),
\end{aligned}\tag{F.66}$$

As we see that there is no ℓ^2 term contributing to $g-2$, we can simply take $d\to 4$.

$$\begin{aligned}
\bar{u}(p')N_1u(p) &= \bar{u}(p')(v^2+a^2)\Big[-4m_\mu(x+y)(p'^\mu x+p^\mu y)-2m_\mu(x+y)(p^\mu+p'^\mu)\\
&\quad+2m_\mu(p'^\mu x+p^\mu y)+(\cdots)\gamma^\mu\Big]u(p).
\end{aligned}\tag{F.67}$$

Replacing $p'^\mu=(P^\mu+q^\mu)/2$ and $p^\mu=(P^\mu-q^\mu)/2$, we arrive at

$$\bar{u}(p')N_1u(p) = \bar{u}(p')(v^2+a^2)\Big[-m_\mu(x+y)P^\mu-2m_\mu(x+y)^2P^\mu\Big]u(p).\tag{F.68}$$

Let us turn to the second terms of the numerator

$$\begin{aligned}
\bar{u}(p')N_2u(p) &= \bar{u}(p')\left[\gamma^\nu(v-a\gamma_5)\not{k}\gamma^\rho(v-a\gamma_5)\right]\\
&\times\left(-g_{\rho\alpha}\frac{(p'-k)_\beta(p'-k)_\nu}{m_W^2}-g_{\beta\nu}\frac{(p-k)_\rho(p-k)_\alpha}{m_W^2}\right)\\
&\times\Big[g^{\alpha\beta}(2k-p-p')^\mu+g^{\beta\mu}(2p'-p-k)^\alpha+g^{\mu\alpha}(2p-p'-k)^\beta\Big]\,u(p),\\
&=-\frac{(v^2+a^2)}{m_W^2}\bar{u}(p')\gamma^\nu\not{k}\gamma^\rho\left[g_{\rho\alpha}(p'-k)_\beta(p'-k)_\nu+g_{\beta\nu}(p-k)_\rho(p-k)_\alpha\right]\\
&\times\Big[g^{\alpha\beta}(2k-p-p')^\mu+g^{\beta\mu}(2p'-p-k)^\alpha+g^{\mu\alpha}(2p-p'-k)^\beta\Big]\,u(p),\\
&=-\frac{(v^2+a^2)}{m_W^2}\bar{u}(p')\gamma^\nu\not{k}\gamma^\rho\Big[(p'-k)_\rho(p'-k)_\nu(2k-p-p')^\mu\\
&+(p'-k)^\mu(p'-k)_\nu(2p'-p-k)_\rho+(p'-k)\cdot(2p-p'-k)(p'-k)_\nu\delta^\mu_\rho\\
&+(p-k)_\rho(p-k)_\nu(2k-p-p')^\mu+(p-k)_\rho(p-k)\cdot(2p-p'-k)\delta^\mu_\nu\\
&+(p-k)_\rho(p-k)^\mu(2p-p'-k)^\mu\Big]u(p),\\
&=\frac{(v^2+a^2)}{m_W^2}\bar{u}(p')\Big[k^2\not{k}P^\mu+m_\mu^2\not{k}P^\mu-2m_\mu k^2P^\mu-2k^2\not{k}k^\mu\\
&-2m_\mu^2\not{k}k^\mu+2m_\mu k^2k^\mu-2m_\mu^3k^\mu+2m_\mu(k\cdot p\not{k}\gamma^\mu+k\cdot p'\gamma^\mu\not{k})\Big]u(p).
\end{aligned}\tag{F.69}$$

We also need the following

$$\begin{aligned}
\bar{u}(p')k^2\not{k}u(p) &= \bar{u}(p')\left[\left(1+\frac{2}{d}\right)m_\mu(x+y)\ell^2+m_\mu^3(x+y)^3\right]u(p),\\
\bar{u}(p')k^2u(p) &= \bar{u}(p')\left[\ell^2+m_\mu^2(x+y)^2\right]u(p),\\
\bar{u}(p')k^2\not{k}k^\mu u(p) &= \bar{u}(p')\Big[(\cdots)\gamma^\mu+\Big(1+\frac{4}{d}\Big)m_\mu(x+y)(p'^\mu x+p^\mu y)\ell^2\\
&\qquad+m_\mu^3(x+y)^3(p'^\mu x+p^\mu y)\Big]u(p),\\
\bar{u}(p')\not{k}k^\mu u(p) &= \bar{u}(p')\Big[\frac{\ell^2}{d}\gamma^\mu+m_\mu(x+y)(p'^\mu x+p^\mu y)\Big]u(p).
\end{aligned}\tag{F.70}$$

Substituting eqs. (F.49) and (F.70) into eq. (F.69), we arrive at

$$\begin{aligned}
\bar{u}(p')N_2u(p) = \frac{(v^2+a^2)}{m_W^2}\bar{u}(p')\Big[\frac{\ell^2}{d}\Big\{&(4-2d)m_\mu+(2d+4)m_\mu(x+y)-(d+4)m_\mu(x+y)^2\Big\}\\
+\Big\{&-m_\mu^3(x+y)^2+2m_\mu^3(x+y)^3-m_\mu^3(x+y)^4\Big\}\Big]P^\mu u(p).
\end{aligned}\tag{F.71}$$

Consider the term proportional to ℓ^2

$$\begin{aligned}
\int\frac{d^d\ell}{(2\pi)^d}\frac{1}{(\ell^2-\Delta)^3}\frac{\ell^2}{d}&\Big\{(4-2d)m_\mu+(2d+4)m_\mu(x+y)-(d+4)m_\mu(x+y)^2\Big\}\\
=&\frac{i}{16\pi^2}\frac{1}{4}\Big[\Big\{4m_\mu-4m_\mu(x+y)+2m_\mu(x+y)^2\Big\}\\
&-\log\Delta\Big\{-4m_\mu+12m_\mu(x+y)-8m_\mu(x+y)^2\Big\}\Big].
\end{aligned}\tag{F.72}$$

The Pauli form factor for the diagram fig. F.3 is given by

$$\begin{aligned} F_2(0) =& 2i\int_0^1 dx \int_0^{1-x} dy(v^2+a^2)\Big[2m_\mu\Big\{m_\mu(x+y)+2m_\mu(x+y)^2\Big\}\Big(\frac{-i}{2\cdot 16\pi^2}\frac{1}{\Delta_0}\Big) \\ &- \frac{2m_\mu}{m_W^2}\Big[\Big\{-m_\mu^3(x+y)^2+2m_\mu^3(x+y)^3-m_\mu^3(x+y)^4\Big\}\Big(\frac{-i}{2\cdot 16\pi^2}\frac{1}{\Delta_0}\Big) \\ &+ \frac{i}{16\pi^2}\frac{1}{4}\Big[\Big\{4m_\mu-4m_\mu(x+y)+2m_\mu(x+y)^2\Big\} \\ &- \log\Delta_0\Big\{-4m_\mu+12m_\mu(x+y)-8m_\mu(x+y)^2\Big\}\Big]\Big]\Big] \end{aligned} \tag{F.73}$$

F.4 Results

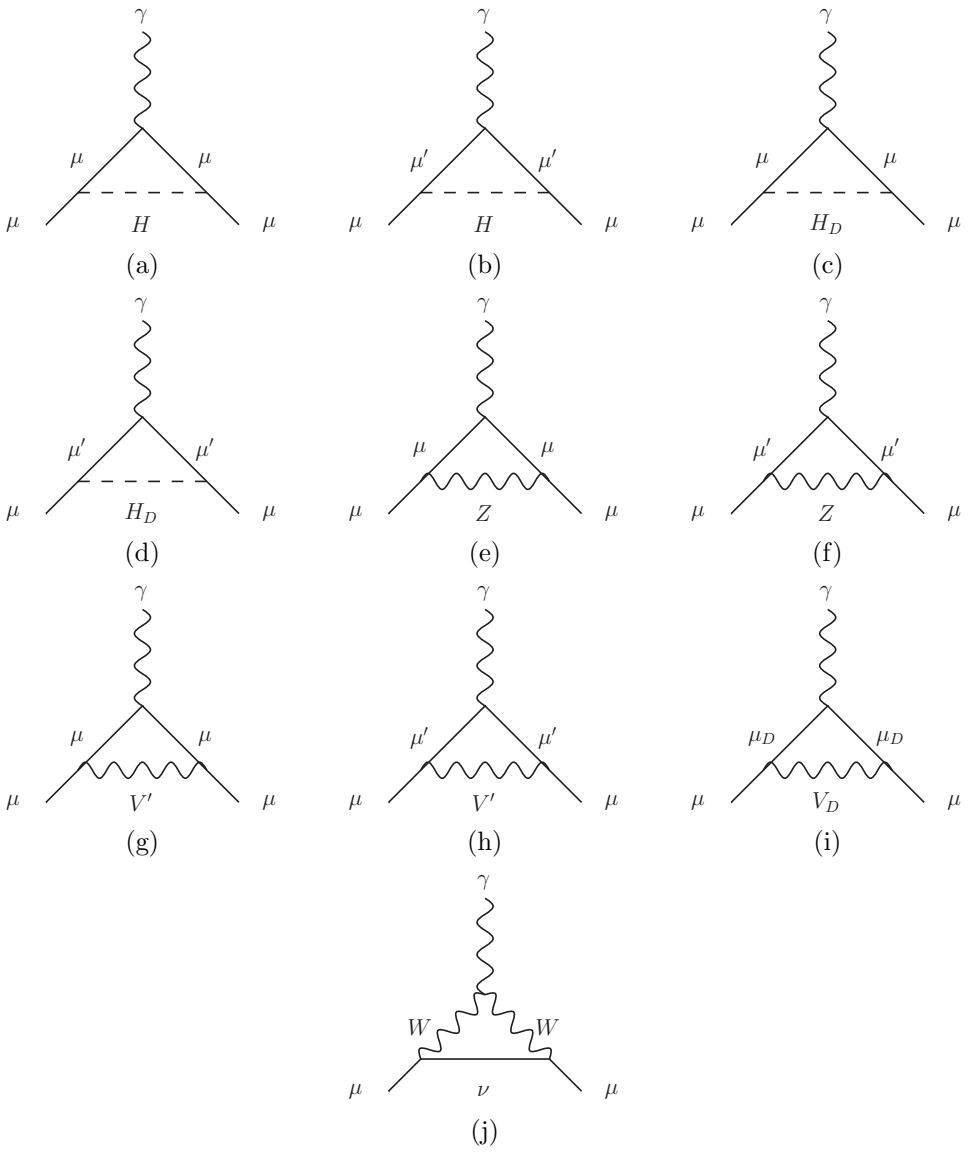

FIGURE F.4: The NP diagrams contributing to g-2 of muon.

We have expanded the contribution to the g-2 of muon from each diagram in the limit that $m_\mu^2 \ll m_H^2, m_{H_D}^2, m_Z^2, m_{V'}^2, m_{V_D}^2, m_W^2$.

$$a_\mu^{(\mathrm{a})} = -\frac{1}{48\pi^2}\left(\frac{m_\mu^2}{m_h^2}\right)\left(\frac{m_\mu^2}{v^2}\right)\left(7+6\log\frac{m_\mu^2}{m_h^2}\right) \tag{F.74}$$

$$\begin{aligned} a_\mu^{(\mathrm{b})} =& -\frac{1}{96\pi^2}\frac{m_\mu^4(m_D^2-m_M^2)}{m_D^2(m_h^2-m_M^2)^4 v^2}\Big(-16m_h^6+45m_h^4m_M^2-36m_h^2m_M^4+7m_M^6 \\ &+6(2m_h^6-3m_h^4m_M^2)\log\frac{m_h^2}{m_M^2}\Big) \end{aligned} \tag{F.75}$$

$$a_\mu^{(\mathrm{c})} = -\frac{1}{48\pi^2}\left(\frac{m_\mu^2}{m_{H_D}^2}\right)\left(\frac{m_\mu^2}{v_D^2}\right)\frac{\left(m_M^2-m_D^2\right)^2}{m_M^4}\left(7+6\log\frac{m_\mu^2}{m_{H_D}^2}\right) \tag{F.76}$$

$$\begin{aligned} a_\mu^{(\mathrm{d})} =& -\frac{1}{96\pi^2}\frac{m_\mu^2(m_D^2-m_M^2)}{m_M^2(m_{H_D}^2-m_M^2)v_D^2}\Big((m_{H_D}^2-m_M^2) \\ &\times\Big(-7m_D^2m_M^4+6m_M^6+2m_{H_D}^2(-8m_D^2+9m_M^2)+m_{H_D}^2(29m_D^2m_M^2-24m_M^4)\Big) \\ &+6m_{H_D}^2\left(-3m_D^2m_M^2+2m_M^4+2m_{H_D}^2(m_D^2-m_M^2)\right)\log\frac{m_{H_D}^2}{m_M^2}\Big) \end{aligned} \tag{F.77}$$

$$a_\mu^{(\mathrm{e})} = \frac{g_W^2}{48\pi^2}\frac{m_\mu^2}{c_W^2 m_Z^2}\left(-1-2s_W^2+4s_W^4\right) \tag{F.78}$$

$$\begin{aligned} a_\mu^{(\mathrm{f})} =& \frac{g_W^2}{384\pi^2}\frac{m_\mu^4(m_D^2-m_M^2)}{c_W^2m_Z^2m_D^2m_M^2(m_M^2-m_Z^2)^4}\Bigg(5m_M^8-14m_M^6m_Z^2+39m_M^4m_Z^4 \\ &-38m_M^2m_Z^6+8m_Z^8+18m_M^4m_Z^4\log\frac{m_Z^2}{m_M^2}\Bigg) \end{aligned} \tag{F.79}$$

$$a_\mu^{(\mathrm{g})} = -\frac{g_D^2}{48\pi^2}\frac{m_\mu^2(m_D^2-m_M^2)^2}{m_M^4m_{V'}^2} \tag{F.80}$$

$$\begin{aligned} a_\mu^{(\mathrm{h})} =& \frac{g_D^2}{384\pi^2}\frac{m_\mu^2(m_D^2-m_M^2)}{m_{V'}^2(m_M^3-m_Mm_{V'}^2)^4}\Bigg((m_M^2-m_{V'}^2) \\ &\times\Big(m_D^2(5m_M^6-9m_M^4m_{V'}^2+30m_M^2m_{V'}^4-8m_{V'}^6) \\ &-6(m_M^8+3m_M^4m_{V'}^4-4m_M^2m_{V'}^6)\Big) \\ &-18m_M^4m_{V'}^4(m_D^2-2m_M^2+2m_{V'}^2)\log\frac{m_M^2}{m_{V'}^2}\Bigg) \end{aligned} \tag{F.81}$$

$$\begin{aligned} a_\mu^{(\mathrm{i})} =& \frac{g_D^2}{192\pi^2}\frac{m_\mu^2(m_M^2-m_D^2)}{m_M^2m_{V_D}^2(m_D^2-m_{V_D}^2)^4}\Big(m_D^8+8m_D^6m_{V_D}^2-21m_D^4m_{V_D}^4 \\ &-4m_D^2m_{V_D}^6+16m_{V_D}^8-18m_D^2m_{V_D}^4(m_D^2-2m_{V_D}^2)\log\frac{m_D^2}{m_{V_D}^2}\Big) \end{aligned} \tag{F.82}$$

$$a_\mu^{(\mathrm{j})} = \frac{5g_W^2}{96\pi^2}\frac{m_\mu^2}{m_W^2} \tag{F.83}$$

References

[1] A. Belyaev, A. Deandrea, S. Moretti, L. Panizzi, D. A. Ross and N. Thongyoi, *Fermionic portal to vector dark matter from a new gauge sector*, *Phys. Rev. D* **108** (2023), no. 9 095001 [2204.03510].

[2] A. Belyaev, A. Deandrea, S. Moretti, L. Panizzi and N. Thongyoi, *A fermionic portal to a non-abelian dark sector*, 2203.04681.

[3] A. Belyaev, L. Panizzi and N. Thongyoi, *The muon anomalous magnetic moment $g_\mu - 2$ from the fermionic portal to vector dark matter*, 2024(to appear).

[4] M. E. Peskin and D. V. Schroeder, *An Introduction to quantum field theory*. Addison-Wesley, Reading, USA, 1995.

[5] S. Weinberg, *The Quantum theory of fields. Vol. 1: Foundations*. Cambridge University Press, 6, 2005.

[6] S. Weinberg, *The quantum theory of fields. Vol. 2: Modern applications*. Cambridge University Press, 8, 2013.

[7] F. Englert and R. Brout, *Broken Symmetry and the Mass of Gauge Vector Mesons*, *Phys. Rev. Lett.* **13** (1964) 321–323.

[8] P. W. Higgs, *Broken Symmetries and the Masses of Gauge Bosons*, *Phys. Rev. Lett.* **13** (1964) 508–509.

[9] **Particle Data Group** Collaboration, M. Tanabashi *et. al.*, *Review of Particle Physics*, *Phys. Rev. D* **98** (2018), no. 3 030001.

[10] Y. Nambu, *Quasiparticles and Gauge Invariance in the Theory of Superconductivity*, *Phys. Rev.* **117** (1960) 648–663.

[11] J. Goldstone, *Field Theories with Superconductor Solutions*, *Nuovo Cim.* **19** (1961) 154–164.

[12] J. Goldstone, A. Salam and S. Weinberg, *Broken Symmetries*, *Phys. Rev.* **127** (1962) 965–970.

[13] **Particle Data Group** Collaboration, P. A. Zyla *et. al.*, *Review of Particle Physics*, *PTEP* **2020** (2020), no. 8 083C01.

[14] M. D. Schwartz, *Quantum Field Theory and the Standard Model*. Cambridge University Press, 3, 2014.

[15] C. Jarlskog, *Commutator of the Quark Mass Matrices in the Standard Electroweak Model and a Measure of Maximal CP Nonconservation*, *Phys. Rev. Lett.* **55** (1985) 1039.

[16] R. B. Palmer *et. al.*, *Muon colliders*, *AIP Conf. Proc.* **372** (1996), no. 1 3–30 [acc-phys/9602001].

[17] A. Liddle, *An introduction to modern cosmology; 2nd ed.* Wiley, Chichester, 2003.

[18] E. Hubble, *A relation between distance and radial velocity among extra-galactic nebulae*, *Proc. Nat. Acad. Sci.* **15** (1929) 168–173.

[19] E. W. Kolb and M. S. Turner, *The early universe*. Frontiers in physics. Westview Press, Boulder, CO, 1990.

[20] P. Di Bari, *Cosmology and the early Universe*. Series in Astronomy and Astrophysics. CRC Press, 5, 2018.

[21] **Planck** Collaboration, N. Aghanim *et. al.*, *Planck 2018 results. VI. Cosmological parameters*, *Astron. Astrophys.* **641** (2020) A6 [1807.06209]. [Erratum: Astron.Astrophys. 652, C4 (2021)].

[22] M. Bauer and T. Plehn, *Yet Another Introduction to Dark Matter: The Particle Physics Approach*, vol. 959 of *Lecture Notes in Physics*. Springer, 2019.

[23] **WMAP** Collaboration, C. L. Bennett *et. al.*, *Nine-Year Wilkinson Microwave Anisotropy Probe (WMAP) Observations: Final Maps and Results*, *Astrophys. J. Suppl.* **208** (2013) 20 [1212.5225].

[24] **COBE** Collaboration, G. F. Smoot *et. al.*, *Structure in the COBE differential microwave radiometer first year maps*, *Astrophys. J. Lett.* **396** (1992) L1–L5.

[25] D. Baumann, *Cosmology*. Cambridge University Press, 7, 2022.

[26] S. Vagnozzi, *Weigh them all! - Cosmological searches for the neutrino mass scale and mass ordering*. PhD thesis, Stockholm U., 4, 2019.

[27] G. Bertone and D. Hooper, *History of dark matter*, *Rev. Mod. Phys.* **90** (2018), no. 4 045002 [1605.04909].

[28] J. Silk *et. al.*, *Particle Dark Matter: Observations, Models and Searches*. Cambridge Univ. Press, Cambridge, 2010.

[29] J. F. Navarro, C. S. Frenk and S. D. M. White, *The Structure of cold dark matter halos*, *Astrophys. J.* **462** (1996) 563–575 [astro-ph/9508025].

[30] A. Del Popolo, *Dark matter and structure formation a review*, *Astron. Rep.* **51** (2007) 169–196 [0801.1091].

[31] J. R. Primack, *Dark matter and structure formation*, in *Midrasha Mathematicae in Jerusalem: Winter School in Dynamical Systems*, 7, 1997. astro-ph/9707285.

[32] E. Bulbul, M. Markevitch, A. Foster, R. K. Smith, M. Loewenstein and S. W. Randall, *Detection of An Unidentified Emission Line in the Stacked X-ray spectrum of Galaxy Clusters*, *Astrophys. J.* **789** (2014) 13 [1402.2301].

[33] R. Massey, T. Kitching and J. Richard, *The dark matter of gravitational lensing*, *Rept. Prog. Phys.* **73** (2010) 086901 [1001.1739].

[34] A. C. Freegard, *Dark matter models : signals and backgrounds at the LHC and future colliders*. PhD thesis, University of Southampton, Southampton U., 2023.

[35] G. Jungman, M. Kamionkowski and K. Griest, *Supersymmetric dark matter*, *Phys. Rept.* **267** (1996) 195–373 [hep-ph/9506380].

[36] S. Dodelson and L. M. Widrow, *Sterile-neutrinos as dark matter*, *Phys. Rev. Lett.* **72** (1994) 17–20 [hep-ph/9303287].

[37] J. E. Kim and G. Carosi, *Axions and the Strong CP Problem*, *Rev. Mod. Phys.* **82** (2010) 557–602 [0807.3125]. [Erratum: Rev.Mod.Phys. 91, 049902 (2019)].

[38] D. J. E. Marsh, *Axion Cosmology*, *Phys. Rept.* **643** (2016) 1–79 [1510.07633].

[39] A. Belyaev, G. Cacciapaglia, I. P. Ivanov, F. Rojas-Abatte and M. Thomas, *Anatomy of the Inert Two Higgs Doublet Model in the light of the LHC and non-LHC Dark Matter Searches*, *Phys. Rev. D* **97** (2018), no. 3 035011 [1612.00511].

[40] **Fermi-LAT** Collaboration, W. B. Atwood *et. al.*, *The Large Area Telescope on the Fermi Gamma-ray Space Telescope Mission*, *Astrophys. J.* **697** (2009) 1071–1102 [0902.1089].

[41] **IceCube** Collaboration, M. G. Aartsen *et. al.*, *Observation of High-Energy Astrophysical Neutrinos in Three Years of IceCube Data*, *Phys. Rev. Lett.* **113** (2014) 101101 [1405.5303].

[42] **AMS** Collaboration, M. Aguilar *et. al.*, *First Result from the Alpha Magnetic Spectrometer on the International Space Station: Precision Measurement of the Positron Fraction in Primary Cosmic Rays of 0.5–350 GeV*, *Phys. Rev. Lett.* **110** (2013) 141102.

[43] **LUX** Collaboration, D. S. Akerib *et. al.*, *First results from the LUX dark matter experiment at the Sanford Underground Research Facility*, *Phys. Rev. Lett.* **112** (2014) 091303 [1310.8214].

[44] **XENON** Collaboration, E. Aprile *et. al.*, *Dark Matter Search Results from a One Ton-Year Exposure of XENON1T*, *Phys. Rev. Lett.* **121** (2018), no. 11 111302 [1805.12562].

[45] **PandaX-II** Collaboration, A. Tan *et. al.*, *Dark Matter Results from First 98.7 Days of Data from the PandaX-II Experiment*, *Phys. Rev. Lett.* **117** (2016), no. 12 121303 [1607.07400].

[46] **WMAP** Collaboration, D. N. Spergel *et. al.*, *First year Wilkinson Microwave Anisotropy Probe (WMAP) observations: Determination of cosmological parameters*, *Astrophys. J. Suppl.* **148** (2003) 175–194 [astro-ph/0302209].

[47] **Planck** Collaboration, P. A. R. Ade *et. al.*, *Planck 2015 results. XIII. Cosmological parameters*, *Astron. Astrophys.* **594** (2016) A13 [1502.01589].

[48] K. Griest and D. Seckel, *Three exceptions in the calculation of relic abundances*, *Phys. Rev. D* **43** (1991) 3191–3203.

[49] L. J. Hall, K. Jedamzik, J. March-Russell and S. M. West, *Freeze-In Production of FIMP Dark Matter*, *JHEP* **03** (2010) 080 [0911.1120].

[50] J. Edsjo and P. Gondolo, *Neutralino relic density including coannihilations*, *Phys. Rev. D* **56** (1997) 1879–1894 [hep-ph/9704361].

[51] G. Belanger, A. Mjallal and A. Pukhov, *Recasting direct detection limits within micrOMEGAs and implication for non-standard Dark Matter scenarios*, *Eur. Phys. J. C* **81** (2021), no. 3 239 [2003.08621].

[52] G. Belanger, F. Boudjema, A. Pukhov and A. Semenov, *MicrOMEGAs: A Program for calculating the relic density in the MSSM*, *Comput. Phys. Commun.* **149** (2002) 103–120 [hep-ph/0112278].

[53] N. Bernal, M. Heikinheimo, T. Tenkanen, K. Tuominen and V. Vaskonen, *The Dawn of FIMP Dark Matter: A Review of Models and Constraints*, *Int. J. Mod. Phys. A* **32** (2017), no. 27 1730023 [1706.07442].

[54] J. M. Gaskins, *A review of indirect searches for particle dark matter*, *Contemp. Phys.* **57** (2016), no. 4 496–525 [1604.00014].

[55] R. K. Leane, *Indirect Detection of Dark Matter in the Galaxy*, in *3rd World Summit on Exploring the Dark Side of the Universe*, pp. 203–228, 2020. 2006.00513.

[56] C. Pérez de los Heros, *Status, challenges and directions in indirect dark matter searches*, *Symmetry* **12** (2020), no. 10.

[57] **Fermi-LAT** Collaboration, M. Ackermann *et. al.*, *Searching for Dark Matter Annihilation from Milky Way Dwarf Spheroidal Galaxies with Six Years of Fermi Large Area Telescope Data*, *Phys. Rev. Lett.* **115** (2015), no. 23 231301 [1503.02641].

[58] **PAMELA** Collaboration, O. Adriani *et. al.*, *An anomalous positron abundance in cosmic rays with energies 1.5-100 GeV*, *Nature* **458** (2009) 607–609 [0810.4995].

[59] J. Chang *et. al.*, *An excess of cosmic ray electrons at energies of 300-800 GeV*, *Nature* **456** (2008) 362–365.

[60] A. Reinert and M. W. Winkler, *A precision search for WIMPs with charged cosmic rays*, *Journal of Cosmology and Astroparticle Physics* **2018** (jan, 2018) 055–055.

[61] **ANTARES** Collaboration, S. Adrian-Martinez *et. al.*, *First results on dark matter annihilation in the Sun using the ANTARES neutrino telescope*, *JCAP* **11** (2013) 032 [1302.6516].

[62] **ANTARES, IceCube** Collaboration, A. Albert *et. al.*, *Combined search for neutrinos from dark matter self-annihilation in the Galactic Center with ANTARES and IceCube*, *Phys. Rev. D* **102** (2020), no. 8 082002 [2003.06614].

[63] **IceCube** Collaboration, M. G. Aartsen *et. al.*, *Search for annihilating dark matter in the Sun with 3 years of IceCube data*, *Eur. Phys. J. C* **77** (2017), no. 3 146 [1612.05949]. [Erratum: Eur.Phys.J.C 79, 214 (2019)].

[64] **IceCube** Collaboration, M. G. Aartsen *et. al.*, *The IceCube Neutrino Observatory: Instrumentation and Online Systems*, *JINST* **12** (2017), no. 03 P03012 [1612.05093].

[65] **Super-Kamiokande** Collaboration, S. Desai *et. al.*, *Search for dark matter WIMPs using upward through-going muons in Super-Kamiokande*, *Phys. Rev. D* **70** (2004) 083523 [hep-ex/0404025]. [Erratum: Phys.Rev.D 70, 109901 (2004)].

[66] **Super-Kamiokande** Collaboration, K. Choi *et. al.*, *Search for neutrinos from annihilation of captured low-mass dark matter particles in the Sun by Super-Kamiokande*, *Phys. Rev. Lett.* **114** (2015), no. 14 141301 [1503.04858].

[67] C. A. Argüelles, A. Diaz, A. Kheirandish, A. Olivares-Del-Campo, I. Safa and A. C. Vincent, *Dark matter annihilation to neutrinos*, *Rev. Mod. Phys.* **93** (2021), no. 3 035007 [1912.09486].

[68] **Planck** Collaboration, O. Perdereau, *Planck 2015 cosmological results*, *AIP Conf. Proc.* **1743** (2016), no. 1 050014.

[69] N. Padmanabhan and D. P. Finkbeiner, *Detecting dark matter annihilation with CMB polarization: Signatures and experimental prospects*, *Phys. Rev. D* **72** (2005) 023508 [astro-ph/0503486].

[70] T. R. Slatyer, *Indirect dark matter signatures in the cosmic dark ages. I. Generalizing the bound on s-wave dark matter annihilation from Planck results*, *Phys. Rev. D* **93** (2016), no. 2 023527 [1506.03811].

[71] **LZ** Collaboration, J. Aalbers *et. al.*, *First Dark Matter Search Results from the LUX-ZEPLIN (LZ) Experiment*, *Phys. Rev. Lett.* **131** (2023), no. 4 041002 [2207.03764].

[72] **NEWS-G** Collaboration, Q. Arnaud *et. al.*, *First results from the NEWS-G direct dark matter search experiment at the LSM*, *Astropart. Phys.* **97** (2018) 54–62 [1706.04934].

[73] **SuperCDMS** Collaboration, R. Agnese *et. al.*, *Search for Low-Mass Dark Matter with CDMSlite Using a Profile Likelihood Fit*, *Phys. Rev. D* **99** (2019), no. 6 062001 [1808.09098].

[74] **DarkSide** Collaboration, P. Agnes *et. al.*, *First Results from the DarkSide-50 Dark Matter Experiment at Laboratori Nazionali del Gran Sasso*, *Phys. Lett. B* **743** (2015) 456–466 [1410.0653].

[75] **LUX** Collaboration, D. S. Akerib *et. al.*, *Results from a search for dark matter in the complete LUX exposure*, *Phys. Rev. Lett.* **118** (2017), no. 2 021303 [1608.07648].

[76] F. Kahlhoefer, *Review of LHC Dark Matter Searches*, *Int. J. Mod. Phys. A* **32** (2017), no. 13 1730006 [1702.02430].

[77] **ATLAS** Collaboration, M. Aaboud *et. al.*, *Search for new phenomena in dijet events using 37 fb^{-1} of pp collision data collected at $\sqrt{s}$ =13 TeV with the ATLAS detector*, *Phys. Rev. D* **96** (2017), no. 5 052004 [1703.09127].

[78] **CMS** Collaboration, A. M. Sirunyan *et. al.*, *Search for new physics in final states with an energetic jet or a hadronically decaying W or Z boson and transverse momentum imbalance at $\sqrt{s} = 13$ TeV*, *Phys. Rev. D* **97** (2018), no. 9 092005 [1712.02345].

[79] **CMS** Collaboration, A. M. Sirunyan *et. al.*, *Search for high-mass resonances in dilepton final states in proton-proton collisions at $\sqrt{s}$ = 13 TeV*, *JHEP* **06** (2018) 120 [1803.06292].

[80] **ATLAS, CMS** Collaboration, N. Trevisani, *Collider Searches for Dark Matter (ATLAS + CMS)*, *Universe* **4** (2018), no. 11 131.

[81] P. A. M. Dirac, *The Quantum theory of electron. 2.*, *Proc. Roy. Soc. Lond. A* **118** (1928) 351.

[82] C. C. Rodegheri, K. Blaum, H. Kracke, S. Kreim, A. Mooser, W. Quint, S. Ulmer and J. Walz, *An experiment for the direct determination of the g-factor of a single proton in a Penning trap*, *New Journal of Physics* **14** (June, 2012) 063011.

[83] G. Charpak, F. J. M. Farley and R. L. Garwin, *A New Measurement of the Anomalous Magnetic Moment of the Muon*, *Phys. Lett.* **1** (1962) 16.

[84] A. Keshavarzi, K. S. Khaw and T. Yoshioka, *Muon g−2: A review*, *Nucl. Phys. B* **975** (2022) 115675 [2106.06723].

[85] F. J. M. Farley and E. Picasso, *The Muon ($g-2$) Experiments at CERN*, *Ann. Rev. Nucl. Part. Sci.* **29** (1979) 243–282.

[86] L. H. Thomas, *The motion of a spinning electron*, *Nature* **117** (1926) 514.

[87] **Muon g-2** Collaboration, D. P. Aguillard *et. al.*, "Measurement of the Positive Muon Anomalous Magnetic Moment to 0.20 ppm." FERMILAB-PUB-23-385-AD-CSAID-PPD, 8, 2023.

[88] J. P. Leveille, *The Second Order Weak Correction to (G-2) of the Muon in Arbitrary Gauge Models*, *Nucl. Phys. B* **137** (1978) 63–76.

[89] J. S. Schwinger, *On Quantum electrodynamics and the magnetic moment of the electron*, *Phys. Rev.* **73** (1948) 416–417.

[90] T. Aoyama *et. al.*, *The anomalous magnetic moment of the muon in the Standard Model*, *Phys. Rept.* **887** (2020) 1–166 [2006.04822].

[91] M. Gourdin and E. De Rafael, *Hadronic contributions to the muon g-factor*, *Nucl. Phys. B* **10** (1969) 667–674.

[92] S. Borsanyi *et. al.*, *Leading hadronic contribution to the muon magnetic moment from lattice QCD*, *Nature* **593** (2021), no. 7857 51–55 [2002.12347].

[93] **Budapest-Marseille-Wuppertal** Collaboration, S. Borsanyi *et. al.*, *Hadronic vacuum polarization contribution to the anomalous magnetic moments of leptons from first principles*, *Phys. Rev. Lett.* **121** (2018), no. 2 022002 [1711.04980].

[94] **RBC, UKQCD** Collaboration, T. Blum, P. A. Boyle, V. Gülpers, T. Izubuchi, L. Jin, C. Jung, A. Jüttner, C. Lehner, A. Portelli and J. T. Tsang, *Calculation of the hadronic vacuum polarization contribution to the muon anomalous magnetic moment*, *Phys. Rev. Lett.* **121** (2018), no. 2 022003 [1801.07224].

[95] **Fermilab Lattice, LATTICE-HPQCD, MILC** Collaboration, C. T. H. Davies *et. al.*, *Hadronic-vacuum-polarization contribution to the muon's anomalous magnetic moment from four-flavor lattice QCD*, *Phys. Rev. D* **101** (2020), no. 3 034512 [1902.04223].

[96] D. Giusti, V. Lubicz, G. Martinelli, F. Sanfilippo and S. Simula, *Electromagnetic and strong isospin-breaking corrections to the muon $g-2$ from Lattice QCD+QED*, *Phys. Rev. D* **99** (2019), no. 11 114502 [1901.10462].

[97] A. Gérardin, M. Cè, G. von Hippel, B. Hörz, H. B. Meyer, D. Mohler, K. Ottnad, J. Wilhelm and H. Wittig, *The leading hadronic contribution to $(g-2)_\mu$ from lattice QCD with $N_{\rm f}=2+1$ flavours of O(a) improved Wilson quarks*, *Phys. Rev. D* **100** (2019), no. 1 014510 [1904.03120].

[98] A. Crivellin, M. Hoferichter, C. A. Manzari and M. Montull, *Hadronic Vacuum Polarization: $(g-2)_\mu$ versus Global Electroweak Fits*, *Phys. Rev. Lett.* **125** (2020), no. 9 091801 [2003.04886].

[99] G. Arcadi, A. Djouadi and M. Kado, *The Higgs-portal for vector dark matter and the effective field theory approach: A reappraisal*, *Phys. Lett. B* **805** (2020) 135427 [2001.10750].

[100] J. Hubisz and P. Meade, *Phenomenology of the littlest Higgs with T-parity*, *Phys. Rev. D* **71** (2005) 035016 [hep-ph/0411264].

[101] T. Hambye, *Hidden vector dark matter*, *JHEP* **01** (2009) 028 [0811.0172].

[102] F. Chen, J. M. Cline and A. R. Frey, *Nonabelian dark matter: Models and constraints*, *Phys. Rev. D* **80** (2009) 083516 [0907.4746].

[103] J. Diaz-Cruz and E. Ma, *Neutral SU(2) Gauge Extension of the Standard Model and a Vector-Boson Dark-Matter Candidate*, *Phys. Lett. B* **695** (2011) 264–267 [1007.2631].

[104] S. Bhattacharya, J. Diaz-Cruz, E. Ma and D. Wegman, *Dark Vector-Gauge-Boson Model*, *Phys. Rev. D* **85** (2012) 055008 [1107.2093].

[105] O. Lebedev, H. M. Lee and Y. Mambrini, *Vector Higgs-portal dark matter and the invisible Higgs*, *Phys. Lett. B* **707** (2012) 570–576 [1111.4482].

[106] Y. Farzan and A. R. Akbarieh, *VDM: A model for Vector Dark Matter*, *JCAP* **10** (2012) 026 [1207.4272].

[107] S. Baek, P. Ko, W.-I. Park and E. Senaha, *Higgs Portal Vector Dark Matter : Revisited*, *JHEP* **05** (2013) 036 [1212.2131].

[108] E. Koorambas, *Vector Gauge Boson Dark Matter for the $SU(N)$ Gauge Group Model*, *Int. J. Theor. Phys.* **52** (2013) 4374–4388.

[109] S. Fraser, E. Ma and M. Zakeri, *$SU(2)_N$ model of vector dark matter with a leptonic connection*, *Int. J. Mod. Phys. A* **30** (2015), no. 03 1550018 [1409.1162].

[110] P. Ko, W.-I. Park and Y. Tang, *Higgs portal vector dark matter for* GeV *scale γ-ray excess from galactic center*, *JCAP* **09** (2014) 013 [1404.5257].

[111] W.-C. Huang, Y.-L. S. Tsai and T.-C. Yuan, *G2HDM : Gauged Two Higgs Doublet Model*, *JHEP* **04** (2016) 019 [1512.00229].

[112] C. Gross, O. Lebedev and Y. Mambrini, *Non-Abelian gauge fields as dark matter*, *JHEP* **08** (2015) 158 [1505.07480].

[113] A. DiFranzo, P. J. Fox and T. M. P. Tait, *Vector Dark Matter through a Radiative Higgs Portal*, *JHEP* **04** (2016) 135 [1512.06853].

[114] P. Ko and Y. Tang, *Residual Non-Abelian Dark Matter and Dark Radiation*, *Phys. Lett. B* **768** (2017) 12–17 [1609.02307].

[115] B. Barman, S. Bhattacharya, S. K. Patra and J. Chakrabortty, *Non-Abelian Vector Boson Dark Matter, its Unified Route and signatures at the LHC*, *JCAP* **12** (2017) 021 [1704.04945].

[116] W.-C. Huang, H. Ishida, C.-T. Lu, Y.-L. S. Tsai and T.-C. Yuan, *Signals of New Gauge Bosons in Gauged Two Higgs Doublet Model*, *Eur. Phys. J. C* **78** (2018), no. 8 613 [1708.02355].

[117] B. Barman, S. Bhattacharya and M. Zakeri, *Multipartite Dark Matter in $SU(2)_N$ extension of Standard Model and signatures at the LHC*, *JCAP* **09** (2018) 023 [1806.01129].

[118] B. Barman, S. Bhattacharya and M. Zakeri, *Non-Abelian Vector Boson as FIMP Dark Matter*, *JCAP* **02** (2020) 029 [1905.07236].

[119] D. Buttazzo, L. Di Luzio, P. Ghorbani, C. Gross, G. Landini, A. Strumia, D. Teresi and J.-W. Wang, *Scalar gauge dynamics and Dark Matter*, *JHEP* **01** (2020) 130 [1911.04502].

[120] T. Abe, M. Fujiwara, J. Hisano and K. Matsushita, *A model of electroweakly interacting non-abelian vector dark matter*, *JHEP* **07** (2020) 136 [2004.00884].

[121] C. Gross, S. Karamitsos, G. Landini and A. Strumia, *Gravitational Vector Dark Matter*, *JHEP* **03** (2021) 174 [2012.12087].

[122] T. A. Chowdhury and S. Saad, *Non-Abelian vector dark matter and lepton g-2*, *JCAP* **10** (2021) 014 [2107.11863].

[123] N. Baouche, A. Ahriche, G. Faisel and S. Nasri, *Phenomenology of the hidden SU(2) vector dark matter model*, *Phys. Rev. D* **104** (2021), no. 7 075022 [2105.14387].

[124] Z. Hu, C. Cai, Y.-L. Tang, Z.-H. Yu and H.-H. Zhang, *Vector dark matter from split SU(2) gauge bosons*, *JHEP* **07** (2021) 089 [2103.00220].

[125] K. S. Babu, S. Jana and A. Thapa, *Vector boson dark matter from trinification*, *JHEP* **02** (2022) 051 [2112.12771].

[126] J. Hisano, A. Ibarra and R. Nagai, *Direct detection of vector dark matter through electromagnetic multipoles*, *JCAP* **10** (2020) 015 [2007.03216].

[127] G. Servant and T. M. P. Tait, *Is the lightest Kaluza-Klein particle a viable dark matter candidate?*, *Nucl. Phys. B* **650** (2003) 391–419 [hep-ph/0206071].

[128] G. Cacciapaglia, A. Deandrea and J. Llodra-Perez, *A Dark Matter candidate from Lorentz Invariance in 6D*, *JHEP* **03** (2010) 083 [0907.4993].

[129] F. Giacchino, A. Ibarra, L. Lopez Honorez, M. H. G. Tytgat and S. Wild, *Signatures from Scalar Dark Matter with a Vector-like Quark Mediator*, *JCAP* **02** (2016) 002 [1511.04452].

[130] M. Garny, J. Heisig, M. Hufnagel and B. Lülf, *Top-philic dark matter within and beyond the WIMP paradigm*, *Phys. Rev. D* **97** (2018), no. 7 075002 [1802.00814].

[131] C. Arina, B. Fuks and L. Mantani, *A universal framework for t-channel dark matter models*, *Eur. Phys. J. C* **80** (2020), no. 5 409 [2001.05024].

[132] C. Arina, B. Fuks, L. Mantani, H. Mies, L. Panizzi and J. Salko, *Closing in on t-channel simplified dark matter models*, *Phys. Lett. B* **813** (2021) 136038 [2010.07559].

[133] A. Crivellin and M. Hoferichter, *Hints of lepton flavor universality violations*, *Science* **374** (2021), no. 6571 1051 [2111.12739].

[134] **CDF** Collaboration, T. Aaltonen *et. al.*, *High-precision measurement of the W boson mass with the CDF II detector*, *Science* **376** (2022), no. 6589 170–176.

[135] S. Baek, P. Ko and P. Wu, *Heavy quark-philic scalar dark matter with a vector-like fermion portal*, *JCAP* **07** (2018) 008 [1709.00697].

[136] S. Colucci, B. Fuks, F. Giacchino, L. Lopez Honorez, M. H. G. Tytgat and J. Vandecasteele, *Top-philic Vector-Like Portal to Scalar Dark Matter*, *Phys. Rev. D* **98** (2018) 035002 [1804.05068].

[137] A. Belyaev, A. Deandrea, S. Moretti, L. Panizzi and N. Thongyoi, *A fermionic portal to a non-abelian dark sector*, 2203.04681.

[138] B. Holdom, *Two U(1)'s and Epsilon Charge Shifts*, *Phys. Lett. B* **166** (1986) 196–198.

[139] T. G. Rizzo, *Kinetic Mixing and Portal Matter Phenomenology*, *Phys. Rev. D* **99** (2019), no. 11 115024 [1810.07531].

[140] T. D. Rueter and T. G. Rizzo, *Building Kinetic Mixing From Scalar Portal Matter*, 2011.03529.

[141] M. Buchkremer, G. Cacciapaglia, A. Deandrea and L. Panizzi, *Model Independent Framework for Searches of Top Partners*, *Nucl. Phys. B* **876** (2013) 376–417 [1305.4172].

[142] A. Djouadi and P. Gambino, *Electroweak gauge bosons selfenergies: Complete QCD corrections*, *Phys. Rev. D* **49** (1994) 3499–3511 [hep-ph/9309298]. [Erratum: Phys.Rev.D 53, 4111 (1996)].

[143] G. Cacciapaglia, A. Deandrea, L. Panizzi, N. Gaur, D. Harada and Y. Okada, *Heavy Vector-like Top Partners at the LHC and flavour constraints*, *JHEP* **03** (2012) 070 [1108.6329].

[144] Y. Okada and L. Panizzi, *LHC signatures of vector-like quarks*, *Adv. High Energy Phys.* **2013** (2013) 364936 [1207.5607].

[145] T. Ma and G. Cacciapaglia, *Fundamental Composite 2HDM: SU(N) with 4 flavours*, *JHEP* **03** (2016) 211 [1508.07014].

[146] Y. Wu, T. Ma, B. Zhang and G. Cacciapaglia, *Composite Dark Matter and Higgs*, *JHEP* **11** (2017) 058 [1703.06903].

[147] L. Ackerman, M. R. Buckley, S. M. Carroll and M. Kamionkowski, *Dark Matter and Dark Radiation*, *Phys. Rev. D* **79** (2009) 023519 [0810.5126].

[148] D. Feldman, Z. Liu and P. Nath, *The Stueckelberg Z-prime Extension with Kinetic Mixing and Milli-Charged Dark Matter From the Hidden Sector*, *Phys. Rev. D* **75** (2007) 115001 [hep-ph/0702123].

[149] **ATLAS** Collaboration, M. Aaboud *et. al.*, *Combination of the searches for pair-produced vector-like partners of the third-generation quarks at* $\sqrt{s} = 13$ *TeV with the ATLAS detector*, *Phys. Rev. Lett.* **121** (2018), no. 21 211801 [1808.02343].

[150] A. Semenov, *Lanhep—a package for the automatic generation of feynman rules in field theory. version 3.0*, *Computer Physics Communications* **180** (Mar, 2009) 431–454.

[151] A. Alloul, N. D. Christensen, C. Degrande, C. Duhr and B. Fuks, *FeynRules 2.0 - A complete toolbox for tree-level phenomenology*, *Comput. Phys. Commun.* **185** (2014) 2250–2300 [1310.1921].

[152] A. Belyaev, N. D. Christensen and A. Pukhov, *CalcHEP 3.4 for collider physics within and beyond the Standard Model*, *Comput. Phys. Commun.* **184** (2013) 1729–1769 [1207.6082].

[153] T. Hahn, *Generating Feynman diagrams and amplitudes with FeynArts 3*, *Comput. Phys. Commun.* **140** (2001) 418–431 [hep-ph/0012260].

[154] C. Degrande, C. Duhr, B. Fuks, D. Grellscheid, O. Mattelaer and T. Reiter, *UFO - The Universal FeynRules Output*, *Comput. Phys. Commun.* **183** (2012) 1201–1214 [1108.2040].

[155] M. Bondarenko, A. Belyaev, J. Blandford, L. Basso, E. Boos, V. Bunichev *et. al.*, *High Energy Physics Model Database: Towards decoding of the underlying theory (within Les Houches 2011: Physics at TeV Colliders New Physics Working Group Report)*, 1203.1488.

[156] J. Alwall, R. Frederix, S. Frixione, V. Hirschi, F. Maltoni, O. Mattelaer, H. S. Shao, T. Stelzer, P. Torrielli and M. Zaro, *The automated computation of tree-level and next-to-leading order differential cross sections, and their matching to parton shower simulations*, *JHEP* **07** (2014) 079 [1405.0301].

[157] V. Shtabovenko, R. Mertig and F. Orellana, *FeynCalc 9.3: New features and improvements*, *Comput. Phys. Commun.* **256** (2020) 107478 [2001.04407].

[158] V. Shtabovenko, *FeynHelpers: Connecting FeynCalc to FIRE and Package-X*, *Comput. Phys. Commun.* **218** (2017) 48–65 [1611.06793].

[159] H. H. Patel, *Package-X 2.0: A Mathematica package for the analytic calculation of one-loop integrals*, *Comput. Phys. Commun.* **218** (2017) 66–70 [1612.00009].

[160] T. Hahn, S. Paßehr and C. Schappacher, *FormCalc 9 and Extensions*, *PoS* **LL2016** (2016) 068 [1604.04611].

[161] **Fermi-LAT** Collaboration, M. Ackermann *et. al.*, *The Fermi Galactic Center GeV Excess and Implications for Dark Matter*, *Astrophys. J.* **840** (2017), no. 1 43 [1704.03910].

[162] R. K. Leane, T. R. Slatyer, J. F. Beacom and K. C. Y. Ng, *GeV-scale thermal WIMPs: Not even slightly ruled out*, *Phys. Rev. D* **98** (2018), no. 2 023016 [1805.10305].

[163] **NNPDF** Collaboration, R. D. Ball *et. al.*, *Parton distributions for the LHC Run II*, *JHEP* **04** (2015) 040 [1410.8849].

[164] A. Buckley, J. Ferrando, S. Lloyd, K. Nordström, B. Page, M. Rüfenacht, M. Schönherr and G. Watt, *LHAPDF6: parton density access in the LHC precision era*, *Eur. Phys. J. C* **75** (2015) 132 [1412.7420].

[165] **CMS** Collaboration, A. M. Sirunyan *et. al.*, *Search for top squarks and dark matter particles in opposite-charge dilepton final states at $\sqrt{s} = 13$ TeV*, *Phys. Rev. D* **97** (2018), no. 3 032009 [1711.00752].

[166] S. Bein, S.-M. Choi, B. Fuks, S. Jeong, D. W. Kang, J. Li and J. Sonneveld, *Implementation of a search for stops in the di-lepton + missing energy channel (35.9 fb-1; 13 TeV; CMS-SUS-17-001)*, .

[167] **CMS** Collaboration, A. M. Sirunyan *et. al.*, *Search for production of four top quarks in final states with same-sign or multiple leptons in proton-proton collisions at $\sqrt{s} = 13$ TeV*, *Eur. Phys. J. C* **80** (2020), no. 2 75 [1908.06463].

[168] L. Darmé and B. Fuks, *Re-implementation of a search for four-top quark production with leptonic final states (137 fb-1; CMS-TOP-18-003)*, .

[169] ATLAS-CONF-2021-024, *Search for pair-production of vector-like quarks in pp collision events at $\sqrt{s} = 13$ ˜TeV with at least one leptonically-decaying Z ˜boson and a third-generation quark with the ATLAS detector*, .

[170] CMS, *Search for pair production of vector-like quarks in leptonic final states in proton-proton collisions at $\sqrt{s} = 13$ TeV*, 2209.07327.

[171] **Muon g-2** Collaboration, G. W. Bennett *et. al.*, *Measurement of the positive muon anomalous magnetic moment to 0.7 ppm*, *Phys. Rev. Lett.* **89** (2002) 101804 [hep-ex/0208001]. [Erratum: Phys.Rev.Lett. 89, 129903 (2002)].

[172] **Muon g-2** Collaboration, G. W. Bennett *et. al.*, *Measurement of the negative muon anomalous magnetic moment to 0.7 ppm*, *Phys. Rev. Lett.* **92** (2004) 161802 [hep-ex/0401008].

[173] **Muon g-2** Collaboration, G. W. Bennett *et. al.*, *Final Report of the Muon E821 Anomalous Magnetic Moment Measurement at BNL*, *Phys. Rev. D* **73** (2006) 072003 [hep-ex/0602035].

[174] **Muon g-2** Collaboration, T. Albahri *et. al.*, *Magnetic-field measurement and analysis for the Muon $g-2$ Experiment at Fermilab*, *Phys. Rev. A* **103** (2021), no. 4 042208 [2104.03201].

[175] **Muon g-2** Collaboration, T. Albahri *et. al.*, *Measurement of the anomalous precession frequency of the muon in the Fermilab Muon $g-2$ Experiment*, *Phys. Rev. D* **103** (2021), no. 7 072002 [2104.03247].

[176] **Muon g-2** Collaboration, B. Abi *et. al.*, *Measurement of the Positive Muon Anomalous Magnetic Moment to 0.46 ppm*, *Phys. Rev. Lett.* **126** (2021), no. 14 141801 [2104.03281].

[177] T. Mibe, *Measurement of muon g-2 and edm with an ultra-cold muon beam at j-parc*, *Nuclear Physics B - Proceedings Supplements* **218** (2011), no. 1 242–246. Proceedings of the Eleventh International Workshop on Tau Lepton Physics.

[178] M. Abe *et. al.*, *A New Approach for Measuring the Muon Anomalous Magnetic Moment and Electric Dipole Moment*, *PTEP* **2019** (2019), no. 5 053C02 [1901.03047].

[179] T. A. et al., *The anomalous magnetic moment of the muon in the standard model*, *Physics Reports* **887** (2020) 1–166. The anomalous magnetic moment of the muon in the Standard Model.

[180] G. Colangelo, M. Hoferichter and P. Stoffer, *Constraints on the two-pion contribution to hadronic vacuum polarization*, *Physics Letters B* **814** (2021) 136073.

[181] T. Aoyama, M. Hayakawa, T. Kinoshita and M. Nio, *Complete tenth-order qed contribution to the muon $g-2$*, *Phys. Rev. Lett.* **109** (Sep, 2012) 111808.

[182] T. Aoyama, T. Kinoshita and M. Nio, *Theory of the anomalous magnetic moment of the electron*, *Atoms* **7** (Feb, 2019) 28.

[183] A. Czarnecki, W. J. Marciano and A. Vainshtein, *Refinements in electroweak contributions to the muon anomalous magnetic moment*, *Phys. Rev. D* **67** (Apr, 2003) 073006.

[184] C. Gnendiger, D. Stöckinger and H. Stöckinger-Kim, *The electroweak contributions to $(g-2)_\mu$ after the higgs-boson mass measurement*, *Phys. Rev. D* **88** (Sep, 2013) 053005.

[185] M. Davier, A. Hoecker, B. Malaescu and Z. Zhang, *Reevaluation of the hadronic vacuum polarisation contributions to the Standard Model predictions of the muon $g-2$ and $\alpha(m_Z^2)$ using newest hadronic cross-section data*, *Eur. Phys. J. C* **77** (2017), no. 12 827 [1706.09436].

[186] M. Hoferichter, B.-L. Hoid and B. Kubis, *Three-pion contribution to hadronic vacuum polarization*, *JHEP* **08** (2019) 137 [1907.01556].

[187] M. Davier, A. Hoecker, B. Malaescu and Z. Zhang, *A new evaluation of the hadronic vacuum polarisation contributions to the muon anomalous magnetic moment and to $\boldsymbol{\alpha(m_Z^2)}$*, *Eur. Phys. J. C* **80** (2020), no. 3 241 [1908.00921]. [Erratum: Eur.Phys.J.C 80, 410 (2020)].

[188] A. Kurz, T. Liu, P. Marquard and M. Steinhauser, *Hadronic contribution to the muon anomalous magnetic moment to next-to-next-to-leading order*, *Physics Letters B* **734** (2014) 144–147.

[189] K. Melnikov and A. Vainshtein, *Hadronic light-by-light scattering contribution to the muon anomalous magnetic moment reexamined*, *Phys. Rev. D* **70** (Dec, 2004) 113006.

[190] P. Masjuan and P. Sanchez-Puertas, *Pseudoscalar-pole contribution to the* $(g_\mu - 2)$*: A rational approach*, *Phys. Rev. D* **95** (Mar, 2017) 054026.

[191] G. Colangelo, M. Hoferichter, M. Procura and P. Stoffer, *Dispersion relation for hadronic light-by-light scattering: two-pion contributions*, *JHEP* **04** (2017) 161 [1702.07347].

[192] M. Hoferichter, B.-L. Hoid, B. Kubis, S. Leupold and S. P. Schneider, *Dispersion relation for hadronic light-by-light scattering: pion pole*, *JHEP* **10** (2018) 141 [1808.04823].

[193] A. Gérardin, H. B. Meyer and A. Nyffeler, *Lattice calculation of the pion transition form factor with* $N_f = 2 + 1$ *Wilson quarks*, *Phys. Rev. D* **100** (2019), no. 3 034520 [1903.09471].

[194] J. Bijnens, N. Hermansson-Truedsson and A. Rodríguez-Sánchez, *Short-distance constraints for the hlbl contribution to the muon anomalous magnetic moment*, *Physics Letters B* **798** (2019) 134994.

[195] G. Colangelo, F. Hagelstein, M. Hoferichter, L. Laub and P. Stoffer, *Longitudinal short-distance constraints for the hadronic light-by-light contribution to* $(g-2)_\mu$ *with large-*N_c *Regge models*, *JHEP* **03** (2020) 101 [1910.13432].

[196] T. Blum, N. Christ, M. Hayakawa, T. Izubuchi, L. Jin, C. Jung and C. Lehner, *Hadronic light-by-light scattering contribution to the muon anomalous magnetic moment from lattice qcd*, *Phys. Rev. Lett.* **124** (Apr, 2020) 132002.

[197] G. Colangelo, M. Hoferichter, A. Nyffeler, M. Passera and P. Stoffer, *Remarks on higher-order hadronic corrections to the muon g-2*, *Physics Letters B* **735** (2014) 90–91.

[198] A. Keshavarzi, D. Nomura and T. Teubner, $g-2$ *of charged leptons,* $\alpha(M_Z^2)$ *, and the hyperfine splitting of muonium*, *Phys. Rev. D* **101** (2020), no. 1 014029 [1911.00367].

[199] G. Colangelo, M. Hoferichter and P. Stoffer, *Two-pion contribution to hadronic vacuum polarization*, *Journal of High Energy Physics* **2019** (feb, 2019).

[200] H. Davoudiasl, H.-S. Lee and W. J. Marciano, *Dark Side of Higgs Diphoton Decays and Muon g-2*, *Phys. Rev. D* **86** (2012) 095009 [1208.2973].

[201] D. K. Hong and D. H. Kim, *Composite (pseudo) scalar contributions to muon g − 2*, *Phys. Lett. B* **758** (2016) 370–372 [1602.06628].

[202] **NA64** Collaboration, Y. M. Andreev *et. al.*, *Constraints on New Physics in Electron $g-2$ from a Search for Invisible Decays of a Scalar, Pseudoscalar, Vector, and Axial Vector*, *Phys. Rev. Lett.* **126** (2021), no. 21 211802 [2102.01885].

[203] P. Das, M. K. Das and N. Khan, *The FIMP-WIMP dark matter in the extended singlet scalar model*, *Nucl. Phys. B* **975** (2022) 115677 [2104.03271].

[204] X. Qi, A. Yang, W. Liu and H. Sun, *Scalar dark matter and muon g-2 in a model **, *Chin. Phys. C* **46** (2022), no. 8 083102 [2106.14134].

[205] S. Arora, M. Kashav, S. Verma and B. C. Chauhan, *Muon $(g-2)$ and the W-boson mass anomaly in a model based on Z4 symmetry with a vector-like fermion*, *PTEP* **2022** (2022), no. 11 113B06 [2207.08580].

[206] J. Kawamura, S. Okawa and Y. Omura, *W boson mass and muon g-2 in a lepton portal dark matter model*, *Phys. Rev. D* **106** (2022), no. 1 015005 [2204.07022].

[207] K. Fukushima and J. Kumar, *Dipole moment bounds on dark matter annihilation*, *Phys. Rev. D* **88** (Sep, 2013) 056017.

[208] J. Kopp, L. Michaels and J. Smirnov, *Loopy constraints on leptophilic dark matter and internal bremsstrahlung*, *Journal of Cosmology and Astroparticle Physics* **2014** (apr, 2014) 022.

[209] G. Arcadi, L. Calibbi, M. Fedele and F. Mescia, *Muon $g-2$ and b anomalies from dark matter*, *Phys. Rev. Lett.* **127** (Aug, 2021) 061802.

[210] Y. Bai and J. Berger, *Muon g-2 in lepton portal dark matter*, 2021.

[211] K. Ghorbani, *Light vector dark matter with scalar mediator and muon g-2 anomaly*, *Phys. Rev. D* **104** (2021), no. 11 115008 [2104.13810].

[212] K.-C. Yang, *Hidden Higgs portal vector dark matter for the Galactic center gamma-ray excess from the two-step cascade annihilation, and muon $g-2$*, *JHEP* **08** (2018) 099 [1806.05663].

[213] S. R. Moore, K. Whisnant and B.-L. Young, *Second Order Corrections to the Muon Anomalous Magnetic Moment in Alternative Electroweak Models*, *Phys. Rev. D* **31** (1985) 105.

[214] B. Yu and S. Zhou, *General remarks on the one-loop contributions to the muon anomalous magnetic moment*, *Nucl. Phys. B* **975** (2022) 115674 [2106.11291].

[215] A. Greljo, P. Stangl, A. E. Thomsen and J. Zupan, *On (g - 2)μ from gauged u(1)x*, *Journal of High Energy Physics* **2022** (jul, 2022).

[216] I. Bars and M. Yoshimura, *Muon magnetic moment in a finite theory of weak and electromagnetic interaction*, *Phys. Rev. D* **6** (1972) 374–376.

[217] P. A. et al., *Search for heavy neutral and charged leptons in e+e- annihilation at lep*, *Physics Letters B* **517** (2001), no. 1 75–85.

[218] **ATLAS** Collaboration, G. Aad *et. al.*, *Search for electroweak production of charginos and sleptons decaying into final states with two leptons and missing transverse momentum in* $\sqrt{s} = 13$ *TeV pp collisions using the ATLAS detector*, *Eur. Phys. J. C* **80** (2020), no. 2 123 [1908.08215].

[219] **CMS** Collaboration, A. M. Sirunyan *et. al.*, *Search for electroweak production of charginos and neutralinos in multilepton final states in proton-proton collisions at* $\sqrt{s} = 13$ *TeV*, *JHEP* **03** (2018) 166 [1709.05406].

[220] **CMS** Collaboration, A. M. Sirunyan *et. al.*, *Search for disappearing tracks in proton-proton collisions at* $\sqrt{s} = 13$ *TeV*, *Phys. Lett. B* **806** (2020) 135502 [2004.05153].

[221] K. Hagiwara, R. D. Peccei, D. Zeppenfeld and K. Hikasa, *Probing the Weak Boson Sector in e+ e- —> W+ W-*, *Nucl. Phys. B* **282** (1987) 253–307.

[222] T. Hahn and M. Pérez-Victoria, *Automated one-loop calculations in four and d dimensions*, *Computer Physics Communications* **118** (1999), no. 2 153–165.